# Mechanical Microscopy of Biological Structures: Investigations on The Mechanical Resonance of Tissues and Cells

**Thesis**

*Submitted in partial fulfillment of the requirements for the degree of*

**DOCTOR OF PHILOSOPHY**

*By*

**Diplesh Gautam**
ID No. 2018PHXF0436P

*Under the supervision of*

**Dr. Venkatesh Kadbur Prabhakar Rao**


BIRLA INSTITUTE OF TECHNOLOGY AND SCIENCE, PILANI, PILANI CAMPUS,
PILANI - 333031, RAJASTHAN, INDIA
October 2023

**BIRLA INSTITUTE OF TECHNOLOGY AND SCIENCE, PILANI**

# Certificate

This is to certify that the thesis entitled, "*Mechanical Microscopy of Biological Structures: Investigations on The Mechanical Resonance of Tissues and Cells*" submitted by **Diplesh Gautam** ID No. 2018PHXF0436P for award of Ph.D. of the Institute embodies original work done by him/her under my supervision.

---

*Supervisor*
**Dr. Venkatesh Kadbur Prabhakar Rao**
Assistant Professor,
BITS Pilani, Pilani Campus
Date:

*"Cells are the fundamental unit of life, and understanding their mechanical behavior is crucial for understanding how tissues and organisms function"*

James Weaver

**BIRLA INSTITUTE OF TECHNOLOGY AND SCIENCE, PILANI**

# *Abstract*

**DOCTOR OF PHILOSOPHY**

**Mechanical Microscopy of Biological Structures: Investigations on The Mechanical Resonance of Tissues and Cells**

by **Diplesh Gautam**

Biological cells are complex dynamic systems with highly integrated structures that can respond to external stimuli such as mechanical forces, chemical potentials, electrical impulses, etc. Their mechanical properties are crucial for maintaining proper physiological function. When these properties are impaired, it can lead to various diseases. Additionally, changes in the mechanical response of cells can sometimes be an indicator of a diseased state and can even contribute to the development of a disorder. The primary objective of this thesis is to investigate the mechanical properties of biological materials such as cells and tissues from an indigenous developed experimental technique and correlate their behavior to computational studies.

Several frequency-based approaches are developed and employed to target diseases. However, these typically function by stimulating cells with their inherent frequency, which causes resonance and cell damage. Hence, it is important to understand the natural frequency of a cell because it is a characteristic determined by their mass and stiffness. Theoretical models are framed for the estimation of cell resonance. In the current study, the natural frequency of biological cells was derived from an extension theory of drop oscillations proposed by Rayleigh and Lamb. Rayleigh derived an equation for the frequency of natural oscillations of a drop, whereas Lamb carried the same for a drop in a viscous fluid. The objective is to develop a technique that provides a framework for identifying pathological conditions such as cancer and vascular disorders. A key part of this objective is to understand the cell response to external mechanical stimuli, which can give insight into its behavior. Even for the same cell type, experimentally obtained material cell characteristics differ by orders of magnitude compared to theoretical methods. The experimental method and the theoretical models were utilized to interpret the results and the fundamental causes of this difference. Experimental and theoretical differences in the mechanical characteristics of the cells can only be reconciled by establishing a strong mathematical framework which was achieved in the present work. Prior validation of the developed experimental techniques was achieved by successfully conducting work on macro-scale biological organs (Femur bone and skin).

In biological systems, like a cell, cytoplasmic viscosity influences biomolecule diffusion, which is essential for diffusion-driven intramolecular interactions to carry out signaling pathways. Changes

in intracellular viscosity may affect molecule transport and basal bio-molecular reaction rates, altering cell homeostasis and health. Therefore, it becomes imperative to monitor intracellular viscosity in live cells. Considering the above parameters, this study reports the development of an experimental setup to evaluate the frequency-based viscosity in cells. Our regimen is sensitive and can also measure slight alterations in intracellular viscosity. Understanding the behavior of a cell in an experimental condition would benefit significantly from its prospective mechanical model. Characterizing the in-vivo response of cells necessitates a mathematical model of the extracellular matrix's embedding environment. Most studies on external stimulation in biomechanics have relied on either an iterative mathematical solution of the individual solid phases or a sequential solution of the whole domain utilizing a linked approach.

Nowadays, cancer research focuses on identifying methods that trigger cancer cell death without damaging the surrounding normal cells. Mechanical vibration is a possible biocompatible treatment approach and is a subject of mechanomedicine in the field of cancer. Hence the effects of low-frequency mechanical vibration (20 Hz to 60 Hz) on Huh-7 cells and their viability were investigated. Further traditional flow cytometry was used to measure the two main cell deaths in the cells i.e. apoptosis and necrosis. Apoptosis and necrosis both involve cell death but differ in how it occurs. Apoptosis is a controlled process of cell death that is important for normal development and function in multicellular organisms. It is regulated and orderly. Necrosis is an uncontrolled process of cell death caused by injury or infection that can lead to inflammation and tissue damage. Which results in rapid cell destruction and the release of cell contents. Despite the fact that the exact mechanisms by which low-frequency mechanical vibration causes cell death through apoptosis and necrosis are not yet fully understood. The findings suggest that mechanical vibration could potentially be used as a form of mechanomedicine in cancer treatment.

Biological cells are the basic unit of life and play important roles in various biological activities. They are responsible for storing and replicating DNA and performing normal physiological functions through biochemical and transport pathways, as well as through their mechanical behavior. Without cells, biological systems could not exist or function, such as the circulation of red blood cells, which transport oxygen to body tissue in vertebrates. Cells also have specialized functions, such as fibroblasts which migrate to wounds and initiate the healing process, and endothelial cells, which line blood arteries and act as filtration barriers. The cytoskeleton, a network of polymeric filaments made up of actin, intermediate filaments, and microtubules, give cells rigidity and allows them to alter their mechanical characteristics in response to their environment. Focal adhesions (FAs) are large macromolecular complexes that allow cells to respond to mechanical force and regulate mechanosensitive information and play crucial roles in cellular functions such as proliferation, differentiation, and motility, as well as pathological processes like cancer and wound repair. These complex structures transmit mechanical force and regulate signals between cells and the extracellular matrix (ECM). It is important to understand the impact of changes in FAs stiffness on cell behavior. In this work, a novel computational

technique for analyzing cell resonance was studied with respect to different focal adhesion stiffness. We used a PSD-based non-invasive technique to measure the dynamics of Huh-7 cells and compared the results with numerical AFM. We evaluated the modal and frequency response of the cell by considering different ranges of focal adhesion stiffness. This work has the potential to improve our understanding of the resonance behavior of cells and could potentially be used to target diseased cells. Additionally, this study highlights the potential of using hyperelastic material models, which can simulate cells and other biological materials, to understand the hyper-elastic-viscoelastic behavior and resonance characteristics of cells.

There is a necessity to develop experimental platforms and techniques that can accurately regulate the mechanical microenvironment in order to understand the mechanisms and processes through which mechanical forces regulate cellular function. There are several experimental tools and methods that have been developed to evaluate a cell's stiffness, adhesion, contractility, and response to mechanical stimuli. Microfabrication technologies can offer viable solutions for addressing challenges in studying cell biomechanics and mechanobiology. Active microfluidics is a field that uses piezoelectric actuators to actively control the interfaces between microchannel boundaries, particles, and fluid. There are two ways in which this interfacial actuation can be achieved, depending on the signal used to drive the actuator: (1) low frequency, high amplitude actuation (typically around 1 MHz and 100 µm), and (2) high frequency, low amplitude actuation (usually around 100 MHz and 1 µm). This piezoelectric actuation can be used to regulate and control the transport of biological particles within microchannels, as well as for diagnostic and targeted treatment purposes in severe diseases. Hence, this research also focused on microfabricated piezoelectric actuation-based microchannel to regulate the transport of biological particles and morphological changes in the cell while flow, which directly applies to lab-on-a-chip approaches in cell separation and diagnosis.

Several drawbacks of experimental techniques such as limited spatial and temporal resolution, cost and time, ethical concern, and limited flexibility motivate us to look into some versatile, speedy, and cost-effective tools or preferred methods for analyzing biological cells and understanding the mechanisms underlying a wide range of biological processes. Molecular dynamics is a powerful tool that can be used to analyze biological cells, and in many cases, it is preferred over experimental methods for various reasons. One of the main advantages of MD simulation is that it allows for investigating processes that may be difficult or impossible to study experimentally. In the current study, computational modeling using the molecular dynamics approach was used to study the impact of external perturbation on the various constituents level of the cell and the behavior of the transmembrane protein in a molecular system. It is basically a biphasic representation of the molecular system comprised of semiviscous fluid and solid phases. The study reveals the significant changes in the biophysical behavior of membrane protein systems, potentially causing transmembrane proteins to become mechanically sensitive under mechanical stress. The

investigation results showed that the individual components of the membrane help to prevent the diffusion and detachment of proteins at high concentrations.

The results obtained from the present study are expected to provide several design development for biological samples. The idealization shall be modified to meet the similar characterizations of the biological samples to provide a better mechanical response. Future research will be devoted to attaining this task.

# *Acknowledgements*

First and foremost, I would like to praise and thank God, the almighty, for granting the blessing, knowledge, and perseverance so that I have finally been able to accomplish my tasks.

I want to express my profound, sincere thanks to my supervisor, **Dr. Venkatesh KP Rao**, for his guidance, support, and continuous encouragement throughout my doctoral study. Their genuine enthusiasm for this research topic created an atmosphere that was truly instrumental in the success of this work. His constructive criticisms have always helped to improve my skills and thereby grow as a student. I have always been impressed and admired by his calm and soothing nature, enthusiasm, and compassion. These qualities set a perfect example for a mentor, which I inspire and carry as an asset for the rest of my career. It was a privilege to carry out research under their supervision.

I express my heartfelt gratitude to **Prof. V Ramgopal Rao**, Vice-chancellor BITS Pilani, and **Prof. Sudhir Kumar Barai**, Director, BITS Pilani, Pilani campus, for their support and blessing. I am grateful to **Prof. Shamik Chakraborty**, Associate Dean, Academic Graduate Studies and Research Division (AGSRD), for his constant encouragement, support, and motivation. I want to thank **Prof. S. Routroy**, Head of the Department, Mechanical Engineering, for his guidance and support. I do sincerely appreciate all the help he has done, especially in challenging situations. I am extremely thankful to the Associate Dean of the Student Welfare Division, **Prof. Navin Singh**, for his kind interaction and willingness to help on many occasions. I would also like to thank **Prof. Rajdeep Chowdhury** and **Prof. Sudeshna Mukerjee** for their unwavering encouragement and support. I am grateful to have been offered the opportunity to work in their cancer laboratory established at the Birla Institute of Technology and Sciences, Pilani. Their mentorship has allowed me to be able to bring my contribution at the interfaces of engineering with medicine and life science toward the development of novel noninvasive techniques. My thanks are also extended to members of their laboratory, in particular **Dr. Abhilasha Shrivastava** and **Miss. Simran Khanna**, for their help on bioassays.

I wish to thank the members of the Department Research Committee (DRC), Department of Mechanical Engineering, for their consideration in many tough situations. Specifically, I take this moment to express my recognition to **Prof. Arun Kumar Jalan**, DRC Convenor, Department of Mechanical Engineering for his valuable suggestions and encouragement. I am extremely grateful to the Doctoral Advisory Committee (DAC) members **Prof. Rajdeep Chowdhury** and **Dr. A R Harikrishnan** for assessing and evaluating my research work and the timely submissions of the reports. The support they gave me throughout my Ph.D. journey is commendable and the feedback provided has greatly helped in self-improvement and value addition. I wish to thank all the faculty members of the Department of Mechanical Engineering for their support, cooperation, and encouragement during my Ph.D. Special thanks to **Prof. Gautam Singhvi**,

**Prof. Inamur Rahaman Laskar**, **Prof. Syamantak Majumder**, **Prof. R.P Mishra** and **Prof. Sharad Shrivastava** for their encouragement and for helping me in the research to build confidence during my difficult times. I also want to thank **Prof. N.V.M. Rao**, Unit Chief of the Centralized Purchasing Unit (CPU) at BITS Pilani, for providing all the necessary equipment and materials in a timely manner, which allowed me to set up the experimental platforms and conduct the experiments smoothly.

I wish to thank my fellow research scholars of the Department of Mechanical Engineering for the direct and indirect support they have given throughout my Ph.D. tenure. Specifically, I thank my dear friend **Mr. Harsh Sharma** for confronting me during tough situations and giving useful advice during this period. I sincerely thank my friend **Mr. Nizam Ahmed**, who help me throughout in understanding the biological keywords. I am grateful to my friend **Mr. Ayush Owhal** for his assistance and support with various academic matters throughout my Ph.D. studies. I thank **Mrs. Pradnya Chabbi**, **Mr. Ashish Khare**, **Mr. Naveen P T**, **Mr. Dhruv Deshwal**, **Mr. Vasudev Singh Senger**, and **Mr. Pradeep Shukla**, who have endlessly supported me in many academic aspects, and motivated me to attain physical well-being. I am thankful to my supervisor's family, **Mrs. Padmini** and **Mr. Sripada**, for the excellent hospitality that they provided during family gatherings.

Finally, I would like to thank my family and friends for their unconditional support during my studies. My profound gratitude goes to my wife, **Mrs. Deepali Gautam**, for her patience, understanding, and unconditional support and help. Words are not enough to express my thoughts for sacrificing the comfort of her life and providing incessant support throughout my PhD. The way she looked after the kids (**Mayra** and **Raghav**) during all stages of the journey is highly appreciable. I am extremely thankful to my dear parents, **Mr. Jagannath Prasad Gautam** and **Mrs. Gauri Gautam**; my brothers **Mr. Deepak Gautam**, **Mr. Abhilash Gautam**, and **Mr. Prakash Gautam**; my sisters **Mrs. Madhu**, **Mrs. Suman**, **Mrs. Mano**, **Mrs. Sarla** and my in-laws for their constant support and cooperation during my PhD Journey. Their contribution is indispensable to fulfilling my dreams. Finally, I take this opportunity to extend my sincere appreciation to all my relatives who actively and passively supported me during my PhD...

**Diplesh Gautam**

# Contents


**1 Introduction** **1**
- 1.1 Background . . . 1
- 1.2 Measurement methods for mechanical properties of single cells . . . 5
  - 1.2.1 Atomic Force Microscopy (AFM) . . . 6
  - 1.2.2 Microfluidics methods (MM) . . . 8
  - 1.2.3 Micropipette aspiration . . . 9
  - 1.2.4 Parallel-plate technique . . . 10
  - 1.2.5 Magnetic twisting cytometry (MTC) and magnetic tweezers(MT) . . . 11
  - 1.2.6 Optical stretchers (OS) and Optical tweezers (OT) . . . 12
  - 1.2.7 Acoustic methods (AM) . . . 13
- 1.3 Modal analysis techniques . . . 15
  - 1.3.1 Classification according to the number of input and output locations . . . 17
  - 1.3.2 Classification according to the type of identified dynamic properties . . . 17
  - 1.3.3 Excitation methods . . . 19
  - 1.3.4 Measurements methods . . . 22
- 1.4 Motivation . . . 23
- 1.5 Gaps in existing research . . . 25
- 1.6 Focus and Scope of the research . . . 26
- 1.7 Objectives of the proposed research . . . 32
- 1.8 Outline of the thesis . . . 32

**2 Nondestructive Evaluation of Mechanical Properties of Femur Bone** **36**
- 2.1 Background . . . 36
- 2.2 Introduction . . . 37
- 2.3 Materials and Methods . . . 41
  - 2.3.1 Numerical Modelling . . . 41
  - 2.3.2 Experimental Studies . . . 44
  - 2.3.3 Response Measurements . . . 45
  - 2.3.4 Evaluation of Young's Modulus . . . 45
  - 2.3.5 Random Vibration Analysis . . . 46
- 2.4 Results . . . 46
  - 2.4.1 Experimental Studies . . . 46
  - 2.4.2 Numerical Analysis . . . 48
- 2.5 Discussions . . . 50
- 2.6 Conclusions . . . 52

**3 Effect of nanocarrier additives on biomechanical response of a rat skin** **53**

3.1 Background . . . 53
3.2 Introduction . . . 54
3.3 Materials and Methods . . . 57
3.3.1 Materials . . . 57
3.3.2 Formulation development . . . 57
3.3.3 Preparation of skin samples . . . 58
3.3.4 Numerical Analysis . . . 58
3.3.5 Non-contact measurements using PSD . . . 60
3.3.6 Estimation of Modulus of Elasticity . . . 61
3.3.7 Uniaxial tensile testing . . . 62
3.3.8 Statistical analysis . . . 62
3.4 Results . . . 62
3.4.1 Characterization of developed formulation . . . 62
3.4.2 Numerical Analysis . . . 63
3.4.3 Experimental Analysis . . . 63
3.5 Discussion . . . 68
3.6 Conclusion . . . 69

**4 Mechanical microscopy of cancer cells: TGF-$\beta$ induced EMT corresponds to low intracellular viscosity in cancer cells 71**
4.1 Background . . . 71
4.1.1 Importance of cell mechanics . . . 71
4.1.2 Understanding the mechanical behavior of cancer cells . . . 72
4.2 Introduction . . . 72
4.3 Materials and Methods . . . 77
4.3.1 Cell culture . . . 77
4.3.2 Confocal microscopy . . . 78
4.3.3 Immunoblotting . . . 78
4.3.4 Analysis of uptake of TPSII . . . 78
4.3.5 Cell Cycle Analysis . . . 78
4.3.6 Measuring frequency response . . . 79
4.3.7 Determination of Viscosity . . . 79
4.3.8 Cell spreading analysis . . . 81
4.3.9 Statistical analysis. . . . 81
4.3.10 Numerical analysis . . . 81
4.3.11 Modal Analysis . . . 83
4.3.12 Harmonic Analysis . . . 83
4.3.13 Hyperelastic model . . . 84
4.4 Results . . . 85
4.4.1 Aggravated extra-cellular viscosity enhances intra-cellular viscosity in cancer cells . . . 85
4.4.2 Intracellular viscosity is associated with migratory/invasive potential of a cell 85
4.4.3 High viscosity suppresses cell migration . . . 87
4.5 Numerical Results . . . 89
4.5.1 Modal Analysis . . . 89
4.5.2 Harmonic Analysis . . . 90
4.6 Discussion . . . 91

4.7 Conclusion . . . 95

**5 Modulating the Mechanical Resonance of Huh-7 Cells Based on Elasticity of Adhesion Proteins 97**
5.1 Background . . . 97
5.1.1 Crosstalk between the cell and extracellular environment . . . 97
5.2 Introduction . . . 98
5.3 Materials and Method . . . 101
5.3.1 Cell culture . . . 101
5.3.2 Mechanical Behavior of Filaments and Cells . . . 101
5.3.3 Experimental frequency response of a cell . . . 102
5.3.4 Microscopic Imaging . . . 103
5.3.5 Computational Model of a Cell . . . 103
5.4 Results . . . 106
5.4.1 Frequency response using non-invasive experimental technique . . . 106
5.4.2 Numerical Force indentation on Huh-7 cell . . . 107
5.4.3 Modal analysis . . . 109
5.4.4 Harmonic analysis . . . 110
5.5 Discussion . . . 111
5.6 Conclusion . . . 113

**6 Effect of low-frequency excitation on the apoptosis of Huh-7 cells 114**
6.1 Background . . . 114
6.2 Introduction . . . 115
6.3 Materials and Methods . . . 117
6.3.1 Maintenance of HCC cell lines . . . 117
6.3.2 Cell vibration . . . 118
6.3.3 Cell Viability Assay . . . 118
6.3.4 Annexin V/Propidium Iodide (PI) staining . . . 118
6.3.5 Cell size quantification . . . 119
6.3.6 Measuring frequency response . . . 119
6.4 Analytical frequency response . . . 120
6.5 Results . . . 121
6.5.1 Cellular morphology of Huh-7 after external excitation . . . 121
6.5.2 Analytical Frequency response of Huh-7 after excitation . . . 123
6.5.3 Experimental Frequency assess of Huh-7 after excitation . . . 124
6.5.4 Low-frequency excitation reduces the viability of Huh-7 cells . . . 124
6.5.5 Low frequency causes apoptotic as well as necrotic cell death in Huh-7 cells 126
6.6 Discussions . . . 126
6.7 Conclusion . . . 129

**7 Development of smart microchannel device for cell diagnostics: Insight of resonance behaviour of Huh-7 and their cellular morphology 131**
7.1 Background . . . 131
7.2 Introduction . . . 132
7.3 Material and Methods . . . 135
7.3.1 Materials . . . 135
7.3.2 Mechanical and electrical characterization of the microchannel. . . . 137

7.3.3 Cell culture and viability analysis . . . 137
7.3.4 Cell morphology analysis . . . 138
7.3.5 Experimental frequency response . . . 139
7.4 Result . . . 140
7.4.1 Characterization of ZnO nanoparticles . . . 140
7.4.2 Mechanical and Electrical characterization of the piezo material based microchannel . . . 141
7.4.3 Morphological changes . . . 142
7.4.4 Experimental Frequency Response . . . 143
7.4.5 Cell death analysis . . . 144
7.5 Discussion . . . 145
7.6 Conclusion . . . 147

**8 Atomistic analysis of effect of cholesterol on cancerous membrane protein system: Unfolding and associated resistance stresses under strain 149**
8.1 Background . . . 149
8.2 Introduction . . . 150
8.3 Methods . . . 153
8.4 Results . . . 156
8.4.1 Structural parameters . . . 156
8.4.2 MSD and Diffusion coefficient . . . 158
8.4.3 Behavior of transmembrane protein under membrane-protein sepration . . . 160
8.4.4 Electron density profile . . . 162
8.4.5 Average resistance stress . . . 162
8.5 Discussion . . . 163
8.6 Conclusion . . . 165

**9 Conclusions and future scope 167**

**A Cells as a standard Voigt model 173**

**Bibliography 178**

# List of Figures


1.1 A schematic of a generalized cell structure: comprehending the fundamental components of life [1]. . . . 2
1.2 Unraveling the influence of microenvironmental stimuli on cell behaviors and functions: A schematic representation of force factors. [2]–[4] . . . 3
1.3 Exploring the mechanics of cancer cells: A comprehensive overview of major techniques. (a) atomic force spectroscopy; (b) magnetic twisting cytometry; (c) cytoindentation; (d) microplate stretcher; (e) micropipette aspiration; (f) laser/optical tweezers; (g) optical stretcher; (h) shear flow; (i) microfluidic assay; (j) microfabricated post array; (k) particle tracking microrheology; (l) magnetic nanoparticle-based stimuli. This figure is reused with permission from Suresh et.al. [1] . . . 4
1.4 Atomic force spectroscopy for the measurement of cell deformation. Inset showing different indentor tips. [11] . . . 6
1.5 An overview of techniques used in 2D microfluidics to study intercellular interactions at the single-cell level. [26] . . . 8
1.6 Schematic illustration of micropipette aspiration technique [32] . . . 9
1.7 Parallel plate technique for measuring the cellular deformation. [39] . . . 11
1.8 MTC technique for the dynamic measurement of the different parts of cellular structure. [27], [53] . . . 12
1.9 Optical trapping and stretching technique for the measurement of the cellular deformation in the structure. [57] . . . 13
1.10 Acoustic wave generation through piezoelectric materials: a) Expanding and contracting surface via the voltage applied to the electrodes. b) Separation of bacteria from blood cells using a standing SAW technique. [66] . . . 14
1.11 Schematic illustration of a controllable method for stimulating cells using gigahertz ultrasonic device-generated acoustic streaming. The system enables observation of cell deformations and excitations. [76] . . . 19
1.12 Nanovibrational Stimulation of Mesenchymal Stem Cells induces therapeutic reactive oxygen species using defined media and chemicals. Adapted from Wich Orapiriyakul et. al. 2020. [77] . . . 20
1.13 External stimulation of cells in cultured Petri dish through the piezo disc attached at the base of the plate. . . . 21

2.1 Structure of femur bone[79]. . . . 37
2.2 Homogenization Process using CMAS. . . . 42
2.3 (a) Experimental setup for the mechanical response of femur bone. (b) Loading and boundary conditions of the femur bone. . . . 45
2.4 (a) Frequency responses of the bone sample and base support. (b) The transfer function of bone w.r.t base . . . 47

2.5 Comparison between experimental and analytical modeshapes. . . . . 47
2.6 Time domain response of the bone sample with exponential decay for vibration amplitude. . . . . 48
2.7 Numerical modeshapes a) First Mode, b) Second Mode, c) Third Mode. . . . . 49
2.8 Random base excitation response of the femur bone. . . . . 49

3.1 Schematic of experimental procedure to measure the dynamics response of skin. . 60
3.2 Experimental setup for noncontact measurements on skin. . . . . 61
3.3 Mode shapes at different frequencies with the color bar showing deformation in mm. 64
3.4 a) Frequency response for skin sample and support. b) Transfer function. . . . . 65
3.5 Effect of time on the fundamental frequency of the skin. Each group represents the mean and standard deviation of the change in the fundamental frequency of the skin samples (n=3) [$\star\star$ represents the significance difference $p < 0.05$ (t-test) as compared to the other groups up to 12 hrs]. . . . . 65
3.6 Effect of time on Elastic modulus of the skin. Each group represents the mean and standard deviation of the change in the fundamental frequency of the skin samples (n=3) [$\star\star$ represents the significance difference $p < 0.05$ (t-test) as compared to the other groups up to 12 hrs.] . . . . . 66
3.7 Stress-strain curve for normal skin. a) Image during Dermis breakage. b) Image during Epidermis breakage. The slope of the curve represents the elastic modulus of the skin. . . . . 66
3.8 a) Deformation with respect to SC thickness. b) Von Mises's stress with respect to SC thickness. . . . . 67
3.9 a) Total deformation distribution in normal skin. b) Maximum von mise's stress distribution in normal skin. . . . . 67

4.1 Cell marker changes in EMT. During EMT, epithelial cells lose their cell membrane epithelial markers and acquire mesenchymal markers and metastatic traits. . . . 73
4.2 Inhibition of Tgf-$\beta$ during EMT showing activation and deactivation of various biological activities. . . . . 75
4.3 Detailed procedure for the PSD-based non-invasive experimental technique a) Experimental setup for the dynamic response of the cancerous cell. b) High contrast image of TGF-$\beta$ induced Huh-7 cells with cell frequency response in blue and base response in red. c) Transfer function of the frequency response of cell and base. d) Estimation of Q factor from frequency response. . . . . 80
4.4 a) Confocal images of the Huh-7 cells treated with 5ng/ml TGF-$\beta$ and control. b) Cell selection for cellular geometry for the numerical simulation in inset I) 3D model obtained from Image-J as STL Format. II) Discretized model in small elements. III) Stress distribution in the model after the application of load on the model. c) Mechanical model of the cell structure along with the boundary conditions. . . . . 82
4.5 Detailed flow diagram depicting the procedure followed for numerical analysis . . 83

4.6 Analysis of intracellular viscosity with viscosity inducers like PEG and Glucose through PSD a) Transfer function plot for different viscosity modulators. Consecutive Peaks represent the natural frequency of the cells treated with different types of drug modulators. b) Frequency comparison plot for PEG and 200 mM glucose compared to control (For n = 3 with the Mean value ± SEM). Obtained frequency for PEG is higher (4350 Hz) compared to glucose and control. c) Viscosity plot for PEG and 200 mM glucose compared to control obtained from the frequency response of the cells shows the higher values for 5% PEG due to higher natural frequency for the 5% PEG treated cells. (For n= 3 with the Mean value ± SEM) 86

4.7 Analysis of intracellular viscosity with viscosity inducers like PEG and Glucose through Viscosity sensitive fluorescent probe a) Fluorescence intensity after PEG and 200mM glucose in cancer cells. b) Shift in peak after TPSII exposure for PEG and 200 mM glucose compared to control. . . . . 87

4.8 Repression in intracellular viscosity post TGF-$\beta$ induced EMT a) Transfer function for control and TGF-$\beta$ and for invasive and non-invasive cell lines. Corresponding higher peaks represents the natural frequency of the cells. b) Frequency comparison plot for TGF-$\beta$ compared to control (For n=3 with the Mean value ±SEM). c) Viscosity comparison for TGF-$\beta$ compared to control (For n=3 with the Mean value ± SEM) d) Transfer function for invasive and non-invasive cell lines. Corresponding higher peaks represents the natural frequency of the cells. f) Frequency comparison plot for MCF-7 compared to MDAMB-231(For n=3 with the Mean value ± SEM) g) Viscosity comparison for MCF-7 compared to MDAMB-231(For n=3 with the Mean value ± SEM) . . . . . 88

4.9 (a) Frequency for cells subjected to different viscosity modulators (b) Viscosity for cells subjected to different viscosity modulators. . . . . 88

4.10 Repression in intracellular viscosity post TGF-$\beta$ induced EMT a) Immunoblot for N-Cad and Vimentin after TGF-$\beta$ exposure with respect to untreated cells. b) Fold change plot in green fluorescence for MCF-7 compared to MDAMB-231 c) Shift in peak after TPSII exposure in TGF-$\beta$ treated Huh-7 cells. . . . . 89

4.11 High intracellular viscosity inhibits migration and proliferation in cancer cells a) Frequency comparison for TGF-$\beta$ , 0.5% PEG and 5% PEG with control. b) Viscosity comparison for TGF-$\beta$ 0.5% PEG and 5% PEG with control. c) Scratch assay after TGF-$\beta$ and 5% PEG treatment at 72 hrs with respect to untreated in Huh-7 cells. d) Percentage viability after TGF-$\beta$ and 5% PEG treatment at 72 hrs with respect to untreated in Huh-7 cells. . . . . 90

4.12 High intracellular viscosity inhibits migration and proliferation in cancer cells a) Cell cycle analysis with TGF-$\beta$ and 5% PEG treatment at 72 hrs with respect to untreated Huh-7 cells. b) Immunoblot representing a difference in PCNA after TGF-$\beta$ and 5% PEG treatment at 72 hrs with respect to untreated in Huh-7 cells. c) Immunoblot representing a difference in N-Cad and Vimentin after TGF-$\beta$ and 5% PEG treatment at 72 hrs with respect to untreated in Huh-7 cells. d) F-Actin stain with phalloidin with Confocal microscope for control, TGF-$\beta$, and 5% PEG. 91

4.13 a) Mode shapes for control and TGF-$\beta$ with color bar representing maximum and minimum deformation. b) Comparison of frequency response for control and TGF-$\beta$ treated Huh-7. c) Frequency comparison for PSD and numerical estimated frequency for 5% PEG treated cell. d) Huh-7 cell area with TGF-$\beta$ , 0.5% PEG, 5% PEG after 72 h. e) Perimeter change with respect to control and different treatment in the cell. Error bars represent the standard error of the mean (N = 20 cells on each case). p-Values are determined from Student's t-test for unpaired samples f (**p $<$ 0.005; *p $<$ 0.05) . . . . . 92

4.14 Viscosity of cells treated with different TGF-$\beta$ concentration for different time point i) after 48 hrs ii) after 72 hrs iii) after 96 hrs. . . . . 94

5.1 Schematic for focal adhesions. (a) Focal adhesions consist of multiple proteins (integrins, vinculin, paxillin, talins, and so on.) and serve as signaling hubs producing biochemical signals (b) Actomyosin contractile forces are essential for the stabilization of FAs. Adapted from Humphries et.al. [266]. . . . . 98
5.2 The illustration of the structure of focal adhesions, which are located at the outer edges of cells and connected to the nucleus or other focal adhesions via actin stress fibers. The enlarged image on the left displays the intricate multi-layer protein complexes that make up focal adhesions [267]. . . . . 99
5.3 Detailed experimental setup for the measurement of cell dynamics. . . . . 102
5.4 a) Microscope image of the Huh-7. Cell model obtained from the image traced from the averaged diameter cell. b) AFM modeling showing boundary conditions with different constituents of the cell c) Meshed model d) Stress distribution in the cell structure. . . . . 104
5.5 a) Experimental frequency response for cell and base for the measurement of cell dynamics. b) Transfer function . . . . . 107
5.6 Force-Depth of indentation response of the cellular structure for the validation of the material properties.[315] . . . . . 108
5.7 Force relaxation response of the cellular structure during indentation test. . . . . 108
5.8 a) Displacement in the cellular structure and indentor during the AFM at different time b) Stress distribution in the cellular structure during indentation at different time. . . . . 109
5.9 Consecutive three mode shapes with frequencies of Huh-7 cell at different elastic stiffness. The color bar represents displacement in the cell structure. All modal frequencies are in kHz. . . . . 110
5.10 (a) Numerical frequency response of the cell structure at different elastic stiffness. Inset showing the fundamental mode frequency for different elastic stiffness at adhesion. (b) Variation in modal frequencies with respect to different elastic stiffness. 111

6.1 Detailed experimental setup used for the measurement of cellular dynamics. . . . 119
6.2 Cell as a standard voigt model.(a) Cell under mechanical actuation. The actuation causes morphological alterations in the cell structure. (b) Standard Voigt model for the mathematical representation of the cell. Dashpot and spring components represent the viscoelastic components of the cell. . . . . 120
6.3 Cellular morphology with and without external actuation . . . . . 122
6.4 Circularity Index for the different cell under different actuation (a) control (b) 20 Hz (c) 40 Hz (d) 60 Hz. . . . . 122
6.5 Variation in cell diameter after different external excitation frequency. . . . . 123
6.6 (a) Analytical frequency response of the cell using standard voigt model under different actuation immediate after excitation.(b) Variation in the fundamental frequency of cell after external excitation using Standard voigt model. . . . . 123
6.7 a) Frequency response of cancer cells. b) Transfer function of cell with respect to the base. . . . . 124

6.8 Effect of vibration on cancer cell viability. MTT assay was used to determine cell viability. A sample without external excitation cells was used as a control. a) Immidiately after the excitation b) 24hrs after the excitation c) 48 hrs after the excitation. Results are presented as means ± SD. ∗ p <0.005, ∗∗ p <0.05,∗ ∗ ∗ p <0.01. . . . . 125
6.9 Apoptotic cell death analysis after 0 hr post vibration treatment (a-d) shows flow cytometric scatter plot depicting various events in the cells. The bottom right quadrant indicates early apoptotic cells, while the top left quadrant depicts necrotic cells. (e) Total percentage of apoptotic cells after 0 hr of incubation (f) Total percentage of the cell death under low-range mechanical vibration. Results are presented as means ± SD. ∗ p <0.005, ∗∗ p <0.05,∗ ∗ ∗ p <0.01. . . . . 126
6.10 Apoptotic cell death analysis after 24 hrs post vibration treatment (a-d) shows a flow cytometric scatter plot depicting various events in the cells. The bottom right quadrant indicates early apoptotic cells, while the top left quadrant depicts necrotic cells. (e) The total percentage of apoptotic cells after 24 hrs of incubation (f) Total percentage of the cell death under low-range mechanical vibration. Results are presented as means ± SD. ∗ p <0.005, ∗∗ p <0.05. . . . . 127
6.11 Apoptotic cell death analysis after 48 hrs post vibration treatment (a-d) shows a flow cytometric scatter plot depicting various events in the cells. The bottom right quadrant indicates early apoptotic cells, while the top left quadrant depicts necrotic cells. (e) Total percentage of apoptotic cells after 48 hrs of incubation (f) Total percentage of the cell death under low-range mechanical vibration. Results are presented as means ± SD. ∗ ∗ ∗ p <0.01. . . . . 128

7.1 The schematic shows the fabrication of piezo ZnO /PDMS nanocomposite. . . . . 136
7.2 Detailed experimental setup for evaluating mechanical and electrical characterization of the ZnO /PDMS microchannel. . . . . 137
7.3 Detailed setup for measuring morphological changes in the cellular structure during the flow of cells in the microchannel. (a) An experimental setup showing a microchannel (without actuation) with the inlets and outlets placed under the microscope connected to the micro syringe pump (at the right) and a High-speed camera attached to the microscope at the left. (b) detailed view of the flow of the cells through the actuating microchannel. . . . . 139
7.4 Detailed experimental setup for the measurement of the frequency response of the flowing cells through the microchannel. . . . . 140
7.5 Material characterization of the ZnO nanoparticles. . . . . 141
7.6 (a) Electrical characterisation of the ZnO/PDMS based microchannel. (b) Mechanical characterization of the ZnO /PDMS based microchannel. . . . . 142
7.7 (a-e) High-speed camera images demonstrate the cells' sequential geometrical changes while flowing through the microchannels at different external actuation cases. (f-j) Changes in major to minor ratio for the different cases. . . . . 143
7.8 (a) High-speed camera image shows the flowing cells in the microchannel. (b) Frequency response of the cellular structure. (c) Frequency response of the base. (b) corresponding transfer function . . . . . 144
7.9 Frequency response graphs demonstrate the alterations in the fundamental frequency of the cells while flowing through the microchannels under different cases of actuation. peaks in the transfer show the frequency for (a) Control (b) Low-Low (c) Low-High (d) High-Low (e) High-High. . . . . 145

7.10 Trypan blue staining. Optical microscopic images of the Huh-7 cells treated with various actuation conditions on the ZNO/PDMS microchannel with a time interval of 2 hrs. The cells were stained using trypan blue dye after the vibration treatments to examine cell death. The cells indicated by red arrows are some examples of dead cells that turned blue after staining for different actuation conditions (a) control (b) Low–Low (c) Low–High (d) High-Low (e) High-High (f) % variation in the cell death after the actuation. Results are presented as means ± SD. $***$ p <0.01. . . . . 146

8.1 Modelling of membrane protein system with the inclusion of cholesterol for CHL8-PRO case. Lipid molecules are shown in yellow color, 2MFR transmembrane protein is shown in magenta color, and Cholesterols are shown in blue color. The tensile strain to the system is applied along the z-direction. . . . . 155
8.2 Equilibration of the membrane protein systems at temperature 310 K and time step 0.001 ps: (a) Temperature equilibration and (b) Potential energy equilibration. 156
8.3 Area per lipid for POPC and Cholesterol at different cholesterol concentrations. . 157
8.4 Order parameter of lipid membrane at different cholesterol concentrations. . . . 158
8.5 Average tilt angle for phospholipids molecules in the membrane-protein systems. 159
8.6 (a) $\overline{RMSD}$ plots and (b) average diffusion coefficients of membrane-protein systems at different cholesterol concentrations. . . . . 160
8.7 Simulation snapshots of membrane protein systems at different timesteps. The observed unfolding of protein during simulation is encircled in black color for CHL32-PRO case. . . . . 161
8.8 Electron density profile of membrane protein systems and respective cholesterols along z-direction at before and after separation. . . . . 161
8.9 Average resistance stress vs. time plot for the lipid bilayer separation in the membrane protein system at different cholesterol concentrations. . . . . 162

A.1 Cell as a standard Voigt model.(a) Cell under mechanical actuation. The actuation causes morphological alterations in the cell structure. (b) Standard Voigt model for the mathematical representation of the cell. Dashpot and spring component represent the viscoelastic components of the cell. . . . . 173

# List of Tables


2.1 Properties of femur bone for homogenization [79], [123] . . . . . 41
2.2 Homogenized Properties of femur bone. . . . . 44
2.3 Geometric properties of femur bone. . . . . 46
2.4 Comparison with other techniques. . . . . 50
2.5 Comparison between experimental and numerical results. . . . . 51

3.1 Average thickness of the skin samples . . . . . 58
3.2 Mechanical properties of the skin samples . . . . . 59
3.3 Comparison of natural frequency of the normal skin. . . . . 69
3.4 Young's Modulus Comparison of Normal Skin with other techniques . . . . . 69

4.1 Reported force and spatial sensitivity of tools used to study cell mechanics [184]–[186] 74
4.2 Geometrical and Mechanical Properties for the cell.[227] . . . . . 83
4.3 Hyperelastic Properties of the homogenized cell [227], [229]–[233] . . . . . 84
4.4 Comparison of experimental and numerical frequencies. . . . . 90

5.1 Mechanical properties of the different domain of the cell for the force indentation analysis [233], [271], [310]. . . . . 104
5.2 Comparison of evaluated frequency for different mode shapes. . . . . 111

6.1 Experimental evaluated the fundamental frequency of the Huh-7 cell. . . . . 125

7.1 Different cases of the vibration conditions to the microchannel . . . . . 140

8.1 Composition of the lipid bilayer systems simulated . . . . . 154
8.2 Lipid distribution in outer and inner leaflets of cancer membranes . . . . . 154

# Abbreviations

| | |
|---|---|
| AFM | Atomic force microscopy |
| LINC | Linker of Nucleoskeleton and Cytoskeleton |
| MM | Microfluidic methods |
| MA | Micropipette aspiration |
| MTC | Magnetic twisting cytometr |
| MT | Magnetic tweezer |
| OT | Optical tweezers |
| OS | Optical stretcher |
| PTM | Particle-tracking microrheology |
| DEP | Dielectrophoresis |
| HUVECs | Human umbilical vein endothelial cells |
| MDCK | Madin-Darby canine kidney |
| VICs | Valve interstitial cells |
| (RT4) | Rhabdomyosarcoma, Transformed 4 |
| T24 | Transitional 24 |
| IRM | Interference reflection microscopy |
| MCF-7 | Michigan Cancer Foundation-7 |
| MDA-MB-231 | Metastatic Breast Adenocarcinoma |
| Huh-7 | Human Hepatocellular 7 |
| HL-60 | Human leukemia |
| TRPV | Transient Receptor Potential Vanilloid |
| LTM | Laser tracking microrheology |
| IAF | Isoacoustic focalization |
| SNACS | Size-normalized acoustic scattering |
| SMR | Suspended microchannel resonator |

| | |
|---|---|
| FRF | Frequency-response functions |
| IFRF | Inverse frequency-response functions |
| EMT | Epithelial to Mesenchymal Transition |
| FEM | Finite Element Method |
| DOF | Degree of freedom |
| SISO | Single input single output |
| SIMO | Single input multiple output |
| MIMO | Multi input multi output |
| MISO | Multi input single output |
| EMA | Experimental modal analysis |
| LDV | Laser doppler vibrometer |
| PSD | Position sensing device |
| PI | Propidium Iodide |

# Publications based on thesis

## Journal

1. **Diplesh Gautam**, S. Abhilasha, C. Rajdeep, L. Inamur R, R. Venkatesh KP, and M. Sudeshna, "Mechanical microscopy of cancer cells: Tgf-$\beta$ induced emt corresponds to low intracellular viscosity in cancer cells,",Vol. 154(3), The Journal of the Acoustical Society of America, 2023, https://doi.org/10.1121/10.0020848

2. Pingale A, **Gautam, D**, Owhal A, Deshwal D, Belgamwar S U, Venkatesh KP Rao, "Development of Non-Destructive Dynamic Characterization Technique for MMCs: Predictions of Mechanical Properties for Al@$Al_2O_3$ Composites", Vol. 1, NDT, 2023, https://doi.org/10.3390/ndt.1010003

3. **Diplesh Gautam**, Owhal, Ayush, Venkatesh KP Rao, and Sachin U. Belgamwar ."Atomistic analysis of effect of cholesterol on cancerous membrane protein system: Unfolding and associated resistance stresses under strain", Vol.49,10, Molecular Simulation, 2023, https://doi.org/10.1080/08927022.2023.2208241.

4. **Diplesh Gautam**, and Venkatesh KP Rao. "Modulating the Mechanical Resonance of Huh-7 Cells Based on Elasticity of Adhesion Proteins." IEEE Transactions on NanoBioscience, 2023, https://doi.org/10.1109/TNB.2023.3235645.

5. Harsh Sharma, Ayush Owhal, **Diplesh Gautam**, Sharad Shrivastava, Jitendra Singh Rathore, Sachin U. Belgamwar, Venkatesh K.P. Rao, "Thermoatomic analysis of mono-vacancy defected single-walled boron nitride nanotube under quasi-static strain: Insights from molecular dynamics", Materials Chemistry and Physics, 294 (2023) 1-10, https://doi.org/10.1016/j.matchemphys.2022.127020.

6. **Diplesh Gautam**, Nizam Ahmed, and Venkatesh KP Rao. "Modelling the Effect of Geometry and Loading on Mechanical Response of SARS-CoV-2." BioNanoScience, 12 (2022) 867-876, https://doi.org/10.1007/s12668-022-00993-z.

7. Owhal, Ayush, **Diplesh Gautam**, Sachin U. Belgamwar, and Venkatesh KP Rao. "Atomistic approach to analyse transportation of water nanodroplet through a vibrating nanochannel: scope in bio-NEMS applications." Molecular Simulation, 48 (2022) 1-8, https://doi.org/10.1080/08927022.2022.2052065.

8. **Diplesh Gautam**, and Venkatesh KP Rao. "Nondestructive evaluation of mechanical properties of femur bone." Journal of Nondestructive Evaluation, 40 (2021) 1-11, https://doi.org/10.1007/s10921-021-00754-0.

9. V. Kachawal, A. Srivastava, S. Thakar, M. Zubiria-Ulacia, **D. Gautam**, S. Majumder, Venkatesh K. P. Rao, D. Casanova, R. Chowdhury, N. P. Rath, S. Mukherjee, P. Alemany and I. R. Laskar. "Engineering a light-driven cyanine based molecular rotor to enhance the sensitivity towards a viscous medium." Materials Advances, 2 (2021) 4804-4813, https://doi.org/10.1039/D1MA00277E.

10. **Diplesh Gautam**, and Venkatesh KP Rao. "Modelling the Influence of Protein Expression Levels on the Mechanical Properties of Femur Bone." Trends in Biomaterials & Artificial Organs, 33 (2019) 98-105.

11. **Diplesh Gautam**, and Venkatesh KP Rao. "Transmembrane Domain of Insulin Receptor in cancerous membrane: Insight study of Physical and Conformational changes using Molecular Dynamics" (under review)

12. **Diplesh Gautam**, Nizam, Ahmed, and Venkatesh KP Rao. "Influence of adhesion on migration of MDA-MB-231 and its resonance behavior", Journal of Biosciences (under review)

13. **Diplesh Gautam**, Nizam, Ahmed, Venkatesh KP Rao, "Effect of low-frequency excitation on the apoptosis of Huh-7 cells", Journal of sound and vibration. (Under Review)

14. **Diplesh Gautam**, Rapalli Vamshi Krishna, Venkatesh KP Rao, Gautam Singhvi. "In-Vitro Experimental and Numerical Evaluation of Mechanical Response of Skin." Journal of Biomaterials. (communicated)

15. **Diplesh Gautam**, Owhal, Ayush, Venkatesh KP Rao , and Sachin U. Belgamwar . "Development of active microchannel for cell diagnostics: Insight of resonance behaviour of Huh-7 and their cellular morphology " (Under Preparation)

## Conferences Proceedings

1. **Diplesh Gautam**, and Venkatesh KP Rao. "Classification of diaphysis based on the mechanical response of femur bone." Vibroengineering Procedia 29 (2019): 182-188. https://doi.org/10.21595/vp.2019.21133

2. **Diplesh Gautam**, Owhal, Ayush, Venkatesh KP Rao , and Sachin U. Belgamwar ."Conformational temporal changes in transmembrane protein using molecular dynamics". ME@75 conference IISc Banglore.

*Dedicated To*
*My Family*

# Chapter 1

# Introduction

## 1.1 Background

Cells are the basic unit of life and the building blocks of all living organisms. They have a complex structure consisting of various organelles, such as the nucleus, mitochondria, ribosomes, and endoplasmic reticulum, each with specific functions that enable the cell to carry out a diverse range of biological processes. The nucleus is the most prominent organelle, housing the cell's genetic material and regulating gene expression. Mitochondria are the cell's powerhouse, generating energy through oxidative phosphorylation. Ribosomes are responsible for protein synthesis, while the endoplasmic reticulum serves as the site for lipid and protein synthesis and transport. The lipid bilayer composing the cell membrane selectively regulates the exchange of materials between the cell and its environment by acting as a permeable barrier. Cells perform numerous functions, including energy production, protein synthesis, cell signaling, metabolism, and cell division. They can be classified into different types based on their structure and function, such as prokaryotic cells, which lack a nucleus, and eukaryotic cells, which have a defined nucleus. The hierarchy of cells in biological systems ranges from individual cells to tissues, organs, and entire organisms, each level building upon the next to create complex living systems.

Mechanobiology is the field of study that examines the relationship between mechanical forces acting on cells and their biology. It includes an understanding of cells' response to mechanical stimuli and characterizing the mechanical properties of cells. Figure 1.1 depicts a generalized cell that includes features from all types of cells, with the main components showing the cytoplasm, nucleus, and cell membrane. The cytoplasm comprises biopolymer filaments known as the cytoskeleton, which includes actin, microtubule, and intermediate filaments, which provide stiffness to the cell's structure.

The mechanical properties of different parts of the cell, such as the membrane, cytoskeleton, nucleus, and organelles, all contribute to the overall mechanical characteristics of the cell. The

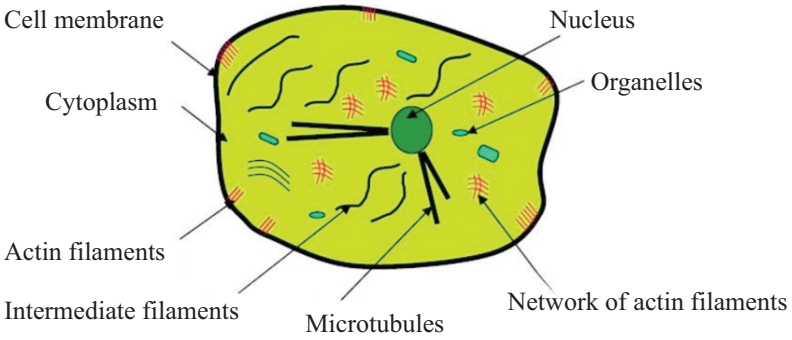


FIGURE 1.1: A schematic of a generalized cell structure: comprehending the fundamental components of life [1].

overall mechanical behavior of cells is understood from the mechanical characteristics of individual cell components and their interaction with their surroundings. The cell membrane, cytoskeleton, nucleus, and organelles are all interconnected and play critical roles in the mechanics of single cells. For example, the cell membrane can transmit stresses and strains from the outside of the cell to the nucleus through the cytoskeleton. The cytoskeleton is made up of different types of fibers, including microfilaments, intermediate filaments, and microtubules, which work together to resist deformation and maintain the shape of the cell. The nucleus is also connected to the cytoskeleton and cell membrane through structures called Linker of Nucleoskeleton and Cytoskeleton (LINC) complexes. LINC complexes are composed of nucleoporins, which are integral membrane proteins of the nuclear pore complex, and cytoskeletal proteins such as actin and intermediate filaments. It plays an important role in various cellular processes including nucleus mechanics, chromatin organization, transcriptional regulation, cell migration, and sensing & responding to mechanical forces. Single-cell analysis can be useful in medical development, stem cell research, and the study of cancer & physiological processes in embryos and adults. Previous research has shown that the mechanical properties of single cells can affect various cell functions such as growth, division, migration, and adhesion. The ability to determine variations in mechanical properties, such as Young's modulus and shear modulus at the single-cell level, has been used in various techniques, including cell separation, disease diagnosis, and drug development. The mechanical stimuli on the cells are another critical area of study that provides insights into mechanical behavior and the response of the cells to their surrounding environment. Mechanical cues can have a profound impact on cellular processes which are vital for tissue development and homeostasis. The research focused on studying mechanical stimuli of cells can facilitate the development of new tissue engineering approaches, improved medical devices, and in-depth investigations into the underlying mechanisms of various diseases.

Microenvironmental stimuli' impact on cell functioning is as shown in Figure 1.2. Mechanical forces, both intrinsic and extrinsic, can have a significant impact on cellular behavior. Changes in these forces can alter cellular function and structure, such as cell differentiation, migration,

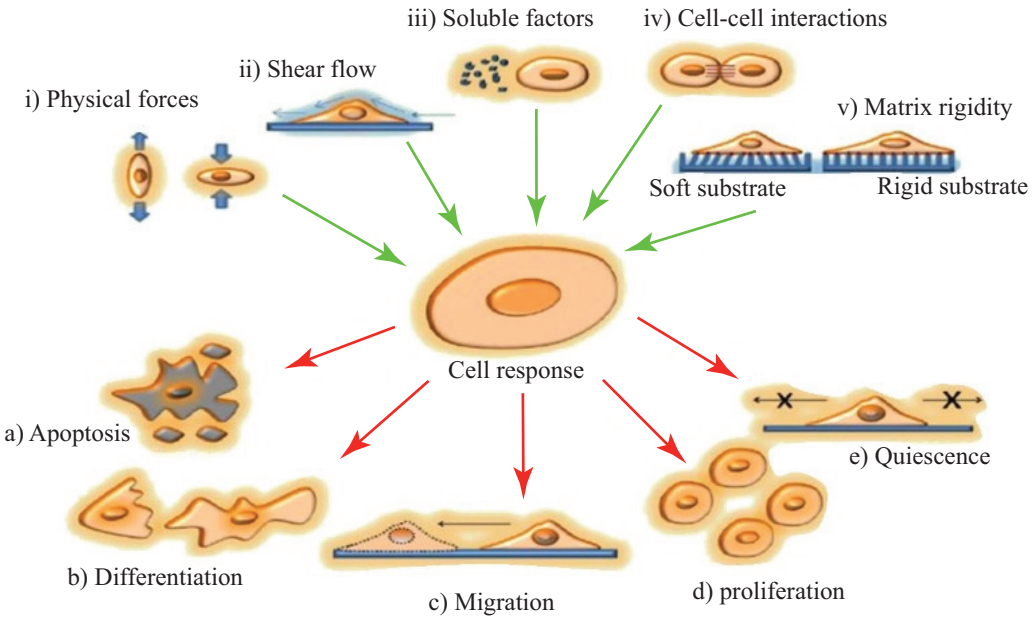


FIGURE 1.2: Unraveling the influence of microenvironmental stimuli on cell behaviors and functions: A schematic representation of force factors. [2]–[4]

proliferation, apoptosis, necrosis, etc. Additionally, mechanical stresses play a role in determining cell fate and shaping embryo development, cell differentiation, and contributing to the function of tissues. When a cell is subjected to mechanical forces, its ability to deform or resist deformation is related to its mechanical properties. Cells can change shape through various mechanisms, such as extension, contraction, protrusion, invagination, blebbing, endocytosis and exocytosis, cytoskeleton remodeling, and migration. To gain insight into the mechanical properties of cells, it is essential to evaluate the cell's deformation in response to a mechanical force. Cells are viscoelastic structures, meaning they can behave elastically (regain their original shape after deforming) and viscously (flowing like a liquid) on the application of the forces. This can lead to phenomena like stress relaxation (stress constant and strain decreases) or creep (strain increases and stress constant). These are important parameters that result in the mechanical properties of the cells.

Several tools are available for studying the impact of mechanical forces on cells, including atomic force microscopy (AFM), microfluidic platforms that assess the effects of shear stress due to interstitial flow on cells, and cellular force measurement techniques that use image processing algorithms. Cells respond to mechanical stimuli such as stretching, surface morphology, and surface stiffness, which help to characterize their mechanical properties. This study aims to review and compare various technologies used to conduct mechanical analysis of biological cells to identify differences and similarities between them. Existing methods can help estimate the mechanical properties of normal and clinically treated cells and potentially aid in the development of new analysis techniques.

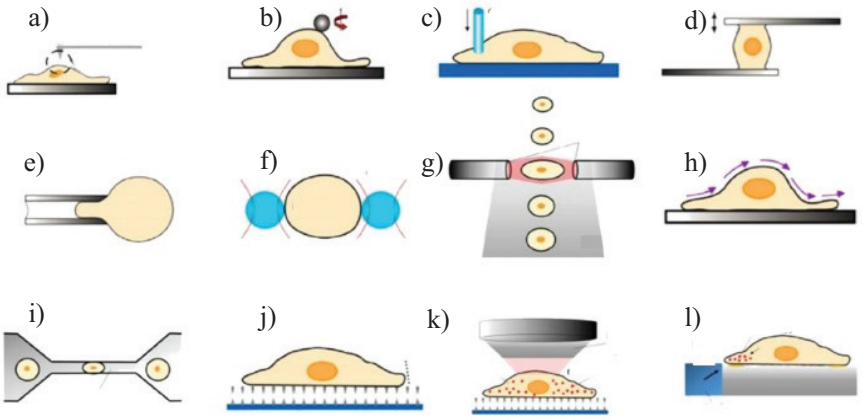


FIGURE 1.3: Exploring the mechanics of cancer cells: A comprehensive overview of major techniques. (a) atomic force spectroscopy; (b) magnetic twisting cytometry; (c) cytoindentation; (d) microplate stretcher; (e) micropipette aspiration; (f) laser/optical tweezers; (g) optical stretcher; (h) shear flow; (i) microfluidic assay; (j) microfabricated post array; (k) particle tracking microrheology; (l) magnetic nanoparticle-based stimuli. This figure is reused with permission from Suresh et.al. [1]

There is a high demand for techniques that accurately, reliably, and sensitively measure the mechanical properties of single cells. In 1986, the atomic force microscope was developed and initially used to capture high-resolution images of hard surfaces. Radmacher et al. later used AFM to measure the mechanical properties of living cells (Figure 1.3a), and it has since become one of the most widely used methods due to its high precision [5]. Microfluidic techniques (MMs) have also been employed to measure the mechanical properties of single cells with high throughput (103–104 cells/s), making them useful for various biological and clinical applications [6]. Other techniques for measuring cell mechanics, such as magnetic twisting cytometry (MTC), magnetic tweezers (MTs) (Figure 1.3b), cytoindentation (Figure 1.3c), and parallel-plate technique (PPT) (Figure 1.3d), exist as well. Micropipette aspiration (MA) (Figure 1.3e) was first developed in 1954 by Mitchison and Swann to measure the surface tension of sea urchin egg cell membranes [7] and is still widely used to measure the viscoelastic properties of local areas and whole cells. Optical tweezers (OT) (Figure 1.3f) and optical stretchers (Figure 1.3g) are also among the techniques that are available to understand cellular mechanics. Additionally, some other microfluidic-based techniques, such as shear flow, microfluidic assay, and microfabricated post array (Figure 1.3h-l), are mostly utilized for cell sorting, cell counting, cell culture, cell analysis, and cell separation. Particle-tracking microrheology (PTM) (Figure 1.3k) is a passive method that can evaluate the mechanical properties of a single cell by recording the random motion of fluorescent beads within the cell using a high-magnification fluorescence microscope.

Apart from the aforementioned techniques, dielectrophoresis (DEP) has the potential to measure the mechanical properties of individual cells. DEP has been used to study cell deformation [8].

However, there are relatively few DEP studies that use accurate parameters like the elastic modulus and shear modulus to characterize the mechanical properties of single cells [9]. Furthermore, there is an insufficiency of comprehensive models for quantitatively characterizing cell deformation by DEP, which can result in an erroneous measurement of mechanical parameters such as the shear modulus under substantial deformation [10].

There are two categories of techniques for measuring the mechanical properties of cells based on the location of the measurement: methods that measure the mechanical properties of single cells at local regions (including the cell surface and interior) and methods that measure the mechanical properties of cells at the whole-cell scale. Techniques such as AFM (including mAFM), MTC, and MTs can measure the mechanical properties of the cell surface and the interior. Conversely, MA only provides measurements of the cell surface. Intracellular measurements are limited to PTM and OTs. Techniques that measure the mechanical properties of single cells at the whole-cell scale include AFM, MMs, MA, MTC, OTs, OS, and parallel-plate technique (PPT).

Several techniques were developed to measure and manipulate cells with stresses on the piconewton scale and displacements on the nanometer scale. Magnetic tweezers (MTs) and optical tweezers (OTs) are examples of such techniques that can detect forces in the piconewton range when cells undergo nanometer-scale deformation. Atomic force microscopy (AFM) is capable of detecting stresses ranging from piconewtons to micro newtons when cells deform within the range of 0.5 to $10^4$ nm. Microfluidic techniques (MMs) are particularly notable for their high-throughput capacity, which enables the mechanical properties of single cells to be measured at a rate of 103–104 cells/s. This feature significantly reduces the workload of cytopathologists and speeds up sample testing. Additionally, some of these techniques have been modified to enhance their effectiveness in measuring cell mechanics. For instance, specialized tips in modified atomic force microscopy (mAFM) have been proposed to measure intracellular and nucleus mechanical properties that would be challenging to obtain using conventional AFM.

## 1.2 Measurement methods for mechanical properties of single cells

This section has provided a detailed explanation of various techniques that are used to determine the mechanical properties of individual cells. We have described how these techniques work, and their technical characteristics, and have provided examples of their use. These techniques will be categorized based on the location of the measurement, namely the cell surface, the inside of the cell, or the entire cell. Some techniques, such as AFM, MA, MTC, MTs, and OTs, can measure mechanical properties at multiple locations. In contrast, others, such as PTM (which can only measure properties within the cell), MMs, PPT, OS, and AMs (which can only deform the entire cell to obtain mechanical properties), are restricted to a single position.

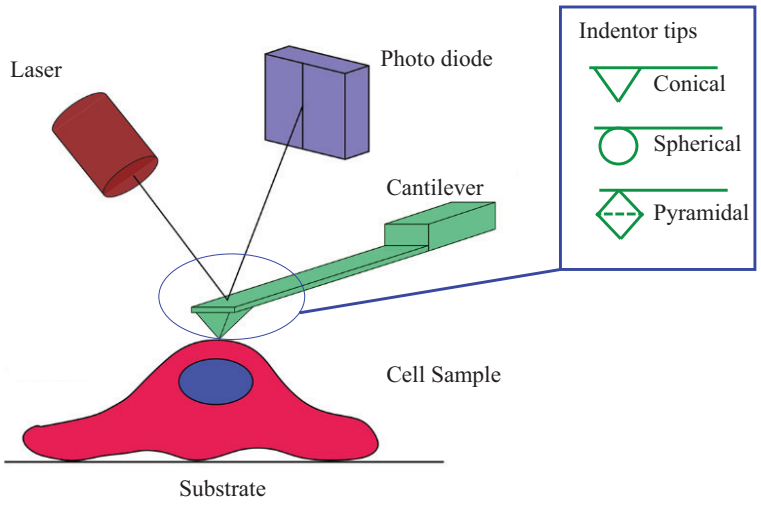


FIGURE 1.4: Atomic force spectroscopy for the measurement of cell deformation. Inset showing different indentor tips. [11]

### 1.2.1 Atomic Force Microscopy (AFM)

AFM involves using a microfabricated, flexible cantilever beam with a tip to indent a cell. A laser is directed at the cantilever beam, which is typically coated with a reflective material. The beam gets deflected due to the indentation of the cell and thus the change in the angle of the reflected laser beam. This change in angle is detected by a position-sensitive photodetector and converted into an electrical signal. These electrical signals correspond to the deformation of the cells that are in correlation with the deflection of the cantilever beam (Figure 1.4). AFM can provide information on the physical properties of the cell, such as its stiffness and elasticity. Since its development in 1986, the capabilities of AFM in terms of multi-parameter, multi-frequency, and high-speed measurements have greatly improved [12]. For instance, high-speed AFM (HS-AFM) can study the dynamic mechanical properties of single cells and even single molecules by reducing the time required to acquire an image.

While evaluating the mechanical properties of single cells using AFM, it is crucial to consider the influence of probe geometry. Different probe shapes and radii may result in different moduli for a given sample (inset in Figure 1.4). For example, the Michigan Cancer Foundation (MCF-7) breast cancer cell line's elastic modulus, measured with a conical probe, is approximately nine times higher than that measured with a spherical probe [11]. The smaller contact area of the conical tip applies more stress on the cell surface, resulting in a stiffer apparent elasticity measurement. The probe's shape may also impact the indentation depth into the cell surface, affecting the measured elasticity. However, in another study, AFM with spherical tips provided more accurate cell elasticity values. Still, pyramidal tips under medium loads (i.e., 3 nN) may result in extraneous contact between the AFM tip and cell surface, leading to an overestimation of elasticity values [13]. Additionally, the contact locations of the probes may affect the measurement results. For example, the elastic modulus near the nucleus differs from that at the cell border [14].

AFM is a commonly employed technique for evaluating the mechanical characteristics of specific parts of cells like the cell nucleus and surface. The AFM-based broad modulus range nanomechanical mapping technique can measure elastic moduli ranging from 1 kPa to 20 GPa by capturing force-distance curves and directly measuring the force and indentation depth of a surface sample. This technique has been used to examine the E. coli cell surface and measure the elastic modulus of flagella. Its potential for studying the mechanical properties of individual cells for various purposes, including exploring mechanoresponse to stimuli and characterizing the mechanical dynamics of heterogeneous surfaces, is significant [15].

Hosokawa et al. [16], [17] utilized atomic force microscopy (AFM) to measure the impulse forces generated by a femtosecond laser pulse. Focusing a laser pulse near a targeted cell produces shockwaves and stress waves, which act as impulsive pressures on the cell. It was predicted that the impulsive force created by the fs laser can replace the force applied to cells during conventional AFM measurement in a non-contact manner. This non-contact approach has been applied to quantify the impulsive force required to break the intercellular adhesion of HL-60 leukocytes attached to human umbilical vein endothelial cells (HUVECs) and Madin-Darby canine kidney (MDCK) cells monolayer [18]. It can also determine the adhesion strength between mast cells and neurite cells at a high throughput of 100 cells per hour. Oikawa et al. (2015) and Yamada et al. (2017) demonstrated the capacity of this non-contact method to assess mechanical interactions in both animal and plant cells, such as zebrafish embryonic epithelia and palisade mesophyll cells [19], [20].

A modified AFM with specialized tips can measure the mechanical properties of intracellular organelles. There are currently two primary techniques for modifying AFM tips: (1) the focused ion beam (FIB) technique and (2) the addition of nanowires or nanotubes onto conventional AFM tips [21]. Researchers have developed a modified AFM with a specific needle tip (depicted in Figure 1.4) that can measure the mechanical properties of the cell nucleus in situ without disrupting the activities of live cells. The study revealed that the isolated nucleus of fibroblast-like valve interstitial cells (VICs) had a much lower Young's modulus than the intact nucleus in situ. Additionally, the Young's moduli of the VICs grown on a hard substrate were higher than those grown on a soft substrate. Moreover, the less metastatic Rhabdomyosarcoma, Transformed 4 (RT4) cells exhibited a stiffer membrane/cytoplasm and nucleus than the more metastatic Transitional cell carcinoma 24 (T24) cells [22]. This technology has the potential to determine the mechanical properties of intracellular organelles, as AFM with a modified tip can penetrate the cell membrane without harming live cells.

AFM can measure the mechanical properties of the entire cell by using a cantilever with the appropriate stiffness (i.e., 0.01–0.06 N/m) and probe geometry (e.g., a spherical tip of about 5 µm), in addition to measuring the mechanical properties of specific areas of cells (e.g., the cell surface and nucleus) [23]. The mechanical properties of the entire cell are often analyzed thoroughly by

combining AFM with advanced theories such as the Hertz contact theory, exponential equation, and parallel-spring recruitment model [24]. Pogoda et al. (2012) studied the mechanical properties of live fibroblasts and found that Young's modulus values of the whole cell decreased as the indentation depth increased [25]. They also demonstrated the ability to detect cancer cells with indentation greater than 500 nm based on the proposed depth-sensing hypothesis in two human melanomas (WM35 and A375). AFM is commonly used to measure the mechanical properties of single cells at various locations, including the cell surface, interior, and whole cell, and to validate the measurement data obtained by other methods. We anticipate that AFM will continue to play a critical role in the study of the mechanical properties of single cells, particularly in the areas of throughput enhancement and multi-parameter measurement, with the continuous advancement of AFM-based techniques.

### 1.2.2 Microfluidics methods (MM)

Microfluidic methods (MMs) typically analyze the deformability of cells and measure cell morphological changes. MMs are unique because they can process cells at a very high rate (103-104 cells/s). Dielectrophoresis, Micro trapping, Micro constrictions, etc are frequent use MMs for cell analysis and cell separation for medical diagnostics (as in Figure 1.5). There are three main ways to use microfluidics to evaluate cell deformability: micro-constriction, extensional flow, and shear flow. In the micro-constriction method, cells are passed through a small constriction, and their passage time is measured to determine their deformability. The shear flow method involves flowing cells through a narrow channel and observing how they are distorted using optical imaging. The extensional flow method uses a microfluidic device with a cross-slot to deform cells, which can be observed through an optical microscope. Extensional flow-based deformability cytometry provides the highest strain rate (10 kHz) and applied stress (nearly 10 kPa) of these three approaches.

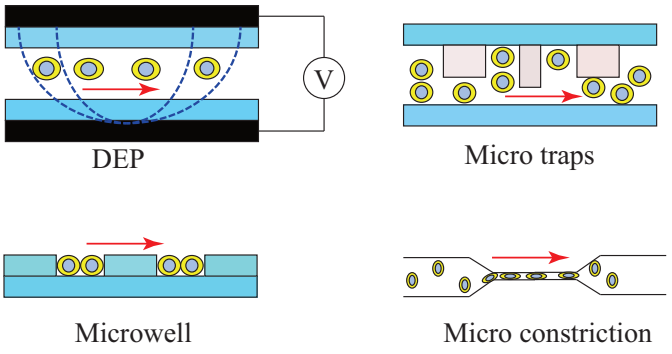


FIGURE 1.5: An overview of techniques used in 2D microfluidics to study intercellular interactions at the single-cell level. [26]

Urbanska et al. [27] compared the efficacy of above mentioned three techniques to measure single-cell deformability. Their findings predicted that the micro-constriction and shear flow methods

are appropriate for measuring mechanical properties related to the actin cytoskeleton. Meanwhile, the extensional flow method is better suited for determining mechanical properties linked to cellular components such as the nucleus [27]. Further, previous studies on microfluidic-based micro-constriction channels in which post-arrays were used to measure the mechanical properties of K562 leukemia and NIH 3T3 cells. The results indicated that as the amount of lamin A increased, the cells became more rigid [28]. Another study utilized the extensional flow technique to analyze the deformability of cells in pleural effusion and accurately predicted the disease state and immune activity of cancer patients with high sensitivity and specificity [29]. A different approach called shear flow with deterministic lateral displacement was used to quickly identify red blood cells' size, shape, and deformability and could potentially provide more information about their mechanical characteristics, such as elasticity and viscosity [30]. Microfluidic methods are capable of high-throughput measurements using either contact or non-contact methods. They can be combined with other techniques, such as micro-aspirators and optical tweezers, to allow for precise manipulation of individual cells and efficient measurement of their mechanical properties.

### 1.2.3 Micropipette aspiration

In this technique, the cell's deformation and geometric changes are observed due to suction pressure applied to the cell surface that helps to determine its elastic or viscoelastic properties (as in Figure 1.6). Micro Aspirator (MA) is generally used to measure single-cell mechanical characteristics, in which the friction between the cell membrane and the walls of the micropipette may be ignored ([31]). This is because the size of the micropipette opening is typically smaller than the cell diameter, which reduces the contact area between the cell membrane and the micropipette walls. Additionally, the low suction pressure used in MA minimizes the force applied to the cell, which further reduces the potential for membrane friction.

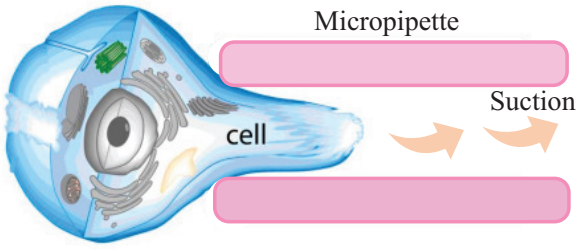


FIGURE 1.6: Schematic illustration of micropipette aspiration technique [32]

The mechanical characteristics of various cell components can be measured on varying the magnitudes of suction pressure; for example, to measure the cell membrane and cell cytoskeleton, threshold pressures of around 1 Pa and 1 KPa (or several hundred Pa) are required ([33]). MA can also be used to determine the mechanical characteristics of the cell nucleus [33], [34]. When

using MA to measure soft biological materials such as tumors and embryos, the impacts of surface energy must be considered. It was observed that if the size of the micropipette or the aspiration length is similar to the elastocapillary length, it can cause the surface energy to decrease the normal surface displacement and internal pressure, resulting in an overestimation of the elastic modulus [35]. Hogan et al. (2015) developed an MA-based technique to analyze cellular adhesion force at the single-cell level [36].

Single interference reflection microscopy (IRM) of the cell depicts the force needed to detach a cell from the substrate and measures the area covered by the adhesive bonds. MA can be used to explore the mechanical characteristics of the membrane and cytoskeleton cortex of Entamoeba histolytica (E. histolytica) by combining it with a theoretical model that explains the polymerization and depolymerization of actin. The findings showed that morphological changes in cells are the foundation for cell motility [37]. MA can also aspirate an entire cell into a micropipette and distort it to test its viscoelastic characteristics. Hochmuth (2000) studied neutrophils' and chondrocytes' elastic and viscous behavior by aspirating whole cells into a micropipette [38]. Findings predicted neutrophils behaved like liquids with a surface tension of 30 pN/m while chondrocytes behaved like elastic solids with an elastic modulus of 0.5 kPa. MA has the ability to measure the mechanical characteristics of individual cell organelles (such as the membrane and nucleus) and the whole cell. Additionally, it can be used in conjunction with MMs to perform high-throughput measurements, reducing the complexity of the equipment and measurement technique.

### 1.2.4 Parallel-plate technique

The Parallel-plate technique (PPT) involves placing a cell between two parallel plates, one flexible and the other rigid (Figure 1.7). The rigid plate has a stiffness that is 1000 times greater than the flexible plate, and both plates are compared to a reference plate with known bending stiffness [39]. This setup allows for the assessment of the mechanical properties of whole cells by inducing dynamic mechanical deformation, which has contributed to the development of theoretical models of single-cell mechanics [40]–[42]. The PPT has been used to evaluate the mechanical characteristics (viscous, elastic, and shear modulus) of specific cell types, such as MCF-7 cells, and has been found to produce results comparable to those obtained using other techniques, such as AFM with dull probes and MTC [42].

The PPT has also been used to study the dynamics of the actomyosin cortex in cells and to measure Young's modulus, deformability, relaxation, and creep functions with high precision [43]. However, obtaining high throughput measurements using PPT can be challenging.

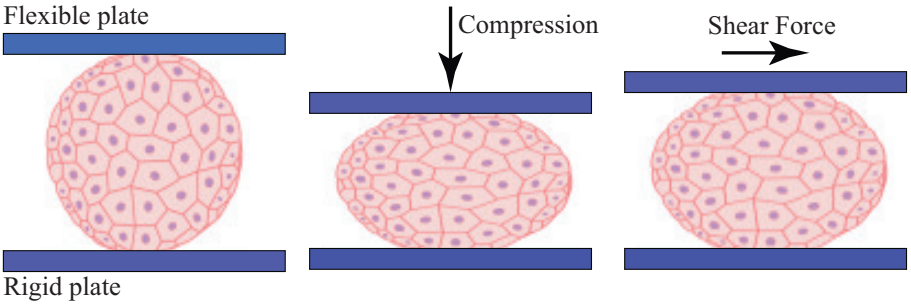


FIGURE 1.7: Parallel plate technique for measuring the cellular deformation. [39]

### 1.2.5 Magnetic twisting cytometry (MTC) and magnetic tweezers(MT)

The MTC technique involves using magnetic beads that respond to a magnetic field by spinning and applying stresses to these beads to assess the mechanical characteristics of cells in different locations, including the surface and interior as shown in Figure 1.8. The motion of the magnetic beads within cells is tracked using a high-resolution imaging system to assess the mechanical properties inside the cells, and the experiments must be conducted under controlled conditions [44]. MTC has been used to study the dynamic responses of various cellular components, such as the cytoskeleton [45], membrane [46], and cytosol [47]. Similar principles are used in MTs, which have been applied to a range of studies, including the investigation of vinculin function in F9 embryonal carcinoma cells [48], the breakdown of endothelial barrier function with MDA-MB-231 cells and endothelial cells [49], high-throughput gene transfection and screening of heterogeneous leukemic cells [50], and the assessment of the nonlinear local viscoelastic response of NIH3T3 mouse embryonic fibroblasts [51]. However, one limitation of MTC and MTs is the restricted force that can be applied to the magnetic beads. Customized MTs have been developed that can apply forces of up to 100 nN on 5 $\mu$m magnetic beads to deform cells [52]. These modified MTs can also be used to study force-regulated processes and mechanotransduction in live cells. The 3D MTs system was developed to study intracellular components such as the cytoplasm and nucleus. The study revealed that the viscosity of mouse embryo cell cytoplasm was 8 times higher than that of water because the concentration of molecules and organelles within the cell, as well as their cytoskeletal network, provides structural support. The central portions of the inner cell were more flexible than the peripheral regions during 3D magnetic bead navigation within the embryo, with forces up to 120 pN [54]. Further, a study based on an optimized 3D magnetic tracking system and applied stable forces for over 30 minutes were conducted to manipulate submicrometer magnetic beads inside T24 cells [55]. Their findings showed that the major axis of the nucleus was more resistant to deformation compared to the minor axis.

The MTs technique has also been used to investigate the force-generating machinery that keeps the spindle at the center of the cell during mitosis in Caenorhabditis elegans embryos, revealing that this high-stiffness machinery can suppress thermal fluctuations to locate the mitotic spindle

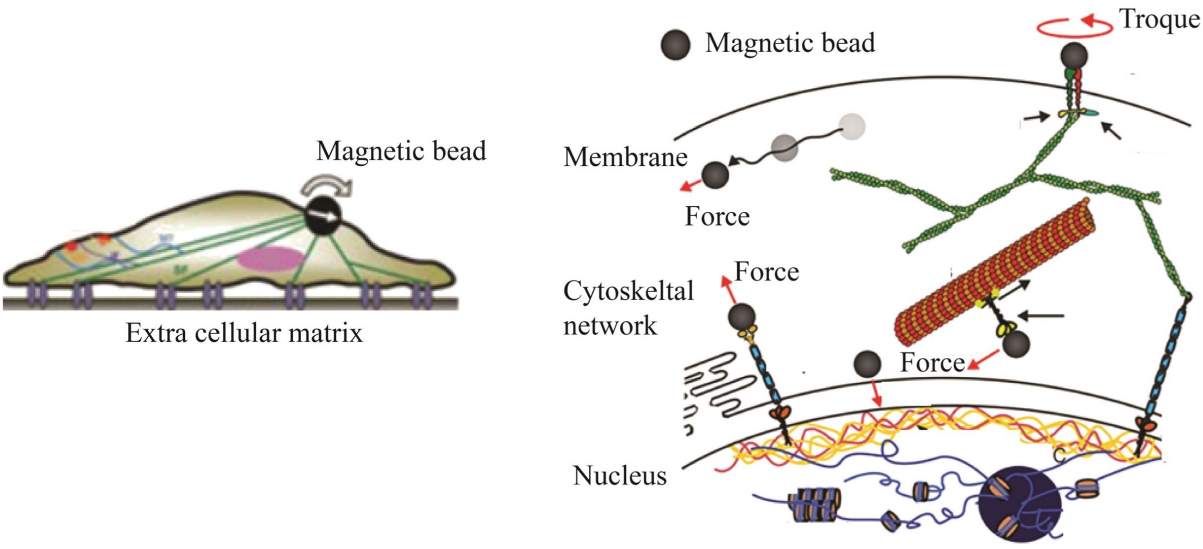


FIGURE 1.8: MTC technique for the dynamic measurement of the different parts of cellular structure. [27], [53]

precisely [56]. Both MTCs and MTs can measure the mechanical properties of the cell surface and interior, and with the advances in the control of magnetic beads, these methods can be used to characterize the mechanical properties of cells more thoroughly, potentially providing new insights into single-cell mechanical phenotypes.

### 1.2.6 Optical stretchers (OS) and Optical tweezers (OT)

An optical stretcher (OS) traps and deforms cells by using two divergent beams (Figure 1.9). Depending on the size and index of refraction, the forces imparted to glass or latex beads vary from piconewton to nanonewton as a function of laser power increases from a few mW to 1.5 W, which is enough to stretch complete cells [57]. The amount of stretch force applied to cells may rise as laser power increases, causing increased cell deformation. However, the too intense laser beam could affect cell mechanical characteristics or harm cells. Bellini et al. (2012) created a monolithic OS by designing optical waveguides in glass with an fs laser and used it to study the influence of temperature on microtubule depolymerization at 0 °C [58], [59].

An optical stretcher has also been utilized to explore the impact of heating on the mechanical characteristics of single cells due to the nature of laser heating. Modified OS causes millisecond temperature variations, leading to the idea of thermorheology, which was developed to characterize the intrinsic features of cells in response to temperature changes [60]. Using OS, Chan et al. (2014) investigated the impact of heating on the mechanical characteristics of suspended HL60 cells [61]. The findings revealed that the compliance of HL60 cells scaled linearly with temperature below a critical threshold (i.e. 52.1°C). Still, when the temperature exceeded the critical point, cells displayed an active contraction in the direction of higher stress owing to

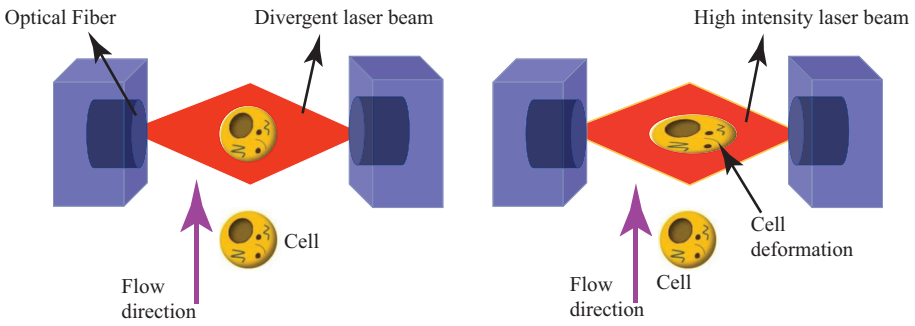


FIGURE 1.9: Optical trapping and stretching technique for the measurement of the cellular deformation in the structure. [57]

TRPV2 ion channel activation. The volume fluctuations of isolated nuclei of HL60 cells were also investigated using OS. Chan et al. ([62]) showed that the volume of isolated nuclei was significantly temperature-dependent. The isolated nuclei may be thought of as highly charged polymer gels with thermoresponsive capabilities.

A concentrated laser produces a 3D light gradient, which may apply attractive and repulsive forces to a bead or cell. However, the force produced by OTs is confined to the piconewton level, which is insufficient to deform the whole nucleated cell but sufficient to test the characteristics of actin filaments. By putting microbeads over F-actin, the viscoelasticity of adhering alveolar epithelial cells could be evaluated with OTs. The findings were equivalent to those obtained with MTC [63]. Aside from actin filaments, the OTs may assess intracellular mechanical characteristics by capturing and oscillating beads inside a cell. Hoffman et al. (2006) used internal laser tracking microrheology (LTM) to evaluate the frequency-dependent shear modulus of mammalian cells, and the digital deflection rate of random beads may reach 50 kHz [44]. Wei et al. ( [64]) employed OTs to alter internal lamellar bodies in alveolar epithelial type II cells to measure viscoelastic moduli.

An optical stretching and optical trap can monitor cell mechanical characteristics without directly contacting the cells. It can collaborate with MMs to accomplish high-precision and reasonably high-throughput manipulation and measurement of single cells. As a result, they have enormous promise for creating automated systems for single cell culture, manipulation, and mechanical phenotypic.

### 1.2.7 Acoustic methods (AM)

The acoustic technique utilizes acoustic waves commonly produced by piezoelectric materials. When a voltage is applied to the electrodes, the piezoelectric material expands and contracts along or normal to the surface. This mode of vibration is called breathing mode. For some material orientations, the piezoelectric material will deform in the perpendicular direction of the applied electric field. This mode of vibration is called the shear mode. On exciting interdigitated

transducers (IDTs) patterned on a piezoelectric crystal, vibrations can be generated on the surface of the material in the form of surface acoustic waves (SAWs). The wavelength of the SAW ($\lambda$) is dependent on the width and spacing between IDT fingers as shown in Figure 1.10. Acoustic methods are often used for size-based cell separation by measuring the compressibility of individual cells using standing surface acoustic waves. However, the measured compressibility parameters are converted into standard viscoelastic parameters to characterize the mechanical properties of individual cells accurately [65].

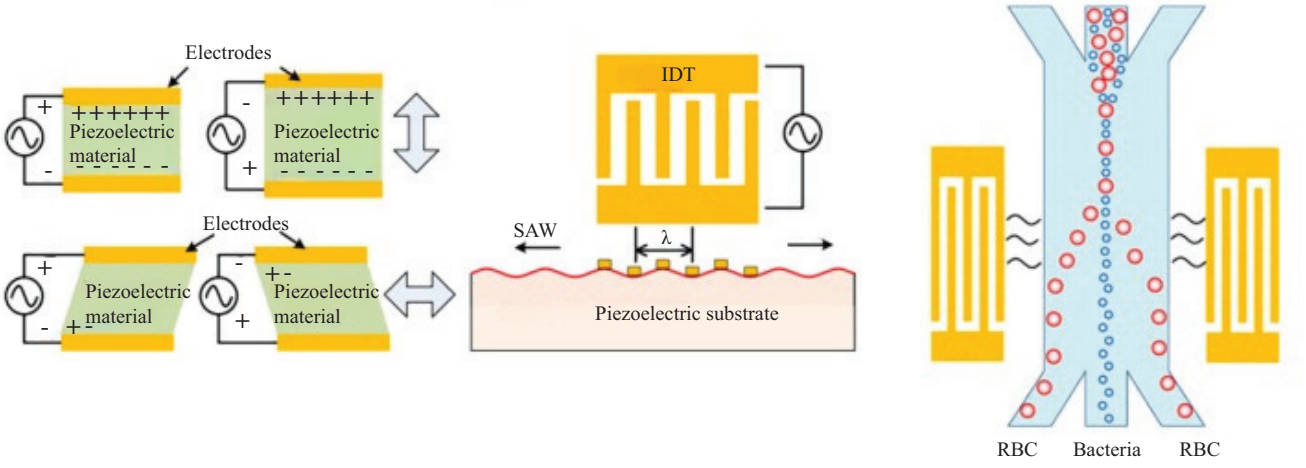


FIGURE 1.10: Acoustic wave generation through piezoelectric materials: a) Expanding and contracting surface via the voltage applied to the electrodes. b) Separation of bacteria from blood cells using a standing SAW technique. [66]

Recent studies have shown accomplished noninvasive cell stiffness measurements using acoustic fields [67]. A study based on an Isoacoustic Focalization (IAF) technique predicted the size-independent results where, distinct cell types, such as monocytes, lymphocytes, neutrophils, BA-F3, and MCF7 cells, exhibit varying effective acoustic impedance values ranging from 1.55 to 1.75 MPa-sm$^{-1}$, due to their different acoustic-mechanical characteristics [68]. Kang et al. (2019) used size-normalized acoustic scattering (SNACS) to determine the size of a particle. During the cell cycle, quantify the mechanical characteristics of the complete cell where a suspended microchannel resonator (SMR) was used as the oscillator [69]. This technique helps us understand how cells in evolution maintain their structural stability and can be used to monitor delicate and transient changes in their mechanical properties.

In the past decade, photoacoustic technology has rapidly progressed in the fields of biological and medical imaging. A photoacoustic microscope is a powerful tool for quantifying and studying the physical and mechanical properties of cells, such as size, shape, temperature, oxygen saturation, and dissolved oxygen [70], [71]. It has been used to detect and characterize single red blood cells and melanoma cells in flowing bovine blood in vitro, as well as leukocytes and platelets in the circulating blood of rat mesenteric microvessels in vivo [72], [73]. When illuminated by

a laser pulse, red blood cells absorb optical energy and produce an ultrasonic pressure wave (photoacoustic wave). The corresponding power spectrum provides information about the size and shape of the cells. The power spectrum also allows for the measurement of healthy red blood cells and the characterization of abnormal ones with irregular shapes [74]. In addition to determining the mechanical characteristics of single cells, acoustic methods can also separate cells based on their mechanical properties, such as deformability, using a high-throughput, non-contact method. However, the metrics measured by acoustic methods, such as compressibility, need to be converted into standard viscoelastic characteristics to describe the mechanical properties of cells.

These reviews showcase the various methods and their developments used in the research on the mechanical analysis of cells. The literature background demonstrates the rapid development in biological research, utilizing various engineering disciplines. As technology and methods have improved over time, researchers have sought out the best alternative methods for a deeper understanding of the mechanics of cells and how they interact with their surrounding structures and environments.

However, the complex internal structure of the cells, consisting of numerous elastic components and cross-connects, and their overall vibrational behavior are not explored much in previous literature. Few studies on healthy and diseased cells demonstrated that their vibrational frequencies are a reliable indicator of most major myopathies. Still, a precise technique is required to study the dynamics of the microscale biological systems. It is a need to develop an experimental setup that helps to conduct research on understanding the dynamics of cells, which does not require the microscale structure to be either 1-D or 2-D structures. This thesis presents the development of a new noninvasive method and highlights the potential of using noninvasive cell vibration frequency measurements for detecting several diseases, opening up a new field in mechano-diagnostics. The measured vibrational frequencies should be quite effective in detecting the state of cells as well as their transition from epithelial to mesenchymal state. In the context of cell dynamics, modal analysis techniques can help to identify the natural frequencies and modes of vibration of cells, which can provide insights into their mechanical properties and behavior. Hence, the next section describes the modal analysis techniques that are necessary to understand the concept of cell dynamics and to analyze the vibrational behavior of a system.

## 1.3 Modal analysis techniques

Developing a reliable mathematical model that accurately reproduces the behavior of all components of the complex structure is difficult. It is relatively simple to model individual parts, but it is typically difficult to model connections and inherent constituents. Additionally, it can be complicated to model damping to understand the dynamic response of a complex biological structure to various loading conditions using only analytical or numerical tools. A common

approach to overcoming these difficulties is to rely on experimental methods, in which response data from the structure is collected, analyzed, and used to develop a model that accurately reflects the behavior of the system. This process is known as experimental modal analysis and became popular in the 1970s. It has since been applied to a wide range of fields, including substructure coupling, model updating, damage detection, and Vibro-acoustics. The current section of the study focuses on the techniques used for identification in experimental modal analysis.

It's important to understand the different measurements that can be made in practice. It includes measuring the dynamic response in a free vibration condition, i.e., the natural decay of vibration, or measuring the force response due to external loading. In contrast, the external force may be unknown or very difficult to quantify (in the case of ambient excitation, such as wind on structures). In these situations, only the response is measured. When the external force can be determined or controlled, measurements are taken of the ratio of the response to the input. These ratios are called frequency-response functions (FRFs) if working in the frequency domain and impulse-response functions (IRFs) if working in the time domain. The IRFs can be obtained from FRFs by applying an inverse Fourier transform. For an N-degree-of-freedom (DOF) system with viscous damping, the dynamic equilibrium equation is given by

$$[M]\ddot{u} + [C]\dot{u} + [K]u = \{F\} \tag{1.1}$$

Where $[M]$ is the mass matrix, $[C]$ is a damping matrix, $[K]$ is the stiffness matrix and $\{F\}$ is the force vector. In steady-state conditions, and from the harmonic excitation case, it is possible to establish the relation between the complex amplitudes of response and the amplitudes of the applied forces, through a matrix $[H]$, Each element of $[H]$ is called a frequency response function, relates the response coordinate to a force coordinate. It is given by

$$X = [H]F \tag{1.2}$$

$$H_{jk}(\omega) = \sum_{r=1}^{N} \frac{{}_rA_{jk}}{(\omega_r\zeta_r + i(\omega - \omega_r(\sqrt{1-\zeta_r^2})))} + \frac{{}_rA^*_{jk}}{(\omega_r\zeta_r + i(\omega + \omega_r(\sqrt{1-\zeta_r^2})))} \tag{1.3}$$

where ${}_rA_{jk}$, $\omega_r$ and $\zeta_r$ are the residue, the natural frequency, and viscous damping ratio of mode $r$, respectively are a real part. While ${}_rA^*_{jk}$ shows an imaginary part. An alternative and simpler version of Equation 1.3 is

$$H_{jk}(\omega) = \sum_{r=1}^{N} \frac{A_r + i\omega B_r}{\omega_r^2 - \omega^2 + 2i\zeta_r\omega_r\omega} \tag{1.4}$$

where the numerator, for $\omega = \omega_r$, is known as the modal constant. The impulse response function is the analogue of Equation 1.3 in the time domain and it is given by

$$h_{jk}(t) = \sum_{r=1}^{2N} {}_rA_{jk}e^{s_r t} \tag{1.5}$$

Where $s_r$ = -$\omega_r\zeta_r + i(\omega_r(\sqrt{1-\zeta_r^2}))$. Equation 1.3 or Equation 1.5 represents the behavior of the structure among the selected points, and one can work in the time domain or the frequency domain. Moving from one domain to the other is a matter of applying Fourier transforms.

The classification is in between identification methods that use data in the time domain and those that use data in the frequency domain. The time domain can always be used, either for free response data or forced response data. Frequency domain methods are only used for forced vibration when the forces are known.

### 1.3.1 Classification according to the number of input and output locations

In each domain, there are methods that use data from one response location and others that simultaneously use data from various response locations. In each case, there may be one force location or various force locations, leading to the following classification.

- Single-Input Single-Output (SISO)→ One response due to one force
- Single-Input Multiple-Output (SIMO) → Many responses due to one force
- Multiple-Input Multiple-Output (MIMO) → Many responses due to various forces
- Multiple-Input Single-Output (MISO) → One response due to many forces

In the time domain, the responses (time histories) naturally possess information about the frequency content. However, this is 'hidden', so it is difficult to say how many resonances are present in a certain time period. Consequently, time domain methods simultaneously identify various resonances of the structure, and for MIMO methods, various modes of vibration. They are known as multi-degree-of-freedom (MDOF) methods. In the frequency domain, because the resonance peaks are visible, it is also possible to make an identification mode by mode. These methods are called single-degree-of-freedom (SDOF) methods.

### 1.3.2 Classification according to the type of identified dynamic properties

There is another classification to consider in both domains (time and frequency): i.e. direct and indirect. Direct methods estimate the dynamic properties in terms of stiffnesses, masses,

and damping coefficients, i.e. It work out the matrices in Equation 1.3; indirect methods evaluate the properties associated with each mode of vibration, the so-called modal parameters: natural frequency, damping ratio, and modal constant (amplitude and phase), as in Equation 1.4–Equation 1.5.

The study of the dynamic behavior of structures emerged primarily in the 1930s due to the increasing importance of comprehending the dynamic performance of aircraft. The available technology at that time was limited, and the only feasible measurements were based on the free vibrations at the wings' tips where a recording device recorded the free decay. These records provided information on the fundamental natural frequency and damping ratio. Resonance testing was used to excite the structure through a shaker, inducing it into resonance. This method of modal testing and analysis was referred to as "resonance testing". Force appropriation, also known as normal mode testing, utilized appropriately tuned shakers along the wing to bring it into resonance, enabling the identification of each resonant frequency and its corresponding mode, and providing insight into the set of forces applied through the shakers.

In the 1960s, a significant advancement with the development of the fast Fourier transforms algorithm, which allowed for faster processing of time signals and more efficient conversion to and from the frequency domain. The advent of digital computers in the 1970s further utilized this algorithm, leading to significant improvements in the analysis and testing of structures. In recent times, the abundance of technical literature on experimental modal analysis has made to categorize the multitude of methods that are available.

The rational fraction polynomial is a SISO frequency domain method proposed by Richardson and Formenti et. al. and is among the most used nowadays [75]. It is based on the viscously damped model and the FRF is expressed as the ratio of two polynomials. Besides the simple methods for the current study, we use the method basically in which the natural frequencies were evaluated directly from the peaks of the frequency response functions (FRFs), and the damping ratios were calculated by the half-power points method.

Modal analysis is a technique used to understand the dynamic behavior of a structure by applying a known force and frequency, measuring the response, and using that information to evaluate the structure's dynamic parameters through Frequency Response Functions (FRFs). Testing biological systems with this method can be difficult due to the challenges of applying and measuring the input force and response. As a result, methods have been developed specifically for the modal testing of small biological cells, which will be discussed in the next section.

### 1.3.3 Excitation methods

Biological cells are extremely small and techniques that rely on direct physical contact, such as using an impact hammer or shaker, cannot be used to study the vibration patterns of these cells. Instead, non-contact methods are used to test the vibrations of such a system. Additionally, the vibrations of cells occur at higher frequencies compared to the macro counterparts, usually in the range of a few kilohertz to several megahertz. This section will describe the various excitation techniques that can be used for testing the vibration patterns of biological systems.

#### 1.3.3.1 Acoustics excitation

This method involves applying a pressure wave with a specific frequency through any acoustic source such as the acoustic resonator (Figure 1.11), SAW and BAW devices, causing harmonic pressure to be applied to the structure. The generated acoustic waves are used to produce mechanical forces that can displace cells and control their position. An acoustic horn is an alternate approach connected to a speaker to generate acoustic excitation.

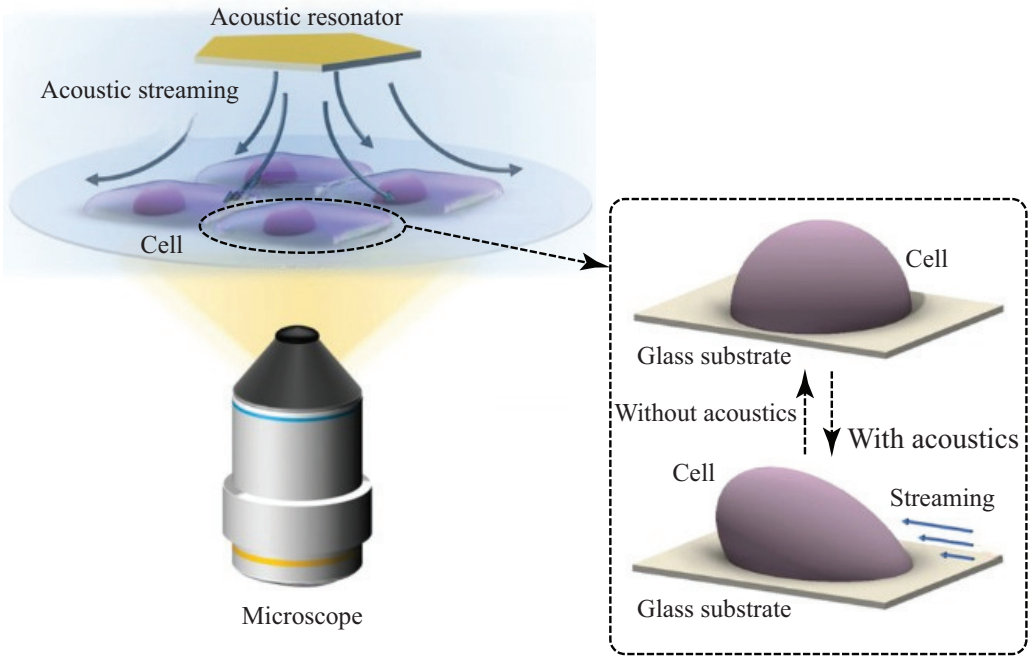


FIGURE 1.11: Schematic illustration of a controllable method for stimulating cells using gigahertz ultrasonic device-generated acoustic streaming. The system enables observation of cell deformations and excitations. [76]

#### 1.3.3.2 Chemical excitations

This method uses chemicals to excite cells or their extracellular matrix, such as neurotransmitters. These chemicals are drugs, which are synthetic or naturally occurring substances that can have a

variety of effects on the cell structure. The changes in the cell's interior and extracellular, resulting

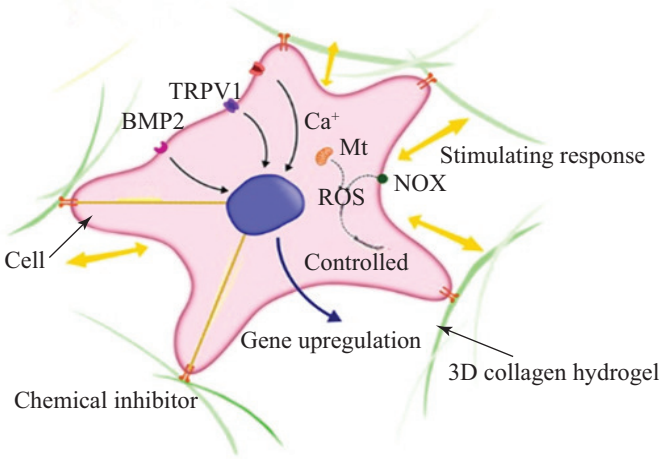


FIGURE 1.12: Nanovibrational Stimulation of Mesenchymal Stem Cells induces therapeutic reactive oxygen species using defined media and chemicals. Adapted from Wich Orapiriyakul et. al. 2020. [77]

from chemical stimulation-induced up and down-regulation of various biological activities within the cell structure, are depicted in Figure 1.12. Drugs can be used to modulate the activity of specific cells or to induce changes in the cell itself. Various biological activity such as, ROS (Reactive Oxygen Species) and NOx (Nitrogen Oxides) both are signaling molecules that play important roles in the cellular response to physical forces such as stretching, compression, and shear stress generated due to chemical stimulation.

ROS are molecules that are produced by cells in response to various stimuli. It can act as signaling molecules, activating pathways that lead to changes in gene expression and cellular function. Furthermore, NOx are also signaling molecules that can be produced by cells in response to mechanical stress due to chemical stimulation. NOx can act as vasodilators, promoting increased blood flow to tissues in response to mechanical stress. NOx can also regulate gene expression and cellular function, particularly in the context of inflammation and immune responses.

Overall, the activity of ROS and NOx during mechanical stimuli on cells is complex and multifaceted, with both molecules playing important roles in regulating cellular responses to physical stress. Depending on the type of drug used, the effects can be temporary or long-lasting and can vary in intensity. Drugs can be used to study cellular function, target specific cells, and have therapeutic effects on the body.

#### 1.3.3.3 Optical excitations

This method uses light to excite cells, such as laser or LED illumination. This technique is commonly known as optogenetics, which is a method that uses light to control the activity of specific cells, typically neurons, in living tissue. The light used in this technique can come from

various sources, such as laser or LED illumination. Laser illumination is a type of light that has a very high intensity and a very narrow wavelength, while LED illumination is a type of light that is less intense and has a broader wavelength.

The purpose of using light to excite cells is to study cellular function, modulation of the specific activity in the cells, or induce changes in the cell itself. Depending on the type of light used, the effects can be temporary or long-lasting and can vary in intensity. Optogenetics is widely used in neuroscience, to study brain functions and to develop therapies for neurological and psychiatric disorders. Additionally, LED illumination is also being used in phototherapy, which is a non-invasive treatment that uses specific wavelengths of light to treat various skin conditions such as acne, eczema, and psoriasis.

#### 1.3.3.4 Base excitations

The problem with the above method is that it is not external. In addition, it is not suitable for generating FRFs, since it is not possible to measure the input accurately. A more promising alternative is the use of base excitation, which is a technique that does not alter the structural dynamics of the system.

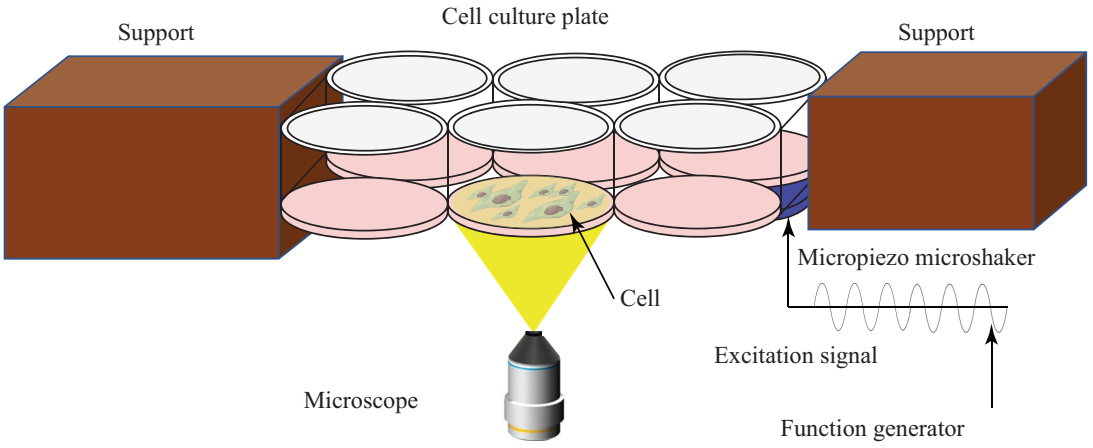


FIGURE 1.13: External stimulation of cells in cultured Petri dish through the piezo disc attached at the base of the plate.

In our study, a micro-shaker is used to excite the structure, as shown in Figure 1.13. The input to the disc is measured and controlled by a function generator. It can be mounted on the base of the cultured disc. It is also possible to find the FRFs of the biological cell by taking base motion as the reference. Since the response is affected by the dynamic characteristics of the testing apparatus, care must be taken during the design of experiments.

### 1.3.4 Measurements methods

It is impossible to place sensors directly on a micro-size biological sample, so various alternative detection methods that mostly use optics have been developed. These methods must use non-contact devices and be able to operate at high frequencies. Measuring the motion of microstructures is challenging because of the high frequencies involved. One technique that has been adopted from optics to overcome this challenge is position-sensing device (PSD). This method uses a LASER light source with 630 nm wavelength on a moving structure at a specific point at a prescribed frequency. This laser reflects or refracts toward the PSD. By coordinating the laser spot with the motion of the micro-size system under excitation frequency, it is possible to record the movement of the structure using the PSD at different times. The highest frequency that can be detected is limited by the pulse time of the refracted laser light.

Since the motion of microstructures generally includes high frequencies, however, the direct observation of the motion requires high contrast microscope or a high-speed camera (CCD). Retrieving the associated data requires a data acquisition unit and image-processing system. Video-imaging techniques can also be applied to measuring structural motion. For instance, a CCD camera can be used in conjunction with an optical microscope to record the motion of microstructures, which can then be analyzed using image processing techniques. Advantages of this method include simplicity of the setup and not requiring expensive equipment, since only an optical microscope, a regular High-speed camera, and a laser light source are required. However, several images must be collected to describe the motion completely. This method is more suitable for measuring in-plane motions.

There are various experimental modal analysis techniques, each with its advantages and limitations. The experimental modal analysis involves physically testing a system in a controlled environment. This method provides accurate and reliable results but can be time-consuming and expensive. Another method is numerical modal analysis, which involves using computer simulations to model the behavior of the system. This method is cost-effective than experimental modal analysis, but the accuracy of the results are limited by the assumptions and inputs used in the simulation. Regardless of the specific technique used, modal analysis is an important tool for understanding the dynamic behavior of structures and mechanical systems. It allows researchers to identify and diagnose problems with the system and to design modifications to improve its performance.

In this study, Vibrations of the structure are measured using non-contact means using an indigenous laser-based position sensing device.

## 1.4 Motivation

Dimensions of the structures range from subatomic particles to celestial bodies such as planets and stars. These structures have various roles in the evolution and functioning of the universe, their impact on the physical and chemical properties of matter, and their potential for supporting life. Macro-scale and micro-scale structures are two distinct categories of structures that differ in size and complexity. Macroscale structures are typically on the scale of meters or centimeters. In contrast, microscale structures are typically on the scale of a micro-meter or nano-meter and are often too small to be seen without a microscope. Micro-scale structures include microelectromechanical systems (MEMS) and biological cells. The micro-scale cells are the fundamental unit of life in all living organisms. They are the smallest unit of life that can function independently and are composed of molecules, including DNA, proteins, and carbohydrates. It is a complex dynamic system with a highly integrated structure and function. The dynamic behavior of such micro-scale structures is a complex and multi-faceted subject of significant importance in various fields, including materials science, engineering, and biology. Understanding the mechanics of cells and their specific behaviors and responses under different conditions can provide valuable insights of their characteristics and facilitate the development of new technologies and applications.

The field of cellular biomechanics studies how cells respond to mechanical stimuli in their native environment and how these mechanical signals can influence cellular physiology. This includes changes in the mechanical properties of cells as they interact with their surroundings, as well as the ways in which cells respond to mechanical signaling pathways. Alteration in mechanical properties will influence their biological behavior, such as cellular growth, nucleation, unfurling, migration, and necrosis. The health condition of the cell and quantification of the mechanical properties of individual cells has been an active area of research. The mechanical properties of cells are closely related to the pathological conditions of humans[1]. Any changes in the mechanical properties can result in the breakdown of the proper functioning of the cells and, consequently, give rise to disease states. Studies on the evaluation of the viscosity of individual cancer cells have the potential to explain the mechanisms of disease onset and progression[2]. The present emphasis of biomedicine is on the genome's and proteomics disease that results from changes in the biophysical or biochemical characteristics of living cells. Recent breakthroughs in mechanobiology and nanotechnology indicate that cells and tissue respond to mechanical or chemical stress to contribute to the progression or delay of disorders actively.

Mechanical diagnosis of cells refers to the measurement of mechanical properties such as stiffness, viscoelasticity, and deformation characteristics of cells. Various techniques have been developed to investigate mechanical properties of cells, including atomic force microscopy (AFM), optical tweezer, and microfluidics-based techniques. AFM is a high-resolution technique that can measure mechanical properties of cells with sub-nanometer resolution. Optical tweezer utilizes focused laser beams to manipulate cells and measure their mechanical properties. Microfluidics-based

techniques use microchannels to apply shear forces on cells and measure their deformation. These techniques have been used to study a wide range of cells, including red blood cells, cancer cells, and stem cells, and have provided valuable insights into cell mechanics in normal and pathological conditions. Mechanical diagnosis of cells has the potential to revolutionize diagnosis and treatment of various diseases by providing a new avenue for identifying biomarkers and developing targeted therapies based on cell mechanics.

Early diagnosis of the disorder reduces incidence, morbidity, and treatment costs and highlights the relevance of studying cellular biomechanics and its behavior. Various techniques use vibration monitoring, ultrasound irradiation, spectrophotometry, and emerging trends in nanotechnology but have their limitations. Meanwhile, the existing bioassays used to investigate these concerns are intrusive, expensive, and time-consuming. To address these limitations, a new technique is required that is rapid, noninvasive, and inexpensive for studying the physiology of biological systems. Hence, it motivates us to develop such diagnostic tools or experimental techniques which help to improve or monitor health conditions.

The existing experimental techniques are conventionally used for the dynamic characterization and assessing the mechanical behavior of macro structures for various applications, including the determination of dynamic parameters of the system (mass, stiffness, and damping). In these techniques, the structure is stimulated with a definite frequency and of various types (impulse, chirp, sinusoidal, etc.) using an actuator, and the subsequent responses are measured from sensors. This thesis examines the experimental assessment of the vibration-based dynamic response of several macro and microscale systems, including biological cells.

Dynamic response refers to the time-varying response of a structure, often in the form of mechanical vibrations, in response to a known stimulus. Such research is well-known for macro-size counterparts. Vibrations in microscale structures often have a very small amplitude and high frequency. Therefore, the initial difficulty is to accurately detect these vibrations and compare them to established theoretical findings for validation. The true objective of this work is to interpret the alteration in vibration characteristics of biological structures that are anticipated and experienced during normal operation. We can predict the condition of a cell structure and monitor changes from its vibration characteristics. The primary concern is to use the well-established theory of modal and harmonic analysis to examine the measured data and develop deterministic conclusions. Our research begins with the femur bone and concludes with a diagnostic of cancer cell research.

This thesis aims to extend the investigation of a simple macroscale biological structure to a complex microscale structure and use experimental measurements based on the vibration characteristics to investigate the behavior of such structures. The valuable information about their internal structure (e.g., changes in elasticity, stiffness, etc.) and the external interface (e.g., boundary conditions) is measured and analyzed for the purposeful work.

This work will be carried out in four sections to meet all the objectives of the proposed thesis. The background of the proposed work informs us about the available recent techniques that are in trend to identify the exact phenomena and process on which it works. This helps to determine the opportunities and obstacles of the method during their use in the mechanical characterization of biological cells.

## 1.5 Gaps in existing research

The present thesis aims to address significant issues that still need to be addressed, as predicted by the shortcomings of existing techniques. The significant issues are as follows:

- Development of a non-contact approach to study the dynamic response of biological structures and evaluate their mechanical properties.
- Lack of noninvasive experimental techniques that can able to characterize healthy and diseased cells based on their dynamic behavior.
- Understanding the dynamic behavior of the cell under low frequency external mechanical stimuli environment.
- Absence of noninvasive techniques for evaluating the dynamics of flowing cells based on their vibration signatures.
- Development of the mathematical framework for assessing the mechanical properties and validated the same with the experimental technique that works under the same environment similar to the analytical boundary conditions.

The present works aimed at addressing these gaps and developing a neat process for the identification of the mechanical properties of normal cells, diseased cells, and clinically treated cells. Along with this, the study also allows us to propose a technique for the measurement of cell dynamics during flow and the associated morphological changes. And also focuses on the measurement of the protein expression level on the basis of their vibration signatures. The work aims to identify a platform that can be able to evaluate the cell properties and can also capture the improved mechanical properties of diseased cells after suitable clinical or drug treatment based on their mechanical responses. Results will be capable of detecting differences in the mechanical properties between cell lines that vary in normal, malignancy, and invasiveness cells and validate these observations through independent measurements with any of the available methods. This technique will enable sensitive measurements for biophysical studies of environmental changes on a cell, which could prove valuable in studying the role of signaling in disease.

## 1.6 Focus and Scope of the research

The subject of the thesis is at the crossroads of various domains of current interest. These include the study of (1) the dynamics of the femur bone, (2) experimental and numerical studies on the influence of nanocarrier additives on the biomechanical response of rat skin, (3) the dynamics behavior of Huh-7 cancer cells, (4) the effect of low-frequency excitation on the apoptosis of the Huh-7 cells, (5) the mechanical resonance of Huh-7 cells based on the elasticity of adhesion proteins, (6) development of Piezoactive ZnO /PDMS microchannel device for cell diagnostics and finally (7) understanding the cancerous membrane and their constituent effect using molecular dynamics. The study provides experimental, analytical, and numerical studies of several biological structures from the body's largest organ i.e. femur bone, to the smallest basic structural and functional unit of life i.e. cells. The pertinent section of the thesis provides a review of the relevant topics.

We begin our study with measurements of vibrational frequencies and mode shapes of a femur bone, a biological structure. The femur is the largest and strongest bone in the body. It plays a vital role in supporting the body's weight, providing leverage for movement, and protecting the delicate organs of the thigh. Vibrational studies of the femur can provide valuable insights into its structural integrity and its ability to withstand the forces applied to it during daily activities. By analyzing the natural frequencies and modes of vibration of the bone, researchers can determine its stiffness, strength, and resilience. This study focused on goat femur bone and was configured as a fixed-fixed beam. The bone material properties were considered homogenized property, a simple assumption from a material point of view (no material complexities as in the case of biological cells) but traced the exact complex geometry. The material simplicity makes modeling simple and focuses attention on the role of geometric features on vibration characteristics. We have explored several modes of vibration of the bone. Experimentally captured frequencies and several mode shapes of the femur bone have been verified with finite element method (FEM) simulations.

The emphasis is on investigating the ease of actuation and measurements of modes of vibration in biological structures and the verification of measured quantities from numerical simulations based on FEM models that have hardly any uncertainties. The vibrational study of the femur bone is an important area of research that has the potential to improve understanding of the mechanics of the vital bone. By analyzing the vibrational properties of the femur, researchers can identify areas of weakness and develop more effective treatments for bone injuries and diseases. The results of this study are not only useful in the design of a non-invasive technique but also in a lab-on-chip device for the exploitation of modes of vibration of such structures. This study is a confidence builder for the employed experimental technique to study more complex structures (taken up subsequently) where there are more uncertainties in modeling the structures, such as human skin.

Next, we studied the vibrations of non-homogeneous skin and their dynamics. The vibrational study of human skin and its mechanics is an important area of research because it provides insight into the complex properties of the skin. The skin is the largest organ in the human body and plays a vital role in protecting the body from the external environment. It is also responsible for regulating body temperature, sensory perception, and the production of certain hormones. This work can help improve our understanding of the skin's functions and its response to different stimuli, leading to better treatments for skin diseases and improve overall skin health.

Similarly, various nanocarrier gels and creams are used for the treatment of different types of skin disorders. Nanocarrier gel and cream are topical products that have been developed to deliver active ingredients to the skin at the nanoscale. This offers several potential benefits for the treatment of various skin conditions. One of the key importance of using nanocarrier gel and cream on the skin is their ability to penetrate the outer layers of the skin and deliver the active ingredients directly to the site of action. The nanoscale size of the active ingredients in these products also enables them to be more easily absorbed by the skin, leading to better and faster results.

This allows for more efficient and effective treatment of a wide range of skin conditions, including acne, psoriasis, eczema, and skin irritations. Hence, we extended the work to study the effect of nanocarrier-formulated gel and cream on the dynamics of the skin using a non-invasive technique. Here the vibration characteristics are affected significantly by the external cream or gel interface, i.e., the top surface of the skin on which the gel or cream is applied. The exposure time for the cream or gel on the skin surface modulates its modal frequencies. This study addresses two major issues: (i) the use of a Position Sensing Device for dynamic measurements on a 3-D structure, and (ii) establishing vibrational correlates with the mechanical properties of the skin that effects due to nanocarriers substances w.r.t time using non-invasive measurements on skin. This research can help to improve understanding of the skin's functions and its response to different stimuli, which can ultimately lead to better treatments for skin diseases and improved overall skin health.

Further, we studied the biological cells that are complex structures both geometrically and materially. Their boundary conditions are nowhere near the two cases studied before. It is essentially because of the complex structure of cells that we first studied simpler, homogeneous structures and carried out many experiments on them so that we could place greater confidence in our experimental results on cells. The study of cells is split into two parts. First, we study the mechanical behavior of normal liver cells and then of cancerous liver (Huh-7) cells. Cellular elasticity and viscosity are emerging indicators of the disease state and its progression. An alteration of intracellular viscosity has the potential to modulate cellular function and hence is often associated with various pathological conditions. Cancer cells at each stage of progression are postulated to show differential viscosity. Viscosity is an essential parameter that regulates bio-molecular reaction rates of diffusion-driven cellular processes. Hence, abnormal viscosity

levels are often associated with various diseases and malfunctions like cancer. For this reason, monitoring intracellular viscosity becomes vital. In comparison, several approaches have been developed for in-vitro and in-vivo measurements of viscosity. Analysis of intracellular viscosity in live cells has not been well explored till day. This study reveals and introduces a novel, natural, frequency-based, non-invasive method to determine the intracellular viscosity in cells. This method can not only efficiently analyze the differences in intracellular viscosity post modulation with molecules like PEG or glucose but is sensitive enough to distinguish the difference in intra-cellular viscosity between normal and cancer cells as well.

Interestingly, TGF-$\beta$, a cytokine reported inducing epithelial to mesenchymal transition (EMT), a feature associated with cancer invasiveness, resulted in reduced viscosity of cancer cells, as captured through our method. To corroborate our findings with existing methods of analysis we analyzed intra-cellular viscosity with a viscosity-sensitive molecular rotor-based fluorophore-TPSII (designed at Prof. Inamur R. Lasker Lab.). In parity with our PSD-based approach, an increase in fluorescence intensity was observed with viscosity modulators, while TGF-$\beta$ exposure resulted in its reduction in the cells studied. This is the first study of its kind that attempts to characterize differences in intracellular viscosity using a novel, non-invasive PSD-based method. Also, recent findings suggest that intracellular viscosity varies significantly between invasive and non-invasive cells, like healthy breast cells exhibit higher viscosity than invasive carcinomas. No wonder the elastic response of tumor cells has been explored earlier as a diagnostic for cancer cells or their metastatic potential.

With experiments on healthy and diseased cells, we also explore the vibrational frequencies of the cells that are an excellent marker for most major cellular disorders. The further extended study on MCF-7 (breast) cancer cells, and their experimental captured vibrational frequencies, turn out to be an excellent marker for detecting cancerous cells and their transition from an epithelial to a mesenchymal state. Although the internal structure of these cells is quite complex, with many more elastic components and cross-connects, their gross vibrational behavior is captured very well using numerical simulations. Numerical simulations are performed on the real 3-D images of the cells obtained from confocal imaging. Experimental and numerical findings of the study have been an eye-opener as it indicates that noninvasive (to the cells) measurements of cellular viscosity and frequencies can be used for detecting perhaps several diseases, thus opening a new area in mechnodiagnostics.

Cancer research focuses on identifying methods that trigger cancer cell death without damaging the surrounding normal cells. The biophysical and biochemical characteristics of tumor cells offer multiple targets for treatments. Recent developments in cellular and molecular oncology have led to significant improvements in diagnostic and therapeutic applications, although antitumor therapies are still ineffective. One of the primary focuses of current research is to improve techniques for suppressing carcinogenesis. Chemotherapy is the most significant method used in

the current anti-cancer endeavor. Due to its unfavorable effect on normal cells, unfortunately, its efficacy is diminished.

Consequently, to improve oncochemotherapy, it is required to expand research efforts on possible novel oncolytic drugs or treatment approaches that would precisely target tumor cells. Mechanical vibration is a possible biocompatible treatment approach and is a subject of mechanomedicine in the field of cancer. Hence, we further study the Huh-7 cells subjected to low sound frequency (20 Hz to 60 Hz) excitation and its effect on apoptosis. Similar PSD-based noninvasive techniques were used to evaluate the frequency response of the cells. Cell viability of Huh-7 cells was determined while subjected to a low range of mechanical vibration. It was observed that the cellular morphology changes in the Huh-7 cells. These changes alter cell shape and size. Cells degrade and attain more polygonal shapes compared to cells without excitation. Further, obtained frequencies were compared from the analytical model (standard Voigt). Apoptosis and necrosis were evaluated after mechanical vibration and compared to cells maintained in static culture. Even though the particular intracellular processes by which low-frequency mechanical vibration induces cell death through apoptosis and necrosis are not well understood. Nevertheless, outcomes imply a potential role of mechanical vibration that might represent a unique application of mechanomedicine to cancer treatment.

In light of the above affirmations, several kinds of research have been required to improve the understanding of cytophysiology and the developmental process of cell aggregates. Translational research is an effective key for this purpose, and nanoparticles, acoustic irradiation, mechanotransduction, and vibration analysis have been shown to potentiate a better understanding of active mechanisms at the cellular, subcellular and molecular levels.

The idea that the cell is a mechanical system has greatly impacted how we think about biology. Hence, the importance of recognizing the cell as a mechanical entity, both in terms of its behavior and response to surrounding mechanical conditions, is becoming more apparent in various biological studies. The application or analysis of the role of mechanical forces in eliciting a molecular response, leading to a quantifiable change in form and/or function. The importance and influence of environmental and mechanical conditions on cell fate and function have been thoroughly established and are the subject of multiple reviews.

Mechanobiology is a key component in pathology; development, and morphogenesis; and in many specialized tissues such as bone, tendon, heart valves, intervertebral disc, and cartilage. The ability to precisely manipulate the mechanical microenvironment to understand the mechanisms and processes by which mechanical forces regulate cell function will require novel experimental platforms and techniques. Several experimental tools and methods have been made to measure a cell's stiffness, adhesion, and contractility and address the cell's response to mechanical stimuli. Microfabrication technology can provide viable solutions to problems associated with understanding cell biomechanics and mechanobiology. Applications of these microtechnologies

in this field have prompted recent reviews on the subjects. Microfabrication studies on cells may provide significant benefits in achieving what has to be done, being helpful, being exact, and completing tasks rapidly. However, there is still a long way to go before most people adopt these technologies. This study aims to look at and summarize the recent changes in microfabricated technologies that are being used to solve experimental problems in the fields of cellular biomechanics and mechanobiology.

Here, we aim to develop a smart microchannel that can be used to study various aspects of mechanobiology. The concept of smart microchannels was carried out to control cells in biomedicine precisely. In this study, a low-cost piezoelectric-based microchannel was developed to evaluate the resonance behavior of targeted Huh-7 cancer cells. A novel opto-mechanical vibration-assisted approach was used on the microchannel, which was made of synthesized ZnO nanoparticles and polydimethylsiloxane (PDMS). The outcome of the study indicates that the fundamental frequencies of the cancer cells were affected by the actuations on the ZnO/PDMS microchannel, and may be useful for developing a resonance-based device for identifying malignant conditions.

There are several drawbacks to existing experimental techniques or methods used in studying the behavior of biological cells. These include:

1. Accuracy: Experimental techniques often have limited spatial resolution, which means that they cannot provide detailed information about processes occurring at the molecular level within a cell. In addition, experimental techniques are often limited in their temporal resolution, meaning they cannot track processes that occur over concise periods of time.

2. Cost and time: Experimental techniques can be expensive and time-consuming, particularly if they require specialized equipment or facilities.

3. Ethical concerns: Some experimental techniques, such as those involving the use of animals or human subjects, raise ethical concerns.

4. Limited control: Experimental techniques often have limited control over the conditions being studied, which can make it difficult to isolate and study specific processes or variables.

5. Limited flexibility: Experimental techniques are limited to studying a specific system or process, and it can be difficult or impossible to modify the conditions of the study once the experiment has commenced.

Thus above listed drawbacks motivate us to look into some versatile, speedy, and cost-effective tools or preferred methods for analyzing biological cells and understanding the mechanisms underlying a wide range of biological processes.

Molecular dynamics (MD) simulation is a computational technique that allows for the prediction of the behavior of a system at the atomic level. It is a powerful tool that can be used to analyze biological cells, and in many cases, it is preferred over experimental methods for various reasons. One of the main advantages of MD simulation is that it allows for investigating processes that may be difficult or impossible to study experimentally. For example, MD simulation can be used to study the dynamics of proteins and other biomolecules in a cell, including their interactions with other molecules and their movements within the cell. This can provide insights into the mechanisms underlying various biological processes, such as enzyme catalysis, protein folding, and signaling pathways. Another advantage of MD simulation is that it allows for examining the effects of different conditions on a system. For example, the impact of different temperatures, pH levels, or chemical modifications on the behavior of proteins or other biomolecules. This can help researchers to understand how these factors influence the function of a cell or the behavior of a particular biological process.

MD simulation can be used to accurately predict how a system will behave in various conditions or environments. It can be used to study how proteins or other biomolecules might behave in different body parts or under different physiological conditions. This can help to understand how drugs might affect a particular biological process and to identify potential therapeutic targets. Finally, MD simulation is generally less time-consuming and more cost-effective than experimental methods, particularly for complex systems or processes. It allows researchers to study a wide range of scenarios in a relatively short period of time without the need for expensive equipment or the time-consuming process of conducting experiments.

Overall, MD simulation can provide valuable insights into the behavior of biological cells and the mechanisms underlying a wide range of biological processes. It is a valuable alternative to experimental methods and is often preferred due to its versatility, speed, and cost-effectiveness. Hence, Further extending the research work to use the capabilities of the molecular simulations to capture the impact of cholesterol levels in the cancerous membrane protein system under external mechanical stimuli.

The low-cholesterol cancerous environment can affect the biophysical behavior of transmembrane proteins. It is difficult to experiment and measure the dynamic behavior of the membrane protein systems under a strained environment. This study adopted an atomistic approach to investigate the transmembrane protein behavior during lipid-bilayer separation under strain at different cholesterol concentrations. Several structural parameters were studied to understand the dynamics of the membrane protein systems. The impact of the decreasing cholesterol across the membrane protein system and their effect on area-per-lipid, average tilt angle, and order parameters. This observation indicates that the decreased cholesterol concentration in a cancerous environment hinders the bonding and compactness of the membrane protein system. Stretching

and unfolding of protein were observed during bilayer separation and the resistance stresses decreased for decreasing cholesterol.

The investigation revealed that cholesterol is an essential membrane constituent that impedes diffusion and resists protein detachment at high concentrations. The transmembrane proteins can retain end terminals positions across the membrane and resist functional failure. This study showed that decreased cholesterol concentration causes significant changes in the biophysical behavior of the membrane protein system that could trigger the mechanosensitivity of transmembrane proteins under mechanical perturbation.

## 1.7 Objectives of the proposed research

We performed a detailed literature review to understand the microstructure and the mechanics of the biological cells. There are several mechanical techniques for biological cell analysis that have their advantages and limitations. For the present study, based on the existing research gap the following objective is refined from the perspective of the development of an indigenous non-contact experimental technique.

- Development of an experimental platform to measure the dynamic response of biological samples on the macro-micro scale.
- Mechanical diagnosis of the macro-sized biological samples based on their vibration signatures and their numerical analysis.
- Study the role of TGF-$\beta$ induced EMT on the intracellular viscosity in cancer cells.
- Comprehending the impact of external low-sound frequency stimulation on the mechanical response of cells.
- Investigation on the mechanical resonance of Huh-7 cells based on the elasticity of adhesion.
- Development of a smart microfluidic platform to study the dynamics of different cells and their characterization based on their resonance.
- Atomistic analysis of the effect of cholesterol on cancerous membrane protein system to reveal the unfolding and associated resistance under strain environment.

## 1.8 Outline of the thesis

In the first chapter of this thesis, we provide motivation to carry out the study on the dynamics of biological cells. We started the work for the prior validation of the developed experimental

technique from the largest organ of the body viz. bone and skin, and further move to the functional basis of life i.e. cells.

In the second chapter, we study the dynamics of a femur bone using PSD based experimental setup. Experimental results are validated by numerical means. This noninvasive experimental technique helps to find out the mechanical behavior of the bone sample. The response of the bone depicts the damping characteristics of bone, which reflects the decay of vibration in the biological sample. These values are auspicious for the evaluation of the modulus of elasticity of the bone sample. The evaluated modulus of elasticity by the proposed experimental technique and finite element modeling are close to each other. Bone is anisotropic material; hence homogenization using Computational Multiscale Analysis (CMAS) gives the optimized material property of the sample, which is further used for the evaluation of the mechanical response of bone. A numerical analysis was done to evaluate the frequency response of the femur bone. The modal analysis shows the various natural frequencies which can aid in designing the prosthetic bone to avoid the failure of the prosthetic parts. Random vibration analysis was carried out to observe the real-life daily activity of the bone sample, and a comparative study for deformation in the bone was done using a non-destructive technique and a numerical approach. This work shows the establishment of the experimental technique for the evaluation of the mechanical properties of the bone sample.

In the third chapter, we study the dynamics of skin (obtained from the dorsal portion of Wistar rat) and show the alteration in the elastic behavior of skin over a period of time with and without nanocarrier additives application. Nanocarrier additives modulate the natural frequency of the skin. This study evaluates the natural frequencies and Young's Modulus of the skin concerning the change with time using a non-destructive optical technique, such as PSD and FE modeling. Based on the results, the normal skin's experimental frequencies were found to be higher than the skin sample with cream and cubosome-loaded gel. The Numerical FE results exhibit the modal frequencies and mode shape at different frequencies. Also, we evaluated the stresses and deformation in the skin with the increase in the stratum corneum thickness. Notably, the described methodology predicts the dynamic behavior of the skin. This experimental technique has enormous scope in the diagnosis of diseased skin. Vibration analysis allows observing the variations in the dynamic behavior of healthy and diseased skin with time. We verify these frequencies with analytical calculations and find that all the measured frequencies are within an acceptable range of theoretically predicted values. Further, this method can be implemented to evaluate the in-vivo mechanical response of the skin, and a lab-on-a-chip device can be developed for real-time monitoring of skin behavior.

In the fourth chapter, we study the vibration signatures of cancer cells. Here we measure the natural frequencies of normal and specific cancerous cells. Findings showed that we could distinguish the two, based on their natural frequencies. We find that the natural frequency of cancerous cells is approximately half that of normal cells. We could distinguish epithelial and

mesenchymal cancer cells based on their natural frequency values. For Epithelial cells, we activate the signaling pathways to induce EMT and notice the reduction in the natural frequency. This mechanical assay based on vibration response corroborates results from biochemical assays such as Western blots and PCR, thus opening a new technique of mechano-diagnostics.

In the fifth chapter, we used noninvasive techniques to examine the effects of mechanical vibration on the frequency response and viability of Huh-7 cells. We observed changes in the shape and size of the cells, with a shift towards more polygonal shapes and degradation. When comparing the obtained frequencies to an analytical model, we found that the fundamental frequency of the cells and the onset of apoptosis and necrosis increased with an increase in the excitation frequency and duration. These results suggest that mechanical vibration may have a potential role in cancer treatment. However, the exact mechanisms by which it leads to cell death through apoptosis and necrosis are not fully understood.

In the sixth chapter, we used a non-invasive technique called the Position Sensing Device (PSD) to evaluate the resonance behavior of Huh-7 cells and compare the results to numerical AFM modeling. The atomic force microscope (AFM) has been used in cell biology for over a decade to investigate the mechanical properties of live cells and map the distribution of these properties, which can provide insight into the cytoskeleton and cell organelles. We developed a new method for numerical AFM characterization of the cells using real images of trypsinized Huh-7 cells, which allowed us to evaluate the natural frequency of the cells and investigate the impact of focal adhesion (FA) stiffness on the natural frequency. These measurements can help to improve our understanding of normal and pathological cell mechanics and potentially aid in disease diagnosis and therapy selection. The proposed technique and numerical approach can also be useful in selecting target therapy parameters and evaluating the mechanical properties of cells.

In the seventh chapter, a low-cost piezo active microchannel was developed to evaluate the resonance behavior of targeted cancer cells using a novel opto-mechanical vibration-assisted approach. The microchannel was made of piezo-active ZnO nanoparticles and biomimetic polydimethylsiloxane (PDMS). The microstructure of the ZnO nanoparticles was analyzed using scanning electron microscopy and X-ray diffraction (XRD). The piezoelectric properties of the proposed ZnO/PDMS microchannels were also evaluated to assess their mechanical and electrical behavior. The morphological changes in Huh-7 cells flowing through the electrically stimulated ZnO/PDMS microchannel were studied using high-speed imaging. The resonance behavior of the cells flowing through the vibrating microchannel was also determined using a position sensing device (PSD) based non-invasive experimental technique. The resonance frequency of cells in control (without actuation), low and high actuation conditions on the microchannel were evaluated and indicate that the fundamental frequencies of Huh-7 cells can be impacted by actuations generated by piezo activity on the ZnO/PDMS microchannel. These results may be useful for developing a resonance-based device for detecting the presence of malignant conditions.

In the eighth chapter, the biophysical behavior of transmembrane proteins in a different cholesterol-level cancerous membrane was investigated using an atomistic approach. Various structural parameters were studied, such as the area per lipid and average tilt angle, and the order parameter. This indicates that decreased cholesterol concentration in a cancerous environment weakens the bonding and compactness of the membrane protein system. The protein was also observed stretching and unfolding during bilayer separation with resistance stresses. The cholesterol molecules were found to be bonded with proteins and the investigation revealed that cholesterol at high concentrations impedes the diffusion and detachment of proteins. Therefore, transmembrane proteins can retain their positions across the membrane and resist functional failure when cholesterol concentration is high. This study demonstrated that cholesterol concentration leads to significant changes in the biophysical behavior of the membrane protein system, which could affect the mechanosensitivity of transmembrane proteins under mechanical perturbation.

The thesis ends by summarizing the findings of the whole work in the ninth chapter and states the future research directions

# Chapter 2

# Nondestructive Evaluation of Mechanical Properties of Femur Bone

## 2.1 Background

Bone mechanics is the study of the mechanical properties of bones and their behavior under various types of loading conditions. This field of study is important because bones play a critical role in the functioning of the human body. They provide the structural support needed for our bodies to move and maintain their shape, and they also protect internal organs from injury. The mechanical properties of bones are determined by their composition and microstructure. Bones are composed of living cells embedded in a matrix of collagen and minerals, primarily hydroxyapatite. Collagen provides flexibility and tensile strength, while minerals give bones their hardness and compressive strength. The arrangement and orientation of these components within the bone determine its overall mechanical behavior.

The mechanical behavior of bones is highly complex and depends on a variety of factors, including the type and amount of loading they experience, their age and health, and the specific region of the bone. For example, bones in the legs and feet are subjected to different types of loading than bones in the arms and hands, and bones in the spine have different mechanical behavior than those in the skull. One of the key factors that affect the mechanical behavior of bones is the type of loading they experience. Bones are subjected to two main types of loading: static and dynamic. Static loading occurs when a constant force is applied to a bone, such as when we are standing still. Dynamic loading, on the other hand, occurs when a bone experiences changing forces, such as when we walk or run. The importance of studying bone mechanics lies in the fact that it can help us understand how bones respond to different types of loading and how they can be injured or damaged. This knowledge can be used to develop better treatments for bone fractures and other injuries, as well as to design medical devices and prostheses that better mimic

the mechanical behavior of healthy bones. Hence, the study of bone mechanics is important because it helps us understand the mechanical behavior of bones and their response to different types of loading. This study can be used to improve the diagnosis and treatment of bone injuries, as well as to design medical devices and prostheses that better support and protect bones.

## 2.2 Introduction

The femur bone is the human body's longest and largest bone. It is also known as the bone of the leg. It attaches to the pelvis at the proximal end, forming the hip joint and joining the knee joint at the tibia's distal end. One of the most frequent fractured bones in the human body is the femur bone, which carries the maximum percentage of body weight [78]. The femur is a strong bone that is difficult to break. It requires a big impact force for them to break. Common injuries to femur bone at a young age are often due to high energy collision. The most common cause of femur fractures is a motor vehicle and motorcycle crash. Lower force incident is also common for fractures in old age who have weaker bones and unable to carry a sustainable body load. Various fragile bone diseases like osteoporosis, Osteopenia, Osteitis deformans, and osteomalacia are responsible for weakening and decreasing the bone load-carrying ability because of reduced bone mass. A decrease in bone mass causes a thinner cortical bone that therefore weakens the bone. This is caused mainly in older people. Due to this illness, people are falling more often and breaking their femur. Femur bone with its various parts are shown in Figure 2.1.

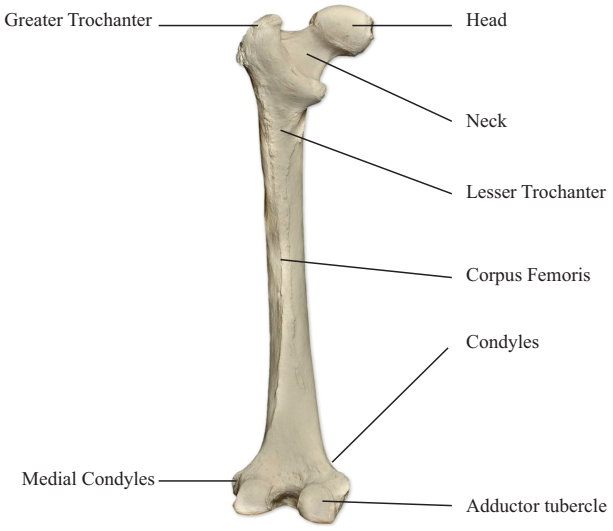


FIGURE 2.1: Structure of femur bone[79].

Femoral head fracture, femoral shaft, and femoral condyle fractures are the distinctive fractures mostly occur in femur bone at different locations. A femoral head fracture is a type of stress fracture. It is chronic and caused due to repetitive activities [80]. This fracture surrounds the head part of the femur. The shaft region is in between the lesser trochanter and the adductor

tubercle of bone. High energy collision in young age people and lower energy fall in elder age humans cause femoral shaft fractures [81]. The femoral fracture can be classified as transverse, comminuted, and open type shaft fractures. A femoral condyle fracture occurs after a medial tendon.

An Anterior Cruciate Ligament (ACL) is located at the center of the knee joint and extends from the backside of the femur. ACL reconstruction with extra-articular tenodesis occurs between the site of fixation of the extra-articular augmentation and the intraosseous femoral tunnel[82]. Several Researchers have performed experimental investigations on the various form of fracture and damages in human bone. Many researchers studied its mechanical behavior in different mechanical loading using techniques such as strain gauges [83], ultrasound testing [84], and universal testing [85].

Lang (1969) developed a method based on the measurement of ultrasonic bulk wave velocities (BWV) propagating along different directions of a bone sample as an alternative to conventional mechanical techniques, which are unsuccessful in measuring multiple elastic constants on the same sample [86]. BWV measurements are used for obtaining elastic longitudinal and shear constants in the various anatomical directions of a sample [87], [88]. The process, however, has some drawbacks: (1) the sample must have standard dimensions greater than a few millimeters (approximately 5 mm) [89]. (2) Multiple measurements with specimen repositioning and delicate manipulation of transducers are included in the BWV process. (3) Greatly increase the time and complexity of preparation of the specimen. (4) The accuracy of the BWV method is dependent on the orientation of the transducer and the acoustic coupling quality between the transducers and the sample [90].

The resonant ultrasound spectroscopy (RUS) method, will overcome the afore mentioned limitations of of BWV technique. The resonant frequencies of the sample are measured by propagating the ultrasound waves and the signals are received using transducers. The elastic constants of the sample are eluated using the resonant frequency data [91], [92]. RUS technique is widely used to characterize single crystals and biological materials such as human dentin [93] and bone [94]. The RUS [95] technique demands for high quality factor around few hundred and above are recommended to show sharp resonant peaks. Usually for crystalline or metallic specimens have higher quality factor(Q), where as biological samples are viscoelastic in nature, this will lead to overlap of resonant peaks, and thus these resonant frequency measurements become a drawback of RUS. RUS was successfully applied to materials with a smaller Q in the range of 150 [96] and to materials with a Q around 50 [97] with the use of a signal processing method for the resolution of overlapping peaks. Lee et al. (2002) estimated Q in the low range(10-30) for bovine cortical bone; however, they did not use any advanced approach to solve overlapping peaks and could not retrieve more than three resonants frequencies. Bernand et al. uses RUS with signal processing unit to characterize the anisotropic human cortical bone specimen in millimeter scale and retrieve

the elastic constants of the specimen [98]. Daoui et al. predicted the elastic modulus of a cuboid shaped trabecular tissue specimen using resonant ultrasound spectroscopy, and evaluate the resonance frequency to evaluate tissue elastic modulus [99]. RUS is a non-destructive technique that is easy to implement compared to traditional mechanical testing but has a limitation in the in-vivo studies. RUS demands the sample size at least millimeter size, and the surfaces should be parallel, this would lead to tedious sample preparation [88]. There should be strong coupling between transducer and specimen, hence the acoustic impedance between transducer and the specimen is a main drawback of the RUS technique [100]. The applicability of RUS in micro-damaged biological samples are still challenging [101].

Bone microdamage is required for the fracture risk assessment. Muller M. et al.[102] proposes the nonlinear ultrasound techniques for damage detection in human bone subjected to fatigue loading. Predicted the correlation of progressive fatigue of human bone to their nonlinear dynamical response. The ultrasound technique is having non-invasive and non-ionizing characteristics for damage detection in biological samples. These characteristics of this technique become merit for in vivo bone damage characterization. Nonlinear resonant ultrasound spectroscopy (NRUS) is one of the powerful techniques for damage assessment in the biological samples [103]. The nonlinear behavior of damaged materials can be significantly evaluated from this resonance-based technique. high-energy X-ray computed tomography imaging is also used for identifying the prominent cracks assessment. But for the samples with an increased quantity of damages, NRUS shows its better ability by revealing a corresponding increase in the nonlinear response.

Several factors need to be considered during the evaluation of the mechanical response of biological samples, such as geometrical data of the tested bones [104], loading rates, and point of application [105], material properties [106]. Inherent damages and voids throughout the sample decreases the overall strength of the bones. Thus, there is an increase in the error while evaluating the mechanical properties of the bone samples through experimental procedures. The femur bone consists of various constituents like cortical bone, trabecular bone, bone marrow, collagen fibers, and inorganic minerals. Both Cortical, and Trabecular, contribute to bone strength and support the load at different parts of the bone. Trabecular bone has a large surface exposed to the bone marrow and blood flow compared to cortical bone [107]. Therefore in terms of loads and strength, these constituents are essential to the bone and are taken into account for the analysis.

Bone is a composite material that shows nonlinear behavior; hence, evaluating its properties is a challenging task. These nonlinearities can be better understood by coupling the mechanical responses of micro and macrostructures together [108]. Homogenization is a process of making the composition of the structures uniform. Furthermore, the material will behave as same as the ideal structure [108].

Finite element analysis is one of the most versatile techniques to analyze complex structures and inhomogeneous material properties and is considered as a tool for biomechanics modeling

[109], which has complicated geometrical shapes and heterogeneous material properties. Viano et al. [110] evaluated the natural frequencies and mode shapes by considering the bone as simple beam models. The natural frequencies of the bone are found to be in the range of 250 Hz to 2250 Hz across several modes of vibration. Most of the researchers have evaluated the mechanical characteristics of the femur bone using strain gauges [111]. Strain gauges can measure the average values of strain, which changes with the applied force over the gauge length of the device and thus provide a source for comparison with numerical solutions, but at particular locations and cross-sections on the bone surface.

Mathukumar [112] found that the end loading and damping influence the natural frequency of bone. The frequency analysis of bones helps to predict the quality of bone or integrity to characterize the various disorders present in the bone structures. The modal analysis was used to determine the failure pattern of remodeled bone in the fractured model. A numerical approach was proposed to evaluate the natural frequencies and mode shapes of an unconstrained femur to get the mechanical response of the bone by changing the material density [113]. Stress analysis predicted the stresses experienced by the femur bone and evaluate the critical load for the ultimate failure of the bone. These findings are essential in the replications of the natural design parameters in the development of synthetic bone replacements [114]. Taylor [115] proposed the finite element model to evaluate the natural frequencies using modal analysis, and predicted the elastic properties of the sample, and compared these frequencies with experimental natural frequencies obtained using ultrasound technique. Keyak [116] proposes the Finite Element modeling of the proximal femur to predict fracture location and fracture type and compare it with mechanical testing. The fracture strength of the bone depends on the necessary constraints like boundary conditions, loading, and mechanical and hydraulic stiffness of the bone [117].

In this work, we experimentally evaluate the natural frequencies and corresponding mode shapes of a goat femur bone. These are a dynamic property of the structure; it represents a pattern of structural deflection corresponding to its natural frequency. Bone is held in mechanical configuration and excited with an impact hammer, and the response is measured using PSD unit-based optical technique. Elastic properties of the bone are evaluated using the measured natural frequencies from the experiments. The elastic modulus of the bone is also estimated using finite element analysis. The numerically predicted values are within 9% of the measured results. We emulate the experimental condition of random vibration, and analysis is carried out. The predicted spectrum followed the measured spectra.

This non-destructive technique helps to predict the mechanical properties of biological samples like bone, although a lot of the techniques are available in which many are based on destructive and imaging techniques [118], [119]. With the versatility of the technique, invivo and invitro experiments can be performed in the biological samples to find the mechanical responses. Each biological sample is having its natural frequency of vibration, and this frequency-based assay will

aid in determining the mechanical properties [120]. Damaged and diseased bone samples have a different natural frequency than a healthy bone sample [121]. Hence this technique will aid in the field of sports engineering to determine bone health conditions and monitor bone health, which can be possible along with the use of some suitable techniques with this technique [122]. Thus, the suggested method will provide the physicians with a tool to investigate the bone's condition/strength (after the proposed method will be clinically proven and regulatory approved).

## 2.3 Materials and Methods

### 2.3.1 Numerical Modelling

The Femur bone is designed and saved as a step file format and imported to ANSYS Geometric modeller. Material assignment to geometry has been done by creating the material library. In this, we assign the homogenized material properties evaluated using Numerical material testing (NMT) in the Computational Multiscale Analysis (CMAS). Table 2.1 provides the general material properties of the bone considered for homogenization.

TABLE 2.1: Properties of femur bone for homogenization [79], [123]

| Parameter | Cortical bone | Trabecular bone | Bone marrow |
|---|---|---|---|
| Hounsfield unit(HU) | 2200 | 800 | 660 |
| Density (g/cmc) | 2.020 | 1.371 | 1.012 |
| Young's Modulus (MPa) | 18155 | 3195.3 | 880 |
| Poisson's Ratio | 0.40 | 0.40 | 0.30 |

Figure 2.2 shows the various steps and a micro-macro decoupling scheme involved in the numerical analysis of homogenization using CMAS to acquire the homogenized property for the bone sample. The nonlinear two-scale analysis was performed on the bone with periodic microstructures (unit cells), based on the available functional macroscopic constitutive equation [108], [124]. Homogenization theory is used to solve the two-scale boundary value problems (BVP) derived within the framework [124], [125]. A series of numerical material tests (NMTs) is conducted on the unit cell model to obtain the data used to identify the material parameters in the assumed constitutive model. For the NMTs with arbitrary patterns of macroscale loading, the governing equations [108], [124] used for modeling microscale boundary value problem (BVP) equipped with the external material points is shown in Equation 2.1

$$F = \nabla_{Y\Phi}(X;Y) = \nabla_{YW}(X;Y) + 1 = H(X) + \nabla_{YU}(X;Y) + 1 \tag{2.1}$$

Where $X$ denotes the macroscopic material point in the macro scale, reference configuration is not an independent variable in the microscale kinematics. Here, $\nabla_Y$ is the gradient operator

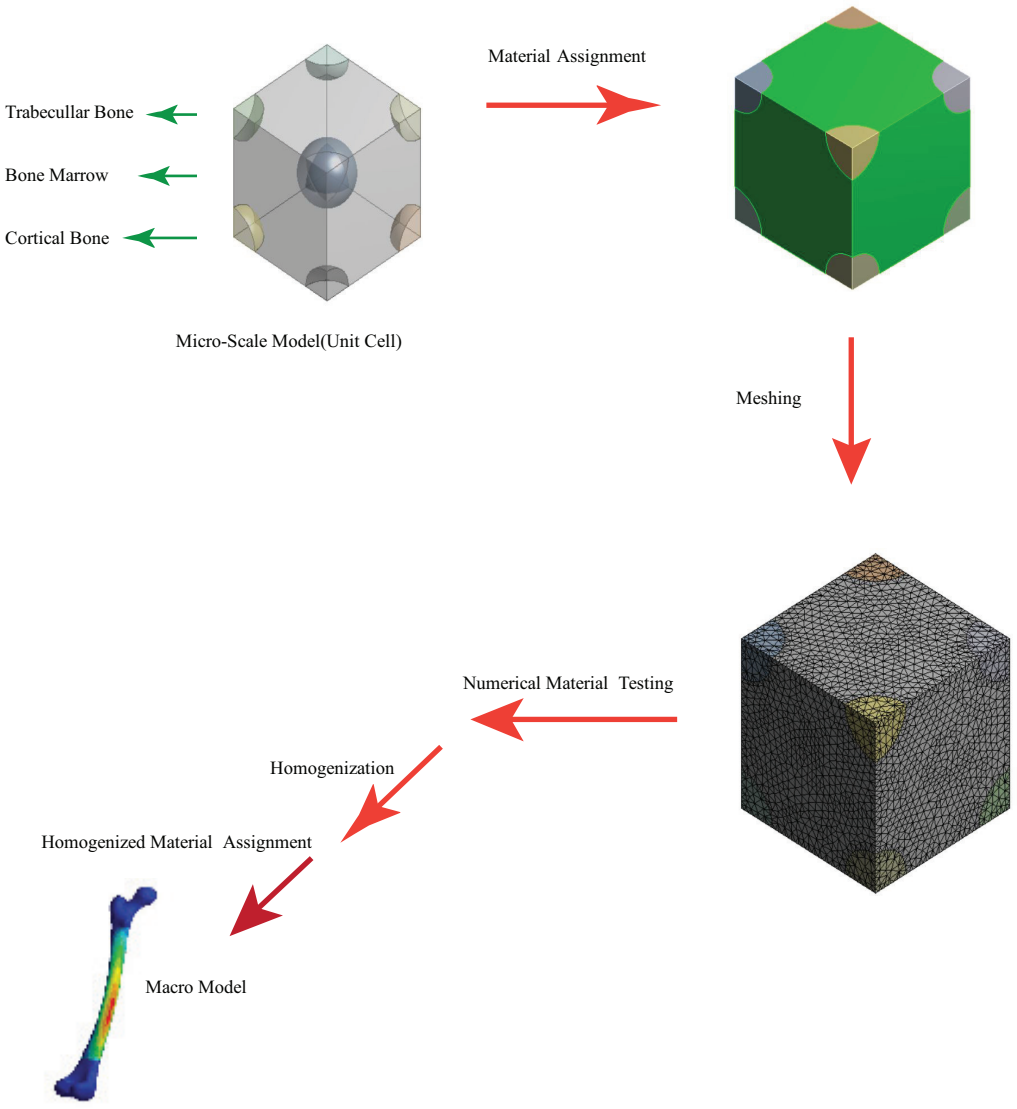


FIGURE 2.2: Homogenization Process using CMAS.

for the microscale $Y$, $H$ is the macroscopic displacement gradient that is independent of $Y$, $1$ is the second-order identity tensor, and $U$ is the $Y$ periodic displacement field that represents a fluctuation due to microscale heterogeneity. Homogenization has been done by considering a unit cell having bone marrow molecules at the center and cortical bone molecules at the corners adjacent by Trabecular bone molecules matrix using Computational Multiscale Analysis System (CMAS) in ANSYS. Computer-Aided engineering tool “CMAS" comprises the homogenization method for multiscale modelling [123]. Homogenization of the various constituting materials of bone in a microscale level carried out and then implemented to the macroscale level human femur bone has been done by the following steps.

#### 2.3.1.1 Create a Micromodel

Creation of a microscaled model of femur bone has been done in ANSYS design modeller using CMAS module. For this unidirectional centered and corner position for individual bone constituents is being opted and assignment of the material properties to the individual elements followed by meshing of the micro model as shown in Figure 2.2.

#### 2.3.1.2 Homogenization Analysis

After unit cell mesh generation and the boundary conditions [124], the numerical material test was conducted in the ANSYS and then equivalent property value such as elasticity modulus, density, and poison's ratio has been evaluated. Following are the steps involved in NMT analysis [124].

- A macroscopic constitutive material model is done by integrating the Equation 2.1.
- NMTs on a unit cell model using Finite Element mesh

1. If $H$ is macroscopic displacement gradient,then the relative displacement vector $q^{[J]}$ on the external points
$$q^{[J]} := H \cdot L^{[J]} \tag{2.2}$$
2. The microscopic BVP Equations are given by
$$\left.\begin{aligned} \nabla y.P &= 0 \\ F &= \nabla y \ . \ \omega + 1 \end{aligned}\right\} \text{in } y_0. \tag{2.3}$$
$$\left.\begin{aligned} P &= \Im F \\ \omega^{[J]} - \omega^{[-J]} &= \widetilde{H} \ .L^{[J]} \\ \widetilde{T}^{[J]} &= \frac{1}{\left|\partial y_0^{[J]}\right|} \int_{\partial y_0^{[J]}}^{\cdot} P.E^{[J]} ds \end{aligned}\right\} \text{in } \partial y_0^{[J]}. \tag{2.4}$$
By imposing
$$w^{[J]} - w^{[-J]} = q^{[J]}$$
Where $P$ is a nominal Stress vector, $F$ is force vector, $T$ is a traction force vector.
3. Obtain 1st Piola-Kirchhoff (PK) or nominal stress $P_{iJ}$ at each incremental step $n$ for all loading patterns $\alpha$ from the reaction force vector directly obtained by solving the extended microscale BVP
$$P_{iJ} = \frac{Ri[J]}{|\partial Y_{0[J]}|}$$
Where $R$ is reaction force and $\partial Y_{0[J]}$ is the area.

- Identifying macroscopic parameters for materials

  1. Using the NMT data, calculate the macroscale 2nd PK stress

$$S^{[n,\alpha]} = \left( \left( F^{[n,\alpha]} \right)^{-1} P^{[n,\alpha]} \right) \tag{2.5}$$

     and the right-CG deformation tensors $C[n, \alpha]$ and store all sets of data over $n_{\text{step}}^{[\alpha]}$

  2. Build a function with the material parameters $p$

  3. Identify the macroscopic material parameters $p$ by solving the obtained algebraic equations $Gp = b$, where $G$ and $b$ are coefficient matrix.

- Macroscopic FE-analysis: Solve the macroscale BVP using the assumed constitutive model with identified material parameters.

After homogenization, the obtained isotropic material properties have been assigned to the femur bone shown in Table 2.2.

TABLE 2.2: Homogenized Properties of femur bone.

| **Property** | **Value** |
|---|---|
| Density (gm/cc) | 2.02 |
| Young's Modulus (MPa) | 14800 |
| Poison ratio | 0.3 |

We emulate the restriction of movement by the adjacent bones by applying fixed boundary conditions at the base of condyles and the femur neck. Modal analysis is done to evaluate the natural frequencies and the corresponding mode shapes.

### 2.3.2 Experimental Studies

Figure 2.3a shows the detail description of the experimental setup. A laser source with 23 mW power and 650 nm wavelength powered by an external AC Voltage source of 240 V and 50 Hz. Ideal goat femur bone was procured and held in fixed-fixed beam configuration using fixtures Figure 2.3a. The length of the bone in between the supports is marked and divided into five equal parts (Figure 2.3b). The bone is actuated using an impact hammer, and the response is measured at the predefined measurement points using PSD.

The laser beam (measurement beam) is incident on the measurement point on the bone surface and gets reflected from the surface, and the reflected beam carries information of the vibrations of the structure is captured using PSD (Figure 2.3a). Displacement of the bone was traced by PSD [Hamamatsu S5990-1], and the vibration amplitude is monitored using AC operating point

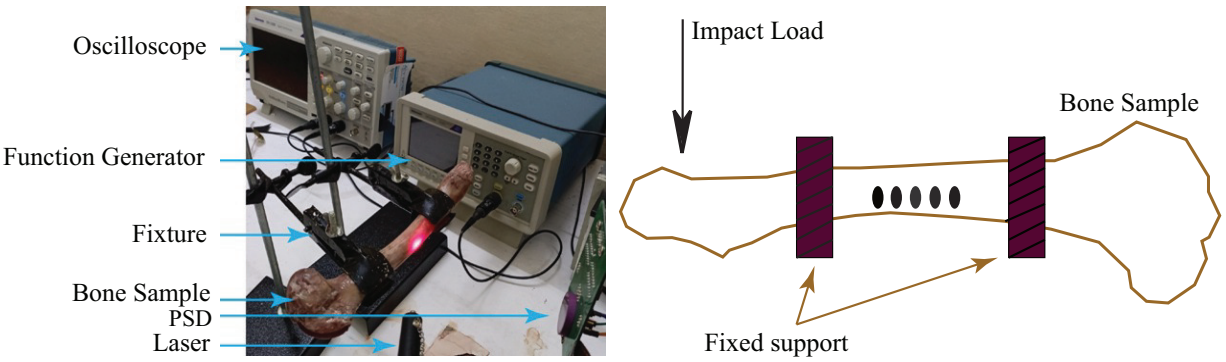


(a) (b)

FIGURE 2.3: (a) Experimental setup for the mechanical response of femur bone. (b) Loading and boundary conditions of the femur bone.

circuit [Hamamatsu C4674-01]. The output of the circuit is readout using an oscilloscope. The amplitude of vibration in X and Y directions are monitored using two channels. We take FFT of the time domain data to obtain the frequency response of bone at the specified measurement point. Sequential measurements are taken on the bone and supports. The response measurements are taken at the predefined measurement point on bone and support [126].

### 2.3.3 Response Measurements

The bone is held in a fixed-fixed beam configuration, and we ensure that the cross-section of the bone remains constant within the measurement zone called the gauge length of the specimen. The structure is actuated using an impact hammer, and the transient response of the bone is measured using PSD. Frequency response is obtained by taking FFT of the time domain data. We take the transfer function of bone with respect to base, to take away all base related modes. The natural frequency of the bone will be extracted using a peak picking approach.

### 2.3.4 Evaluation of Young's Modulus

Natural frequency of the system is a function of mass and stiffness. We consider the bone sample held in a fixed-fixed beam as a discrete model, upon neglecting the damping present in the system. The elastic modulus is estimated using measured natural frequencies. Table 2.3 provides the geometric parameters of the bone within its gauge length.

The natural frequency of any structure is a function of stiffness and mass, for a fixed-fixed beam of length $l$ the natural frequency is given by

$$f_n = \frac{k_n}{2\pi}\sqrt{\frac{EI}{wl^4}} \tag{2.6}$$

TABLE 2.3: Geometric properties of femur bone.

| Parameter | Value |
|---|---|
| Length of the bone (mm) | $248.52 \pm 4.02$ |
| Gauge length of the bone (mm) | $173.78 \pm 2.82$ |
| Diameter of the bone (mm) | $16.49 \pm 2.02$ |
| Mass of the bone (gm) | $70.04 \pm 1.08$ |

Where, $f_n$ is natural frequency, $E$ is the modulus of elasticity, $w$ is linear density of the sample, $l$ is gauge length, $k_n$ is a frequency parameter, and $I$ is the moment of inertia. Modulus of elasticity $(E)$ of the bone sample was evaluated using the experimentally measured natural frequency.

### 2.3.5 Random Vibration Analysis

The response of a structure under generalized loading conditions is modeled using random vibration analysis. As the structural dynamics predict the response, we are first carrying out modal analysis of bone to evaluate the natural frequencies and their corresponding mode shapes. Boundary conditions and modal results are transferred to the random vibration analysis environment in ANSYS. We provide base excitation to the structure at the support. The support motion data obtained by the experimental means is provided as an input for random vibration analysis. The power spectral density is evaluated at the predefined points on the sample, and from the power spectral density, the response spectrum is obtained.

## 2.4 Results

### 2.4.1 Experimental Studies

Measurements were taken at five predefined positions on the bone spaced equidistant from the center. The transient response of the bone is obtained by applying an impulse load of 100 N for 60 ms near point 1 on the bone. Frequencies are evaluated by plotting the frequency domain data of the specimen obtained from the oscilloscope in the MATLAB. A peak in the frequency spectrum corresponds to the natural frequencies. Figure 2.4a depicts the frequency responses in the frequency domain for the bone sample and the support. We take the transfer function of bone with respect to base to take away all base related modes. Figure 2.4b shows the transfer function response of the sample for capturing the most prominent frequency of the bone sample by removing the effect of support excitation and other vibration influencing noise acting on the supports. The transfer function plot shows the fundamental frequency at 1496 Hz and other natural frequencies at 3164 Hz and 4894 Hz. These values represent the different modal frequencies. Measurements are taken at predefined positions to evaluate the modeshapes of bone.

All the points on the bone sample show the same frequency response for the corresponding mode shapes.

Figure 2.5 shows the measured deformation at predefined points on the bone under the base excitation. Impulse excitation was given to the base, and the response was recorded in the frequency domain, and the amplitude corresponding to the natural frequencies are extracted. Since the sample is held in fixed-fixed configuration, maximum deformation was noticed at the center and less deformation in the points near the fixed supports compare to the center point in the bone sample. The experimentally measured modeshape follows as expected to Equation 2.6 (Figure 2.5).

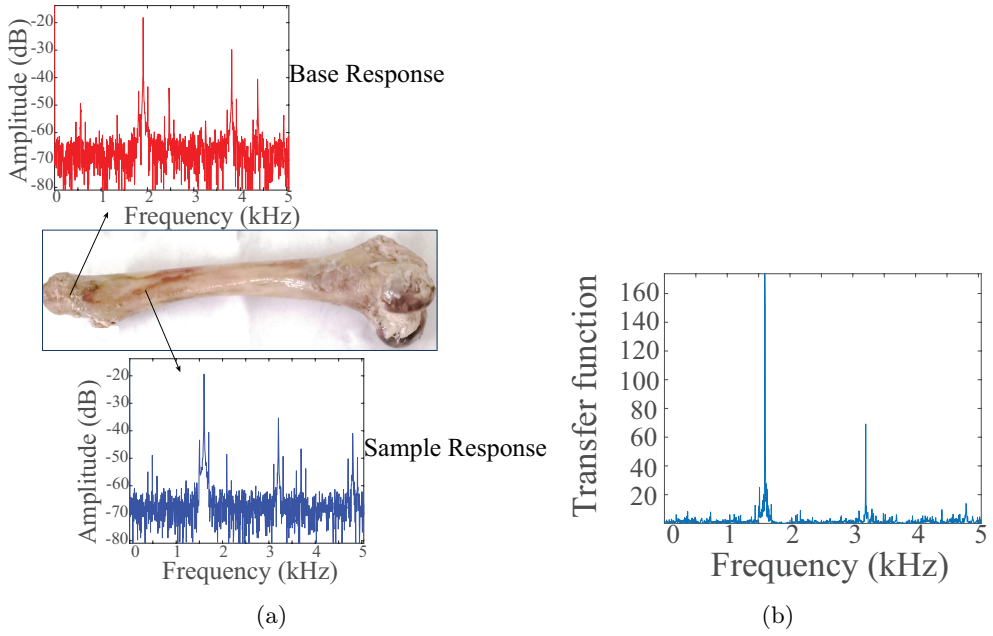


FIGURE 2.4: (a) Frequency responses of the bone sample and base support. (b) The transfer function of bone w.r.t base

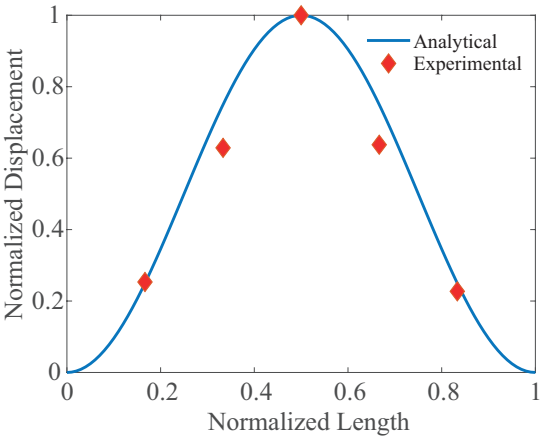


FIGURE 2.5: Comparison between experimental and analytical modeshapes.

Figure 2.6 shows the time domain response of a sample for an impulse excitation at the support. The amplitude of oscillation is decaying exponentially with time. We fit the decay with an exponential function (inset Figure 2.6) The time constant of the bone, which predicts the damping present in the system. The damping ratio for the bone sample is found to be 0.0394 ± 0.0011. The elastic modulus calculated from the measured natural frequencies is found to be 14.91 ± 1.21 GPa.

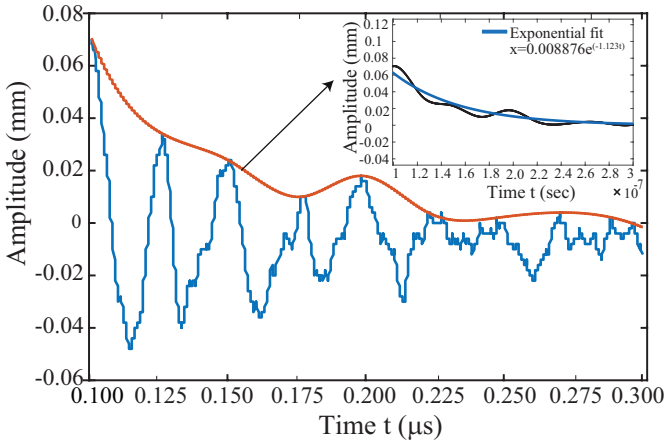


FIGURE 2.6: Time domain response of the bone sample with exponential decay for vibration amplitude.

### 2.4.2 Numerical Analysis

Numerical material testing was done using CMAS module in ANSYS to evaluate the homogenized properties of human bone. Elastic modulus and density of bone are found to be 14.8 GPa and 2.02 gm/cc, respectively. We use these properties for subsequent analysis. Zero displacement boundary conditions are applied at the supports and the modal analysis was carried out to evaluate the natural frequencies and corresponding modeshapes. Figure 2.7 shows the natural frequencies and modeshapes of the first three modes of vibration of femur bone held in fixed-fixed beam configuration.

Random vibration analysis of the bone sample was used to calculate the structural response to non-deterministic loads during normal daily human activities. In this study, support motion measured experimentally was provided to the fixed support of the bone sample. Displacement response on each point on the bone sample was evaluated in the ANSYS. The structure was found to have maximum amplitude at the center (point 3 in Figure 2.3b) and zero least displacements near support (point 1 and 5 in Figure 2.3b). In this study, we monitor the deflections at the center for the applied load. Figure 2.8 shows that the maximum displacement of 0.124 mm at the center of the bone. Numerical results were found to overpredict the amplitude which can be attributed to the amount of damping present in the bone sample. The actual bone sample shows the changes in damping behavior with time as compared to the ideal modeled femur bone.

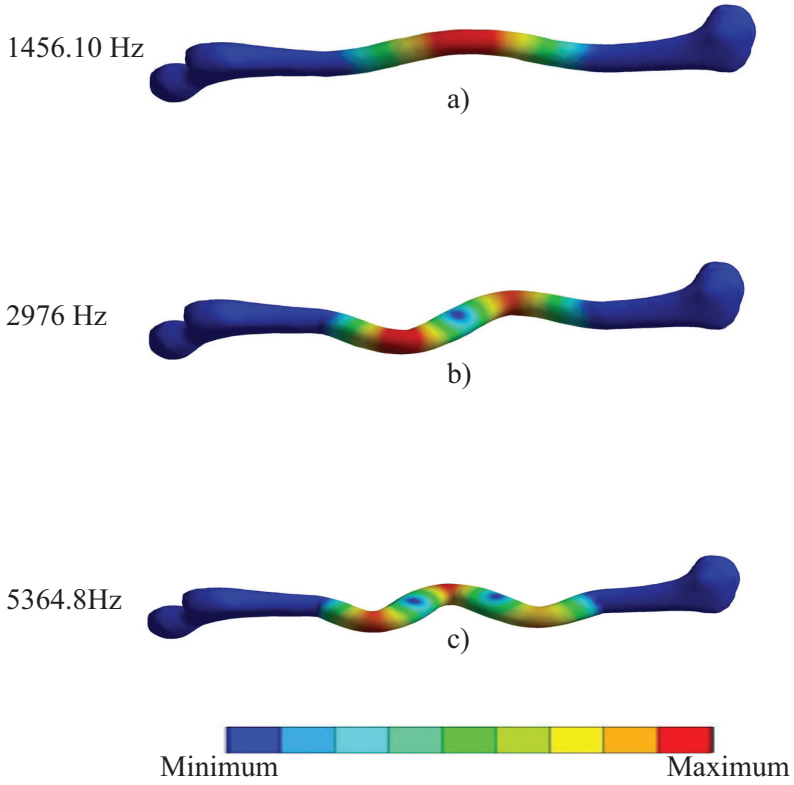


FIGURE 2.7: Numerical modeshapes a) First Mode, b) Second Mode, c) Third Mode.

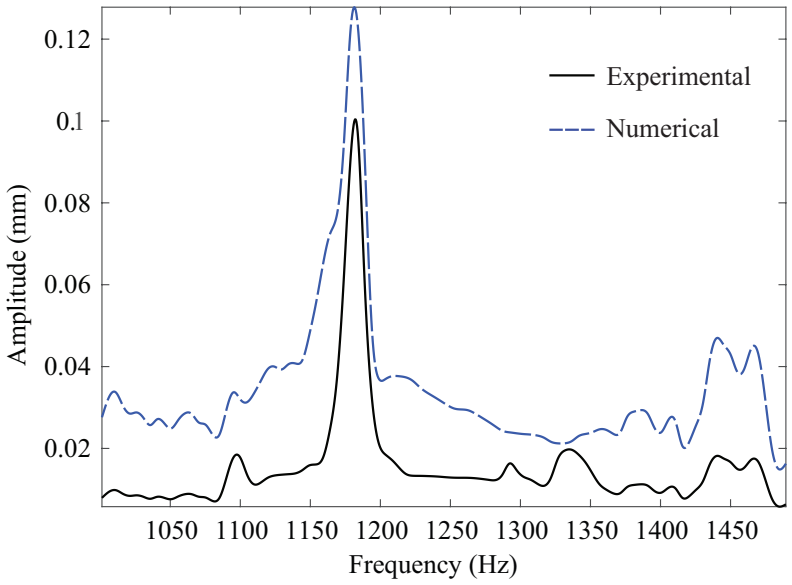


FIGURE 2.8: Random base excitation response of the femur bone.

## 2.5 Discussions

The proposed experimental method is a noninvasive technique that can be used to evaluate the mechanical properties of the bone sample. Furthermore, the combination of optical position sensing device method and finite element modeling is an immensely powerful methodology, with great potential for evaluating the mechanical responses of biological samples like tissues and cells. In the present study, we derived the resonant frequencies of the goat femur bone from the obtained responses in the time and frequency domain using an oscilloscope and further signal analysis. Figure 2.3 and 2.7 represent the frequencies from the optical position sensing device and mode shape frequencies from the numerical modeling, respectively. Frequencies range from 1496.0 Hz to 4894.0 Hz for three consecutive modes in the case of the experimental study, while frequencies range from 1456.10 Hz to 5364.80 Hz from the numerical study, thereby supporting the result that the three consecutive modal frequencies of the bone could be in the range of the 1496.00 Hz to 5364.80 Hz. The difference between experimental and numerical results can be attributed to neglecting the nonlinear behavior and mechanical properties of the bone. The difference in results can be due to elasticity variation across the length of the bone, and the blood flow carries veins and arteries within the sample, inside the constructive model and uneven morphology of the bone throughout the length [125], time-dependent properties such as changes in elastic modulus and mass with time, which directly influence the natural frequency of the bone sample [127], [128]. Since this study focused on evaluating the resonant frequencies and elasticity of the bone, mass and stiffness are an essential factors affecting the results.

Table 2.4: Comparison with other techniques.

| | **Experimental** | **Numerical** | **Bernand et al.**[98] | **H daoui et al.**[99] | **Rho et al.**[129] | **Niebur et al.**[130] |
|---|---|---|---|---|---|---|
| Young's Modulus(GPa) | 14.91 | 14.80 | 12.80 | 13.92 | 11.70 | 18.70 ± 3.40 |

The Table 2.4 compares the evaluated Young's modulus by PSD (proposed technique) with other methods reported in the literature, it was noticed that evaluated values are close to the reported values. The difference can be attributed to sample size, heterogeneity, experimental artifacts, anatomical location, etc. The reported values of elastic modulus using other techniques are evaluated by considering trabecular and cortical bone separately. Bernand et al. [98] consider cortical bone, while Daoui et al. [99] consider trabecular bone only. Rho [129] uses the ultrasonic wave velocity techniques to measure the Young's modulus value of cortical and Cancellous bone and found around 11.7 GPa. The difference in Young's modulus between the reported and present techniques can be due to measuring the properties of complete bone.

TABLE 2.5: Comparison between experimental and numerical results.

| | | Experimental | Numerical | % Error |
|---|---|---|---|---|
| $f_n$ (Hz) | Mode 1 | 1496.00 | 1456.10 | 2.66 |
| | Mode 2 | 3097.00 | 2976.00 | 3.907 |
| | Mode 3 | 4894.00 | 5364.80 | 9.619 |
| E (MPa) | | 14912.00 | 14800.00 | 0.75 |

In this work, studies were conducted on goat femur bone at different locations to propose a nondestructive technology in biological sciences. As the test result demonstrates, the constitutive model could represent the mechanical properties of the bone very well, as by the difference between the measured and predicted frequencies and young's modulus. It can be noticed (Table 2.5) that the higher mode frequencies are linearly increases compared to fundamental frequencies of the femoral shaft portion of the bone. A significant cause for uncertainty in the results is the material properties used in the theoretical and finite element models to evaluate the mode shape with its corresponding natural frequency. The FE model uses isotropic and linearly elastic material; however, the real bone has anisotropic material properties, nonlinear, and hyperelastic behavior [131]. This behavior leads to changes in theoretical and experimental mode shape (Figure 2.5). From Table 2.5 we can notice that the calculated elastic modulus is within 1% of experimentally measured values. For this study, bone material properties were estimated from the literature data; however, bone of different age and size is likely to behave differently[132], indeed, exciting areas for further investigation would be to use ultrasound technique to predict the inherent structure and voids and incorporate the same in the FE model to calculate the results with greater accuracy. In this work, random vibration analysis was done to emulate the real-life conditions experienced by the femur bone in the normal daily activities. Results predict the acceptable range of the deformation and showing the damping nature of the bone by absorbing and decay of the excitation vibration. Porous structure with various constitutive material in the bone forms a matrix-shaped structure that absorbs the vibrations and reduces the amplitude.

The results show the mechanical properties of bone based on their natural frequency. When a bone sample vibrates with these frequencies, the bone sample follows a specific modeshape and deformation [133]. When the excitation frequency coincides with the natural frequency of bone leads to resonance condition, and bone attains maximum deformation undergoing the dynamic fracture. Hence it is essential to avoid the resonance for the smooth functioning of organs. This technique depicts the avoidable resonant frequency of bone samples to avoid the failure of the bone. This is the advantage of this method and can be used in bone prosthesis and biological tissue rampage or failure [134], especially in the field of medical and sports engineering.

## 2.6 Conclusions

This noninvasive experimental technique helps to find out the mechanical behavior of the bone sample in dynamic conditions. The time response of the bone depicts the damping characteristics of bone, which reflects the decay of vibration in the biological sample. These values are auspicious for the evaluation of the modulus of elasticity of the bone sample. The evaluated modulus of elasticity by the proposed experimental technique and finite element modeling are close to each other. Bone is anisotropic material; hence homogenization using CMAS gives the optimized material property of the sample, which is further used for the mechanical response of bone. A numerical analysis was done to evaluate the frequency response of the femur bone. The modal analysis shows the various natural frequencies which can aid in designing of the prosthetic bone to avoid the failure of the prosthetic parts. Random vibration analysis was carried to observe the real-life daily activity of the bone sample, and a comparative study for deformation in the bone was done using a nondestructive technique and numerical approach. This work shows the establishment of the experimental technique for the evaluation of the mechanical properties of the bone sample. This proposed experimental technique can be extended to other biological samples for calculating their mechanical response.

This technique can be implemented in the field of medical and sports engineering to determine the inherent flaws, deficiencies, and wide range of mechanical properties of the biological samples and their substitute implants. These techniques would lead to a new incitement in designing and material selection for the bone prosthesis and sports equipment.

# Chapter 3

# Effect of nanocarrier additives on biomechanical response of a rat skin

## 3.1 Background

Nanocarriers, such as liposomes and polymeric nanoparticles, have been widely investigated as delivery systems for drugs and other therapeutic agents. These systems have the potential to improve the efficacy and safety of transdermal drug delivery by enabling the transport of drugs across the skin barrier. However, in order to fully realize the potential of these systems, it is important to understand the effect of nanocarrier additives on the biomechanical properties of skin.

The biomechanical properties of skin, including stiffness, strength, and elasticity, play a critical role in determining the ability of the skin to act as a barrier to the transport of drugs and other molecules. Alterations in these properties can affect the permeability of the skin and, therefore, the effectiveness of transdermal delivery systems.

Sevreal previous experimental studies have been conducted to evaluate the effect of various nanocarrier additives on the biomechanical properties of the skin. These studies typically involve mechanical testing, such as tensile and compression testing, to measure the stiffness, strength, and elasticity of skin samples. However, these studies have yielded inconsistent results, with some studies reporting a decrease in the biomechanical properties of skin with the addition of nanocarrier additives, while others have reported no significant change. Numerical studies have also been used to complement the experimental findings on the biomechanical response of skin to nanocarrier additives. Finite element models of skin have been developed and the mechanical properties of skin have been analyzed using various nanocarrier additives as inputs.

These simulations have the potential to provide a more detailed understanding of the underlying mechanisms of the biomechanical response of skin to nanocarrier additives.

Thus, understanding the influence of nanocarrier additives on the biomechanical properties of skin is important for the design and optimization of transdermal delivery systems using nanocarriers. Experimental and numerical studies have been conducted to evaluate the effect of nanocarrier additives on the biomechanical properties of skin, with some inconsistent results.

## 3.2 Introduction

Skin is a biomechanically nonlinear, viscoelastic, multi-layered largest organ that protects the human body from the external environment. The superficial layer of the skin, the stratum corneum act as a barrier preventing the passage of various pathogens and hazards such as UV radiations, dehydration, and extreme weather conditions by maintaining body temperature [135], [136]. Skin is susceptible to a variety of acute and chronic disorders. Diagnostic techniques commonly used to identify skin diseases include a visual inspection, histopathological analysis, and blood sample testing. In cases where cutaneous diseases show early symptoms, the blood-based analysis may not provide accurate results. Thus, necessitating the development of alternative cost-effective and non-invasive approaches for diagnosing skin disorders such as psoriasis, atopic dermatitis, and autoimmune diseases such as cutaneous lupus erythematosus (LE) [137]. Identifying autoimmune skin conditions can be challenging as lupus erythematosus may have specific morphological lesions, and psoriasis may present with diverse clinical and pathophysiological features. [137].
The on-time detection of skin disorders has a significant effect on reducing the severity and managing the impact of the disease [138]. Epiluminescent microscopy, high-resolution MRI, and ultrasound were used to determine the mechanical behavior and magnitude of the severity of skin disease in−vivo from the measured deformation of the skin structures [137], [139], [140]. Crichton et al. [141], characterized the full-thickness skin at micro scales through elastic modulus and viscoelastic properties using customized probes of scales from sub- to super-cellular (0.5 $\mu$m-20 $\mu$m radius). You et al.[142] explored the use of water resorption-desorption techniques to measure the depth of terahertz radiation penetration in the skin, including the stratum corneum (SC) and a portion of the viable epidermis layer. The results revealed that the skin's tendency to absorb terahertz radiation was frequency-dependent, and this finding has potential clinical significance. Several other methods like ultrasound, tangential traction, twistometer, wave propagation, single-axis extension method are important methods to characterize the skin based on their mechanical properties [143]–[145]. Ultrasound and tangential traction techniques aid in determining Young's modulus, induced stresses, and the point of non-elasticity in the skin. Meanwhile, the traction and twistometer method provides information on the stress-strain relationship, enabling the determination of Young's modulus and conducting in-vivo experiments

to comprehend the role of elastin in the skin's mechanical properties. However, wave propagation and single-axis methods were used to evaluate the viscoelastic behavior of the skin in-vitro and in-vivo, respectively. Skin thickness changes at distinct locations in the body due to aging and pathological changes significantly affect the skin's mechanical behavior.

In recent times, image-based techniques become popular because of their ability to provide high resolution and rapid detection of the morphological changes in the skin caused by diseases by assessing the mechanical properties [146]. Advancements in optical techniques have resulted in increased utilization of Digital Image Correlation (DIC) and photogrammetry. These techniques serve as non-intrusive methods for computing the skin's mechanical properties and are now being used for health monitoring [147]. Optical coherence tomography (OCT), and photoacoustic imaging technique provide the results to quantify the skin properties and determine the full field deformations in the study of biomechanics of skin ([148]–[150]. Digital image speckle correlation (DISC) showed the potential in measuring the deformation, strain field, and mechanical properties of skin, with and without the application of a glycerin-fruit-oil-based cream, and successfully compared the results with uniaxial tensile testing [151]. Guan et.al. [152] successfully studied the deformation to the failure point in newborn rat skin.

Skin health can be monitored using various invasive and non-invasive techniques, and one such method involves quantifying changes in elasticity by analyzing their effects on the skin's natural frequencies and mode shapes. Researchers have conducted several numerical modeling and simulation studies to understand skin behavior, as reported in [153]. However, modeling the properties of the skin remains challenging due to its complex biological structure. A study reported several multi-layer finite element models of the skin using commercial FEM software to understand the modeled skin consists of stratum corneum, viable epidermis, and dermis layers and simulated to predict the skin deformations that cause wrinkles and investigated the formation of wrinkles around contracting healing scars with age [154]. Skin anisotropy studies are utilized to investigate the mechano-biology of the skin in the fields of skin aging, cosmetics, plastic surgery, and the detection of various skin diseases. To estimate the hyper-elastic parameters of the skin and study the deformation characteristics of soft tissues, numerous Finite Element (FE) models have been developed, including a multi-layered FE model [155], [156].

The mechanical properties of human skin using FE modeling put efforts to focus on static analysis to measure the elasticity of skin [157]. However, the dynamic behavior of the human body also has an impact on elasticity. Various organs of the human body vibrate at different natural frequencies [158]. The variations in the stiffness of tissue and organs result in differences in the natural frequencies of organs between healthy and diseased skin tissue. [159]. The significant difference between the biomechanical parameters of healthy and diseased skin highlights the importance of assessing mechanical parameters to observe treatment efficacy and differentiate between healthy and diseased conditions.

Few studies have been conducted which are based on significant parameters such as Trans-epidermal water loss (TEWL) to measure the moisture content in maintaining skin's permeability

function [160]. It also signifies the density gradient of water evaporation. In atopic dermatitis, psoriasis, and other skin disorders, the skin's barrier functions change (disrupted or enhanced due to hyperproliferation)[161]. These variations in the skin properties affect the mechanical properties of the skin, which can be utilized in the diagnosis of skin disorder [137]. A relationship between TEWL and change in skin elasticity has been reported in a study involving healthy volunteers and patients suffering from psoriasis [162].

In addition to its diagnostic value, maintaining the skin's moisture content is crucial for the effectiveness of topical pharmaceutical formulations in treating skin diseases [162]. Previous studies stated that pharmaceutical formulations improve skin moisture content through two different mechanisms − the formation of an occlusive layer on the skin surface, or the permeation of hygroscopic components that can retain moisture content within the stratum corneum [163]. However, the transportation of these components deep into the skin layers is restricted due to complex skin structure and selective permeation [163]. Thus, different formulations are explored to overcome this limitation among which nanocarriers were found to be the most successful delivery systems for topical application in maintaining skin hydration [164].

Cubosomes are new-generation lipid-based vesicular systems consisting of cubic bicontinuous liquid crystalline systems having two non-intersecting hydrophilic areas separated through a lipid bilayer [165]. In a study, drug-loaded cubosomal nanogel showed better permeability and retention in skin layers as compared to cream due to strong bioadhesive property and occlusive nature supporting decreased TEWL ([166]). In addition to this another study demonstrated the improved permeation of dapsone loaded in cubosomal structure as compared to its corresponding marketed formulation [167] as well as from solution of free drug [168]. As a result, Cubosomal drug delivery systems have been shown to offer advantages over conventional formulations to treat skin disorders. Thus, a technique needs to be developed to assess the impact of these drugs by analyzing the mechanical properties of the skin post their topical application. This would provide insights into their effectiveness.

Numerous research studies are ongoing in the area of invasive technology, which may provide in-vivo analysis of skin diseases with a higher level of diagnostic accuracy with its limitations. While, non-invasive techniques are ideal for in-vivo experiments for measuring skin mechanical properties due to their accuracy, reliability, and ability to perform repeated measurements without causing tissue damage or disrupting the natural state of the skin. Therefore, noninvasive techniques for the measurements of the skin's mechanical properties and correlate them with various factors that affect the skin (cream and nanocarrier loaded gel) become a motivation for intervention.

There has been no prior investigation into the potential use of optical sensing techniques combined with vibration analysis techniques for monitoring skin mechanical properties. In this work, a non-invasive technique based on an optical position-sensitive detector (PSD) unit was used to evaluate the mechanical properties of the skin. Young's modulus was evaluated using frequencies obtained from the experiments. Nanocarrier gel and ketoconazole cream have been formulated and

used for maintaining skin hydration through topical application. This approach aims to address the challenge of transporting drug formulation deep into the skin. A time-based investigation was conducted to assess the effect of cream and cubosomal-based nanogel on skin elasticity using the aforementioned methodology.

The skin used in our experimentation was provided by our collaborating laboratory (Prof. Gautam Singhvi Lab.). This section on skin dissection and formulation development preparation was performed by Dr. Vamshi Krishnan and included in this thesis solely for the purpose of completeness. As the author of the thesis, I did not carry out the skin dissection and formulation development part of this work. All experimental protocols were approved by the institutional animal ethics committee (IAEC) before the commencement of work.

## 3.3 Materials and Methods

### 3.3.1 Materials

Ketoconazole was received as a gift sample from Intas Pharmaceuticals Ltd., India. Polyvinyl alcohol was procured from Sigma Aldrich, India. Poloxamer 407 (Pluronic F 127) and Carbopol 971P were obtained from BASF, India, and Lubrizol. Glyceryl monoolein was obtained as a gift sample from Mohini Organics Pvt. Ltd. Ketomac® (2% W/W Ketoconazole cream) Torque Pharmaceuticals, India, purchased from the local market from Pilani, India. Other chemicals, solvents, and reagents used were of analytical grade.

### 3.3.2 Formulation development

The ketoconazole cubosome loaded gel was prepared, as mentioned in the reported method [138]. In brief, the batch quantity of Glycerol Mono-oleate (2g) was melted at 80°C, poloxamer 407 (400g) as a surfactant was added and stirred until the formation of a clear molten solution. Ketoconazole was added to the molten lipid and mixed until complete solubilization of the drug. The polyvinyl alcohol (3.30% w/w of lipid) dissolved in milli-Q water was preheated to 80°C and added to the lipid phase under continuous stirring. The formed pre-emulsion was cooled to room temperature, and an additional batch quantity of water was added to the pre-emulsion. To the above formed cubosomes mixture, 1.00 % of Carbopol 971P was added, and the gel was formed after neutralization with triethanolamine. The prepared cubosomal dispersion was evaluated for particle size and percentage entrapment efficiency and in-vitro release. The methods followed were similar, as mentioned in the previous report [169], [170]. Further, the optimised formulation was embedded in hydrogel system and characterized for viscosity and spreadibility.

TABLE 3.1: Average thickness of the skin samples

| Sample | Thickness (mm) |
|---|---|
| Normal Skin | 2.607 ± 0.22 |
| Skin loaded with cream | 2.605 ± 0.43 |
| Skin loaded with gel | 2.611 ± 0.32 |

### 3.3.3 Preparation of skin samples

The skin from dorsal portion of the male Wistar rat was freshly collected and the hair was removed carefully using a hair trimmer to avoid damage to the skin. The subcutaneous fat was removed, and the skin was washed thoroughly with phosphate buffer saline. The cubosome-loaded gel formulation and ketoconazole-marketed cream (200 mg) were applied to the skin towards the stratum corneum. The blank sample was used without the application of any formulation on the skin [169]. Six samples were obtained from three groups of specimens; the first group's specimens were the normal skin extracted from the rat and left in a low-temperature environment for 24 hours. The second group of skin was gently massaged with a ketoconazole cream for 3 min and left for 30 minutes, and the third group of samples was applied with ketoconazole nanocarrier gel. The above experiments were performed in triplicate. Digital vernier calliper was used for the calculation of skin thickness same as followed in the previous peer-reviewed work [171], [172]. The average thickness of the skin samples is shown in Table 3.1.

### 3.3.4 Numerical Analysis

An Eigen solution is performed on a FE model of normal skin. Numerical analysis of the skin has been carried in the commercial FEA package, ANSYS workbench. Micro-scale geometry with three layers of the skin developed in the Design Modular. The top three layers i.e., outermost layer Stratum Corneum (SC), viable epidermis, and dermis, were considered for the analysis. A circular-shaped geometry of the radius 20 mm with the layers of different thickness is considered, as shown in Table 3.2 [153]. Modal analysis was carried out for the eigenvalues and eigenvectors. Eigenvalues show the skin sample's natural frequency, while eigenvectors show the normalized shape of the skin sample's deformation. The essential mechanical properties of the different skin layers required for the analysis were assigned and shown in Table 3.2.

The outermost layer has a higher value of modulus of elasticity than the other skin layers and is significant in evaluating frequency. Skin behavior is complex, uncertain, nonlinear, and consists of anisotropic nature. In a certain range of vibration analysis, skin can be a nonlinear isotropic [173]. For this work, finite element simulations were carried by considering material properties for the isotropic skin model. The isotropic and homogeneous model with the tetrahedral elements

TABLE 3.2: Mechanical properties of the skin samples

| **Skin layer** | **Thickness ($\mu$m)** | **Density (kg/m$^3$)** | **Poison's Ratio** | **Young's Modulus (MPa)** |
|---|---|---|---|---|
| Stratum Corneum | 20 | 1500 | 0.49 | 6.00 |
| Epidermis | 80 | 1119 | 0.49 | 1.00 |
| Dermis | 1500 | 1116 | 0.49 | 0.66 |

were considered for the simulations. Numerical parameters remain the same as experiments to replicate the skin's actual phenomenon. All skin samples' outer end surface was fixed and considered as a clamped end boundary condition. The skin model was considered as a vibrational model governed by the homogeneous differential Equation 3.1 [174].

$$M\ddot{X}(t) + K\dot{X}(t) = 0 \tag{3.1}$$

consider the solution for the above equation as shown in Equation 3.2

$$X(t) = \phi sin(\omega t + \theta) \tag{3.2}$$

where $X$ is the displacement, $\phi$ is the vector of amplitudes, $\omega$ is the frequency of harmonic response, and $\theta$ is the phase angle.$M$ and $K$ are the mass and stiffness matrix. Further on Differentiation

$$\ddot{X}(t) = -\omega^2 \phi sin(\omega t + \theta) \tag{3.3}$$

Substituting Equation 3.2 and Equation 3.3 into (3.1),we get

$$(K - \omega^2 M)\phi = 0 \tag{3.4}$$

Now, the nontrivial solutions of Equation 3.4 are only possible if the determinant of the coefficient matrix is equal to zero, that is,

$$\mid K - \omega^2 M \mid = 0 \tag{3.5}$$

For n homogenous algebraic equations,the above equation leads to a polynomial of order n in $\omega^2$ that possesses, n distinct roots. These roots, represented by ${\omega_1}^2$,${\omega_2}^2$,${\omega_3}^2$.....${\omega_n}^2$ or $\lambda_1$ ,$\lambda_2$,$\lambda_3$.....$\lambda_n$ are known as eigenvalues. Their square roots represent the natural frequencies. For each eigenvalue $\omega_i$, there is an n dimensional vector $\phi_i$ , whose elements are real numbers. The

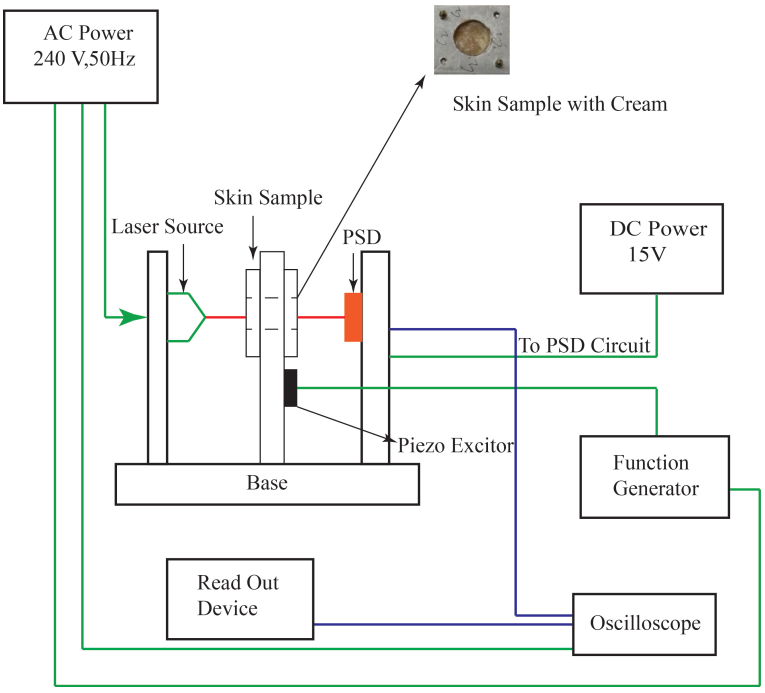


FIGURE 3.1: Schematic of experimental procedure to measure the dynamics response of skin.

vector can be obtained by using Equation 3.4 as follows:

$$(K - \omega_i^2 M)\phi_i = 0 \tag{3.6}$$

The vector $\phi_i$ (i = 1,2, ... , n) is known as an eigen vector or modal vector and has the form

$$\phi_i = [\phi_{1i}, \phi_{2i}, \phi_{3i}.....\phi_{ni}]^T \tag{3.7}$$

The eigenvector represents the mode shape of vibration.

### 3.3.5 Non-contact measurements using PSD

The schematic experimental procedure is shown in Figure 3.1 to evaluate the skin sample's elastic modulus with respect to time.

A fresh skin sample was kept in between the fixture with a circular hole of a 20 mm radius. Fixture was kept in vertical position. Skin with dorsal portion faces the laser. Laser from the laser source (Laser Century) (23 mW power and 650 nm wavelength powered by AC voltage of 240 V) was incident on the skin surface and got refracted and falls on the PSD (Figure 3.2). PSD is placed at the other end of the fixture to capture the laser's position on the skin sample. The Piezo actuator is attached to the support for the actuation of the sample at the micro-level. Actuating vibration signal parameters are controlled through a Function Generator (Tektronix

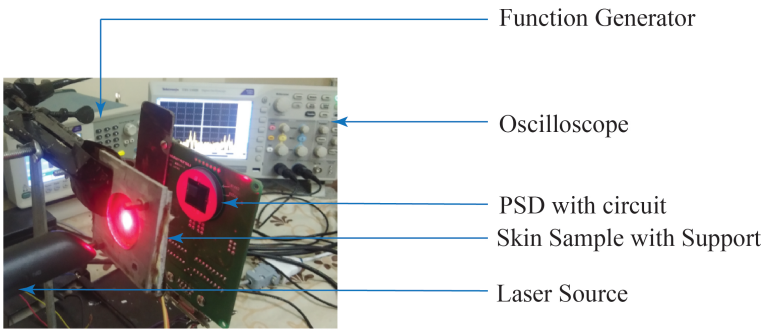


FIGURE 3.2: Experimental setup for noncontact measurements on skin.

AFG 1022). The chirp signal was applied to the Piezo disc. Generated vibration by Piezo disc passed to the support, which vibrates the sample. The laser passing through the sample gets refracted and falls on the PSD (Hamamatsu S5990-1). The continuous movement of the laser in the form of displacement on the PSD was monitored. Displacement was observed using DC operating PSD Circuit (Hamamatsu C4674- 01). The output of the circuit is read out using an Oscilloscope (Tektronix 1102B). Displacement in the form of vibration amplitudes is taken out in the frequency domain. The detailed experimental setup is shown in Figure 3.2.

### 3.3.6 Estimation of Modulus of Elasticity

This was achieved by assuming a circular plate theory, a case of axisymmetric vibration, with a clamped end boundary condition.

$$E = 0.144(2\pi^2)(1-\mu^2)\rho\left(\frac{f}{h}\right)^2 r^4 \tag{3.8}$$

where, $E$ is a young's modulus, $f$ is natural frequency, $r$ is the radius, $h$ is the thickness of the sample, $\mu$ is poison ratio, $\rho$ is density.

To evaluate the Fundamental frequency, we considered the free vibration analysis of axisymmetric laminated orthotropic composite circular plate using Chebyshev collocation considering Clamped boundary conditions. The following boundary condition has been considered for the present work. Clamped boundary condition.

At outer boundary $r = a, u = \alpha = w = 0$. At the inner boundary $r = b, u = \alpha = dw/dr = 0$

Where $r$ is the cylindrical coordinate, $u$ and $w$ are in-plane displacement in $r$ and $z$-direction and $\alpha$ is rotation in $r$ direction. Hence the Frequency parameter for the isotropic skin composite [175], [176] is shown in Equation 3.9.

$$\lambda = \omega a^2\sqrt{\rho h/D_{ij}} \tag{3.9}$$

$\lambda$ is the frequency parameter, $\omega$ is a fundamental frequency, $a$ is the radius, $\rho$ is the density, $h$ is the thickness of the skin sample and $D_{ij}$ is the bending stiffness.

### 3.3.7 Uniaxial tensile testing

Skin samples were extracted and taken out from the dorsal surface of male Wistar rats. The skin samples consisted of different layers of skin, including the stratum corneum, epidermis, and dermis. Using a standard template, all the specimens were prepared as per the ASME standards. Six samples were obtained from the specimens. Specimens of normal skin were extracted from the rat and left in a low-temperature environment for 24 hours. The average thickness of the samples was 2.617 ± 0.19 mm. For comparison, all the samples were kept in the same environment for the same time before testing. Tensile tests were performed on a universal tensile testing machine (ITW Hydraulics). An electronic strain gauge was used to measure the applied force (F). The normal stress $\sigma$ along the longitudinal direction was estimated by Equation 3.10.

$$\sigma = \frac{F}{A} \tag{3.10}$$

in which A is the uniform cross-sectional area. Displacement controlled tensile tests were performed on the samples, and during the test, crosshead speed was kept constant at the rate of 0.508 mm/min.

### 3.3.8 Statistical analysis

All data are expressed as a mean ± standard deviation (SD). The two-tailed unpaired t-test or one-way ANOVA were used for statistical analysis, followed by Tukey multiple comparison tests using Origin (for three or more groups). A statistically significant difference was defined with $p < 0.05$.

## 3.4 Results

### 3.4.1 Characterization of developed formulation

#### 3.4.1.1 Particle size, % entrapment efficiency and in-vitro drug release study

The prepared ketoconazole-loaded cubosomal nano dispersion was optimized using quality by design approach. The optimized formulation was then evaluated for particle size using Zetasizer (Malvern instruments, Nano ZS 2000). As described in our previous report [169], [170] the diluted samples were analyzed at 25 °C with 173° back scattering resulted into the size of 241 ± 4.80

nm and 248 ± 25.19 nm. The entrapment efficiency and in-vitro drug release were determined using ultracentrifugation and dialysis bag method followed by sample analysis at 232 nm by UV spectrophotometer. The calculated % entrapment efficiency of drug was found in the range of 41 – 48 % respectively and cumulative percentage drug release was calculated after 24 hr which resulted towards the release up to 67.63 and 67.59.

#### 3.4.1.2 Rheological evaluation of cubosomal embedded hydrogel

The selected batch of ketoconazole-loaded cubosomal dispersion was incorporated into 1% w/w of Carbopol 971P gel which was further subjected to viscosity and spreadability analysis along with the marketed formulation. The marketed cream resulted with high viscosity values of 84,100 and 48,726 cP as compare to the hydrogel formulation with 32,833 and 25,586 cP at 0.5 and 1.0 rpm communicating a significant difference between the two topically applied formulations. Further, spreadability factor was calculated and found to be 11.74 and 13.06 for cream and cubosomal hydrogel formulation. This concludes towards better spreadability of cubosomal gel formulation than the marketed cream.

### 3.4.2 Numerical Analysis

Frequencies were evaluated from the modal analysis, and the boundary conditions are kept the same as in the experiments. Frequency and mode shapes are shown in Figure 3.3 for different frequencies. The first resonant frequency is observed at 243.53 Hz, and maximum deformation is observed at the skin center as shown in the mode shape. The fundamental mode shape is observed at a frequency 243.53 Hz. The model number is designated as (0,1) since there are no nodal diameters but one circular node (the outer edge). This shows no wrinkles in the skin at the fundamental frequency.

### 3.4.3 Experimental Analysis

#### 3.4.3.1 Frequency Response

The frequency response was extricated from the experiments for the different skin samples at different time intervals. The frequency response of the skin sample and support is shown in Figure 3.4a. The transfer function shows the peak after removing the support response from the sample response. The higher peak corresponds to the sample's natural frequency (Figure 3.4b).

From Figure 3.5 we can observe the frequency behavior of the skin samples. Frequencies are increasing for normal skin with time. Initially, normal skin is having a frequency of 263.3 Hz

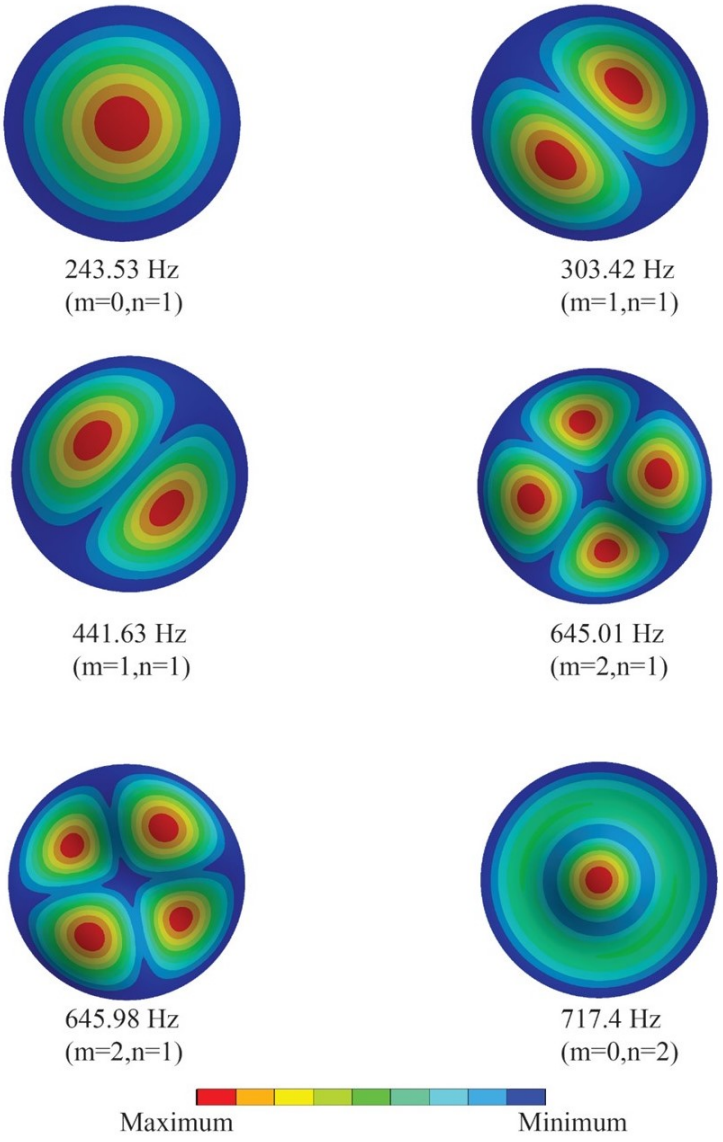


FIGURE 3.3: Mode shapes at different frequencies with the color bar showing deformation in mm.

while for the cream 184.43 Hz and gel−coated skin is 147.5 Hz. There is a continuous increase in the frequencies of normal skin compared to other samples. While for the gel and cream sample, it decreases up to 6 to 8 hr. The gel samples have lower frequencies compared to the cream sample.

#### 3.4.3.2 Youngs Modulus Response

Young's modulus of the normal skin increases with the time from 7.52 MPa to 58.50 MPa at 36 hr. This leads because of the direct dependence of Young's modulus and frequency as shown in Equation 3.8. This can be predicted from Figure 3.6 which shows an increase in the stiffness

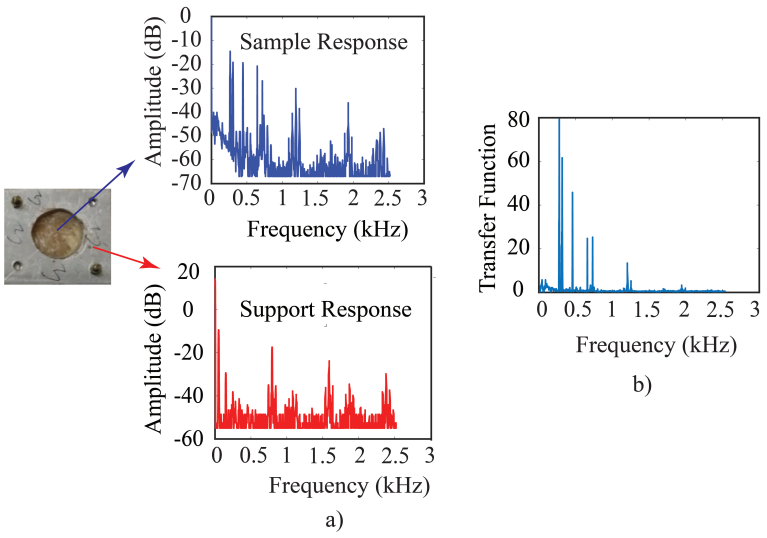


FIGURE 3.4: a) Frequency response for skin sample and support. b) Transfer function.

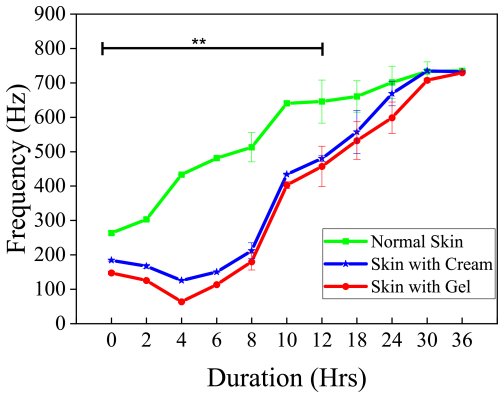


FIGURE 3.5: Effect of time on the fundamental frequency of the skin. Each group represents the mean and standard deviation of the change in the fundamental frequency of the skin samples (n=3) [$\star\star$ represents the significance difference $p < 0.05$ (t-test) as compared to the other groups up to 12 hrs].

proportional to Young's modulus of the normal skin with time. While for the skin sample loaded with cream and gel, Young's modulus is decreased for a particular time duration and increased after 8 hr. Initially, the addition of gel and cream increases the effective mass of the sample and undergoes the chemical reaction to make the skin flexible and hence reduction in the frequency leads to decrease in the Youngs modulus and further increase in Young's modulus. This implies because of as time prolongs, the applied formulation gets dried and loses its properties, which leads to the increased young modulus. Gel's effectiveness was more significant as compared to the cream on the skin sample. Gel decreases the stiffness of the skin and increases the flexibility of the skin compared to the cream. The moisture content and presence of nanoparticles (cubosomes) in the gel preparation are expected to increase effectiveness compared to cream preparation.

Young's Modulus from PSD results were compared by mechanical tensile testing on the different samples. The stress-strain curve (Figure 3.7) obtained from the Micro universal testing machine

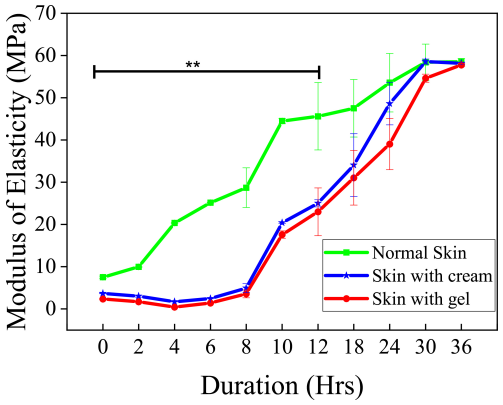


FIGURE 3.6: Effect of time on Elastic modulus of the skin. Each group represents the mean and standard deviation of the change in the fundamental frequency of the skin samples (n=3) [⋆⋆ represents the significance difference $p < 0.05$ (t-test) as compared to the other groups up to 12 hrs.]

illustrate the response of a skin sample to the external load. The slope of this curve represents Young's modulus of the samples. The Young's modulus for normal skin is 8.42 MPa, and the skin with cream and gel has 3.685 MPa and 2.371 MPa, respectively, measured after half an hour taken out from the refrigeration chamber.

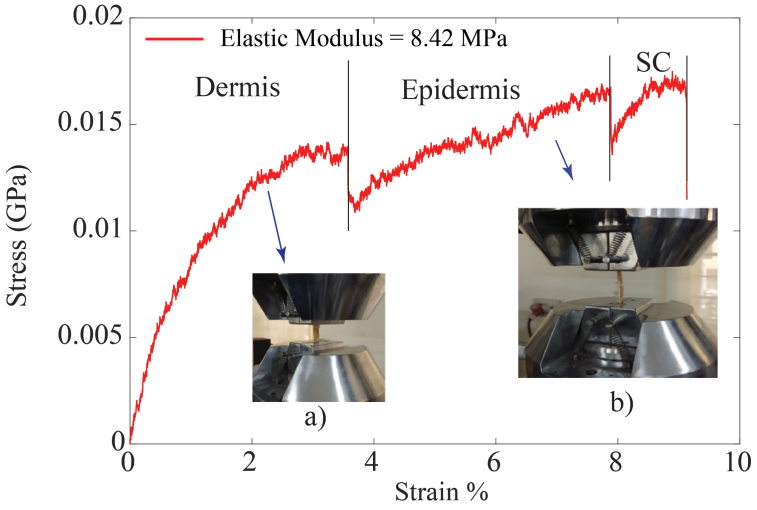


FIGURE 3.7: Stress-strain curve for normal skin. a) Image during Dermis breakage. b) Image during Epidermis breakage. The slope of the curve represents the elastic modulus of the skin.

#### 3.4.3.3 Effect of stratum corneum thickness

The stratum corneum plays a vital role in deciding the mechanical properties of the skin. This layer is dominant on other layers of the skin. Its thickness is generally varying from 10 $\mu$ m to 50 $\mu$ m as per the early studies [177], [178]. This layer is directly exposed to the environment, and hence its thickness changes frequently with age as compared to other layers. In this study, we

carried out a numerical analysis to see the effect of change in the thickness of stratum corneum in the von−Mises stresses and deformation due to the self−weight of the normal skin.

It has been noticed that as the thickness of the skin increases, deformation and stress decrease (Figure 3.8). This predicts that if the skin's thickness is optimum, environmental changes will have no effect on the innermost layer of the skin since the layer is adequate to protect the surrounding layers.

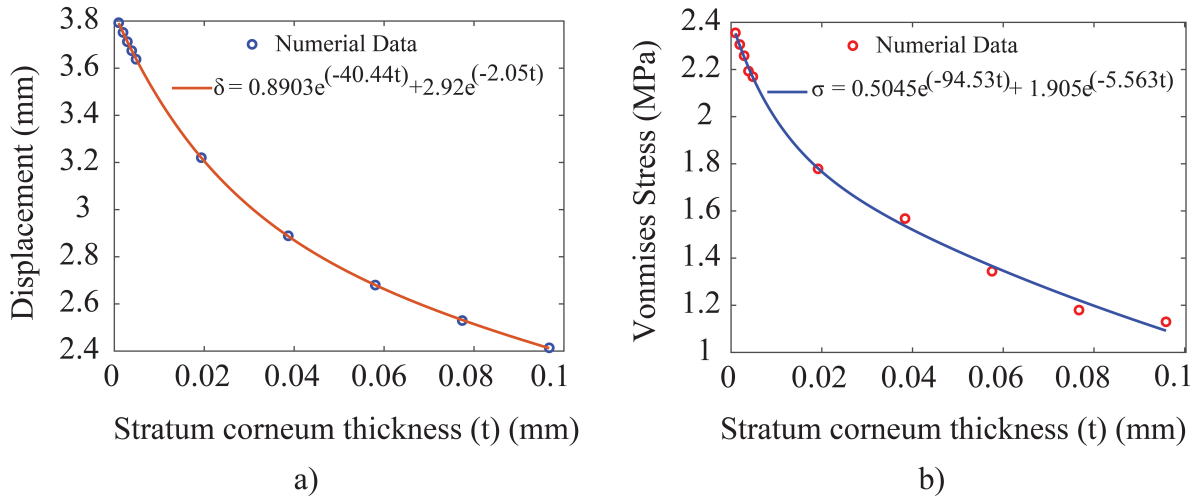


FIGURE 3.8: a) Deformation with respect to SC thickness. b) Von Mises's stress with respect to SC thickness.

The numerical surface plot shows the distribution of stress and deformation in the skin model under static loading (Figure 3.9). Maximum deformation occurs at the center of the skin, corresponding to the first natural frequency. In contrast, stresses are maximum at the clamped end surface and center of the skin.

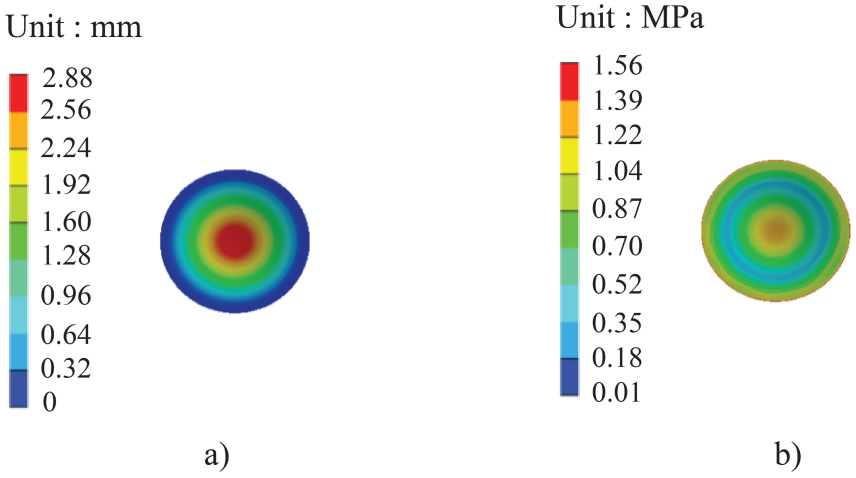


FIGURE 3.9: a) Total deformation distribution in normal skin. b) Maximum von mise's stress distribution in normal skin.

## 3.5 Discussion

This non-destructive technique has been used to evaluate the natural frequency and Young's modulus of the skin samples using a PSD-based setup. Frequency and Young's Modulus are correlated with time. Frequencies of the normal skin are is increased with time, as shown in Figure 3.5. In contrast, frequencies for the cream and gel-applied skin follow the complex nature of variation. Initially, the skin was loaded with cream and gel possessing lower frequencies than normal skin and decreased for a specific duration and further increased. As time wears on, the cream and gel get aspirated from the skin's surface, increasing the skin's stiffness. Cream and gel are continuously reacting with the skin layer's surface and penetrate the stratum corneum. The cream and cubosome-loaded gel's lipid content favored the occlusive effect and inhibited the water loss (TEWL). The reduced TEWL value maintains the moisture content and increases the softness of the skin. Similarly, the pharmaceutical results of this study depict that the hydrogel formulation including cubosomes loaded with ketoconazole may have a lower viscosity than the cream formulation, resulting in greater spreadability and application efficiency. A higher spreadability indicates that the gel will adhere more closely to the skin, thereby increasing the contact area for a small amount of the formulated gel and allowing the distribution of a larger quantity of drug due to the larger surface area for drug transposition through the skin layers. Previous literature exhibits systematic dependence of the viscosity and stiffness and predicted that the system gets stiffer with the increases in its viscosity [179], [180]. Hence, as a result, the gel will be more effective and penetrate deeper into the skin in a shorter amount of time, resulting in softer skin.

Softness leads to a decrease in stiffness with a decrease in frequency. As Young's Modulus is a function of frequency shown in Equation 3.8, justifies the decrease in young modulus with decreasing frequency. There is a decrease in Young's Modulus with a decrease in the frequency. When compared to gel preparation, it was anticipated that the cream would have the greatest occlusive effect. However, the cubosomes' nano-size and lipid content provided a high occlusive effect due to a lower TEWL, which further encourages better drug absorption and retention within the skin layers. The TEWL values are positively affected in the disease conditions due to variations in the skin barrier properties. The hyperproliferation in psoriasis, abnormal growth of skin in cancer, inflammation, itching, and dryness in atopic dermatitis are the significant reasons for the skin barrier function variations. From Table 3.3, we found an acceptable range of error between experimental and numerical results.

These errors are based on the assumption made during the analysis. The skin possesses anisotropic and heterogeneous behavior with a lot of inherent complexities. Factors like viscoelastic behavior, subcutaneous layer, fat layer, blood flow, relative humidity, temperature, etc. affect the mechanical response of the tissues [181], [182]. In this study, we evaluate the mechanical response

TABLE 3.3: Comparison of natural frequency of the normal skin.

| **Parameter** | **Experimental** | **Numerical** | **Analyical** | **% Error** |
|---|---|---|---|---|
| Frequency (Hz) | 263.62 | 243.53 | 246.26 | 7.62 |

TABLE 3.4: Young's Modulus Comparison of Normal Skin with other techniques

| **Parameter** | **Experimental PSD (present work)** | **Mechanical Testing (present work)** | **Crichton et al**[a1] | **M.A.F. Kendall et al.**[b2] | **Haut et al and Dombi et al.**[c3] |
|---|---|---|---|---|---|
| Youngs Modulus (MPa) | $7.56 \pm 2.60$ | $8.42 \pm 1.70$ | $1 - 30$ | $2.9 - 11.1$ | $1.2 - 24$ |

[a1]Mice skin.
[b2]Murine ear skin.
[c3]Rat skin.

of skin using a non-contact optical technique. This technique demonstrates and establishes the similarity between experimental and numerical results.

Table 3.4 shows the comparison of the evaluated Young's modulus of the normal skin with the other techniques used in the literature [141], [183]. The evaluated Young's modulus is in the range predicted by the earlier reported work using different techniques. Thus, the results suggested that this experimental procedure can be explored to determine changes in the skin's mechanical properties. The alteration in the skin thickness and barrier functions are mostly observed in chronic skin disorder conditions. As mentioned, the hyper-proliferation in psoriasis, cancer, and the effect on the epidermis in atopic dermatitis, and fungal diseases alter the skin properties. These changes can be used to determine the severity of the disease.

## 3.6 Conclusion

This study evaluates the natural frequencies and Young's Modulus of the skin concerning the change with time using a non-destructive optical technique, such as PSD and FE modeling. Based on the results, the normal skin's experimental frequencies were found to be 263.53 Hz while the skin sample with cream and cubosome loaded gel had 184.53 Hz and 147.5 Hz, respectively. The Numerical FE results exhibit an ordinary deformation mode shape at a frequency of 243.53 Hz and a wrinkling mode shape at a higher frequency. Also, we found an exponential decrease in the stresses and deformation in the skin with the increase in the stratum corneum thickness.

Literature, however, shows that the natural frequencies of the skin differ because of the elasticity of the skin, which is different at different locations and parts of the body. Young's modulus is a function of frequency. Age is also an essential aspect because the skin loses its elasticity with age, thereby affecting the natural frequencies. There are several areas for further study, including the possibility of developing different FE models that integrate nonlinearity, Hyper elasticity, and anisotropy. Besides, restricting rigid body movements induces internal and external environmental variables to minimize experimental error. Notably, the described methodology describes the dynamic behavior of the skin. This experimental technique has enormous scope in the diagnosis of diseased skin. Analysis of vibration allows observing the variations in the dynamic behavior of healthy skin and diseased skin with time. Further, this method can be implemented for the evaluation of the in-vivo mechanical response of the skin and a lab-on-a-chip device can be developed for real-time monitoring of skin behavior.

# Chapter 4

# Mechanical microscopy of cancer cells: TGF-$\beta$ induced EMT corresponds to low intracellular viscosity in cancer cells

## 4.1 Background

### 4.1.1 Importance of cell mechanics

Cell mechanics involves the study of the mechanical properties of cells and their behavior under various types of loading conditions. Cells are the fundamental building blocks of all living organisms, and their mechanical behavior plays a crucial role in many biological processes. The mechanical properties of cells are determined by their composition and microstructure. Cells are composed of various biomolecules, including proteins, carbohydrates, and lipids, which are organized into complex structures such as the cytoskeleton, the cell membrane, and the nucleus. The mechanical behavior of cells is highly complex and depends on several factors, including the type and amount of loading they experience, their age and health, and the specific type of cell. One of the key factors that affect the mechanical behavior of cells is the type of loading. Cells are subjected to a wide range of loading conditions, including mechanical forces, chemical signals, and thermal stresses. The way in which cells physically behave is essential to several biological processes, such as cell division, migration, and differentiation.

The importance of studying cell mechanics lies in the fact that it can help us understand how cells respond to different types of loading and how they can be damaged or diseased. This knowledge can be used to develop better treatments for a variety of diseases, including cancer, cardiovascular disease, and neurodegenerative disorders. In addition, a better understanding of cell mechanics

can also help us design medical devices and therapies that better mimic the mechanical behavior of healthy cells.

### 4.1.2 Understanding the mechanical behavior of cancer cells

Cancer is a group of diseases characterized by the uncontrolled growth and division of cells. In normal cells, growth and division are carefully regulated by a complex network of signals and feedback mechanisms. However, in cancer cells, these regulatory mechanisms are disrupted, leading to uncontrolled proliferation. The mechanical behavior of cancer cells, such as their stiffness and motility, plays a crucial role in the development and progression of the disease. For example, cancer cells can become stiffer than normal cells, which allows them to resist the mechanical forces exerted by the surrounding tissue and to invade other organs. This increased stiffness is often the result of changes in the cells' cytoskeleton, the network of protein filaments that provides structural support and enables cell movement. Additionally, cancer cells can exhibit increased motility, which allows them to migrate to other parts of the body and to form metastases. This increased motility is often the result of changes in the cells' adhesion to the extracellular matrix, the network of proteins and other molecules that provides structural support to the tissue. By loosening their adhesion to the extracellular matrix, cancer cells can more easily detach from the tissue and move to other areas of the body.

Understanding the mechanical behavior of cancer cells is therefore crucial for developing effective treatments for the disease. For instance, targeting the cytoskeleton or the adhesion mechanisms of cancer cells could potentially disrupt their ability to invade other tissues and form metastases. Additionally, understanding the mechanical properties of cancer cells could also help to identify biomarkers for early detection of the disease, as well as to predict how the disease will progress in individual patients.

Hence, the mechanical behavior of cancer cells is an important factor in the development and progression of the disease. Further research on the subject could potentially lead to new and improved treatments for cancer.

## 4.2 Introduction

The vast majority of cancer-related fatalities are due to metastasis i.e. the migration of tumour cells from the initial location to distant organs. This process involves the invasion of cells from a primary tumour into the surrounding tissue, their intravasation into the nearby microvasculature, their migration through the blood and lymphatic vessels, their extravasation at a distant organ site, and their proliferation to form a secondary macroscopic tumour.

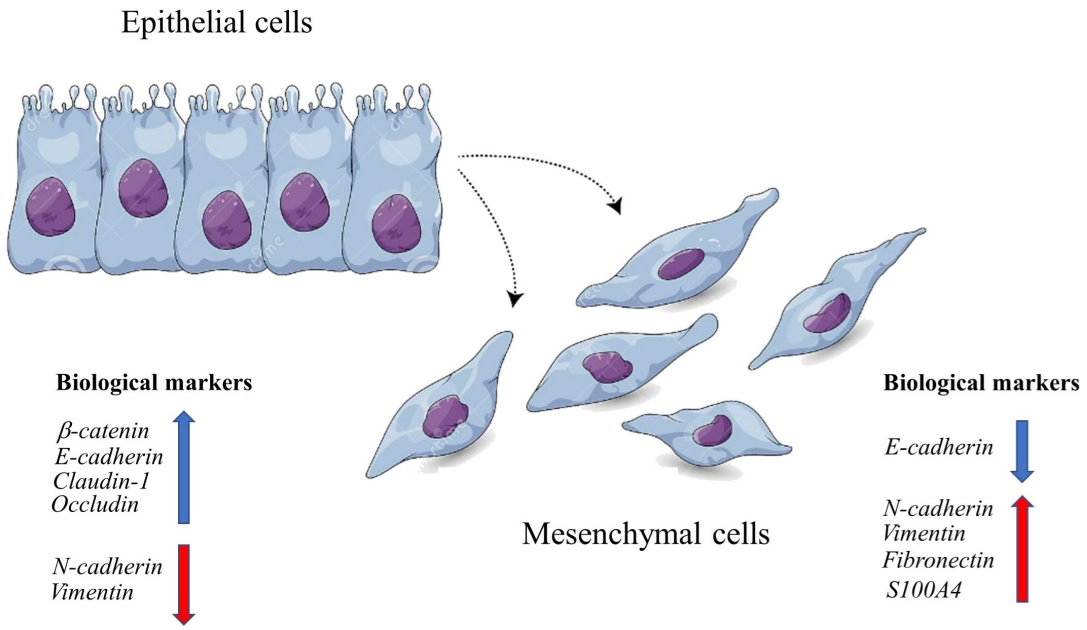


FIGURE 4.1: Cell marker changes in EMT. During EMT, epithelial cells lose their cell membrane epithelial markers and acquire mesenchymal markers and metastatic traits.

It is hypothesized that the evolutionarily conserved epithelial-mesenchymal transition (EMT) developmental pathway permits cancer cells to launch the invasion-metastasis cascade. Indeed, EMT is considered a significant factor in the invasion and metastasis of several cancer types. During an EMT, epithelial cells lose their intercellular connections, cell-extracellular matrix contacts, and cell polarity. Hence it acquire more mesenchymal characteristics such as enhanced expression of mesenchymal markers, motility, and invasiveness as shown in Figure 4.1. Additionally, the development of an EMT is related to greater medication resistance and a bad prognosis. Indeed, the transcription factors that cause an EMT are also involved in the induction of the ABC family of drug transporters that are responsible for drug efflux, resulting in drug resistance and tumor relapse.

In addition, the mesenchymal cancer cells inside a malignancy are known to be more drug-resistant than the epithelial cancer cells. Even among cancer cells circulating in the blood, it is known that mesenchymal cells are more capable of beginning metastasis than epithelial cancer cells. Therefore, cancer growth may be predicted by identifying EMT-transformed cells inside a tumor and those in circulation (termed circulating tumor cells). Currently, this is accomplished by biochemical analyses including laborious biochemical marker analysis employing flow cytometry, immunocytochemistry, western blotting, or RT-PCR. Although variations in the cytoskeletal structure of actin fibers are crucial to the changes in cellular shape and polarity, it is unknown to what degree changes during an EMT influence the biomechanical characteristics of cancer cells.

Cancer progression is often associated with the chemical, physical and mechanical behavior of cancer cells. Intracellular viscosity is an essential property of cancer cells, which influences the

overall cell characteristics at molecular as well as morphological levels. Variations in intracellular viscosity have been associated with a plethora of diseases, however, the correlation of intracellular viscosity with Epithelial to Mesenchymal Transition (EMT) is yet unexplored. Viscosity is an essential parameter that regulates bio-molecular reaction rates of diffusion-driven cellular processes. Hence, abnormal viscosity levels are often associated with various diseases and malfunctions like cancer. For this reason, monitoring intracellular viscosity becomes vital. While several approaches have been developed for in-vitro and in-vivo measurement of viscosity, analysis of intracellular viscosity in live cells has not been well realized. Several indicators have been developed to identify the morphology of cancer cells in order to predict metastasis. As epithelial markers, epithelial cells express E-cad and Epcam, whereas mesenchymal cells express Vimentin. Several additional procedures have been utilized to examine the cellular stiffness of cancer cells of different grades and have shown changes in the rigidity of cells at various stages. Micropipette aspiration, atomic force microscopy, microplate manipulation, sorting in microfabricated sieves, and optical tweezers were used earlier. All of these strategies increase metastatic cancer's flexibility, allowing it to escape the main cancer cells and enter the bloodstream, from where it may spread to distant organs and progresses.

A range of test methods has been used to study the mechanical properties of cells, with the method chosen depending on the size of the structure being studied. Microscale structures require microscale tools, while nanoscale structures require nanoscale tools. Generally, two types of tools are used to examine cell mechanics: force application techniques and force sensing techniques. The former applies force to a cell and records the cell's mechanical and/or biochemical response, while the latter uses cells on a deformable substrate to measure their traction forces. In both cases, the devices used have limitations in terms of spatial and force resolution (Table 4.1), which affects their usefulness.

TABLE 4.1: Reported force and spatial sensitivity of tools used to study cell mechanics [184]–[186]

| Technique | Force application | Force sensing | Spatial sensitivity | High-throughput |
|---|---|---|---|---|
| Micropipette aspiration | 0.1-$10^3$ nN | - | 1-100 $\mu$m | Potentially |
| Microneedle manipulation | 1-$10^3$ pN | - | 1-1000 $\mu$m | Potentially |
| AFM | 10-$10^7$pN | 10-$10^5$ pN | 1-$10^5$ $\mu$m | Potentially |
| Optical tweezers | 0.01-$10^3$ pN | 1-$10^2$ pN | 10-$10^5$ $\mu$m | Potentially |
| Optical strecthers | 10-$10^3$ pN | - | 10-$10^6$ nm | Potentially |
| Magnetic tweezers | 0.1-$10^4$ pN | 10-$10^3$ pN | 0.1-$10^2$ $\mu$m | No |
| Magnetic tweezers cytometry | 1-$10^2$ pN | - | 1-$10^3$ $\mu$m | No |

All of the above-mentioned methodologies to investigate the mechanics of cells, however, suffer from the issue of poor throughput, which results in less meaningful data. In addition, the majority

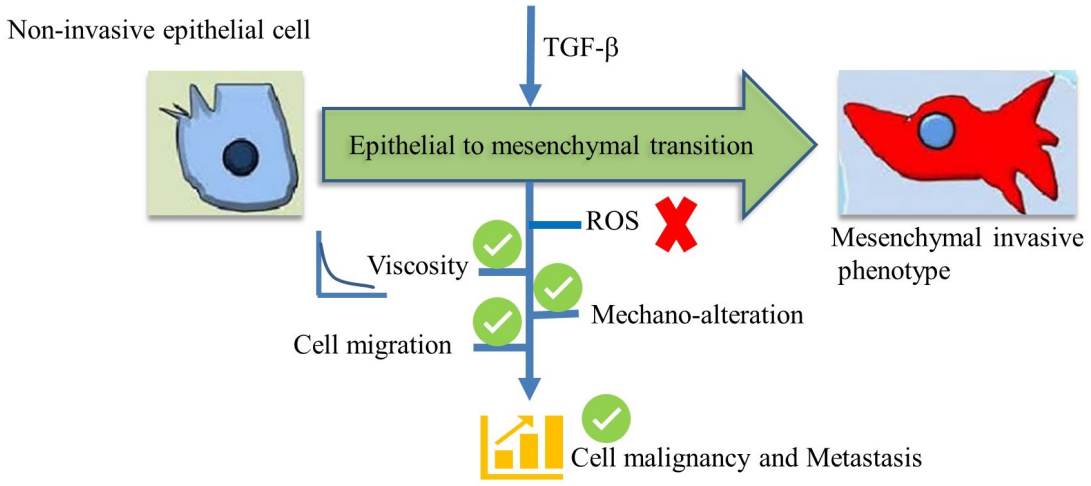


FIGURE 4.2: Inhibition of Tgf-$\beta$ during EMT showing activation and deactivation of various biological activities.

of these procedures are invasive to cells, since they often involve probing cells or applying localized stresses to portions of the cell surface. Therefore, the response contains probing errors and is too confined for generalization.

Our research introduces a novel, natural frequency-based, non-invasive method to determine the intracellular viscosity in cells. This method can not only efficiently analyze the differences in intracellular viscosity post modulation with molecules like PEG or glucose but is sensitive enough to distinguish the difference in intra-cellular viscosity between normal and cancer cells as well. Interestingly, TGF-$\beta$ a cytokine reported to induce epithelial to mesenchymal transition (EMT) a feature associated with cancer invasiveness resulted in reduced viscosity of cancer cells and is responsible for various biological activities shown in Figure 4.2.

To corroborate our findings with existing methods of analysis, we analyzed intra-cellular viscosity with a previously described viscosity-sensitive molecular rotor-based fluorophore-TPSI I. In parity with our PSD-based approach, an increase in fluorescence intensity was observed with viscosity modulators, while, TGF-$\beta$ exposure resulted in its reduction in the cells studied. This is the first study of its kind that attempts to characterize differences in intracellular viscosity using a novel, non-invasive PSD-based method.

Viscosity is often referred to thickness of a fluid, which consequently leads to resistance to flow. In biological systems, like a cell, cytoplasmic viscosity determines the diffusion of biomolecules, which is essential for basal diffusion-driven intramolecular interactions to carry out effective signalling pathways. Importantly, a change in intracellular viscosity may lead to altered diffusion of molecules and consequently affect the basal bio-molecular reaction rates, disrupting homeostasis, and healthy functioning of a cell. Therefore, it becomes imperative to monitor intracellular viscosity in live cells. In 1939 and 1941, in their pioneering research, Guyer et al used ultra-centrifugation technique to determine that intracellular viscosity varies between normal and

tumor cells [187]. Since then, there has been enormous progress in the development of methods to measure viscosity. In this regard, capillary viscometer, rotational viscometer, falling sphere viscometer, Zahn cup method, vibrational viscometer, and VROC viscometer are a few classical and popular methods available to quantify bulk viscosity (macroscopic viscosity) which require voluminous samples [188]–[192]. On the other hand, in the current scenario, fluorescent probe-based techniques are the most recent and popular means to measure microscopic intracellular viscosity or the viscosity of specific intracellular compartments. Other relatively novel approaches to studying intracellular viscosity are time-dependent collision and fusion of nucleoli in human cells based on the fluctuating surface tension of nucleoli, and gravity-sensitive cellular responses to measure the viscosity of cell membrane under hyper-gravity.

However, it has been challenging to measure intracellular viscosity or microscopic viscosity levels and the mechanisms that caused the change in live cells. Therefore, in this study, we devised a natural frequency-based viscosity detector method in live cells. As every system tends to vibrate by its own natural frequency, this natural frequency corresponds to the rate at which the oscillations occur and is a function of the stiffness and mass of any system. Although several frequency-based methods are developed and used to target diseases. These existing methods work on the principle of exciting the cells with their natural frequency, with which resonance will be achieved (the excitation frequency and natural frequency of the cells coincide), and it leads to damaging the cells [193].

Previous studies related to the natural frequency of biological cells were derived from an extension theory of drop oscillations proposed by Rayleigh and Lamb's [194]. Rayleigh derived an equation for the frequency of natural oscillations of a drop in air, whereas Lamb carried the same for a drop in a viscous fluid [195]. Further, Ackerman et al. explored the resonance in mechanical vibrations of cells [196] and proposed the resonance frequencies and characteristics of red blood cells by modelling the cells as spherical, isotropic elastic shells with viscous fluids [194], [197]. Ackerman [198] studied the influence of viscous damping on the resonance of the cells. However, reduced cell model and mathematical flaws in the calculation of the quality of oscillations of natural cells [199], [200] restrict the possible application of work [194].

Experimental techniques such as scanning acoustic microscopy (SAM) where time-resolved signals were used to determine the mechanical properties of the single cell [201]–[203] while ultrasound was used to evaluate the natural frequency and resonance. These techniques are mostly focused on the modeling of sound interactions with the biological cells and the associated dynamics that damage the cells and their internal constituents. Hence, this motivated us the development of an experimental technique without harming the biological system and investigate the mechanical properties. Furthermore, it is worth mentioning that the cell system consists of a network of cytoskeleton framework [204] that organizes cellular content, regulates forces for shape and its motion, and interacts with the external environment [205], [206]. This organizational network of

cells responds to external stimuli and dampens the frequencies. Herein, damping is a phenomenon that occurs inside or on an oscillatory system and reduces its oscillation [207], [208].

In parallel, numerous observations based on different approaches have convincingly demonstrated the significance of filamentous network and adhesion complexes in regulating elastic and viscous properties of the cells [209], [210] and persuasively demonstrated that any changes in its cytoskeletal arrangement can be related to changes in mechanical property of the cells. Thus, cellular mechano-elastic properties are highly correlated with the phenomenon of damping and frequency [211], [212] . Considering the above parameters this study reports the development of an experimental setup to evaluate the frequency-based viscosity in cells. Our regimen is sensitive and can also measure minor alterations in intracellular viscosity.

In this work, we studied at the mechanical dynamic response of Huh-7 cell lines. As evidence of concept, we show substantial changes in the frequencies of immortalized cells, epithelial cells, and mesenchymal cells. Furthermore, we promote EMT in epithelial cells by TGF-$\beta$ and found a clear shift in vibrational frequencies toward the mesenchymal grade. Interestingly, when we suppress EMT genetically, a shift in vibrational frequencies toward an epithelial signature. Our results suggest that our approach might be utilized to identify transformed and metastatic cells in various stages of cancer and could be used as a non-invasive tool for diagnosing cancer progression.

The cells used in our experimentation were provided by our collaborating laboratory (Prof. Rajdeep Chowdhury and Prof. Sudeshna Mukherjee Lab.). This section on cell culture and the biological assay of the cells was performed by Dr. Abhilasha Shrivastava and included in this thesis solely for the purpose of completeness. As the author of the thesis, I did not carry out the cell culture and biological assay part of this work.

## 4.3 Materials and Methods

### 4.3.1 Cell culture

Huh-7 cells (human hepatocellular carcinoma) were procured from National Centre for Cell Science, Pune, India. Cells were cultured at 5% $CO_2$ 37 °C in Dulbecco's Modified Minimal Essential Medium (DMEM; Gibco, # 12800-017) which was supplemented with 10% fetal bovine serum (FBS; Invitrogen, # 26140-079) and antibiotics (1% penicillin–streptomycin solution; Invitrogen, # 10378-016). Huh-7 cells were grown up to 70% confluency in 10% FBS containing DMEM and rinsed with phosphate-buffered saline (PBS). Thereafter, complete medium was replaced with serum starved medium (DMEM containing 2% FBS) and incubated for 12 h prior to TGF-$\beta$ (# 100-35B-10, Peprotech) treatment [213].

### 4.3.2 Confocal microscopy

Cells were seeded on coverslips at $2.5\times10^5$ cells/well and then treated with required concentrations of cytokines. Treated cells were then washed with 1x PBS and fixed with 4% paraformaldehyde followed by incubation at room temperature for 10−15 min. Thereafter, cells were treated by 0.2% tritonx for approximately 2 min. Post multiple PBS washes, cells were incubated with phalloidin solution for 1 h, which was followed by washing twice with 1x PBS, followed by mounting the coverslips on slides using antifade DAPI and imaged under a confocal microscope (Zeiss). Images were analyzed using Zen 3.2 software [214].

### 4.3.3 Immunoblotting

Immunoblotting was performed following methods described elsewhere. Briefly, RIPA buffer (Sigma−Aldrich) was used to extract protein and total protein was estimated using Bradford reagent (Sigma) at 595 nm wavelength. The cellular protein lysates were run in denaturing polyacrylamide gels and transferred to polyvinylidene fluoride membranes (PVDF, Bio-Rad) which were followed by blocking with 5% skimmed milk (HiMedia). Afterward, blots were probed and re-probed with specific primary antibodies. The secondary antibodies were horseradish peroxide-conjugated and hence detected using the ECL detection system following the manufacturer's protocol using ChemiDoc (Bio-Rad). Wherever required, the blots were cut to probe with different antibodies against proteins of different molecular weights. Quantitation of differential protein expression was done using ImageJ software and analyzed through Graph-pad Prism software 8.0.1 [215].

### 4.3.4 Analysis of uptake of TPSII

As mentioned earlier, cells were seeded in 6 well plates at a density of $2.5\times10^5$ cells/well. The following day, the cells were treated with the desired PEG/TGF-$\beta$ /Glucose for a required period of time. Thereafter, the cells were harvested, washed with PBS, and re-suspended in 500 $\mu$l of fresh PBS. To detect the percentage of TPSII positive cells, flow cytometric (Cytoflex, Beckmann Coulter) analysis was performed, and the acquired data were analyzed using CytExpert software [216].

### 4.3.5 Cell Cycle Analysis

Propidium Iodide binds to the DNA in live cells, therefore, based on total DNA content cells were seeded in 6 cm dishes. Post overnight incubation, cells were treated with cytokine for 72 h, cells were harvested and washed with PBS followed by 5000 rpm for 10 min at 4 °C, the pellet was

re-suspended in a fixative (100 $\mu$L of PBS and 900 $\mu$L of ice cold 70% ethanol) fixed cells were stored at 4 °C overnight. After which, cells were centrifuged, and the pellet was re-suspended in 495 µL PBS with five µL of propidium iodide solution (PI; 2 mg/ml). The samples were then incubated in dark for 10 min followed by acquisition using flow cytometer (Cytoflex, Beckmann Coulter) and analysis using CytExpert software [213].

### 4.3.6 Measuring frequency response

Figure 4.3a shows the detailed working principle of the experimental setup. A laser source was used with a maximum of 23mW and 650nm wavelength powered by an external AC Voltage source of 240V and 50 Hz. Cultured cells were placed over the cross slide and input was applied on the slide for the actuation of the cells. A micro actuator was used and driven by the function generator (Tektronix AFG 1022) for the actuation of the cells. To vibrate the cells, a harmonic signal was applied to the actuator. The position of the cancer cells in the wells of the plate was determined with an optical microscope. A Position Sensitive Device (PSD) was used to detect an incident light spot precise position in two dimensions on a sensor surface. Laser from the source is focused and impinged on the cell surface and gets refracted to the PSD. Which was used to trace the cell movement due to actuation, and the digital output voltage corresponded to cell displacement in the X and Y directions, as measured by the Oscilloscope (Tektronix 1102B). The cell and support response was measured sequentially as shown in Figure 4.3b. We have considered the transfer function of the cell with respect to the base to avoid all the base-related modes (Figure 4.3c).

### 4.3.7 Determination of Viscosity

Experiments were performed on cancer cell samples. The frequency response and viscosity of the cells were evaluated using the proposed non-invasive technique. The time domain and frequency domain responses were recorded from the oscilloscope. A transfer function or frequency response function between the input and output of the system was used to characterize the response of a cell's structure to forced vibrations applied at the support of cells.

$$H(\Omega) = \text{Output/Input} \tag{4.1}$$

The frequency corresponding to maximum amplitude was considered as a natural frequency of the cell [217]. The quality factor, a measure of the sharpness of resonance was calculated using the half power point method (Figure 4.3d).

$$Q = f_{max}/(f_2 - f_1) \tag{4.2}$$

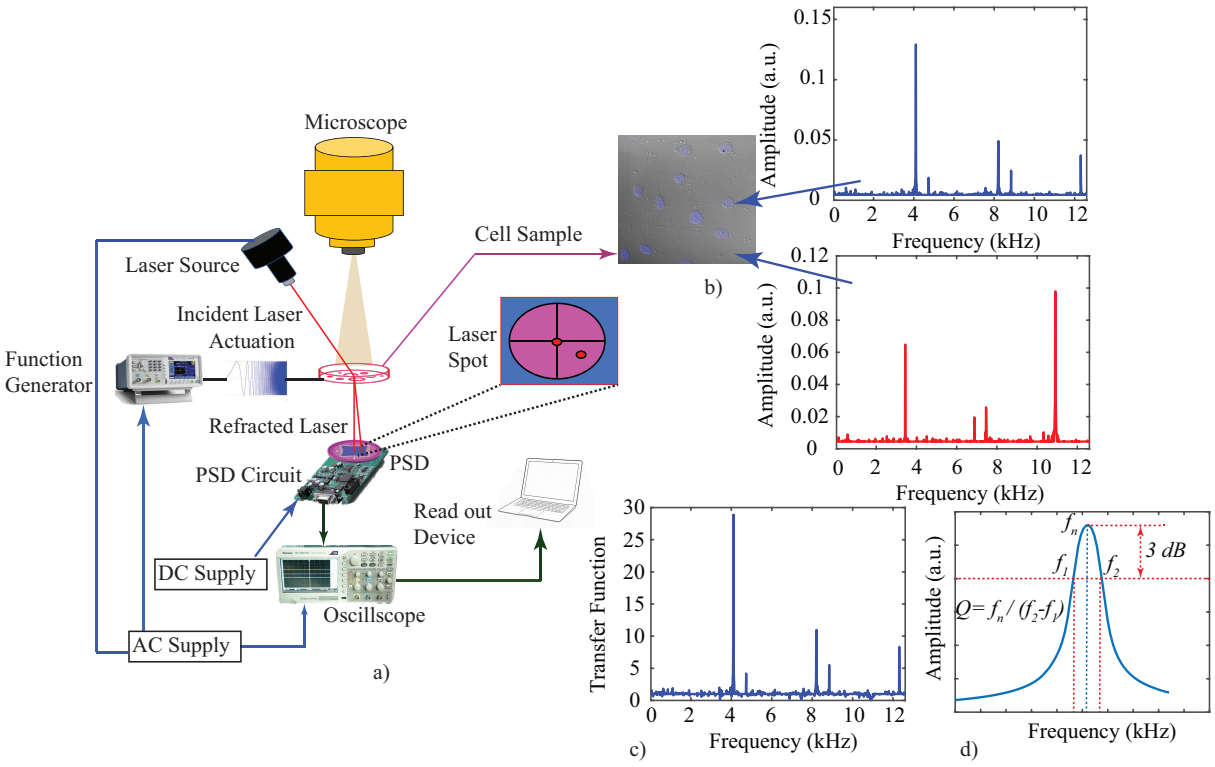


FIGURE 4.3: Detailed procedure for the PSD-based non-invasive experimental technique a) Experimental setup for the dynamic response of the cancerous cell. b) High contrast image of TGF-$\beta$ induced Huh-7 cells with cell frequency response in blue and base response in red. c) Transfer function of the frequency response of cell and base. d) Estimation of Q factor from frequency response.

Where Q is a Quality factor, $f_{max}$ is maximum Frequency, $f_1$ and $f_2$ are the 3 dB frequencies. The relation between Quality Factor and Damping Ratio ($\zeta$) [195] was shown by using the Equation 4.3.

$$Q = 1/(2\zeta) \tag{4.3}$$

Where $\zeta$ is the damping ratio. In this work, cells were assumed as sessile drops [218], [219] and considered as translucent structures mediated in a low-viscosity fluid. For low−viscosity liquids like water and ethanol and relatively micron size droplets that are in dynamically ideal surroundings are given by the general modified expression obtained by Lamb [195]). Hence the exponential decay time and the natural frequency were obtained from the equation of the viscosity and damping ratio

$$\tau = (\rho r^2)/(\nu(n-1)(2n+1)) \tag{4.4}$$

Where $\tau$ exponential time is constant, $\rho$ is the density of the cell medium, r is the radius of the cells and $n$ is a number of the mode of the resonant frequency, $\nu$ is the dynamic viscosity of the cells. Also

$$\tau = 1/(\omega_n \zeta) \tag{4.5}$$

Equation 4.5 shows the relation between the time constant and damping ratio. Where $\omega_n$ is a natural frequency in rad/sec.

### 4.3.8 Cell spreading analysis

Morphology assessment was carried out after 48 h of cell seeding (see materials and method) with nonconfluent density on coverslips at $2 \times 10^5$ cells per well. Coverslips were mounted on slides using antifade DAPI and imaged under a Confocal microscope (Zeiss). Subsequent images were then imported in the Image J software in czi format. Images were analyzed and the area and perimeter of cells in each image were quantified. A uniform background subtraction to the entire image and subsequent adjustments to the brightness and contrast were applied as necessary.

### 4.3.9 Statistical analysis.

All experiments were repeated thrice for observing any deviations and accuracy. Every group of specimens subjected to the experiments consists of 10 sets of observations. All data are expressed as a mean ± standard error of the mean (SEM). The two−tailed unpaired t−test or one−way ANOVA were used for statistical analysis, followed by Tukey multiple comparison tests using Origin Software (Origin (Pro), Version 2021, OriginLab Corporation, Northampton, MA, USA.) (for three or more groups). A statistically significant difference was defined with $p < 0.05$.

### 4.3.10 Numerical analysis

Confocal images were extracted from the confocal microscopy (Zeiss) in the czi format. 3D images of the cancer cells were imported into ImageJ (an open-source image analysis tool developed by the National Institutes of Health) and converted to STL format for further analysis as shown in Figure 4.4a. STL files were imported in the geometric modeler of COMSOL (COMSOL Multiphysics Inc. Stockholm, Sweden) as a cell model. Cells are composed of various constitutive elements and behave as a soft matter [220]. In this work, we consider two cases for assigning the material to the cell structure to validate the responses from the numerical modeling. In the first case we considered the cell modeled as an incompressible, isotropic, and homogeneous [221] with a density of 1 g/cm$^3$ and a poison's ratio of 0.49 and in the second case as a hyperelastic constitutive model to simulate isotropic and nonlinear cell scaffold and cell plasma aggregates all together, which have an elastic response to high stresses. For hyperelastic material, we adopted the Mooney−Rivlin material [222], [223] to model the cell structure. Cell model extraction and discretization of the cell model into a smaller segment was done using physics-controlled fine meshing with the tetrahedral mesh elements as shown in Figure 4.4b I and II. Detailed boundary conditions are shown in Figure 4.4c. Cells were modeled to be supported on an elastic foundation.

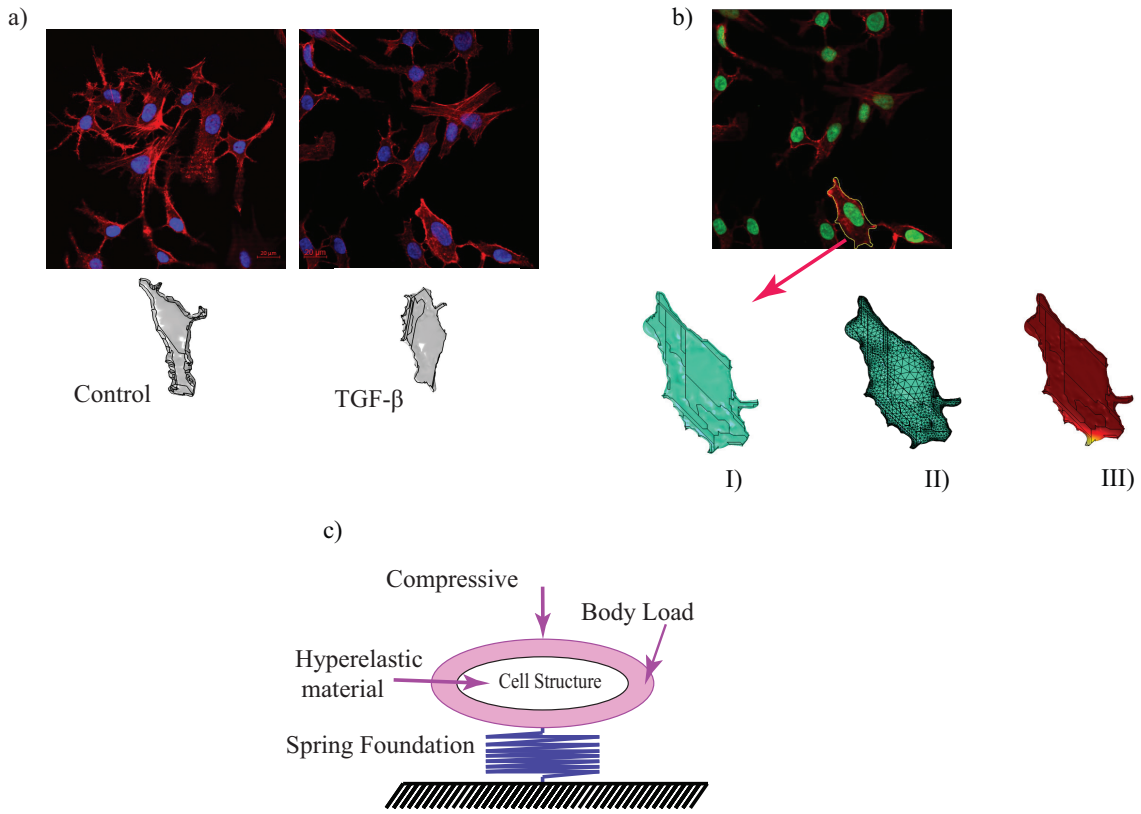


FIGURE 4.4: a) Confocal images of the Huh-7 cells treated with 5ng/ml TGF-$\beta$ and control. b) Cell selection for cellular geometry for the numerical simulation in inset I) 3D model obtained from Image-J as STL Format. II) Discretized model in small elements. III) Stress distribution in the model after the application of load on the model. c) Mechanical model of the cell structure along with the boundary conditions.

Previous studies state Vinculin as a protein in focal adhesions and adherence complexes that is responsible for cell−to−ECM adhesion[224]. The focal adhesion stiffness was found to be in the range of 0.001 to 0.1 N/m [225] and the top surface of the cell was exposed for the loading. A compressive load on the cell surface in the transverse direction was applied to get the frequency response of the cells. Modal and harmonic analyses were carried out using numerical modeling. The modal analysis illustrates the deformation pattern on the structure at each of the natural frequencies as the excitation coincides with one of the natural frequencies of the system [226]. Such as those induced by the lateral force created by the microactuators and identifies the vibration characteristics viz. Natural frequencies and mode shapes of the cell structure. While the steady-state dynamic response of a cell structure subjected to varying loads was predicted from harmonic analysis. Detailed numerical steps are shown in Figure 4.5. Natural frequencies and associated displacement during the actuation of cells and their frequency responses were assessed to visualize the dynamic spectra of the cells.

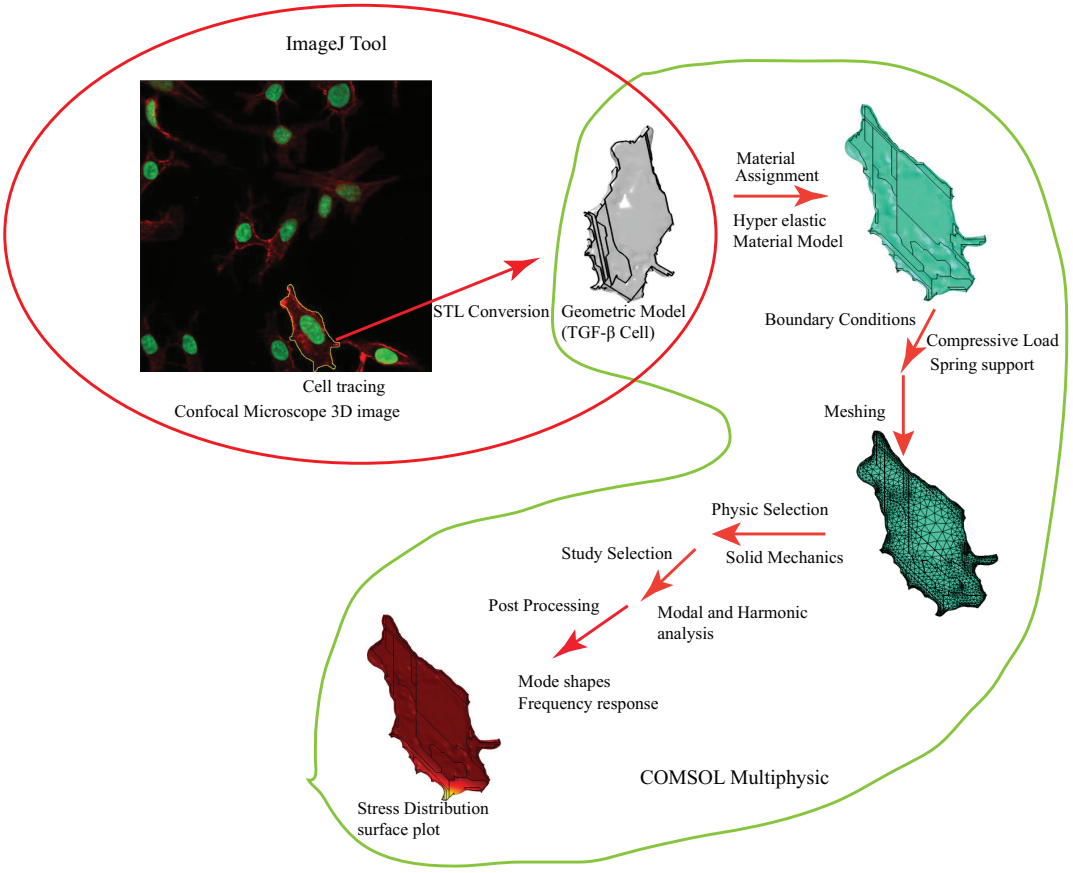


FIGURE 4.5: Detailed flow diagram depicting the procedure followed for numerical analysis

TABLE 4.2: Geometrical and Mechanical Properties for the cell.[227]

| **Parameter** | **Value** |
|---|---|
| Youngs Modulus | 100 Pa |
| Density | 1000 kg/m$^3$ |
| Poison ratio | 0.49 |
| Average length of the cell | 35 $\mu$m |

### 4.3.11 Modal Analysis

In this work, we analyzed the modal characteristics of the cell structure obtained from the phalloidin-stained confocal microscopy images. The natural frequency of the cells and their corresponding mode−shapes was depicted and analyzed. Homogenized mechanical properties for the modal analysis are shown in Table 4.2.

### 4.3.12 Harmonic Analysis

After obtaining resonance frequencies of the various cells using modal analysis, we evaluated the frequency responses of the cells. The effect of vibrating load on a cell structure was calculated

TABLE 4.3: Hyperelastic Properties of the homogenized cell [227], [229]–[233]

| **Parameter** | **Value** |
|---|---|
| Young's Modulus | 100 Pa |
| Density | 1000 kg/m$^3$ |
| Poison ratio | 0.49 |
| C10 | 0.21 kPa |
| C01 | 0.1 kPa |
| Bulk Modulus (k) | 300 Pa |

using a harmonic response analysis. Considered mechanical properties of cells are shown in Table 4.3. In this analysis, we derive the frequency response by applying body load on the cell. The other boundary conditions are kept the same as those in the modal analysis.

### 4.3.13 Hyperelastic model

For hyperelastic material, we adopted the modified Mooney-Rivlin material model [228] to model the cell structure. The strain energy density function W for the hyperelastic material is given as

$$W = C_1(I_1 - 3(I_3)^{1/3}) + C_2(I_2 - 3(I_3)^{2/3}) + 1/2(\lambda(\log I_3)^2) \tag{4.6}$$

where $C_1$, $C_2$, and $\lambda$ are material constants and $C = F^T F$ is the right Cauchy–Green deformation tensor; and the three invariants of the right Cauchy–Green tensor are defined as

$$I_1 = tr(C) \tag{4.7}$$

$$I_2 = 1/2[((tr(C))^2 - tr(C^2)] \tag{4.8}$$

$$I_3 = det(C) \tag{4.9}$$

The corresponding constitutive relations can be expressed in terms of the second Piola–Kirchhoff stress tensor $S$, and the invariants of the right Cauchy–Green tensor,

$$S = 2[(C_1 + C_2 I_1)I - C_2 C - (C_1 I_3^{1/3} + 2C_2 I_3^{2/3} - \lambda \log I_3)C^{-1}] \tag{4.10}$$

After the second Piola–Kirchhoff stress is obtained, the first Piola–Kirchhoff stress tensor can be immediately computed as $P = SF^T$, which can then be substituted into the later developed meshfree Galerkin formulation to calculate the internal nodal force.

## 4.4 Results

### 4.4.1 Aggravated extra-cellular viscosity enhances intra-cellular viscosity in cancer cells

The external cellular environment is persistently occupied site with macromolecules and hence has tissue-specific density and viscosity. This high viscosity is achieved due to the constant accumulation and exchange of precursors and products of degradation in the extracellular environment. However, the consequences of higher external viscosity on intracellular viscosity remain largely unexplored. Therefore, to analyze intracellular viscosity, cancer cells were exposed to extra-cellular viscosity enhancers like PEG and glucose, which were then subjected to measure the frequency response from the optical position sensing method that comprises PSD, which shows altered frequencies and transfers function with the difference in viscosity of treated cells (Figure 4.6a). Based on the design of the experiment, our observations revealed that the consecutive peaks of transfer function represent the natural frequency of cells treated with 5% PEG was observed as 4120 $\pm$ 191.71Hz and that of glucose-treated cells showed 3024 $\pm$ 394.93 Hz frequency, the natural frequency of untreated cells was observed as 2180 $\pm$ 267.92 Hz (Figure 4.6b). The frequency of cells treated with viscosity modulators increases in comparison to the untreated cells. Additionally, from PSD analysis of cells exposed to different concentrations of PEG and Glucose, intracellular viscosity drastically surges 12 times with 5% PEG and 1.8 times with glucose when compared with untreated cells as shown in (Figure 4.6c). Alongside this, to validate our results, intracellular viscosity was measured using a viscosity-sensitive fluorescent probe TPSII (30). In correlation with the above results, an increase in green fluorescence intensity was reflected after cells were exposed to 5 % PEG and 200mM glucose as shown in the (Figure 4.7a and b) suggesting that our setup is capable of differentiating the enhanced intracellular viscosity levels and can be used in determining diseased conditions in patients.

### 4.4.2 Intracellular viscosity is associated with migratory/invasive potential of a cell

Tumour progression is associated with the acquisition of migratory potential and differentiation of epithelial cells into a mesenchymal type, a process known as Epithelial to Mesenchymal Transition (EMT), which is the initial step towards metastasis of tumor cells [234]. TGF-$\beta$ a pro-inflammatory cytokine is widely accepted as an EMT inducer [235]. Based on our hypothesis, cells undergoing EMT will shed their viscosity-based density to facilitate the swift migration of tumor cells. Therefore, EMT-associated viscosity was analyzed by PSD in cells treated with TGF-$\beta$, and dose kinetics and time kinetics was performed after TGF-$\beta$ treatment. Our results show the transfer function for TGF-$\beta$ treated cells was reduced by 25.4% in comparison with untreated

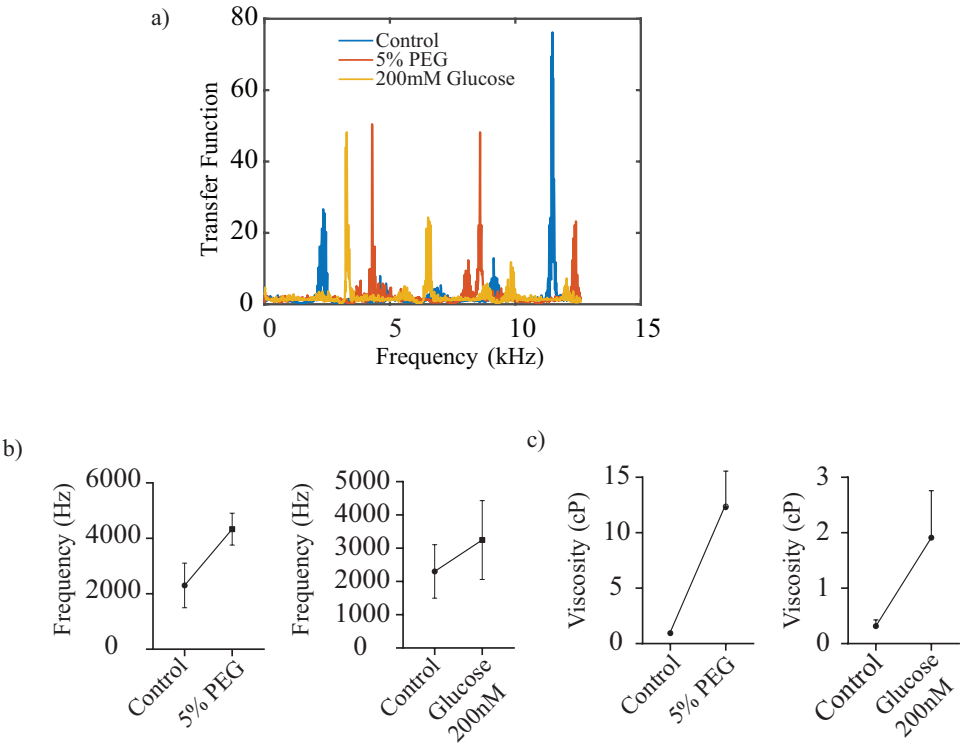


FIGURE 4.6: Analysis of intracellular viscosity with viscosity inducers like PEG and Glucose through PSD a) Transfer function plot for different viscosity modulators. Consecutive Peaks represent the natural frequency of the cells treated with different types of drug modulators. b) Frequency comparison plot for PEG and 200 mM glucose compared to control (For n = 3 with the Mean value ± SEM). Obtained frequency for PEG is higher (4350 Hz) compared to glucose and control. c) Viscosity plot for PEG and 200 mM glucose compared to control obtained from the frequency response of the cells shows the higher values for 5% PEG due to higher natural frequency for the 5% PEG treated cells. (For n= 3 with the Mean value ± SEM)

cells (Figure 4.8a). Moreover, a decrease in natural frequency was also observed upon TGF-$\beta$ treatment when compared to untreated cells (Figure 4.8b). Similarly, to validate a correlation between invasiveness and viscosity a PSD analysis was done on invasive and non-invasive cell lines i.e., MDAMB-231 and MCF-7 respectively [236]. A Transfer function plot shows the higher frequency for MCF-7 by 12.38 % compared to MDAMB-231 as shown in Figure 4.8c and d. We found that the frequency of the TGF-$\beta$ induced cancerous cells reduces substantially due to EMT-induced change in the morphology of the cells. Cells lose their stiffness and as result, we observed reduced viscosity at different time points and with different doses (Figure 4.9) as shown in Figure 4.8e.

We can observe a similar trend in an invasive (MDA-MB-231) and non-invasive (MCF-7) cancer cell type as shown in Figure 4.8f. Immunoblot analysis was also carried out and observed an increase in the mesenchymal marker like N-cad and Vimentin post-TGF-$\beta$ exposure in hepatocellular carcinoma cells. Figure 4.10a shows the N-Cad and Vimentin expression after TGF-$\beta$ exposure with respect to untreated cells. To have an insight in the difference in internal viscosity of cells with different invasion/metastatic potentials, we compared two cell lines MCF-7

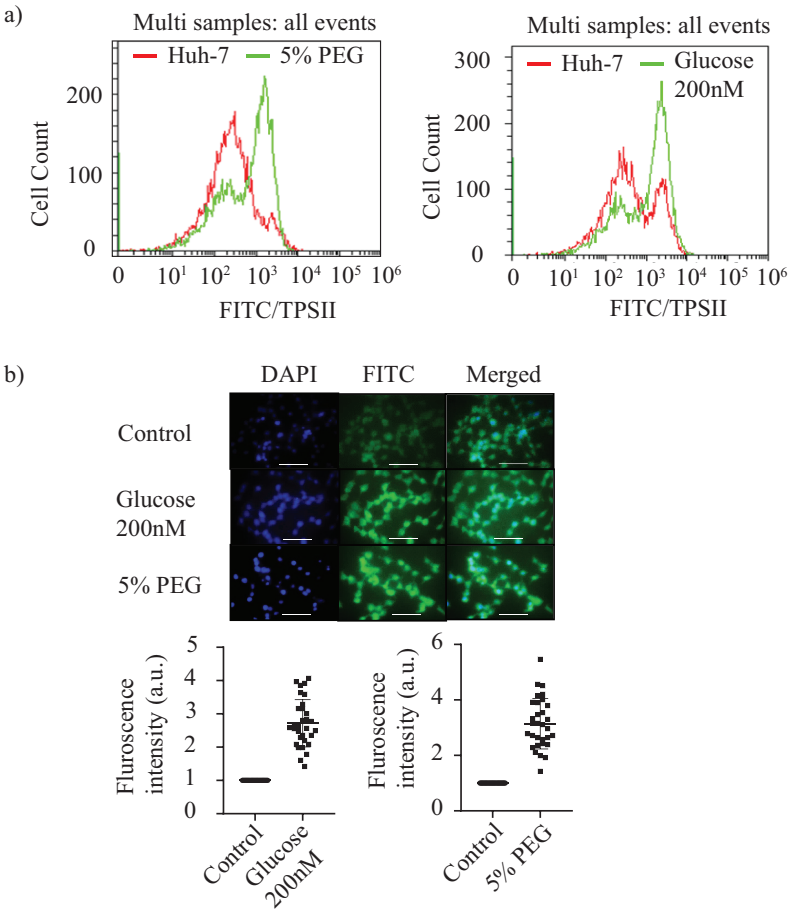


FIGURE 4.7: Analysis of intracellular viscosity with viscosity inducers like PEG and Glucose through Viscosity sensitive fluorescent probe a) Fluorescence intensity after PEG and 200mM glucose in cancer cells. b) Shift in peak after TPSII exposure for PEG and 200 mM glucose compared to control.

and MDA-MB-231 from the fluorescence test. Figure 4.10b depicts decrease in green fluorescence for MDA-MB-231 compared to MCF-7. Thus, it was revealed that the viscosity of MDA-MB-231 (invasive) had lower internal viscosity as compared to MCF-7 (non-invasive) cell line. Along with, our results show the shift in green fluorescence of TPSI1(fluorescent viscosity probe) post TGF-$\beta$ exposure as compared with the untreated cells as shown in Figure 4.10c. These results indicate the change in intracellular viscosity upon induction of EMT.

### 4.4.3 High viscosity suppresses cell migration

Frequency and viscosity for different cells treated with TGF-$\beta$ and different PEG concentrations have been shown in the Figure 4.11a. From the plot, we observed, a decrease in the frequency for TGF-$\beta$ concentrated cells compared to PEG and control. This signifies the decrease in the viscosity for the TGF-$\beta$ treated cells compared to other PEG-treated cells and control (see Figure 4.11b). High intracellular viscosity in cancer cells leads to heftiness and consequently inhibition of migration. Hence, post 5% PEG treatment where cancer cells have achieved the

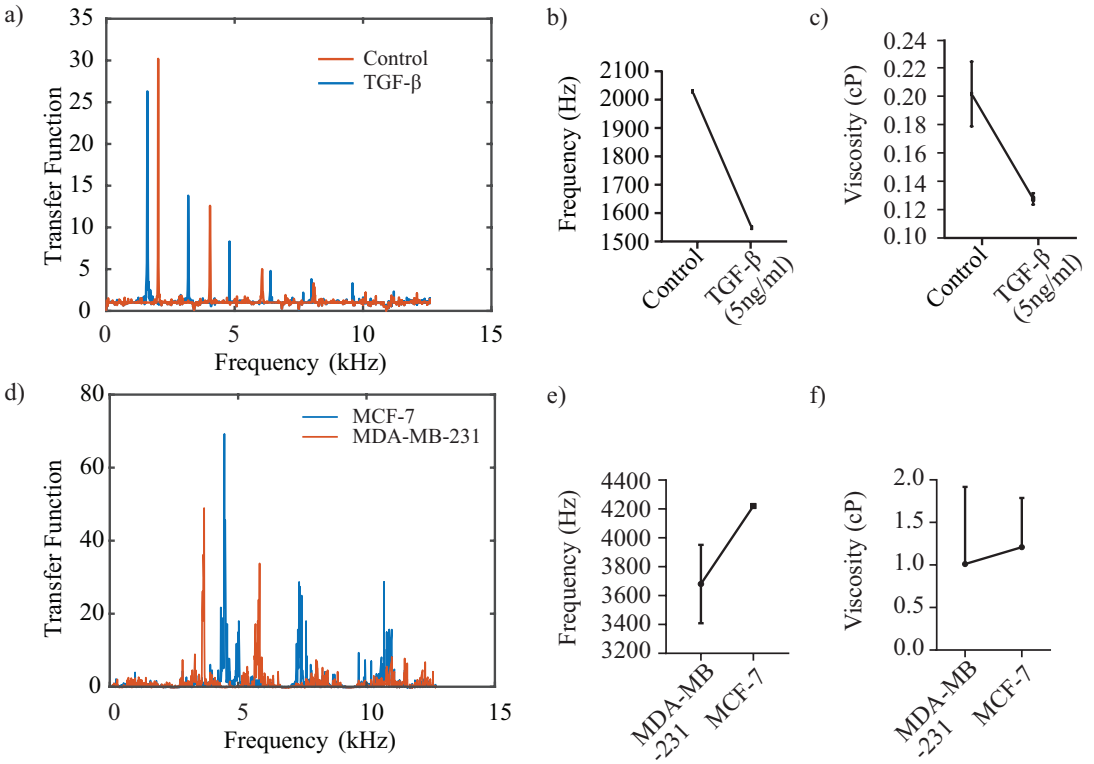


FIGURE 4.8: Repression in intracellular viscosity post TGF-$\beta$ induced EMT a) Transfer function for control and TGF-$\beta$ and for invasive and non-invasive cell lines. Corresponding higher peaks represents the natural frequency of the cells. b) Frequency comparison plot for TGF-$\beta$ compared to control (For n=3 with the Mean value ±SEM). c) Viscosity comparison for TGF-$\beta$ compared to control (For n=3 with the Mean value ± SEM) d) Transfer function for invasive and non-invasive cell lines. Corresponding higher peaks represents the natural frequency of the cells. f) Frequency comparison plot for MCF-7 compared to MDAMB-231(For n=3 with the Mean value ± SEM) g) Viscosity comparison for MCF-7 compared to MDAMB-231(For n=3 with the Mean value ± SEM)

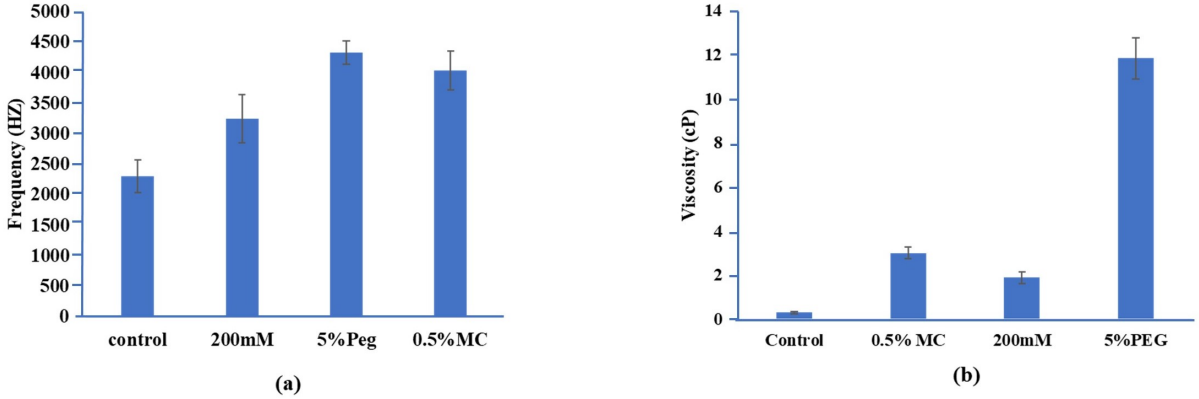


FIGURE 4.9: (a) Frequency for cells subjected to different viscosity modulators (b) Viscosity for cells subjected to different viscosity modulators.

highest viscosity, Huh-7 cells fail to heal the scratch in the wound healing assay (Figure 4.11c). Since cells fail to migrate, yet are viable, and undergo cell growth arrest in Huh-7 cells treated with 5% PEG was highly suspected, from cell viability assay, percentage cell viability of 5% PEG

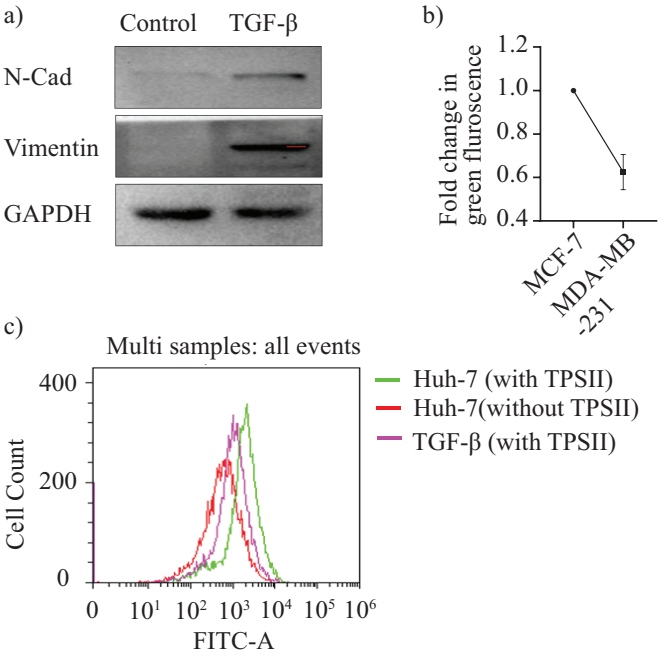


FIGURE 4.10: Repression in intracellular viscosity post TGF-$\beta$ induced EMT a) Immunoblot for N-Cad and Vimentin after TGF-$\beta$ exposure with respect to untreated cells. b) Fold change plot in green fluorescence for MCF-7 compared to MDAMB-231 c) Shift in peak after TPSII exposure in TGF-$\beta$ treated Huh-7 cells.

treated cells was low in comparison to untreated cells (Figure 4.11d). This led to understanding cell cycle arrest induced after 5% PEG treatment. From our data, we observed a G1 arrest after 5% PEG treatment in Huh-7 cells as shown in Figure 4.12a. Followed by a reduction in PCNA, a proliferation marker (Figure 4.12b). which suggests higher intracellular viscosity fails to potentiate migration and proliferation in cancer cells. TGF-$\beta$ induces EMT in cancer cells and viscosity modulators suppress the EMT markers. Figure 4.12c shows the vimentin down-regulates after the PEG treatment. We observed the lower EMT marker expression compared to untreated cells. Thus, an inverse correlation can be made between TGF-$\beta$ induced EMT and intracellular viscosity. This can be predicted from the alteration in the cell's morphology post-TGF-$\beta$ exposure as shown in Figure 4.12d.

## 4.5 Numerical Results

### 4.5.1 Modal Analysis

Modal analysis determines the intrinsic dynamic characteristics of the cells such as natural frequencies, and mode shapes. The natural frequencies for the control and TGF-$\beta$ treated cells are found to be 2330.3 Hz and 1703.00 Hz respectively. Figure 4.13a shows the corresponding mode shape along with the frequency for control and TGF-$\beta$ considering the support stiffness of

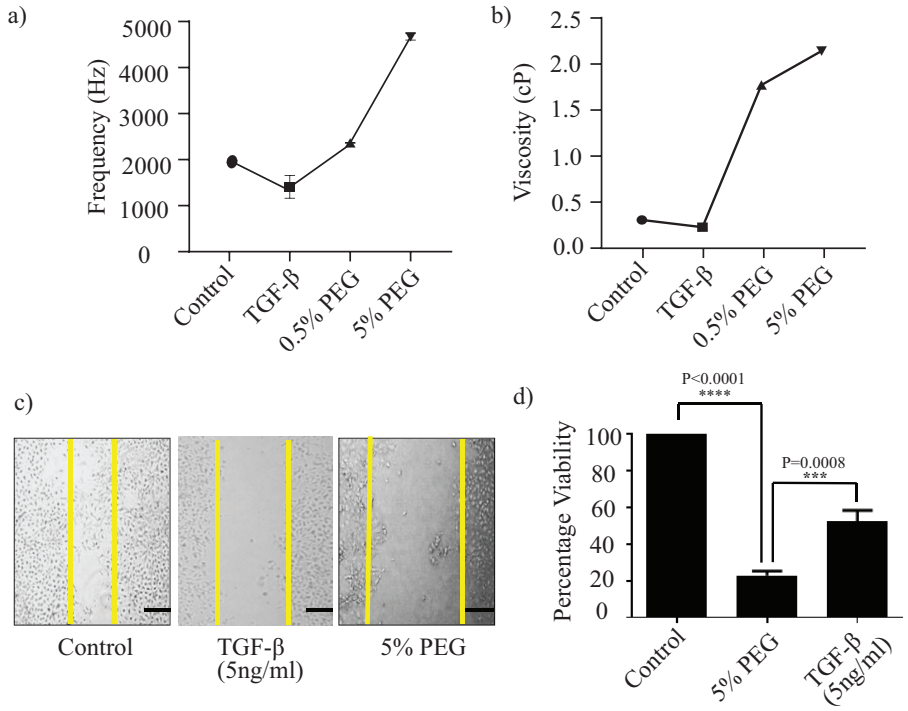


FIGURE 4.11: High intracellular viscosity inhibits migration and proliferation in cancer cells a) Frequency comparison for TGF-$\beta$ , 0.5% PEG and 5% PEG with control. b) Viscosity comparison for TGF-$\beta$ 0.5% PEG and 5% PEG with control. c) Scratch assay after TGF-$\beta$ and 5% PEG treatment at 72 hrs with respect to untreated in Huh-7 cells. d) Percentage viability after TGF-$\beta$ and 5% PEG treatment at 72 hrs with respect to untreated in Huh-7 cells.

TABLE 4.4: Comparison of experimental and numerical frequencies.

| **Parameter** | **Experimental (Hz)** | **Numerical (Hz)** | **% Error** |
|---|---|---|---|
| Control | 2108 | 2330.40 | 9.52 |
| 5 ng/ml treated TGF-$\beta$ | 1596.84 | 1703.007 | 6.23 |
| 5% PEG | 4120 | 4634.40 | 11.09 |

0.01 N/m. Further, frequencies for the cells treated with TGF-$\beta$ and 5% PEG were evaluated and presented in Table 4.4 with the percent of the error compared to the experimental results.

### 4.5.2 Harmonic Analysis

A harmonic response analysis computes the influence of external perturbation on a cell structure. External perturbations were applied to the cells in terms of harmonic motion. In this analysis, we derive the frequency response of the cell. Frequency response for the control and TGF-$\beta$ were obtained and shown in the Figure 4.13b. The peaks in the frequency response show the natural frequency of the cells. Natural frequency is at 1703.40 Hz and 2330.40 Hz for the TGF-$\beta$ and control respectively. A comparison between the experimental and numerical frequency response for cells treated with 5% PEG and control is shown in Figure 4.13c. Differences in the frequencies

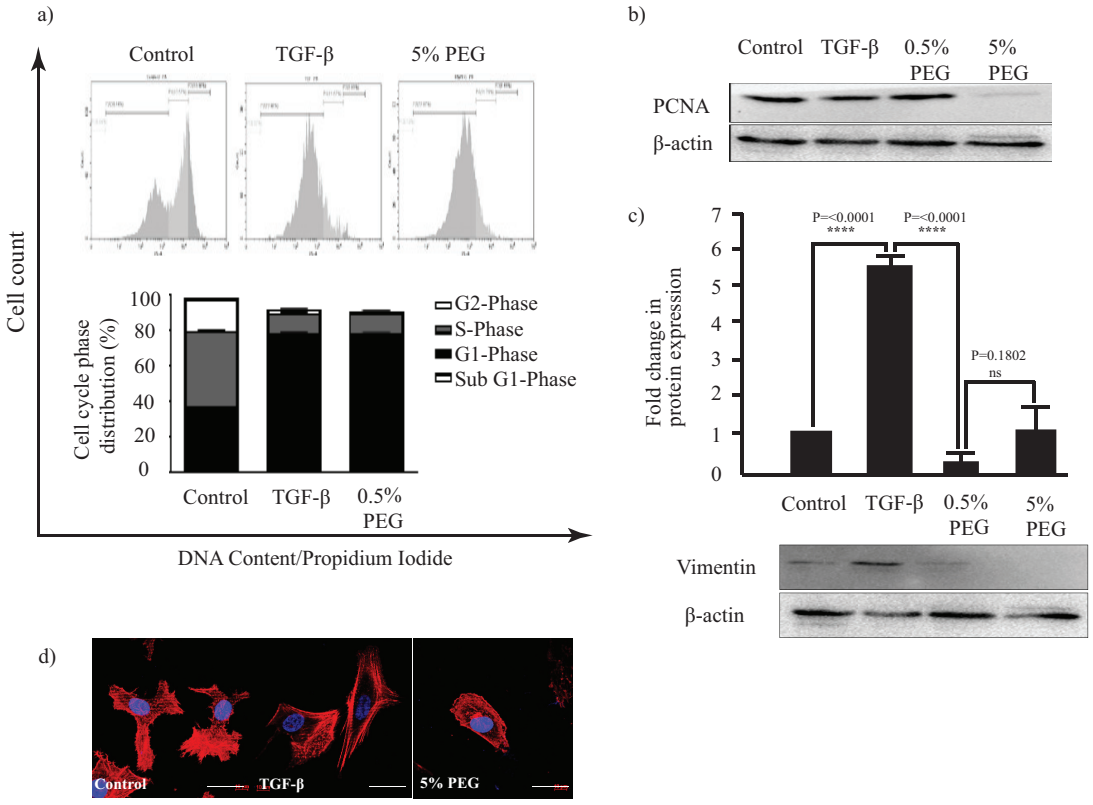


FIGURE 4.12: High intracellular viscosity inhibits migration and proliferation in cancer cells a) Cell cycle analysis with TGF-$\beta$ and 5% PEG treatment at 72 hrs with respect to untreated Huh-7 cells. b) Immunoblot representing a difference in PCNA after TGF-$\beta$ and 5% PEG treatment at 72 hrs with respect to untreated in Huh-7 cells. c) Immunoblot representing a difference in N-Cad and Vimentin after TGF-$\beta$ and 5% PEG treatment at 72 hrs with respect to untreated in Huh-7 cells. d) F-Actin stain with phalloidin with Confocal microscope for control, TGF-$\beta$, and 5% PEG.

are attributed to the various biomechanical constituents and changes within the cells and human error during the experiments.

## 4.6 Discussion

Cellular elasticity and viscosity are emerging indicators of disease state and its progression [237]–[239]. An alteration of intracellular viscosity has the potential to modulate cellular function and hence is often associated with various pathological conditions including cancer. In fact, cancer cells at each stage of progression are postulated to show differential viscosity [240]. Also, recent findings suggest that intracellular viscosity varies significantly between invasive and non-invasive cells like healthy breast cells exhibit higher viscosity than invasive carcinomas [241]. No wonder, the elastic response of tumor cells has been explored earlier as a diagnostic for cancer cells or its metastatic potential [217], [242]. Herein it is reported that viscosity can influence the intracellular

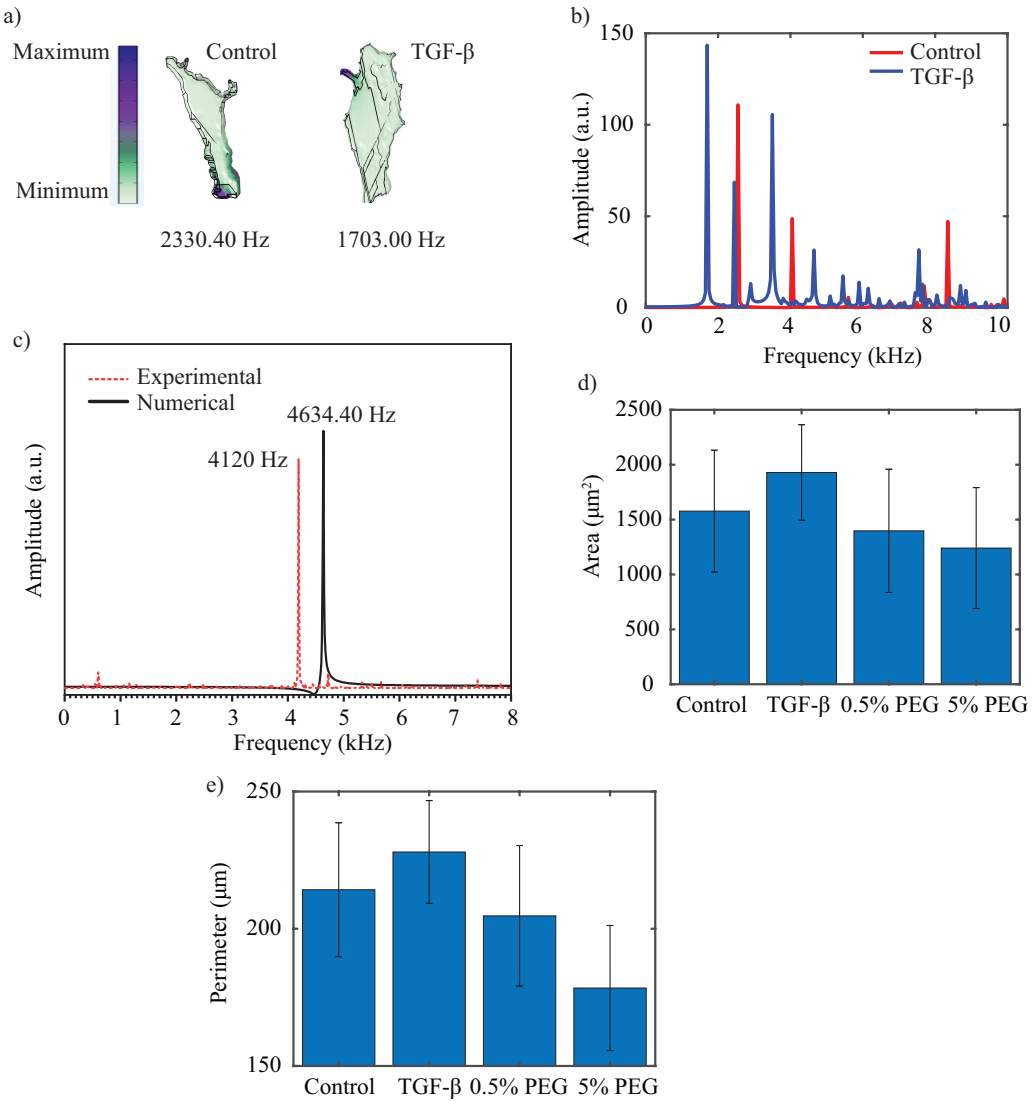


FIGURE 4.13: a) Mode shapes for control and TGF-$\beta$ with color bar representing maximum and minimum deformation. b) Comparison of frequency response for control and TGF-$\beta$ treated Huh-7. c) Frequency comparison for PSD and numerical estimated frequency for 5% PEG treated cell. d) Huh-7 cell area with TGF-$\beta$ , 0.5% PEG, 5% PEG after 72 h. e) Perimeter change with respect to control and different treatment in the cell. Error bars represent the standard error of the mean (N = 20 cells on each case). p-Values are determined from Student's t-test for unpaired samples f (**p $<$ 0.005; *p $<$ 0.05)

transmission of substances, bio-macromolecular exchange processes, and chemical transportation [243].

Previous studies predict that the changes in intracellular viscosity may influence not only the rate of intracellular chemical reactions but also the rate at which the catalytic protein adjusts its conformation to respond to its external environment [244]. Therefore, the control of malignant and non-malignant growth can essentially include changes in the chemical reaction rate caused by viscosity alterations [244], [245]. Other disorders and dysfunctions are linked to abnormal variations in cell viscosity [246]. As a result, it is important to develop an experimental setup

or tool that can measure the changes in the natural frequency of cells. Importantly, other mechanical properties such as viscosity can be derived from the frequency by considering the cells as micron-size droplets using the Lamb relation for a drop. Hence, in this study, we developed the experimental setup to evaluate the frequency-based viscosity under invasive and non-invasive conditions in cancer. This regimen is useful in estimating viscosity with minor alterations in intracellular viscosity. Although an array of techniques are available to measure viscosity for a fluid medium, like rotational viscometer, capillary viscometer, and falling ball viscometer yet they are unlikely to determine intracellular viscosity.

Many molecular rotor fluorescences and aggregation-induced emission (AIE) based techniques have also been designed to measure intrinsic and extrinsic viscosity, yet they might be rendered to shortcomings in the efficacy of detection under minute changes in viscosity levels and their lesser feasible complicated synthesis approaches. Therefore, it is essential to explore simplified approaches to detect viscosity. Keeping in view these limitations, we have designed and synthesized a remarkably high sensitivity fluorescence viscosity probe molecule TPSII to detect intracellular viscosity [216]. Apart from the molecular rotor approaches, we have designed and implemented a position-sensitive device (PSD) based technique to measure intracellular viscosity by dynamic measurements. Herein, displacement in the cells was observed using PSD and OPS after applying chirp signals of up to 3V and 1 MHz frequency range to a piezo disc attached to the cell culture plate having adhered cultured cells [247]. The rationale behind the PSD-based dynamic measurement was successfully employed to determine alterations in intracellular viscosity in cancer cells exposed to TGF-$\beta$. Since TGF-$\beta$ is a potent inducer of epithelial-to-mesenchymal transition (EMT) and is one of the major cytokines, which promotes metastasis of tumor cells, thus, it defers cancer cells to undergo spindle-like morphological alterations, which aids cellular motility and invasion [248].

TGF-$\beta$ induced EMT is often coupled with metabolic reprogramming to preserve energy resources to acquire aggressive explosion of tumor cells by proliferation, invasion, extravasation, and re-localization. In the course of conserving energy resources, TGF-$\beta$ suppresses the transcription of genes involved in multiple pathways. Overall, from our hypothesis, post TGF-$\beta$ exposure onset of EMT is associated with lesser viscosity in cancer cells, which might facilitate the movement of cancer cells.

Previous studies used AFM to suggest that there is a decrease in intracellular viscosity in cancer cells compared to normal tissue [249]. From our results, we observed that TGF-$\beta$ exposed cells exhibit the expression of specific mesenchymal markers like N-Cad and Vimentin indicating the transition of epithelial cells to mesenchymal-like cells. Additionally, our results show a left shift in green fluorescence of TPSII (fluorescent viscosity probe) post-TGF-$\beta$ exposure as compared with the untreated cells which again refers to lesser intracellular viscosity after TGF-$\beta$ administration. To validate our results, we observed TGF-$\beta$ mediated alterations in intracellular viscosity in time

(48 hrs, 72 hrs, and 96 hrs) and dose-dependent (2ng/ml, 5ng/ml and 10ng/ml) manner with PSD as well as through TPSI1 associated fluorescence.

Importantly, the behavior of the cells was unpredictable at the beginning of the time point study. The frequencies for various TGF-$\beta$ concentrations are lower compared to control during the 48 hrs of the time study and continue to decrease for the subsequent 72 hrs and 96 hrs when TGF-$\beta$ reached its saturation point (Figure 4.14) with acceptable variations during experiments. This variation is primarily from the fact that, during the experiments, intrinsic changes in the biological structure and biochemical responses can all potentially interfere with the mechanical properties that are being measured.

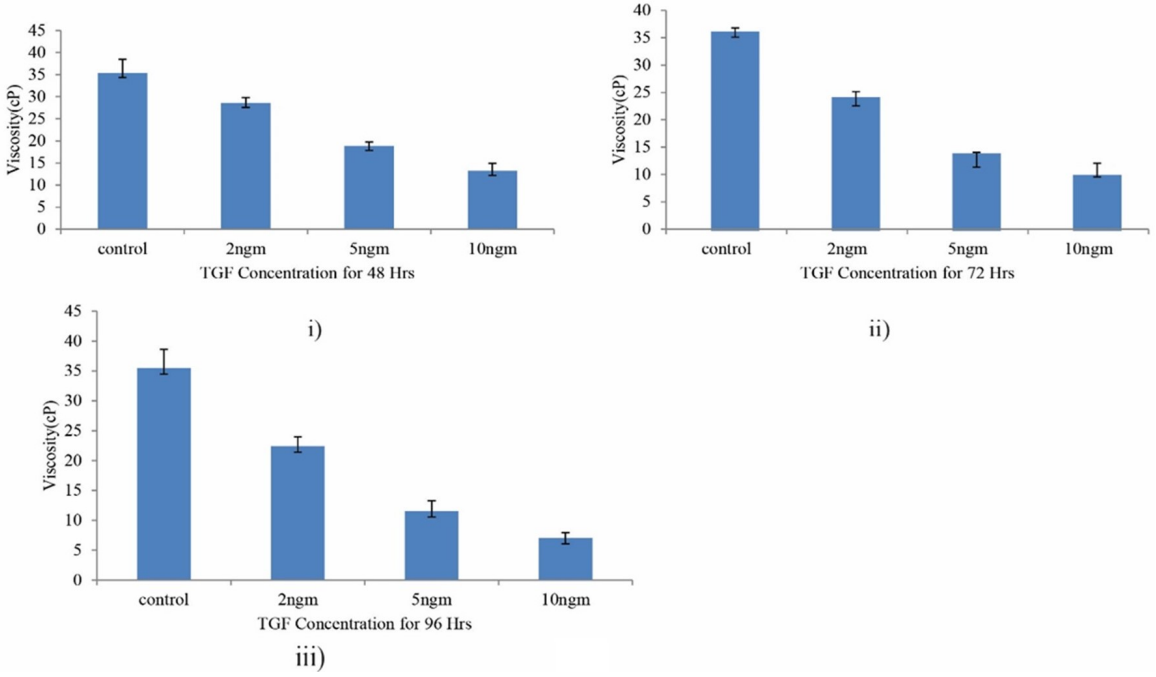


FIGURE 4.14: Viscosity of cells treated with different TGF-$\beta$ concentration for different time point i) after 48 hrs ii) after 72 hrs iii) after 96 hrs.

Furthermore, the microscopic cell and its mechanical behavior may vary at different times and locations because of its reorganization dynamics that are triggered by adhesion, migration, and polymerization–depolymerization processes [247], [250]–[252]. This alters the internal arrangement of the cytoskeleton and results, in a non-homogeneous distribution of stiffness and deformation [253], [254]. Hence, this leads to variation in the measured frequency. For the confirmation of the PSD results, we performed the numerical analysis procedure discussed in the previous section.

We found that the natural frequency of the cells induced with 5ng/ml of TGF-$\beta$ had the same experimental frequency with 6.23% acceptable margins of error as shown in Table 4.4. This would be suspected because of the changes in the intracellular morphology and geometric configuration of the cell structure. Figure 4.4a and Figure 4.12d , depicts the changes that occur in cells undergoing TGF-$\beta$ treatment. To observe the morphological changes, we carried out a cell

spreading analysis of the cells treated with different concentrations of the TGF-$\beta$ and PEG. We found that the cell spreading area and perimeter are higher for the case of TGF-$\beta$ compared to the control as shown in Figure 4.13d and e. This gave an indication of an increase in the migratory behavior of the cellular structure. This can be correlated to the rheological parameter termed viscosity. Although many aspects impact the stiffness of the cells such as the substrate on which the cells are dispersed, the cell size, elastic strength, mechanical perturbation as well as the position and time of cell excitation may also influence the rheological properties (viscosity) of the cells [255]–[259]. Previous research reveals that the total cell viscosity and rheological properties show strong dependency on frequency bands and measurement techniques [260], [261].

In this work, we follow the non-contact, non-invasive experimental approach. Further, frequency-dependent viscosity was evaluated to observe the changes in the migration of cells. It was observed that the viscosity of the cells with different drug concentrations was decreased with the increase in the TGF-$\beta$ concentration. Throughout each time point, with the increase of the drug concentration viscosity was decreased. Hence, TGF-$\beta$ exposure suppresses intracellular viscosity in cancer cells when compared to untreated cancer cells. It can be attributed to the changes that occur in the cellular structure and causes stress fibers and actin filaments reorganization. This promotes the alterations in the cytoskeletal network [262], [263]. Further, impacts the focal adherence complexes that contribute to the cellular changes and its migration [264]. Thus, this predicts that the intracellular viscosity is associated with the migratory capability of a cell.

Our findings show the viscosity in the range of 1-100 cP as stated in the previous studies for various cell lines. To have an insight into the difference in internal viscosity of cells with different invasion/metastatic potentials, we compared two cell lines MCF-7 and MDA-MB-231. The MDA-MB-231 cell lines are more invasive, metastatic, and deformable than MCF-7. Numerous studies predict that the lower deformable MCF-7 possesses higher elastic strength and natural frequency compared to MDA-MB-231 [265]. Hence, our results show a higher frequency for MCF-7 when compared to MDA-MB-231 and thus, MDA-MB-231 has a lower internal viscosity than MCF-7.

## 4.7 Conclusion

In this work, we presented the non-invasive technique to determine the frequency of cancer cells. Natural frequency was estimated for the cells with various viscosity modulators. Both experimental techniques and numerical analyses yielded the same frequency response for the cells with an acceptable range of error. This frequency-based cell analysis helps in characterizing the cell on its dynamic behavior. Our findings show that the EMT inducing in the cancer cells using TGF-$\beta$ corresponds to the lower frequency. Lower frequency leads to lower intracellular viscosity within the cancer cells. This causes more mortality and the spreading of cancer and affects other

organs. Earlier diagnosis of change in the frequency response of the cells suggests starting the appropriate selection of therapeutic treatment of cancer. The proposed technique is a key model of this work. Using this technique, healthy and diseased cells can be distinguished based on their frequencies. The same can be followed for selecting the frequency-based treatment of cancer in the earlier stage.

# Chapter 5

# Modulating the Mechanical Resonance of Huh-7 Cells Based on Elasticity of Adhesion Proteins

## 5.1 Background

Mechanical resonance of biological cells refers to their ability to vibrate in response to certain mechanical stimuli. This phenomenon has been studied to understand the role of adhesion proteins in the dynamic behavior of cells. Adhesion proteins are molecules that help cells interconnect with each other and to the extracellular matrix (ECM)(the network of proteins and carbohydrates) that surrounds and supports cells. These proteins are important for the study of cells from a mechanical perspective, as they act as a scaffold that gives cells structural support and allows them to maintain their shape and respond to mechanical forces.

Studying the mechanical resonance of Huh-7 cells can provide insight into how adhesion proteins contribute to the mechanical properties of cells and how these properties may be altered in cancer cells. This can be useful in understanding the behavior of cancer cells and developing new treatments for cancer. However, it is important to note that this research is still in the early stages and further studies are needed to fully understand the mechanical resonance of Huh-7 cells and its implications in cancer.

### 5.1.1 Crosstalk between the cell and extracellular environment

Living cells utilize specialized receptor-mediated contact foci to establish stable attachments to the extracellular matrix (ECM) in order to perform functions such as proliferation, differentiation,

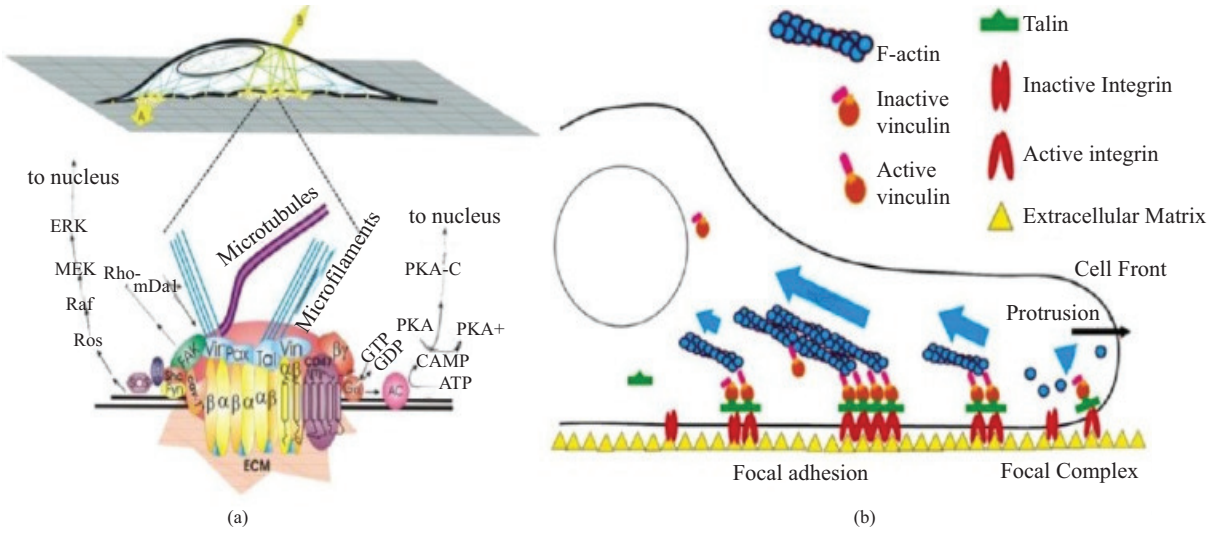


FIGURE 5.1: Schematic for focal adhesions. (a) Focal adhesions consist of multiple proteins (integrins, vinculin, paxillin, talins, and so on.) and serve as signaling hubs producing biochemical signals (b) Actomyosin contractile forces are essential for the stabilization of FAs. Adapted from Humphries et.al. [266].

and locomotion. Focal adhesions (FAs) are among the best-known adhesion structures and are composed of a diverse population of structural and signaling proteins, as depicted in Figure Figure 5.1.

Additionally, FAs display directional growth that is parallel to an externally applied load. Studies have also shown that cells form larger FAs on stiffer substrates, as well as exhibit higher intracellular traction forces. There has been a significant effort, both experimental and theoretical, to investigate the cell-ECM interactions. A typical FA is composed of several parts, including a layer of transmembrane receptors known as integrin, which connect the ECM to the adhesion plaque composed of vinculin and other plaque proteins. The FA is typically connected to the cell nucleus or another FA by an actin stress fiber, which generates contractile force and is responsive to the mechanical properties of the microenvironment. A schematic representation of the full structure is illustrated in Figure 5.2.

## 5.2 Introduction

Biological cells are fundamental units for life. Cells store and replicate their DNA, showing significant functions in various biological activities. Normal physiological activities of the cells depends on biochemical/transport pathways and their mechanical behavior [268]. Biological systems would not exist or operate without cells, such as Vertebrates transport oxygen to body tissue through the circulation of red blood cells. Fibroblasts, as contractile machinery, migrate to wounds and initiate the healing process [269]. Endothelial cells lines in the blood arteries and function as filtration barriers [270]. The cytoskeleton is the linked network responsible for giving

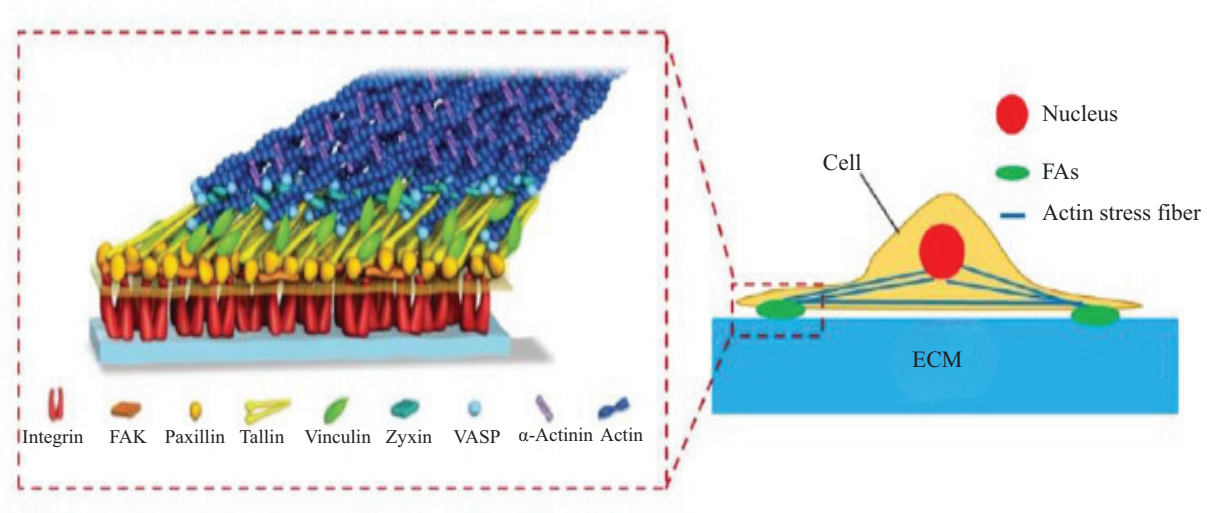


FIGURE 5.2: The illustration of the structure of focal adhesions, which are located at the outer edges of cells and connected to the nucleus or other focal adhesions via actin stress fibers. The enlarged image on the left displays the intricate multi-layer protein complexes that make up focal adhesions [267].

cellular rigidity [271]. This cytoskeleton consists major of three polymerized filaments, each with its unique structure and mechanical properties: actin, intermediate filaments, and microtubules [272], [273]. This intricated framework enables cells to alter their mechanical characteristics to their surroundings instantly and, over time [274], [275]. Similarly, Focal Adhesion (FA's) has crucial roles in several cellular functions, including proliferation, differentiation, and motility, as well as pathological processes, such as cancer and wound repair [255], [276]–[279]. These are massive macro molecular complexes via which cells respond to the mechanical force and regulate mechanosensitive information [280]. Any alteration in the mechanical characteristics of the FA's may change the mechanical behavior of the cells, and their function [23]. Hence, it is important to understand the cell and FA's interactive mechanical model that explain the impact of changes in its properties on the cells.

Although multiple techniques, such as micropipette aspiration [1], optical tweezers [281], and acoustic force microscopy [282], demonstrated that single cells of distinct tumor types were almost twice as soft as similar cells of normal tissue [283], [284]. These disparities in elasticity between normal and tumor cells are caused by variations in the size of the actin cortex connected to the cellular membrane [285], the cytoskeleton (mostly owing to varying numbers of intermediate filament proteins), and the nuclear lamin network [1]. The intermediate filament network may collapse around the nucleus, or cell spreading may accelerate (closely linked to the actin cytoskeleton) through focal adhesions [286]. It is often seen that the cytoskeleton of cancer cells behaves differently from that of healthy cells. Cancer cells are known to display large differences in stiffness compared to normal cells. Several studies suggest that abnormal mechanical characteristics of diseased cells promote the development of pathology. In recent years, it has been shown that low-frequency ultrasound, magneto-mechanical force, and mechanical vibration

induce biological changes in cancer cells [287]–[291] despite different sensitivity in normal cells. Frequency-based techniques such as radiotherapy and chemotherapy can kill normal tissue cells and are often accompanied by severe side effects.

In this context, the variations in subcellular structure between cancer cells and normal cells may be exploited to induce a selective approach to cytotoxicity [1]. These structural variations influence the elasticity of entire cells, or subcellular structures that can be represented by the material properties of the cells [268]. Thus, there is a need for therapy approaches that target tumor cells more precisely. Hence it is important to evaluate the frequency and material properties of the cells. Previous atomic force microscopy (AFM) experiment predicts that both cells and cytoskeletal networks are extremely viscoelastic [292], [293]. It was reported that the response of a composite network composed of actin and intermediate filaments is the most important load-bearing constituent of the intracellular cytoskeleton [294]. Microtubules are essential for retaining the shape, and structural features of the intermediate filament network [295], and the cortical actin underlying the lipid bilayer is anticipated to provide further stiffness to the cell's resistance to deformation [296].
Several numerical AFM-based studies have examined the effects of indentor geometry, cell morphology, and their influence on a model cell with a wide range of shapes, including an elliptical surface, an axisymmetric model, and a double symmetrical model [297], [298]. These shows the parameter that was determined by fitting the experimental force-indentation curve of the cell to predict the cell model properties [299], [300]. Studies revealed that the homogeneous distribution of intracellular components that provide cellular stiffness might be unrealistic, and anticipated that the cell shape influence the mechanical characteristics [271]. An elliptical cell has a stiffer nucleus than a cytoplasm, whereas the reverse is valid for a more realistic structure. This is consistent with experimental findings (and those of prior AFM research [301]) of a stiffer peripheral area that could be partially attributable to the morphology of cells. Similar results are observed for compression of endothelial cells ( geometrically round and sphere-shaped models before the force initiation) between microplates were found in a study of the mechanical properties of the cell nucleus ([233], [302]. However, observations on the fibroblast cells, where the average thickness was greater, show the influence on the cell behavior and concluded that a stiffer cytoplasm is primarily a result of cellular shape [303]. Further, the previous findings show that both the material response and the cell's shape contribute to the measured stiffness at large indentations [304]. Consequently, it is important to use the actual shape and geometries to obtain the actual dynamic response of the cells.

In this work, we carried out the dynamic measurement of the Huh-7 cells using a non-invasive technique and its results were compared with numerical AFM. The modal and frequency response of cells was evaluated by considering the different ranges of the focal adhesion stiffness. Focal adhesions (FAs) are macromolecular complexes that transmit mechanical force and regulatory information between extracellular matrix (ECM) and cells. Hence, it is essential to comprehend

the effect of its alterations on cell behavior. This study is significant in predicting the resonance behavior of the cells for targeting the different diseased cells. This research shows some intriguing potential in the realm of biomechanical modeling. In general, hyperelastic material models may be used to simulate cells and other biological materials. This approach could be used to obtain the hyper-elastic-viscoelastic behavior as well as resonance characteristics and compute the transient development of stresses within the cell structure.

The cells used in our experimentation were provided by our collaborating laboratory (Prof. Rajdeep Chowdhury and Prof. Sudeshna Mukherjee Lab.). This section on cell culture was performed by Mr. Nizam Ahmed and included in this thesis solely for the purpose of completeness. As the author of the thesis, I did not carry out the cell culture part of this work.

## 5.3 Materials and Method

### 5.3.1 Cell culture

Huh-7 cells (human hepatocellular carcinoma) were procured from National Centre for Cell Science, Pune, India. Cells were cultured at 5% $CO_2$ 37 °C in Dulbecco's Modified Minimal Essential Medium (DMEM; Gibco, # 12800-017) which was supplemented with 10% fetal bovine serum (FBS; Invitrogen, # 26140-079) and antibiotics (1% penicillin–streptomycin solution; Invitrogen, # 10378-016). Huh-7 cells were grown up to 70% confluency in 10% FBS containing DMEM and rinsed with phosphate-buffered saline (PBS). Thereafter, the complete medium was replaced with serum-starved medium (DMEM containing 2% FBS) and incubated for 12 h prior to TGF-$\beta$ (# 100-35B-10, Peprotech) treatment [213].

### 5.3.2 Mechanical Behavior of Filaments and Cells

As previously discussed, the structural integrity of cells is dependent on the cytoskeleton, a major component of the cytoplasm consisting of actin filaments (F-actin), microtubules (MT), and intermediate filaments (IFs) [305]. The mechanical properties of cytoplasm regulate the ability of cells to withstand deformation, transport biological activities, and alter shape during external stimuli. Both the filaments and the polymeric network as a whole are extremely nonlinear rather elastic systems [306]. It is a dynamic entity capable of remodeling itself owing to its viscoelastic behavior. Previous research has suggested the behavior of the cytoskeleton under various environmental conditions [307]. It was observed that the cytoskeleton's network behaves as a solid and liquid at different time scales. This is due to alterations in the dynamic and thermal properties of semiflexible filaments. This fluctuation depends on the external stimuli and temperature, which influence the mechanical behavior as well as the presence of several

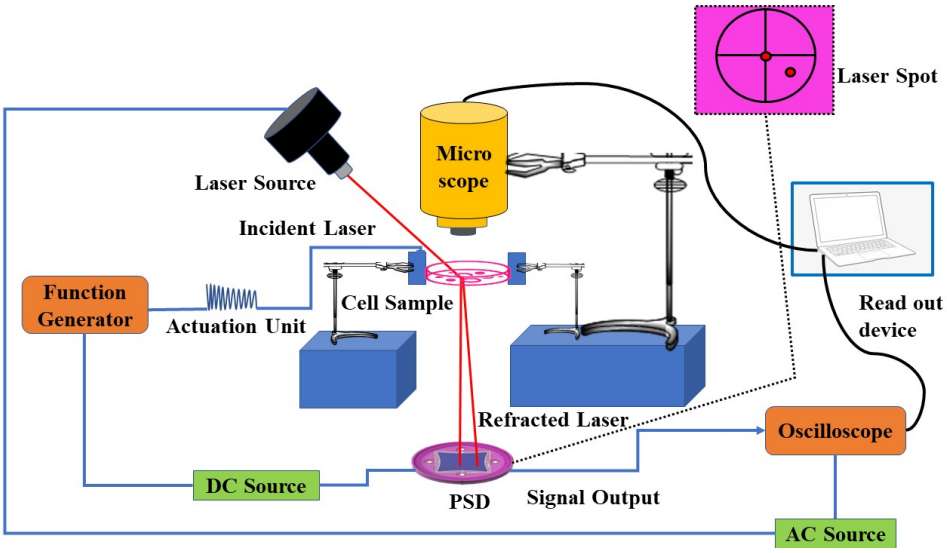


FIGURE 5.3: Detailed experimental setup for the measurement of cell dynamics.

adhering and interacting proteins. Modeling the mechanical model of an underlying polymer network, in conjunction with other cellular components (e.g., the cell nucleus and membrane), and their analysis is difficult to anticipate. Despite this challenge, it is possible to obtain results by analyzing the cell at a microscopic size using numerical modeling. Although various research considered the various constituents of the cell for the analysis. In this work, the cytoplasm and nucleus were considered as the part of model geometry. This study observed the viscoelastic behavior of the cell structure by incorporating viscoelastic components into the computational analysis.

### 5.3.3 Experimental frequency response of a cell

Figure 5.3 shows the detailed working principle of the experimental setup. A laser source RLM650TA-020R was used with a maximum of 23mW and 650nm wavelength powered by an external AC Voltage source of 240V and 50 Hz. The cell was taken out from the $CO_2$ incubator and was placed over the cross slide, and input is applied on the slide for the actuation of the cells. A microactuator (Piezoelectric transducer) was used and driven by the function generator (Tektronix AFG 1022) to actuate the cells. A harmonic signal was applied to the actuator through the function generator to vibrate the cells. The position of the cancer cell in the wells was determined using an optical microscope. Laser from the source is focused and impinged on the cell's surface and gets refracted to the Position Sensitive Device (PSD) as shown in Figure 5.3. PSD was used as an optical position sensor (OPS) that can sense the incident laser position on a two-dimensional sensor surface. The cell movement with respect to applied actuation was traced, and the output voltage corresponding to cell displacement in the X and Y directions was measured by the Oscilloscope (Tektronix MSO 46). The cell and support responses were

measured sequentially. The frequency response of the cells was obtained using the Fast Fourier transform (FFT) of the time domain signal acquired from the oscilloscope. The transfer function was used to take away the support-based frequency response to predict the cell's natural frequency. The obtained peaks in the transfer function corresponding to the natural frequency of the cells. Each measurement on the cells and support was repeated for a particular sample, and the mean frequencies for each sample were considered for the analysis.

### 5.3.4 Microscopic Imaging

Cells were imaged in a phase contrast microscope (Carl Zeiss inverted light microscope). The size of the cells was quantified from the images obtained after the trypsinization and resuspended of the cells in 1ml culture media using ImageJ. Furthermore, the area of each cell was determined and the mean area was calculated [308].

### 5.3.5 Computational Model of a Cell

A model of a cell with typical dimensions is shown in Figure 5.4a. Numerical analysis was performed on the traced geometry extracted from microscopy images of Huh-7 cells. The geometry of the Huh-7 cells was obtained by tracing the trypsinized and resuspended cells for numerical analysis. Spherical conformation was used for the 3D cell model obtained from the traced image (cell membrane) for the numerical analysis. The nucleus was assumed as spherical in shape. Several previous studies considered and predicted that the cells after suspension, possess a spherical shape [261], [309]. Cell geometries are then imported into the COMSOL Multiphysics for analysis. The cellular domain was created around the centreline. The semi-circular section is considered as the cell nucleus, which influences the mechanical response. Cytoplasm (traced geometry), nucleus, and an indenter were modeled in the geometry modular for analysis. The cell selection for the modeling was based on the mean area of the cells.

Numerical AFM was used for the evaluation of the material parameters. Earlier, it was observed that the softer model with the lower Young's modulus of cell cytoplasm and nucleus lowered the resonance frequencies of the cells. The material properties of the nucleus and cytoplasm clearly influenced the natural frequencies of cells. Additionally, the size of the cell had a substantial effect on the amount of the natural frequency. A linear elastic model is too simplistic since cells can endure huge loads and show substantial strain hardening. In this study, a primary hyperelastic material for the cytoplasmic response was considered for the analysis. The neo-Hookean model was used, in which stresses and strains are computed from a strain energy density function $\psi$ as shown in Equation 5.1.

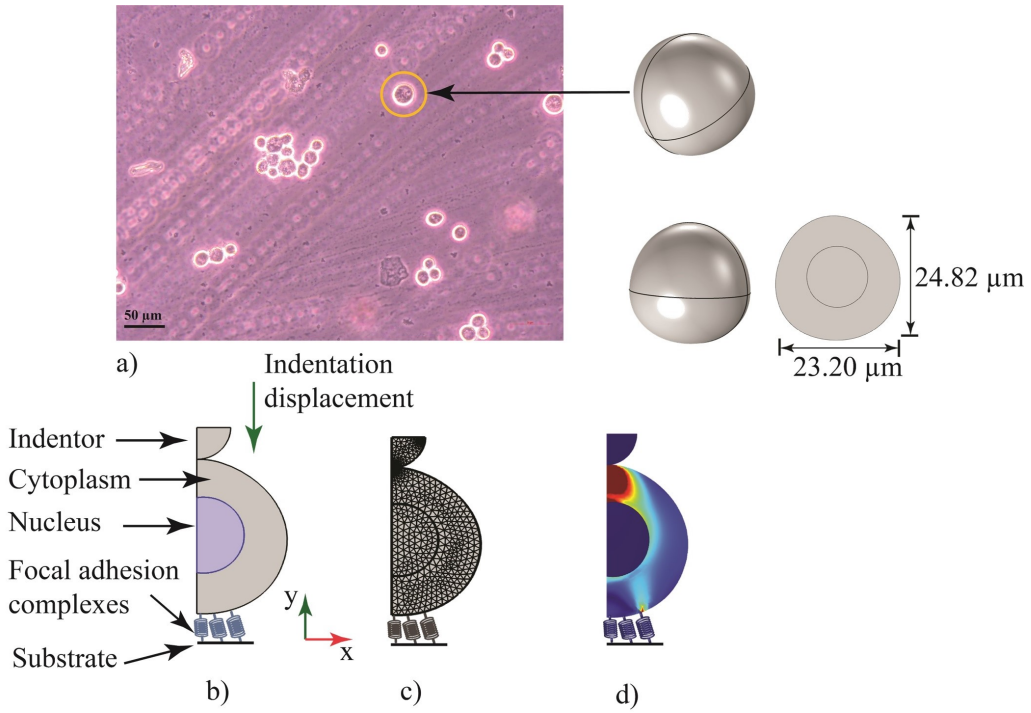


FIGURE 5.4: a) Microscope image of the Huh-7. Cell model obtained from the image traced from the averaged diameter cell. b) AFM modeling showing boundary conditions with different constituents of the cell c) Meshed model d) Stress distribution in the cell structure.

TABLE 5.1: Mechanical properties of the different domain of the cell for the force indentation analysis [233], [271], [310].

| Domain | **Shear Modulus** | **Bulk Modulus** | **Energy Factor 1** | **Relaxation time 1** | **Energy Factor 2** | **Relaxation time 2** |
|---|---|---|---|---|---|---|
| Nucleus | 1.67 kPa | 5000 kPa | N/A | N/A | N/A | N/A |
| Cytoplasm | 0.15 kPa | 1000 kPa | 10 | 0.5 s | 10 | 100 s |

$$\psi = \mu/2(I_1 - 3) + k/2(J_e l - 1)^2 \tag{5.1}$$

Here the material is assumed (nearly) to an incompressible, where the $\mu$ is the shear modulus, $J_e l$ is the elastic volume ratio, $k$ is the bulk modulus, and isochoric first invariant $I_1$ is included in the function. To incorporate the viscoelastic behavior, two generalized Maxwell branches are also included. The nucleus is modeled without viscoelastic branches assuming that it is primarily elastic. The selected material parameters are listed in Table 5.1

Figure 5.4b shows the substantial applied boundary conditions on the cell models. The vertical constraint was applied to the cell's base. The cell adheres to the substrate via focal adhesions and is provided in the modeling by considering it as an elastic foundation. This should be an important impact aspect that does substantially affect the force response of the cells. In this study, a comparison between the adhesion behavior of cells with and without focal adhesions was

made to illustrate the changes in their dynamics. A penalty formulation using the indenter as the source boundary enforces contact between the indenter and the cell. The indenter domain was specified to move at a rate of 0.6 $\mu$m/s until the total vertical displacement reached 4.6 $\mu$m. After that, it is then kept constant up to 100 s [311]. The model is meshed with 2D elements and refined under the indenter as shown in Figure 5.4c. A parametric study was opted to study the impact of stiffness of the focal adhesion. Further, post-processing was followed to observe the cellular response.

#### 5.3.5.1 Modal analysis

A modal analysis was conducted using the reference values for Young's modulus of cytoplasm and nucleus acquired from the numerical AFM. The modal analysis was used to determine the natural frequencies and eigenforms of Huh-7 cells modeled as a real geometry obtained from the microscope images. Modeled cells illustrate the morphology of deformed cells. As discussed in the previous section, the cell size, Young's modulus of the cytoplasm and nucleus, and embedding circumstances have an impact on the natural frequencies. Modal analysis was used to analyze the oscillation behavior of the structure in the absence of external stimulation. The determined mode shapes and natural frequencies provide information regarding the frequency in which the structure oscillates freely based on its mass and stiffness as well as under specified boundary conditions.

#### 5.3.5.2 Harmonic analysis

Harmonic vibration analysis was carried out on single-cell models subjected to external harmonic forces. The measurement of resonance frequencies and related amplitudes was used to predict the cell dynamics. The cellular system was considered as the mass spring damper system as reported in the previous studies [261], [312]. The such cellular system as excited by external force can be represented by the general governing equation of motion as shown in Equation 5.2 where $[M]$ represents the mass matrix, $[C]$ is a damping matrix, $[K]$ is the stiffness matrix and $F$ is the force vector.

$$[M][\ddot{u}] + [C][\dot{u}] + [K][u] = F \tag{5.2}$$

The displacement $u(x, y, z)$ can be represented as a function of $n$ eigenvectors $\phi_i(x, y)$ and the time-dependent modal coordinate $q_i(t)$ [313].

$$u(x, y, t) = \sum_{i=1}^{n} \phi_i(x, y) q_i(t) \tag{5.3}$$

Using equilibrium equations and orthogonal properties of eigenvectors, the natural frequency of an $i^{th}$ mode can be written as

$$\omega_i^2 = \frac{M_i}{K_i} \tag{5.4}$$

where $M_i$ and $K_i$ are the mass and stiffness of the structure in $i^{\text{th}}$ mode corresponding to eigenvector $\phi_i$ and resonant frequency $\omega_i$.

The described modal analysis was performed in COMSOL Multiphysics using an eigenfrequency study to determine the natural frequency. This study provides a set of eigenvalues and eigenvectors that represent the natural frequency of a vibration mode and the corresponding mode shapes, respectively.
In this work, we propose a non-invasive and non-contact experimental technique for the frequency response of the cells and later compare it with the numerical simulations. A finite element model was modeled in the COMSOL Multiphysics and considered as a continuum model, while the heterogeneous intracellular structure was not considered for the computation. This approximates to quantify the macroscopic cell response to external stimuli. This study describes a relaxation test as the computational model and used to validate the material properties. A rigid indenter was used for compression into the soft, viscoelastic cell, and the subsequent relaxation of the indentation force was evaluated and compared with previous experimental data. This comparison helps in validating the assumed material properties for the modeling. The numerical model was further used to evaluate the modal behavior and frequency response of the Huh-7 cells at different stiffness of the focal adhesion complexes.

## 5.4 Results

### 5.4.1 Frequency response using non-invasive experimental technique

The maximal dynamic behavior of the cells was measured using a non-invasive position-sensing technique. The oscillating cells are subjected to a transitory movement in the transverse direction with respect to the excitation direction. Fast Fourier Transform was used to convert acquired time domain data to frequency domain (FFT) from the spectrum analyzer. The frequency response of the oscillating cells and the base is shown in Figure 5.5a. Figure 5.5b depicts the derived transfer function of the cell in relation to the base to exclude any base-related modes. The plots depict the significant peaks of the transfer function of cell response. These peaks reflect the natural frequency by removing the effect of support and other noise impacting the supports. The natural frequency of the cells was predicted by the maximum amplitude peak in the frequency spectrum. The plot indicates that the natural frequency of the cells is 26.4 kHz. The subsequent higher peak corresponds to higher modal frequencies of the cells.

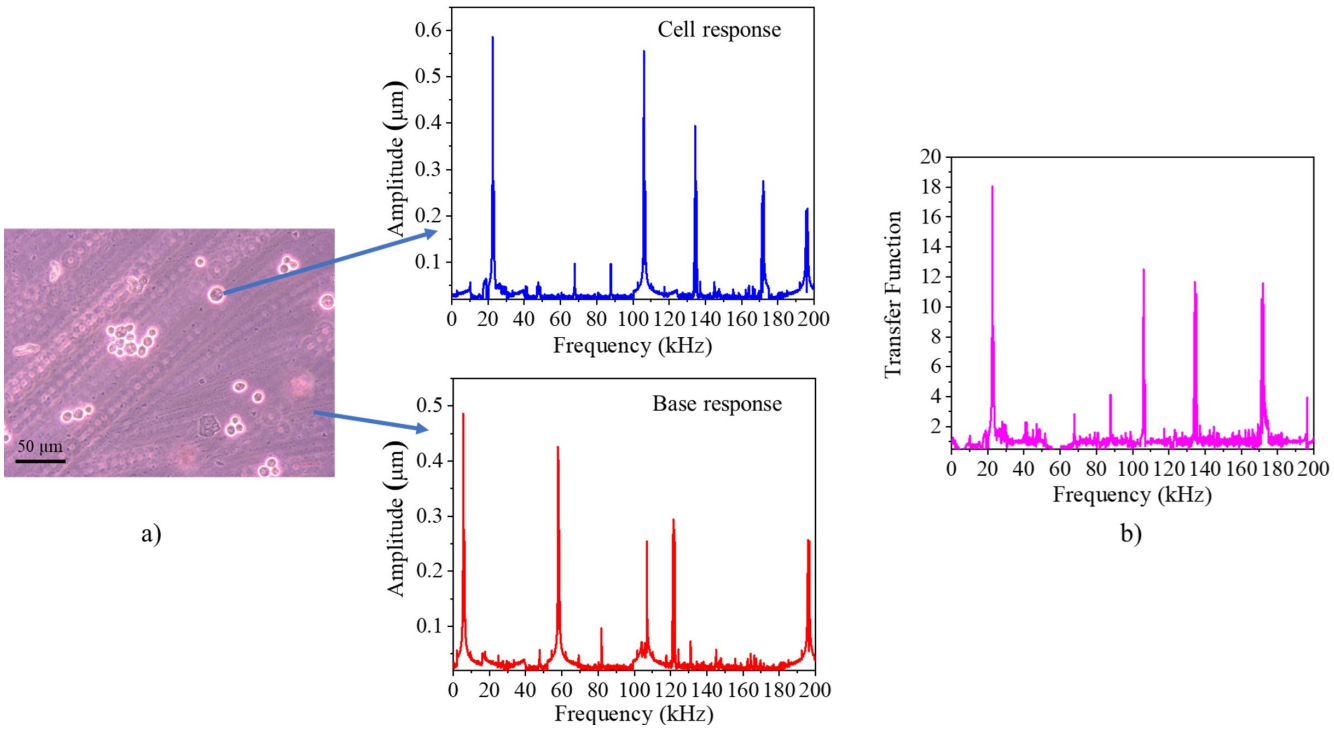


FIGURE 5.5: a) Experimental frequency response for cell and base for the measurement of cell dynamics. b) Transfer function

### 5.4.2 Numerical Force indentation on Huh-7 cell

#### 5.4.2.1 Validation test

Validation of the cell material properties considered for the numerical modeling was performed using a finite element method (FEM) study reproducing the AFM measurements described in the literature (Li et al, 2008, Lekka et al. 1999). The vertical reaction force on the indenter was extracted from COMSOL Multiphysics. In this context, the reaction force-deformation response for the cell was obtained and compared with the reference plots determined experimentally during the AFM test for different cancerous cell lines [314], [315]. The elasticity and other viscoelastic parameters for cytoplasm and nucleus were validated based on the possibility of a good fit between the numerical simulations and the previous experimental AFM data curve for different cancer lines, as depicted in Figure 5.6. Mechanical properties of the cell are shown in Table 5.1 for Huh-7 cells.

The indentation test was carried out on the Huh-7 cell to validate the material parameter. The indentation simulations were performed on Huh-7 with an identifiable nucleus and peripheral region. An example of such a control cell is shown in Figure 5.3, with points of indentation indicated. We also observed the relaxation behavior of the cells during the simulations. The force-relaxation curve shows (Figure 5.7) the subsequently measured relaxation force after the cell indentation was reached by setting a delay time of 100 s between the point of the strain and

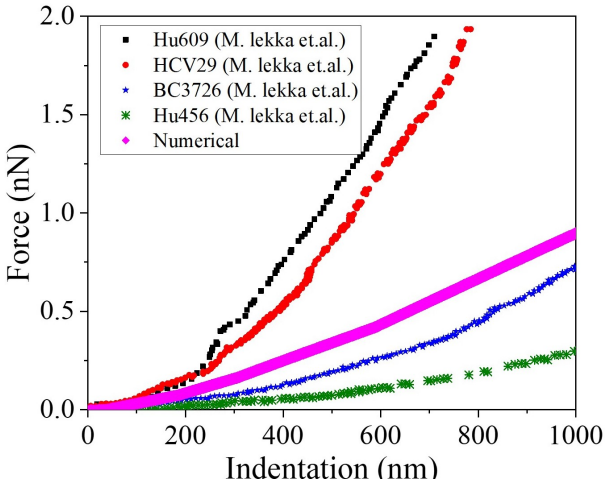


FIGURE 5.6: Force-Depth of indentation response of the cellular structure for the validation of the material properties.[315]

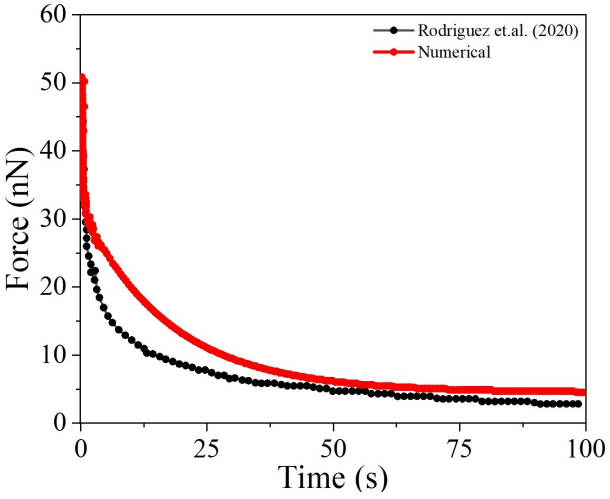


FIGURE 5.7: Force relaxation response of the cellular structure during indentation test.

the retraction of the tip to illustrate the mechanical behavior. The force produced by the cell on the indentor probe diminished quickly, then slowly over longer durations. It should be noted that this finding is consistent with previous studies on the relaxation behavior of HT-29 cancer cells [311] and exhibits similar trends as those observed for various types of cells, including cancer cells, fibroblast cells, and chondrocytes cells, when subjected to AFM under different boundary conditions. [309], [316]. The obtained relaxation behavior of the cells indicates that the cell's outer portion is stiffer than the region above the nucleus. The dense polymerized network at the cell's periphery and stress fibers connected to focal adhesions may influence relaxation response [275], [301], [317], [318]. Sato et al. reported comparable findings with a harder periphery of the cell while doing AFM indentation on endothelial cells [301].

The local displacement in the cell after indentation is shown in Figure 5.8a. It has been observed that the deformation in the cellular structure increases as the indentor progress in depth. The equivalent von Mises stresses at times 0 sec, 15 sec and 30 sec are shown in Figure 5.8b. Naturally,

stress decreases due to stress relaxation because of the inclusion of viscoelastic branches for the cytoplasmic material model. These deformation and stresses contour are shown similar responses compared to the previous work. Hence, the numerical findings are in good agreement with the previous experimental results. Thus, this indicates the appropriate assumption of the material model for further numerical analysis to obtain the mode shape and frequency response of the Huh-7 cells at different stiffness of the focal adhesion complexes.

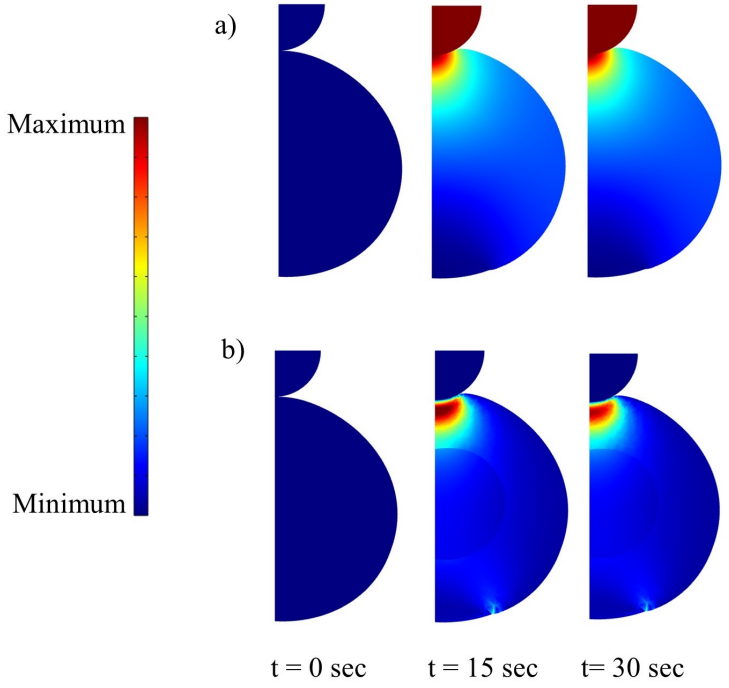


FIGURE 5.8: a) Displacement in the cellular structure and indentor during the AFM at different time b) Stress distribution in the cellular structure during indentation at different time.

### 5.4.3 Modal analysis

Modal analysis was used to study the cell structure's oscillation without external stimulus. The computed mode shapes and natural frequencies reveal the cell structural shape and frequency at which the structure oscillates freely with respect to its mass, stiffness, and boundary conditions. Figure 5.9 depicts the mode shape and associated frequency of the cell structure considering the material parameters stated in the preceding section and assuming various elastic spring foundations that describe the focal adhesion behavior between the cell surface and the substrate. It has been observed that the increase in the stiffness of the focal adhesion increases the natural frequency of the cellular structure. We obtained the natural frequency at 3.67 kHz with the focal adhesion stiffness of 5 pN/nm and it increases 6.5 % times with stiffness at 500 pN/nm. This is attributed to the strengthening of the stress fibres, which eventually leads to the stiffening of the cell structure. Correspondingly, it has been shown that the higher modal frequency increases

when focal adhesion stiffness increases. The obtained natural frequency of the cell was 24.450 kHz with an elastic stiffness of 450 pN/nm.

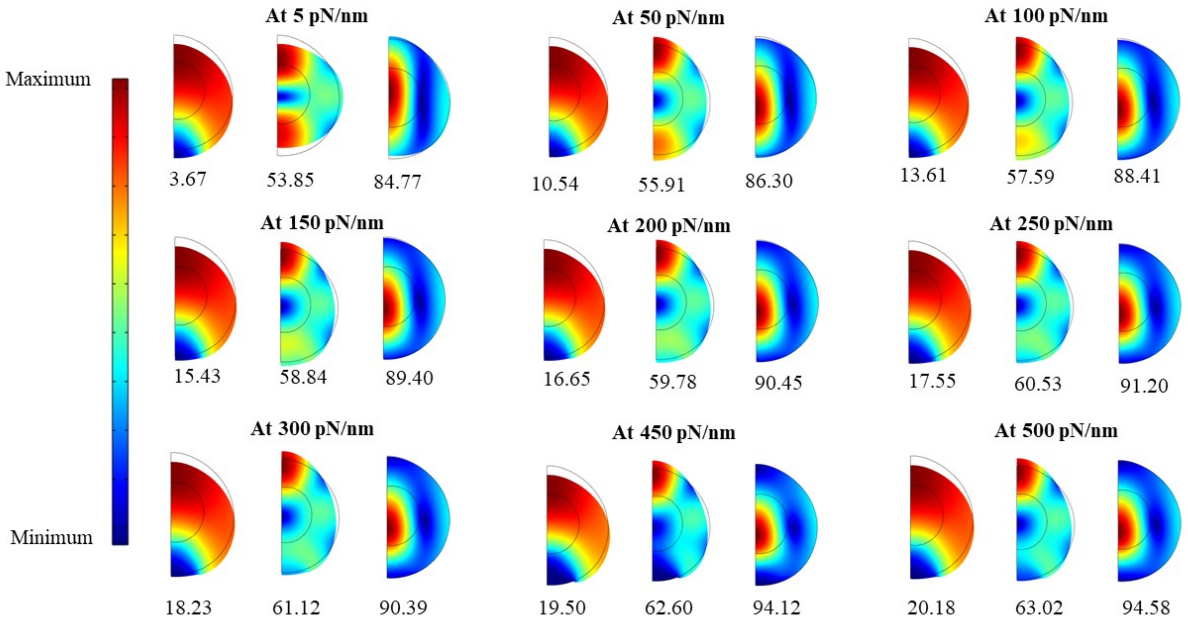


FIGURE 5.9: Consecutive three mode shapes with frequencies of Huh-7 cell at different elastic stiffness. The color bar represents displacement in the cell structure. All modal frequencies are in kHz.

### 5.4.4 Harmonic analysis

A harmonic analysis was carried out to determine an amplitude-frequency response that provides resonance frequencies and the related amplitudes of the Huh-7 cells. The range of excitation frequency was applied from the natural frequency to 1 MHz for examining the dynamics of cell models extracted from the mean diameters of cells representing the Huh-7 cell. Dimension of cells had a significant impact on the amplitude-frequency response. For Huh-7 cells, a typical amplitude frequency response is shown in Figure 5.10(a). Significant amplitude peaks were observed in the frequency response at different frequencies after the actuation. Huh-7 cells show natural frequencies in the range of 3.67 kHz to 36.6 kHz on varying the stiffness of the focal adhesion complex from 5 pN/nm to 500 pN/nm. Previous studies predicted the Huh-7 cell line frequency in the above-stated range [261], [265]. Furthermore, we observe the frequency shift for higher modes. The Inset figure depicts the natural frequency for different stiffness of the focal adhesions. Figure 5.10(b) shows the shift in the associated frequencies at different elastic stiffness for three consecutive modes. It has been observed that there has been an increase in the frequency with the increase in the elastic stiffness. This is attributed to the combined role of the viscoelastic and adhesive cues that regulate the cell mechanobiology [319]. Specifically,

TABLE 5.2: Comparison of evaluated frequency for different mode shapes.

| **Technique** | $f_1$ **(kHz)** | $f_2$ **(kHz)** | $f_3$ **(kHz)** | $n$ |
|---|---|---|---|---|
| Experimental | 26.40±0.23 | 105.97±0.18 | 134.29±0.20 | 50 |
| Numerical | 24.62 | 101.723 | 134.29 | - |

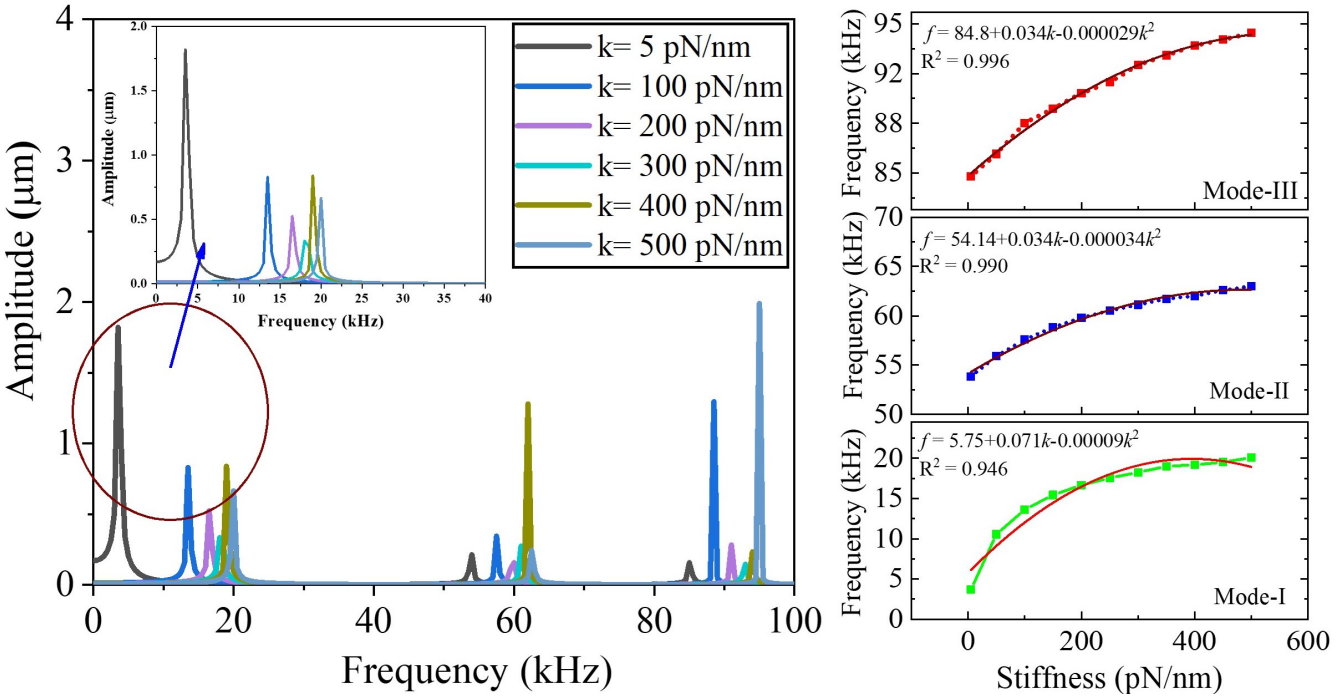


FIGURE 5.10: (a) Numerical frequency response of the cell structure at different elastic stiffness. Inset showing the fundamental mode frequency for different elastic stiffness at adhesion. (b) Variation in modal frequencies with respect to different elastic stiffness.

the maximum resonance amplitude of Huh-7 cells indicates the maximal stress on the integrity of the cells. Considering the stiffness of Huh-7 cell lines to be 450 pN/nm, experimental and numerically determined frequencies are in consonance as shown in Table 5.2; however, there was a small percentage of error in the resonance frequencies.

## 5.5 Discussion

The force depth of the indentation curve and observed relaxation behavior during the simulations validate the material properties. Intriguingly, the force response of the identified Huh-7 cells has a minor variance, likely owing to a heterogeneous structure with a denser meshwork of branching actin networks. Furthermore, the variation in the numerical and experimental response attributed to the assertion of the peripheral region that being rather thin [233]. However, in previous observations on fibroblast cells, the thickness dimension is generally much greater, 3–4 $\mu$m, as moves away from the nucleus. We performed our measurements in the region thickness of

approximately 3.8 $\mu$m, far from the edge of the cell, to avoid influence of the external environment and influence of boundary conditions. This widens the cytoplasm area and results in a stiffer structure. Therefore, we conclude that a stiffer cytoplasm is primarily a result of cell shape that depends on region thickness. Furthermore, we hypothesize that both the material response and the shape of the cell contribute to the force response of the cells.

The results of a numerical analysis suggested the cellular deformation and stress of Huh-7 cells during indentation at different times. It is observed that the stress decreases over time due to the incorporation of viscoelastic branches in the cytoplasmic material model. The previous studies validate the results of the analysis. The validated material model is used for further analysis to determine the mode shape and frequency response of Huh-7 cells at varying stiffness of the focal adhesion complexes.

The modal analysis was performed to study the oscillation of the cell structure in the absence of an external stimulus. The mode shapes and natural frequencies reveal the structural shape and frequency at which the structure oscillates freely with respect to its mass, stiffness, and boundary conditions. Findings revealed that as the stiffness of the focal adhesion increases, the natural frequency of the cellular structure also increases. It is also observed that the higher modal frequency increases as the focal adhesion stiffness increases. This is attributed to the strengthening of the stress fibers, which ultimately leads to the stiffening of the cell structure. Previous findings have explained that as the focal adhesions become stiffer, they can transmit more force to the cytoskeleton, which in turn can lead to a higher natural frequency of the cellular structure [320]. The significance of this is that it provides insight into how the mechanical properties of the cell structure change in response to changes in the stiffness of the focal adhesion, which is important for understanding cellular behavior.

Further, the harmonic analysis aimed to determine the amplitude-frequency response of the cells, which provides information about the resonance frequencies and associated amplitudes of the cells under external excitation. The analysis revealed significant amplitude peaks in the frequency response at various frequencies after actuation. For varying stiffness of the focal adhesion complex, the Huh-7 cells exhibited natural frequencies in the range of 3.67 kHz to 36.6 kHz, which agrees with previous studies. Additionally, a frequency shift for higher modes was observed, with an increase in frequency with an increase in elastic stiffness. This shift in frequency is attributed to the combined role of viscoelastic and adhesive cues that regulate cell mechanobiology. Specifically, the maximum resonance amplitude of the cells indicates the maximal stress on the integrity of the cells. With the stiffness of the cell lines at 450 pN/nm, the experimental and numerically determined frequencies were in concordance, although there was a small percentage error in the resonance frequencies.

These errors are based on the assumption made during the analysis. The cells possess an-isotropic and heterogeneous behavior with a lot of inherent complexities. In this study, we evaluate the

mechanical response of cells using a non-contact optical technique. This technique demonstrates and establishes the similarity between experimental and numerical results. Selected material properties were validated from the numerical modeling, and the influence of FA's was evaluated and shown to have a crucial role in determining the cell dynamics.

## 5.6 Conclusion

In this work, we proposed a non-contact PSD-based technique to evaluate the natural frequencies of the cells. This illustrates the relevance of the cells' resonance. These experimental frequencies were compared from the numerical analysis for validation. Further, numerical analysis shows a new approach to numerical modeling that is based on the real geometry acquired from the microscopic images. Material properties are selectively predicted from the simulations. Modal and harmonic analysis was carried out based on the different stiffness of FA's to estimate the natural frequencies and frequency response of the cells. Validated material models (hyper-elastic material models) can be used to simulate cells and other biological materials. Viscoelastic filament properties may also be accommodated depending on material and time scale for more accurate behavior. Estimated frequencies predict resonance, which improves the selection of the therapeutic frequency for targeting diseased cells. This study shows potential in the fields of medical devices and biomechanical modeling.

# Chapter 6

# Effect of low-frequency excitation on the apoptosis of Huh-7 cells

## 6.1 Background

Tumor cells exhibit various morphological, structural, biophysical, biochemical, and antigenic characteristics that can be targeted by various chemotherapeutic, immunotherapeutic, and biochemical cancer treatments. Despite advancements in cancer diagnosis and treatment through recent research in cellular and molecular oncology, structural and functional genomics, metabolomics, pharmacogenomics, and toxicogenomics, current antineoplastic therapy remains ineffective. Developing improved methods for preventing carcinogenesis is a crucial goal of ongoing research. Chemotherapy is the primary method currently used in the fight against cancer, but it is ineffective due to its negative impact on healthy cells. To improve oncochemotherapy, research on a novel, selectively targeted oncolytic drugs or treatment methods needs to be expanded.

In light of the above assertions, further study is essential to enhance our knowledge of cytophysiology and cell aggregation generation. Translational research is an effective tool for achieving this goal, and nanoparticles, acoustic irradiation, mechanotransduction, and vibration analysis have been demonstrated to facilitate a greater understanding of action mechanisms at the cell aggregate, cellular, subcellular, and molecular levels. Cancer research focuses on identifying methods that trigger cancer cell death without damaging the surrounding normal cells. Mechanical vibration is a possible biocompatible treatment approach and is a subject of mechanomedicine in the field of cancer. Low-frequency mechanical excitation has been shown to have a significant effect on the apoptosis of cancer cells. Studies have demonstrated that exposure to low-frequency mechanical vibrations (LFMVs) can induce apoptosis in Huh-7 cells through the activation of caspase-3, a key enzyme in the apoptotic pathway. Additionally, LFMVs have been found to disrupt the mitochondria, the cell's primary energy source, leading to the

release of pro-apoptotic factors such as cytochrome c. Furthermore, LFMVs have been shown to upregulate the expression of pro-apoptotic proteins, including Bax and Bak, while downregulating the expression of anti-apoptotic proteins such as Bcl-2 and Bcl-xL. Overall, the combination of these mechanisms results in an increase in the rate of apoptosis in Huh-7 cells following exposure to LFMVs.

The significance of low-frequency excitation on the apoptosis of Huh-7 cells is crucial as it can provide insight into the mechanisms by which these vibrations induce cell death. The cells are exposed to LFMVs of different frequencies and amplitudes, and the rate of apoptosis is measured using techniques such as flow cytometry or western blot analysis. Despite the fact that the particular intracellular processes by which low-frequency mechanical vibration induces cell death through apoptosis and necrosis are not well understood. In order to study the effects of LFMVs on Huh-7 cells, researchers use in-vitro techniques such as cell culture and mechanical vibration exposure. Furthermore, in-vivo studies can be performed to validate the in-vitro findings and to understand the importance of LFMVs in the apoptosis of cancer cells in a more physiological context. The mechanisms by which LFMVs induce apoptosis in Huh-7 cells could lead to the development of new cancer therapies that target the apoptotic pathway, potentially providing a non-invasive and less toxic treatment option for cancer. Hence, It is important to develop a model and understand the effect of low-frequency vibration on the dynamic behavior of cells. Nevertheless, findings imply a potential role of mechanical vibration that might represent a unique application of mechanomedicine to cancer treatment.

## 6.2 Introduction

Cells can repair, regenerate, and protect themselves. Its characteristics are influenced by the microenvironment, and depends on external mechanical stimuli [321], [322]. Mechanotransduction is the process in which cells convert external stimuli response into biochemical and biophysical responses via mechanosensory proteins and the cytoskeletal network [323], [324]. Naruse et. al. highlighted many medicinal treatments based on mechanotransduction [325], including ion channels responsive to mechanical stimuli [326], manipulating tissue constructions etc and also mention the numerous applications in regenerative medicine for different disorder's. Previous studies reveal the "mechanomedicine" as a new emerging medical discipline that use mechanotransduction to promote health [327]. Mechanomedicine shows it effects to improve health in various area on embryonic stem cells, adult stem cells, cancer stem cells [328], [329], increasing bone formation in osteoporotic mice [330] and diabetes-induced wound healing in mice [331], [332]. In recent years, mechanomedicine fundamentals have been used to find new ways to study and treat cancer.

Cancer cells proliferate uncontrolled and rapidly, producing malignant tumours and affecting surrounding organs. Cancer cells can travel to distant organs via the lymphatic system and bloodstream. Chemotherapy is a medical treatment that uses potent chemicals to kill rapidly dividing cells in the body. It is most commonly used to treat various form of cancers. During chemotherapy, cancer cells develop multidrug resistance (MDR), which is a key challenge in cancer treatment [333]. Cancer chemotherapies have several side effects [289], [334], and hence, necessitating new biocompatible treatments.

Several research has explored mechanical vibration as a possible therapeutic. Vibration is a mechanical phenomenon in which oscillations take place about a point of equilibrium. All physical systems have their unique mass, stiffness, damping coefficient, and natural frequency. Resonance is a phenomenon that could occur in any structure and is characterized by a sensitivity to a definite vibration frequency. Resonance occurs when a natural frequency is equal to or near an external excitation frequency. At the resonant frequency, the system oscillates with the maximum amplitude, which results in the failure of the system [335]. As a result of the peculiarities of the physical system parameters, every organ and cell in the human body has a natural resonance frequency. In addition, the complex body will vibrate in multiple ways, and each mode of vibration will have its own oscillation frequency.

Resonance-dependent therapeutic methods are used to kill cancer cells based on their resonance behavior. These methods rely on the notion of resonance, which states that displacements in the cells will be amplified till their inherent resonant frequencies. This would annihilate the cellular system. Therefore, the natural frequency of the cell is an important parameter. These methods work on low to high range of frequencies for the treatments. However, high-frequency mechanical vibration may destroy cancer cells while injuring adjacent healthy cells [336]. More recently, some novel approaches were developed to destroy cancer cells based on low-frequency mechanical effects on the cancer cell membrane. Further whole-body vibration has been studied as an adjunct to standard chemotherapy, reducing adverse effects such weight loss and nausea [337]. However, there is no direct evidence that whole-body vibration affects cancer cells.

During carcinogenesis, autophagy and apoptosis are restricted, and necrosis dominates [338]. However, promoting necrotic cell death as a cancer treatment is undesirable because it causes cell damage, which may stimulate inflammatory responses that favor tumor formation [339]. On other hand, balancing apoptosis and necrosis together can be a better way to combat cancer tissue growth and spreading. To limit the risk of inflammation and immune cell activation, apoptosis should be used to kill cancer cells [289], [340], [341]. Anisotropic magnetic nanoparticles connected to cell membranes cause apoptosis at sub kilohertz frequencies [289], [342]. The Leulmi et al. [289] investigation showed that mechanical vibrations at 20 Hz may regulate cell fate, which is essential since a temperature rise at that frequency is rare. Heat diffusion also reduces the danger of damaging or necrosis in surrounding healthy cells [343]. This investigation uses

magnetic particles and a magnetic field, and the role of mechanical vibration in the increase in apoptosis was unclear.

Previous studies show the response of cancerous cell systems exposed to low-magnitude mechanical vibrations. Low magnitude vibration promotes the mesenchymal precursor cell growth, and differentiation [344]. At the molecular level, low magnitude vibration triggers a signaling cascade that results in enhanced phosphorylation of focal adhesion kinase (FAK) and Akt, which leads to RhoA activation and the production of filamentous actin structures [345]. The effects of low-magnitude vibration are cumulative, increasing FAK phosphorylation and F-actin contractility after further dosing of vibrations [346]. The synergistic effects of the cells provide a more robust response to excess mechanical stimuli. Xin Yi et. al.investigated the mechanisms by which cancer cells detect and respond to mechanical vibrations of low amplitude [347]. Their findings predict that the mechanical vibration lowers the metastatic potential of human breast cancer cells, where the nucleus functions as a mechanosensory gear to modify cellular morphology and intercellular communication.
In this work, we studied the influence of mechanical vibration on cancer cell metabolism and mortality using the Huh7 cancer cell line as a model. We compared the frequency responses of cells exposed to low-frequency excitation (20 Hz to 60 Hz) of mechanical vibration to those of control cells cultured without mechanical stimulation. Further, measurements of cell viability and cell death after the external excitation were carried out using an MTT assay. In addition to cell viability, apoptosis, and necrosis were also observed using flow cytometry analysis. These findings are helpful in assessing the state of disease based on their vibrational behaviour and targeting the cancer cells depending on their mechanical dynamics.

The cells used in our experimentation were provided by our collaborating laboratory (Prof. Rajdeep Chowdhury and Prof. Sudeshna Mukherjee Lab.). This section on cell culture and the biological assay of the cells was performed by Mr. Nizam Ahmed and included in this thesis solely for the purpose of completeness. As the author of the thesis, I did not carry out the cell culture and biological assay part of this work.

## 6.3 Materials and Methods

### 6.3.1 Maintenance of HCC cell lines

The Hepatocellular Carcinoma cell line Huh-7 (procured from National Centre of Cell Sciences (NCCS), Pune) was cultured in DMEM (Dulbecco's Modified Eagle Medium, Hi-Media) with 10 % FBS (Fetal Bovine Serum, Hi-Media) (v/v) and 1 % Penstrep (Gibco) (v/v) and maintained at 37 °C in 5 % $CO_2$ in a carbon-dioxide incubator. The required amount of cryovials was made for all the cell lines and stored for further use in -80 °C.

### 6.3.2 Cell vibration

Huh-7 cancer cells were seeded into 96-well plate at a density of 1.5× $10^5$/250 $\mu$L/well in 10% FBS DMEM and cultured for 48 hr. The plate was divided into four compartments and each occupying 12 wells. Each compartment having cells was subjected to vibration using micro shake while control was kept such that it does not experience any vibrations. The entire experimental system was placed in a sterile condition for 1 hr at 37 °C. After the 1-hr vibration at 20, 40, and 60 Hz, test plates were placed into the incubator without vibration for 24 and 48 hr, and another plate was processed immediately after the vibration. The sample which was not subjected to vibration was treated as a control, and for other cases, it was named after their excitation frequency, viz. 20 Hz, 40 Hz, 60 Hz. For the flow cytometry experiment, a 35 mm petri dish was taken in which cells were cultured for 48 hr. Afterward, that cell was given the vibration for 1 hour for each case and placed in an incubator for 24 and 48 hours. Accordingly, one set of experiments was processed immediately for the flow cytometry.

### 6.3.3 Cell Viability Assay

To determine the cell viability after frequency treatment, cells were seeded in 96 well plates at a density of 5,000 cells /well as these cells attained 60- 70 % confluency than they were exposed to different frequencies of vibration for 1 hour. Afterward, 3-(4,5-dimethylthiazol-2-yl)-2,5-diphenyl-2H-tetrazolium bromide (MTT) assay [348] was done at 0, 24 and 48 hours. MTT was dissolved in 1X PBS and DMEM media (1:5 ratio) with 1mg/ml concentration, and 100 $\mu$l of MTT was added to each well after removing the prior media from the wells. The plate was incubated at 37 °C for 4 hr following the 150 $\mu$l of DMSO addition in each well. The absorbance was taken at 570 nm and 630 nm wavelength in spectroscopy.

### 6.3.4 Annexin V/Propidium Iodide (PI) staining

For determination of apoptosis, cells were seeded in 6 well plates at a density of 3× $10^5$ cells/well. After the cells had attained 60- 70 % confluency, the cells were exposed to different frequencies for 1 hour each. After this, the flow cytometry was done at 0, 24, and 48 hours. After that, the cells were harvested, washed with PBS, and resuspended in 500 $\mu$l of 1X binding buffer (BD BioSciences). To detect both early and late apoptotic cells, 3 $\mu$l of AnnexinV and 3 $\mu$l of PI were added to the cells in a binding buffer, followed by incubation for 10 min. The samples were then acquired using a flow cytometer (Cytoflex, Beckmann Coulter), and analysis of acquired data was performed using CytExpert software [349]. The apoptotic cells are represented in percentage.

### 6.3.5 Cell size quantification

After the treatment with vibration, cells were imaged in a phase contrast microscope at 0, 24, and 48 hours. The size of the cells was quantified before and after the exposure to mechanical vibration using ImageJ. The circularity index of the cells was determined using the measured area and perimeter of the cells [308], and the results were afterward analyzed.

### 6.3.6 Measuring frequency response

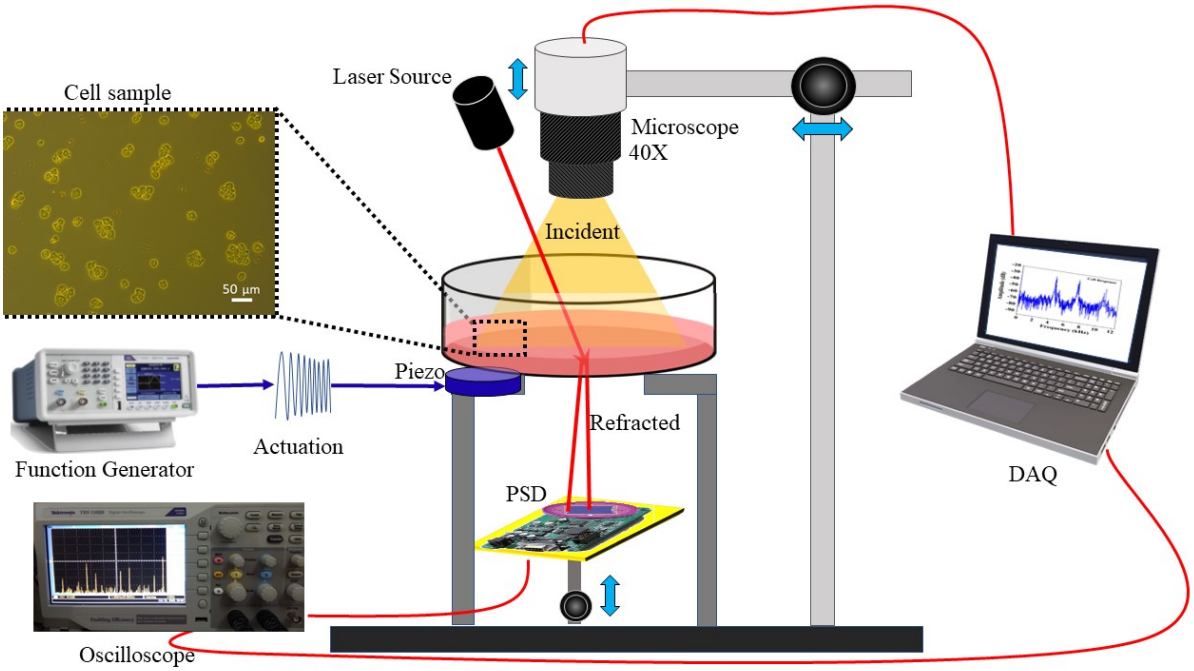


FIGURE 6.1: Detailed experimental setup used for the measurement of cellular dynamics.

Figure 6.1 shows the detailed working principle of the experimental setup. A laser source RLM650TA-020R was used with a maximum of 23 mW and 650 nm wavelength powered by an external AC Voltage source of 240V and 50 Hz. The cell, after the external stimulation, was taken out from the $CO_2$ incubator and was placed over the cross slide, and input was applied on the slide for the actuation of the cells. A microactuator was used and driven by the function generator (Tektronix AFG 1022) for the actuation of the cells. A chirp signal was applied to the actuator through the function generator to vibrate the cells. The position of the cancer cell in the wells was determined with an optical microscope. Laser from the source is focused on the cell's surface and gets refracted to the Position Sensitive Device (PSD) as shown in Figure 6.1. PSD was used as an optical position sensor (OPS) that can sense the incident laser position on a two-dimensional sensor surface. The cell movement with respect to applied actuation was traced, and the output voltage corresponded to cell displacement in the X and Y directions was measured by the Oscilloscope (Tektronix MSO 46). The cell and base responses were measured

sequentially during the experiments. The frequency response of the cells was obtained using the Fast Fourier transform (FFT) of the time domain signal acquired from the oscilloscope. The transfer function was used to take away the support-based frequency response to predict the cell's natural frequency. Each measurement on the cells and base was repeated for a particular sample, and the mean of frequencies for each sample was considered for the analysis.

## 6.4 Analytical frequency response

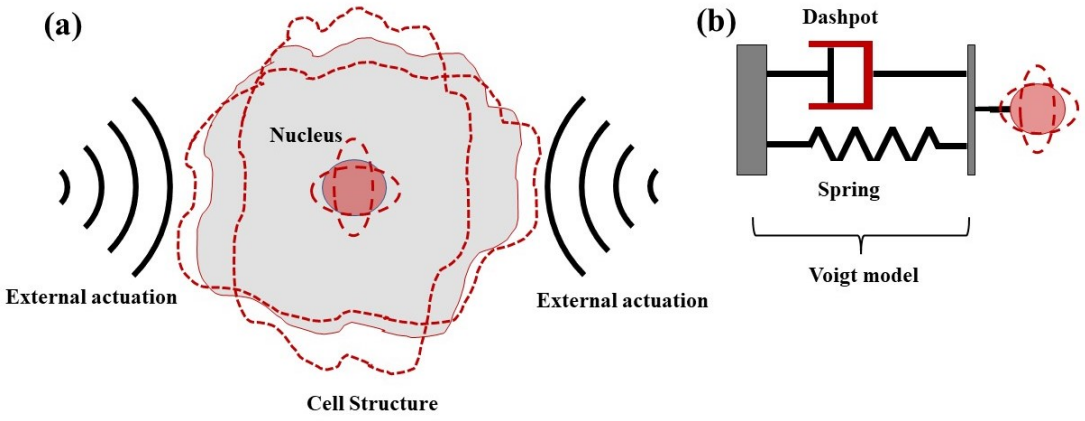


FIGURE 6.2: Cell as a standard voigt model.(a) Cell under mechanical actuation. The actuation causes morphological alterations in the cell structure. (b) Standard Voigt model for the mathematical representation of the cell. Dashpot and spring components represent the viscoelastic components of the cell.

Consider a single cell subjected to oscillating displacement exerted by an external force inside a viscoelastic medium (Figure 6.2a ). Assuming the cell as a spherical object with a radius of R and considering it as a homogeneous and isotropic viscoelastic material (Figure 6.2b). The elastic and viscoelastic components of the cell were represented by a spring and dashpot as reported in the previous literature [312]. The equation of motion for the cell system can be written as [261].

$$f_m = m_c a_c = \frac{4}{3}\pi\rho_c R^3 \frac{d^2 u_c}{dt^2} = f_d - f_r \tag{6.1}$$

where $t$ is the time, $f_m$ represents the inertial force, $m_c$ is the mass of cell whose density is $\rho_c$, and $u_c$ is the associated displacement. Furthermore, $f_d$ is the basic driving force in the system, that are induced by the external source. While response force $F_r$ is the combination of the two components together as follows:

$$F_r = F_\mu + F_G \tag{6.2}$$

where $F_G$ denotes the elastic contribution and $F_\mu$ denotes the viscous force response.

Detailed mathematical modeling is described in the Appendix A. The analytical solution in terms of amplitude for the relative displacement $\Delta U_c$ and frequency ($\omega$) between the cell and its surroundings after Laplace transform is shown as follows in Equation 6.3 [261].

$$\|\Delta U_c\|_{s=\iota\omega} = \left\| \frac{\frac{4}{3}\pi\gamma\zeta\rho_c R^3 s V_m}{c_{0G} + (c_{1\mu} + c_{1G})s + ((c_{2\mu} + c_{2G}) + \frac{4}{3}\pi\rho_c R^3)s^2} \right\|_{s=\iota\omega} \tag{6.3}$$

Where,

$$c_{0G} = 6\pi GR,\ c_{1G} = 6\pi R^2\sqrt{G\rho_m},\ c_{2G} = 6\pi R^2\sqrt{G\rho_m} \tag{6.4}$$

and

$$c_{1\mu} = 6\pi R\mu\left(1 + \sqrt{\frac{\omega R^2}{2\nu}}\right),\ c_{2\mu} = \frac{2}{3p}\pi R^3\rho_m\left(1 + \frac{9p}{2}\sqrt{\frac{2\nu}{\omega R^2}}\right) \tag{6.5}$$

Here,$V_m$ is the velocity of the cell in the medium, $\mu$ and $\nu$ the dynamic and the kinematic viscosity's of the medium respectively, $\omega$ is the natural frequency of the system, and $G$ denotes the medium's elastic shear modulus, cell density is $\rho_c$, and $\rho_m$ is the medium density. Additionally, the following dimensionless constant is defined:

$$\zeta = \frac{\rho_c}{\rho_m} = \frac{1}{1+\gamma} \tag{6.6}$$

Here, $\gamma = \rho_m\rho_c^{-1} - 1$

## 6.5 Results

### 6.5.1 Cellular morphology of Huh-7 after external excitation

An important factor, such as cell vitality can be estimated from the cell morphology and its geometrical parameters. Phase contrast microscopy images (Figure 6.3) and a circularity histogram of single cells (Figure 6.4) indicate that the cells subjected to external excitation lose the circularity and become polygonal shape than the cells without excitation. This leads to a larger and rougher periphery of the cells. Moreover, it was also confirmed that the cells with the proposed method decreased in size and become more irregular than the cells exposed to a higher frequency. Additionally, the cells with low-frequency excitation were observed to be less damaged than those exposed to higher external-frequency excitation. These findings indicate that the cells exposed to the lower frequency are more active than cells excited by, the higher frequency.

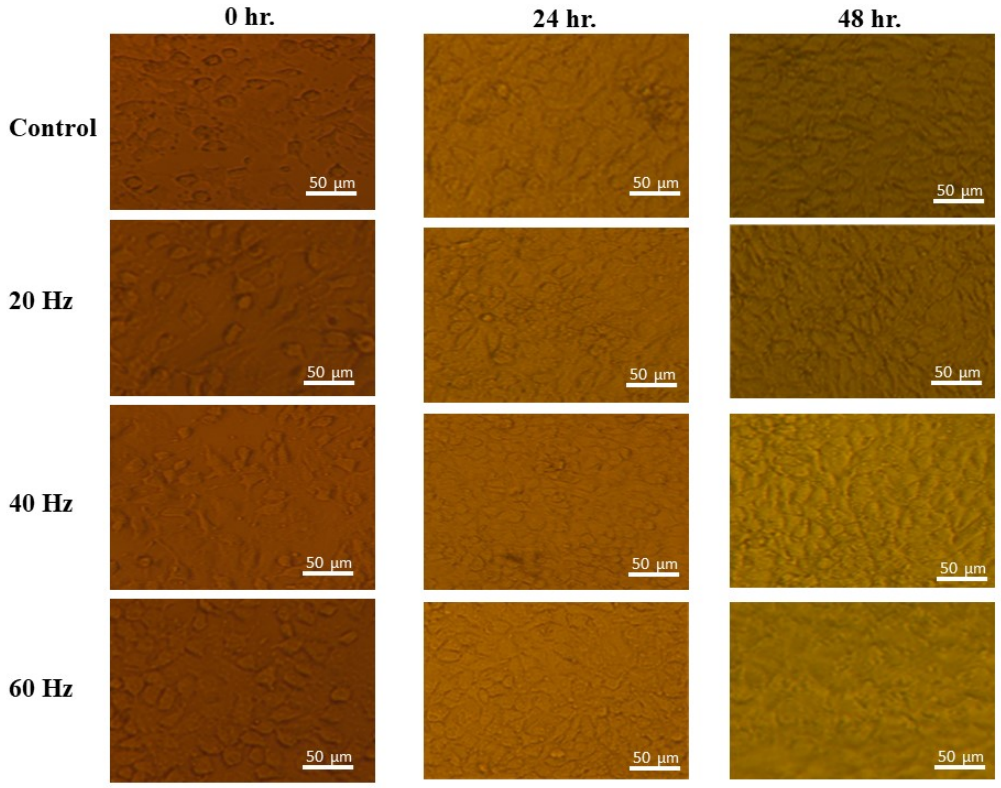


FIGURE 6.3: Cellular morphology with and without external actuation

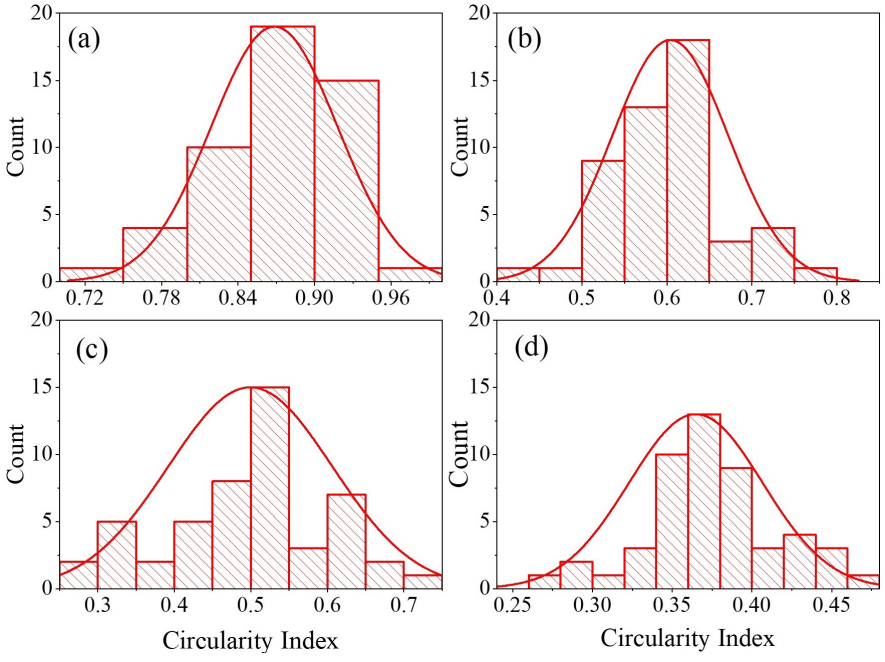


FIGURE 6.4: Circularity Index for the different cell under different actuation (a) control (b) 20 Hz (c) 40 Hz (d) 60 Hz.

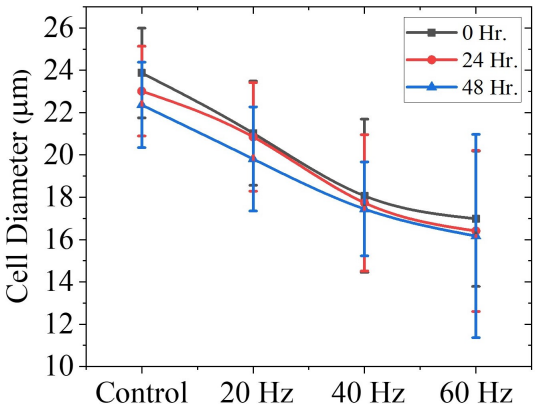


FIGURE 6.5: Variation in cell diameter after different external excitation frequency.

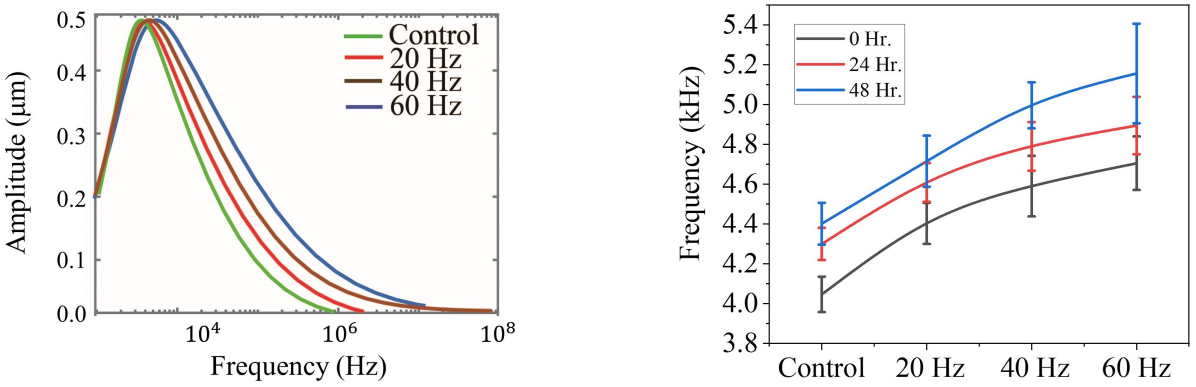


FIGURE 6.6: (a) Analytical frequency response of the cell using standard voigt model under different actuation immediate after excitation.(b) Variation in the fundamental frequency of cell after external excitation using Standard voigt model.

### 6.5.2 Analytical Frequency response of Huh-7 after excitation

Cells were subjected to a different frequency of excitation. Images obtained for each case were taken using a microscope. Further, these images were used for calculating the cell area and perimeter using ImageJ. After excitation, cells were trypsinized and resuspended in 1ml culture media. The image was taken with Carl Zeiss's inverted light microscope. Cells are almost circular in shape. Analytical frequency responses were calculated by considering the average diameter of the cells. Variation in the cellular diameter is shown in Figure 6.5. The diameter of the cells was found to decrease with the increase in the excitation frequency. This lead to the degradation of the cell structure. Analytical cellular frequency response considering the cellular system as a standard Voigt model is shown in Figure 6.6a. It is observed from the plot that the fundamental frequency of the cells increases with the increase in the excitation frequency. Similarly, at a different time point, there has been an increase in the fundamental frequency observed, as shown in Figure 6.6b. Theoretically, it can also be predicted from the decrease in the cellular diameter. This can be attributed to alterations in the cytoskeletal structure and focal adhesion of the cells.

### 6.5.3 Experimental Frequency assess of Huh-7 after excitation

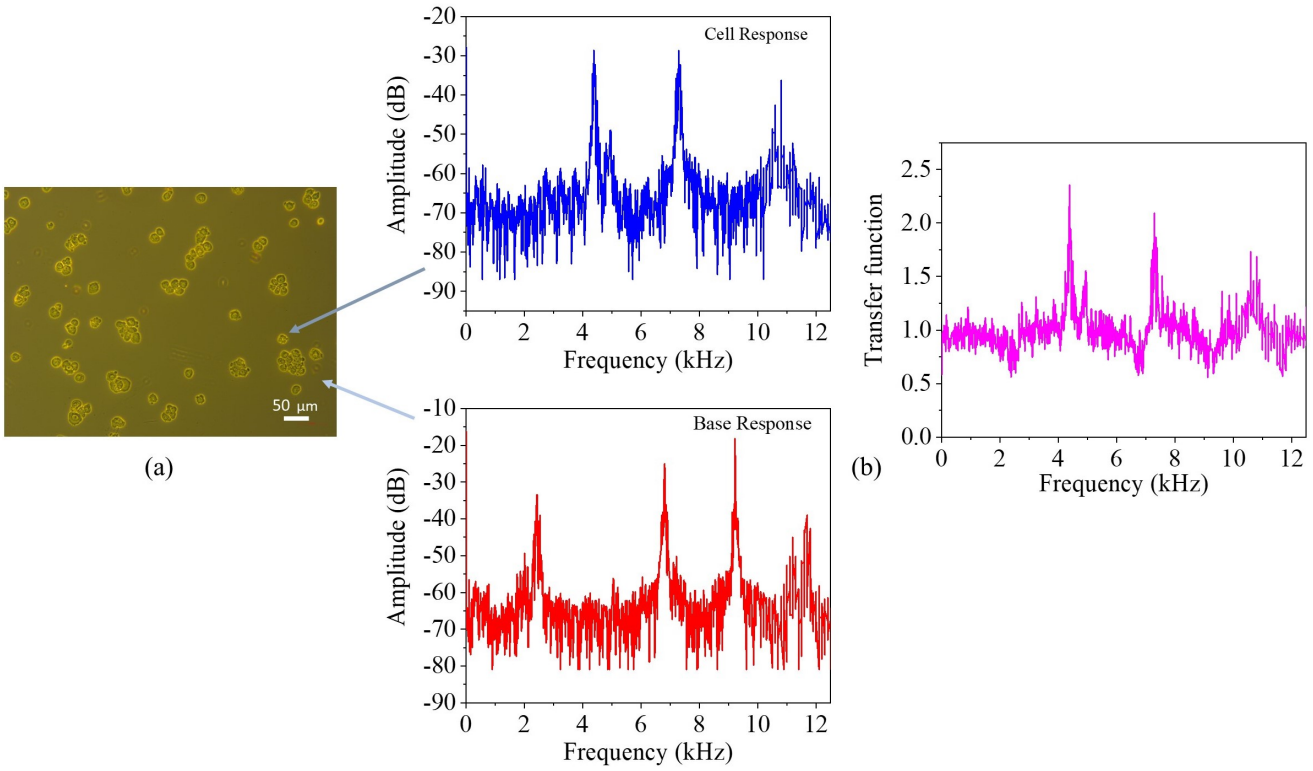


FIGURE 6.7: a) Frequency response of cancer cells. b) Transfer function of cell with respect to the base.

Figure 6.7 shows the frequency response for the control Huh-7 cell without actuation. Figure 6.7a shows the cell and base response. We take the transfer function of the cell wrt base to take away base-related modes. Figure 6.7b shows the transfer function. Peaks in the transfer function plot (Figure 6.7b) at 4147 Hz show the fundamental frequency of the cell without actuation. Similarly, fundamental frequencies were evaluated for other actuation cases. Table 6.1 shows the variation in the experimental obtained natural frequencies of the cells with and without external excitation. It has been observed that the fundamental frequency of the cells increases with the increase in the external excitation frequency. Timepoint behavior suggests that the frequency of the cell increases with the duration after the excitation. External excitation leads to changes in the cellular geometry as well as distorts the cellular structure. This distortion decreases the mass and the size of the cell. Thus affecting the fundamental frequency. There has been a substantial increase in the frequency of the cell excited by 60 Hz compared to the control with no excitation. These experimental frequency responses correspond close to the analytical frequency responses.

### 6.5.4 Low-frequency excitation reduces the viability of Huh-7 cells

MTT assay was performed to check the cellular viability of Huh-7 after low-frequency treatment for 1 hour at three different frequencies 20 Hz, 40 Hz, and 60 Hz. The result displayed that

TABLE 6.1: Experimental evaluated the fundamental frequency of the Huh-7 cell.

| Time (hr.) | Control | 20 Hz | 40 Hz | 60 Hz |
|---|---|---|---|---|
| 0 | $4147.84 \pm 82.24$ Hz | $4305.83 \pm 94.06$ Hz | $4603.75 \pm 98.24$ Hz | $4873.06 \pm 102.08$ Hz |
| 24 | $4299.81 \pm 74.22$ Hz | $4502.44 \pm 74.86$ Hz | $4843.00 \pm 92.12$ Hz | $5029.04 \pm 104.24$ Hz |
| 48 | $4577.94 \pm 78.02$ Hz | $4723.88 \pm 88.36$ Hz | $4920.00 \pm 99.64$ Hz | $5231.86 \pm 108.88$ Hz |

cell viability decreases as frequency increases from 20 to 60 Hz (Figure 6.8). After frequency treatment, plates were kept in an incubator for 24 and 48 hours, and later MTT was performed. The result showed that Huh-7 viability decreased in frequency-treated cells even after giving them time to rescue themselves. Immediately after the frequency treatment, about 85 % of cells remain viable at 20 Hz, 70 % of cells were viable at 40 Hz while only 52 % of cells remained viable at 60 Hz treatment. After 24 and 48 hours of frequency treatment, 85 and 80 % viable cells at 20 Hz, 69 % and 67 % viable cells at 40 Hz, and 58 % and 52 % cells remained viable at 60 Hz respectively. The result suggests as frequency increases; there is an increase in cell death. Findings demonstrate that even a low sound frequency up to 60 Hz can kill the cancer cell.

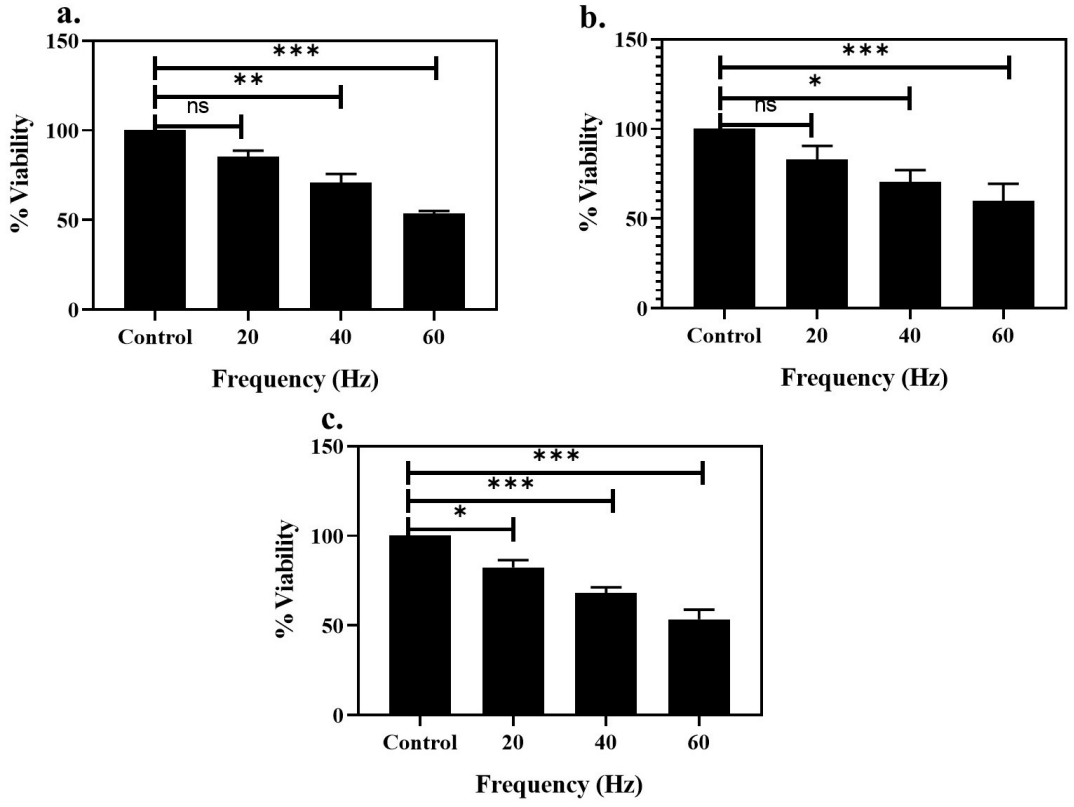


FIGURE 6.8: Effect of vibration on cancer cell viability. MTT assay was used to determine cell viability. A sample without external excitation cells was used as a control. a) Immidiately after the excitation b) 24hrs after the excitation c) 48 hrs after the excitation. Results are presented as means ± SD. $*$ p <0.005, $**$ p <0.05,$***$ p <0.01.

### 6.5.5 Low frequency causes apoptotic as well as necrotic cell death in Huh-7 cells

As a result showed that the viability of cancer cells decreased upon vibration treatment and to further analyze the death type, annexin PI staining was performed. Annexin PI staining-based flow cytometry can differentiate between apoptotic and necrotic cells [350]. It is observed that as the frequency of excitation increases from 20 Hz to 60 Hz, cellular apoptosis increases. There is very low apoptotic cell death at zero hours after the treatment (Figure 6.9) which suddenly increased after 24 (Figure 6.10) and 48 hours (Figure 6.11) of incubation after the frequency treatment.

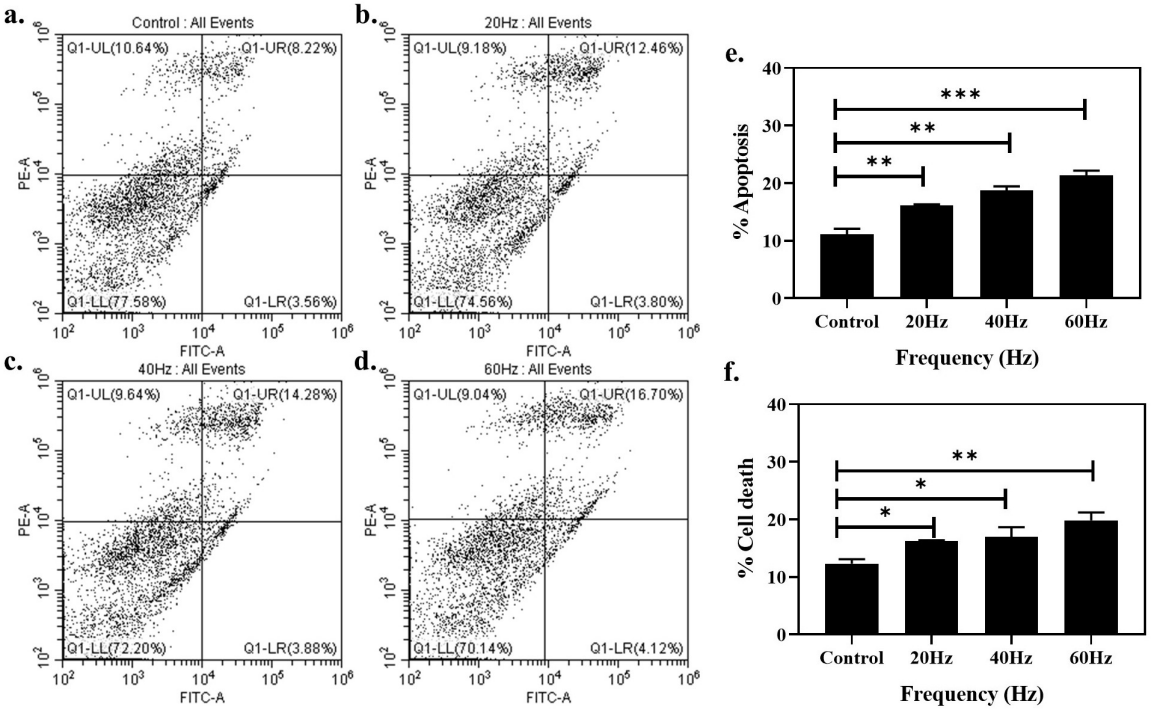


FIGURE 6.9: Apoptotic cell death analysis after 0 hr post vibration treatment (a-d) shows flow cytometric scatter plot depicting various events in the cells. The bottom right quadrant indicates early apoptotic cells, while the top left quadrant depicts necrotic cells. (e) Total percentage of apoptotic cells after 0 hr of incubation (f) Total percentage of the cell death under low-range mechanical vibration. Results are presented as means ± SD. ∗ p <0.005, ∗∗ p <0.05,∗ ∗ ∗ p <0.01.

## 6.6 Discussions

The cell morphological study suggests that cellular shrinkage occurred over time, with a decrease in cell size under external actuation. The specific cause of cellular shrinkage and the mechanism by which it occurs are not explored, but it is a response to changes in the cellular environment. The probable mechanism of shrinkage can be attributed to the changes in cytoskeletal structure

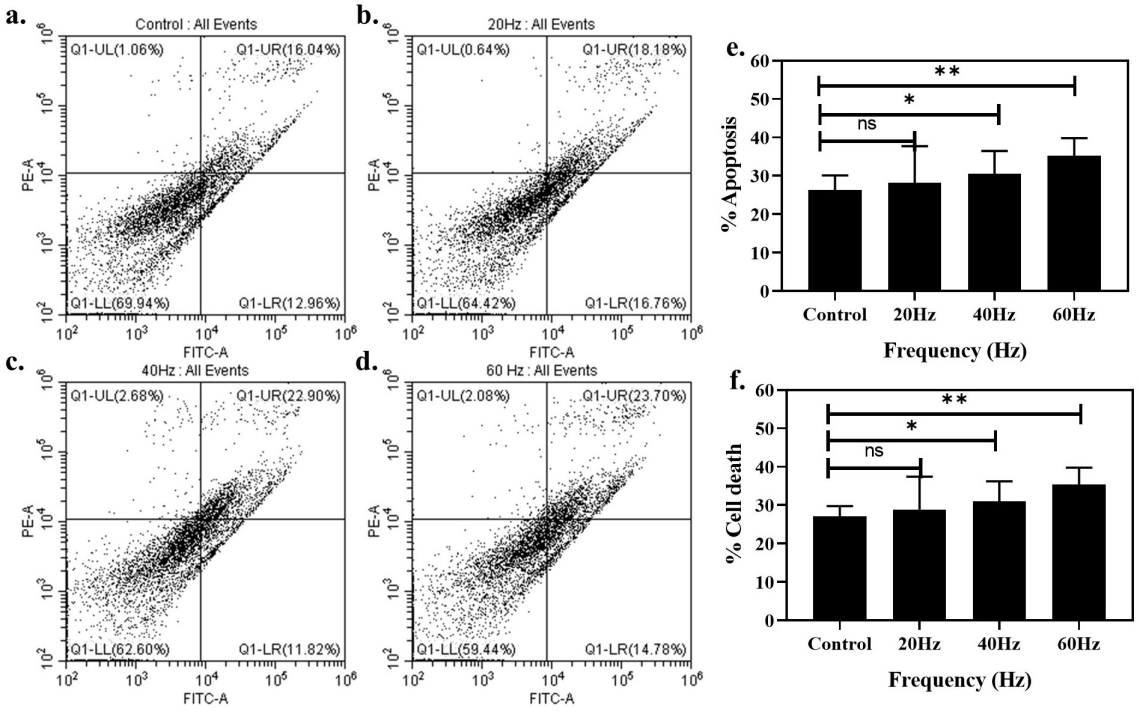


FIGURE 6.10: Apoptotic cell death analysis after 24 hrs post vibration treatment (a-d) shows a flow cytometric scatter plot depicting various events in the cells. The bottom right quadrant indicates early apoptotic cells, while the top left quadrant depicts necrotic cells. (e) The total percentage of apoptotic cells after 24 hrs of incubation (f) Total percentage of the cell death under low-range mechanical vibration. Results are presented as means ± SD. ∗ p <0.005, ∗∗ p <0.05.

or changes in the cell's metabolism [351], [352]. Additionally, when cells were exposed to low-frequency excitation, they exhibited less damage than those exposed to higher-frequency excitation [353], [354]. Furthermore, previous research has indicated that external excitation may provide a protective effect on cell surface proteins, preserving cell surface receptors [355]. The cells were able to receive outer signaling molecules, such as hormones, and absorb nutrients, such as vitamins and glucose effectively [321]. This lead to the proper functioning of the cells. The protective effects of the external excitation on cell surface proteins apparently preserved cell surface receptors. Notably, minimal cell death was observed within the range of external excitation frequencies applied in this study. These findings indicate that the cells exposed to the lower frequency are more active than cells excited by, the higher frequency.

The cellular system was modeled as a standard Voigt model for analytical frequency response, as shown in Figure 6.6. The results of this analysis indicate that the fundamental frequency of the cells increases as the excitation frequency increases. This trend can also be observed at different time points, as shown in Figure 6.7. Theoretically, this increase in fundamental frequency can also be predicted based on the decrease in cellular diameter. This can be attributed to alterations in the cytoskeletal structure and focal adhesion of the cells. These changes in the structural properties of the cells can have a significant impact on the overall mechanical behavior of the

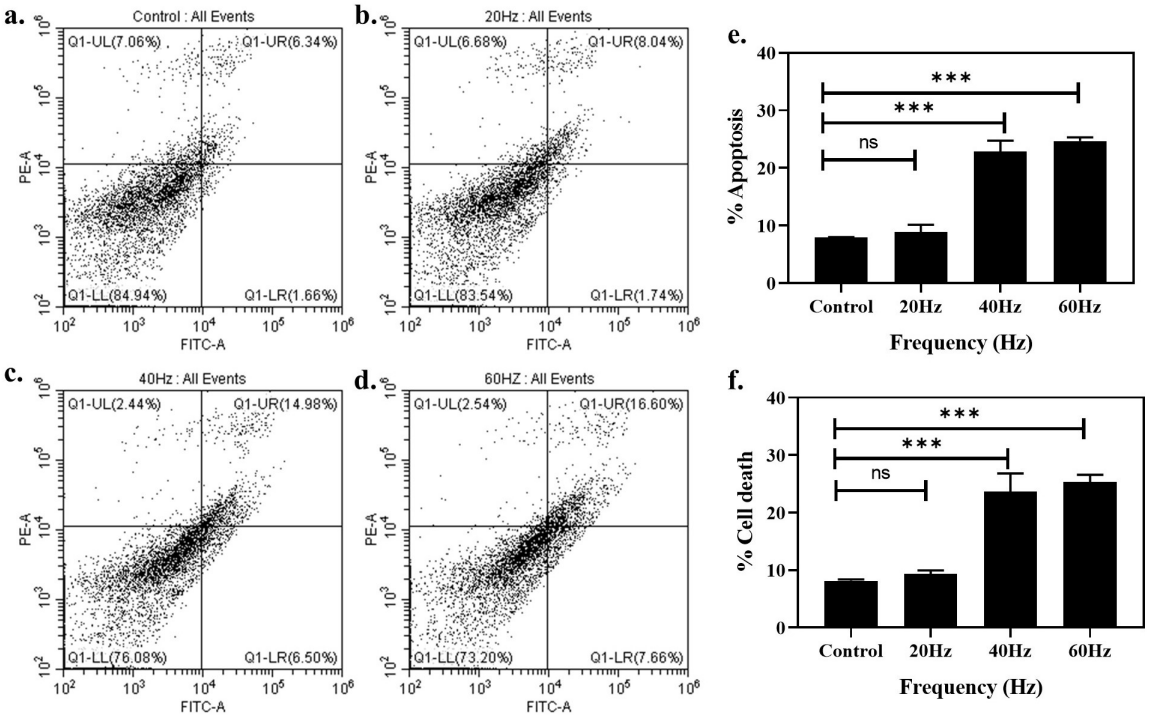


FIGURE 6.11: Apoptotic cell death analysis after 48 hrs post vibration treatment (a-d) shows a flow cytometric scatter plot depicting various events in the cells. The bottom right quadrant indicates early apoptotic cells, while the top left quadrant depicts necrotic cells. (e) Total percentage of apoptotic cells after 48 hrs of incubation (f) Total percentage of the cell death under low-range mechanical vibration. Results are presented as means ± SD. $***$ p <0.01.

cellular system. It is important to note that this relationship between the frequency response of cells and their structural properties is not fully understood. Further research is needed to fully understand the underlying mechanisms.

The noninvasive experimental results indicate that the fundamental frequency of cells increases with an increase in the external excitation frequency. Additionally, the time-point behavior suggests that the frequency of the cell also increases as the duration after the excitation increases. These findings can be attributed to the changes in cellular geometry and distortion of the cellular structure caused by external excitation. The distortion leads to a decrease in both the mass and size of the cell, thereby affecting the fundamental frequency. The data shows a substantial increase in the frequency of the cell excited at 60 Hz compared to the control with no excitation. It is worth noting that the experimental frequency responses correspond closely to the analytical frequency responses. The measured experimental frequency has been within an acceptable range of difference compared to the analytical frequency response with 3.6 %, 2.31 % and, 4.07 % for control at 0 hr, 24 hr, and 48 hr respectively. The results of the study suggest that as the frequency of the external excitation increases, cell death increases. This trend has also been observed in previous studies on A431 carcinoma cells, where cell death was reported using trypan blue dye [321].

The effect of mechanical vibration on cell behavior has been widely studied on primary cells [356], however, the effect of vibration on cancer cell death has been less studied. Our results demonstrate that even a low sound frequency of up to 60 Hz can kill cancer cells. The results showed that the viability of cancer cells decreased upon vibration treatment. To further analyze the death type, annexin PI staining was performed. Annexin PI staining-based flow cytometry is a technique that can differentiate between apoptotic and necrotic cells. As suggested by Angatasti et al. (2020), A431 cells follow the apoptotic cell death path after vibration treatment, while our result on Huh7 cell lines shows that cell death occurs due to apoptosis as well as necrosis in almost equal proportion. Necrotic cell death of HepG2 due to the vibration of magnetic beads was first reported by Birang et. al. (2013), which showed that mechanical vibration can lead to necrotic cell death [357]. Cell death due to necrosis suggests not only an apoptotic pathway but vibration can cause some irreversible damage which leads to necrotic cell death. It is important to note that the balance between apoptotic and necrotic cell death can be a key factor to combat cancer growth. Our results show that low frequency can induce both apoptotic and necrotic cell death [358]–[360]. Findings indicate that as the frequency increases from 20 Hz to 60 Hz, cellular apoptosis increases. There is low apoptotic cell death at zero hours after the treatment (Figure 6.9) which suddenly increased after 24 hours (Figure 6.10) and 48 hours (Figure 6.11) of incubation after the frequency treatment.

These findings are new and suggest that vibration treatment at different frequencies can be useful in inhibiting cancer progression. Further studies are needed to investigate the underlying mechanisms and to optimize the vibration parameters for the most effective cancer cell death.

## 6.7 Conclusion

Mechanical features of the cells, such as size, stiffness, and elasticity, provide the best indicators of cell status. The differences in the frequency of normal and malignant cells will affect the mechanical behavior of the cells. Hence, frequency is an important parameter to target and reveal the characteristics of the cell. In this work, the non-invasive method is proposed to evaluate the fundamental frequency of the cells under dynamic conditions. Fundamental frequencies of the oscillating cells increase with the increase in external actuation. It was observed that there has been a 10% increase in the fundamental frequency of the cells with an increase in the excitation frequency from 20 Hz to 60 Hz. Similarly, findings revealed that the cell viability decreased with the increase in mechanical vibration. The mechanical vibration was found to increase apoptosis, as compared to control circumstances. Thus, low-range mechanical vibration may represent a possible method to trigger apoptosis in cancer cells while reducing necrosis. In conclusion, it is possible that mechanical properties and vibration characteristics are influenced by changes in fundamental frequencies and vice-versa which are caused by changes in environmental conditions

and external stimuli. Hence, these findings are helpful in developing the device based on resonance in the field of determining the state of a malignant condition.

# Chapter 7

# Development of smart microchannel device for cell diagnostics: Insight of resonance behaviour of Huh-7 and their cellular morphology

## 7.1 Background

Cancer cells are characterized by their ability to rapidly divide and grow, which can lead to the formation of tumors. This uncontrolled cell growth is the result of genetic and epigenetic changes that occur in cancer cells, which disrupt the normal mechanisms that regulate cell growth and division. The dynamic behavior of cancer cells refers to the way in which cancer cells move, grow, and interact with their environment. Understanding the dynamic behavior of cancer cells is important for a variety of reasons, including the development of effective diagnostic and therapeutic approaches for cancer. One of the key features of the dynamic behavior of cancer cells is their ability to move and migrate. Cancer cells are able to move through the body using a process called metastasis, which allows them to spread from the primary tumor to other parts of the body. This ability to migrate is an important characteristic of cancer cells and is a key factor in the development and progression of cancer. In addition to their ability to move and migrate, cancer cells also exhibit a range of other dynamic behaviors. For example, cancer cells are often able to evade the immune system and avoid being detected and destroyed. They are also able to adapt to changes in their environment, such as changes in nutrient availability or exposure to chemotherapy drugs, and can develop resistance to these challenges. The dynamic behavior of cancer cells is also influenced by their interactions with other cells and their environment. For example, cancer cells can secrete a range of molecules, such as growth factors and extracellular

matrix proteins, that can promote their own growth and survival, as well as the growth and survival of other cancer cells. These interactions can help cancer cells form complex networks that enable them to survive and thrive in the body.

Hence, the dynamic behavior of cancer cells is a complex and multifaceted process that is essential for the development and progression of cancer. Understanding the dynamic behavior of cancer cells is crucial for the development of effective diagnostic and therapeutic approaches for cancer.

In this study, the concept of active microchannels was carried out for the precise control of cells in biomedicine. A novel external vibration-assisted approach is described for the efficient development of a microchannel of a nanocomposite piezo polymer thin film. In this approach, external actuation of varying amplitude and frequency is used for exciting the microstructure. The synthesis of ZnO nanopowder was carried to fabricate the piezoelectric effect-based microchannel. In PDMS, the ZnO was combined with the hardener to fabricate the microchannel. One electrode was attached to its top surface and another ground electrode was formed on its bottom surface to generate the actuation in the microchannel. Structural and chemical composition was analyzed using scanning electron microscopy and XRD. Mechanical and electrical properties were evaluated to study the piezoelectric effect in the ZnO /PDMS microchannel. The behavior of Huh-7 cells in a ZnO /PDMS microchannel was studied by stimulating the channel structure and then analyzing the morphological changes in the cellular structure using high-speed camera imaging. The position sensing device (PSD) based non-invasive experimental technique was used to determine the resonance behavior of the flowing cells through the actuating channel using their frequency response. Further, studies reveal that the developed shear stresses affect the cells while flowing through the channel. This leads to higher geometrical changes with an increase in the frequency of mechanical vibration and which alters the resonance behavior of the cellular structure. The mechanical properties and vibration characteristics are impacted by variations in fundamental frequencies and vice versa, under external stimuli. Therefore, these findings are applicable to the development of a resonance-based device for identifying the presence of a malignant condition.

## 7.2 Introduction

Microfluidic systems are used to control and regulate the microlitre-scale laminar fluid flow, discrete fluids, micro-particles, and cells [361], [362]. Nowadays microfluidic systems are appropriate for use in biology, life sciences (e.g., cytometry), diagnostic lab-on-chip devices, microscale cell culture, etc. [363]–[365]. Their operational, analytic, and sampling characteristics are important aspects to understand the durability of microfluidic systems. Initially, microchannels were produced in silicon and glass substrates [366]–[368]; however, with the advent of innovative and biocompatible resin materials and their low-cost, microchannels are now fabricated in polymer resins. Poly (methyl methacrylate) (PMMA), polystyrene (PS), polycarbonate (PC), and cyclic olefin copolymer

(COC) have been used in fabrication technologies because of their biocompatibility and more efficient production [369]–[371]. Polydimethylsiloxane (PDMS) is a transparent, elastic, and biocompatible polymer that has been widely used as a substrate material in microfluidic devices. Currently, there are various techniques used for increasing the vitality of the microchannel which reduces its working duration and cost. Active and passive techniques are used in the development of the microfluidic-chip-based system. Active microchannels rely mostly on external fields to impart force for microfluidic channels (e.g., electrophoretic [372], acoustic [373], [374], magnetic [375], and optical [376]. The passive microchannel system is composed mostly of gravitational inertia analysis [377], micro-scale technique [378], deterministic lateral displacement [379], and hydrodynamic fractionation [380]. The dominant multiphase microfluidic technologies, such as droplet microfluidics and segmented flow microfluidics, rely on passive approaches to create and control multiphase flow [381]. Passive multiphase microfluidics has a simple design and a high throughput. This simplicity, however, has poor control and limited adaptability [382], [383]. In the past few years, there has been a significant increase in interest in the integration of piezoelectric actuators into multiphase microfluidics for increased controllability [384]. Numerous studies based on the concept of an active microchannel were carried out in microfluidics. The primary benefit is that piezoelectric actuators enable active control of multiphase interfaces. Active microchannels fabricated in piezo polymer material is having the functional ability to transport fluids, droplets, or biological cells with the wave-type deformation of their walls. Several techniques, such as acoustophoresis, control droplets or particles using acoustic radiation force. Nowadays, surface acoustic waves (SAW) based microchannels have wide applications in the field of biology [385], [386]. Biological particles can be patterned and streamed in the required direction and location as a result of generated standing surface acoustic waves (SSAW) and the action of traveling surface acoustic waves in a microchannel [387]. These techniques require the IDT electrode to be printed on the piezo-activated surface to produce the waves on the surface of the microchannel [388]. These electrodes require higher precision and cost to be printed on the microchannel surface. Zinc oxide (ZnO) is a highly piezoelectric material that has been widely used in various applications such as sensors, actuators, and energy generation devices [389]. In recent years, ZnO has been utilized as an active material in polydimethylsiloxane (PDMS) microchannels for cell diagnosis [390], [391]. The combination of PDMS and ZnO allows for the creation of active microchannels that can generate an electrical signal in response to mechanical strain or vice-versa. The use of ZnO-based PDMS active microchannels has several advantages for cell diagnosis. First, the piezoelectric properties of ZnO allow for the detection of very small mechanical strains, making it possible to accurately measure the mechanical properties of individual cells. Second, the transparent and biocompatible nature of PDMS allows for non-invasive imaging of the cells as they flow through the microchannel. Finally, the ability to fabricate these microchannels using standard photolithography techniques makes them easy to integrate with other microfluidic devices [392]. Overall, ZnO-based PDMS active microchannels offer a promising platform for cell

diagnosis, and further research is needed to explore their potential for use in a wide range of applications in the field of treatment of cancer.

Cancer cells proliferate uncontrolled and rapidly, producing malignant tumors and affecting surrounding organs [393]. Chemotherapy is an important treatment technique that involves potent chemicals to kill uncontrolled dividing cells mostly targeting cancer cells [394]. It induces multidrug resistance (MDR) in cancer cells, a significant obstacle to cancer treatment [395], [396]. These side effects need unique biocompatible treatment. Several researchers have explored mechanical vibration as a possible therapeutic work on the principle of resonance [289], [397]. Any structure may experience resonance, which is characterized by sensitivity to a certain vibration frequency [398]. At the resonant frequency, the system oscillates with the maximum amplitude which results in the failure of the system. As a result of the peculiarities of the physical system parameters, every organ and cell in the human body has a natural resonance frequency. Resonance-dependent therapeutic methods are used to kill the cancer cells based on their resonance behavior [321], [399]. These methods rely on the notion of resonance, which states that displacements in the cells will be amplified till their inherent resonant frequencies. This would annihilate the cellular system. Therefore, the natural frequency of the cell is an important parameter. These methods work on low to high range of frequencies for the treatments. However, high-frequency mechanical vibration may destroy cancer cells while injuring adjacent healthy cells. Hence it is necessary to evaluate the natural frequency of the flowing cells and easy to target by controlling the frequency of the external excitation. In microfluidics, the primary benefit is that piezoelectric actuators enable active control of interfaces between microchannel boundaries, particles, and fluids. Two types of interfacial actuation are possible, depending on the actuation signal [371], [383]: (1) high amplitude and low frequency (usually 100 µm and 1 MHz) and (2) high frequency and low amplitude (typically, 100 MHz and 1 µm). The piezoelectric actuation in the microchannel regulates and control the transport of biological particle. Furthermore, these actuations can be used for diagnosis and selectively targeted treatment of severe diseases. In this work, we synthesized the ZnO nanoparticle (NPs) and fabricated the piezoelectric-based microchannel. Structural and chemical characteristics of the nanoparticle were examined using a scanning electron microscope (SEM), and their mechanical and electrical properties were estimated using experimental techniques and numerical modeling. Flow studies were carried out on the hepatocellular carcinoma cell line (Huh-7) under the actuation of the microchannel at a different range of amplitude and frequency. The impact of the actuation on the flowing cells was estimated using high-speed camera imaging. This work focused on piezoelectric actuation to regulate the transport of biological particles as well as morphological changes in the cell while flow, which has direct application to lab-on-a-chip approaches in cell separation and diagnosis.

The cells used in our experimentation were provided by our collaborating laboratory (Prof. Rajdeep Chowdhury and Dr. Sudeshna Mukherjee Lab.). This section on cell culture and the biological assay of the cells was performed by Mr. Nizam Ahmed and included in this thesis

solely for the purpose of completeness. As the author of the thesis, I did not carry out the cell culture and biological assay part of this work.

## 7.3 Material and Methods

### 7.3.1 Materials

Zinc sulfate heptahydrate powder (ZnSO4.7H2O), sodium hydroxide (NaOH) pellets, polydimethylsiloxane (PDMS), and sulfuric acid (H2SO4) of AR grade were purchased from Merck Specialties Pvt. Ltd. and used as received. DI water was used as the solvent.

#### 7.3.1.1 Fabrication of piezo ZnO nanoparticles.

The sulphate bath consisted of 50 g of $ZnSO_4.7H_2O$ and 15 ml of aqueous $H_2SO_4$ diluted in 500 ml DI water. The burette was filled with 0.3 M NaOH(aq.) and placed on top of the sulphate bath. Then, a probe sonicator (ultrasonic frequency of 20 kHz and ultrasonic power of 500 W) was placed in the sulphate bath and continuous agitation was provided to the solution using a magnetic stirrer at 90 °C of temperature, as shown in Figure 7.1. The running drops of NaOH(aq.) in the heated sulphate bath at a flow rate of 3 ml/min to fabricate ZnO nanoparticles. Here, a strong acidic solution of sulphate bath reacts with strong base drops of NaOH(aq.) to form nanosized particulates of ZnO. Then, obtained ZnO nanoparticles were separated from the sulphate bath using a centrifuge and washed several times with DI water. Thereafter, ZnO nanoparticles were dried in a rotary evaporator at 70 °C for 60 min and stored in an inert amber glass vial.

#### 7.3.1.2 Characterisation of ZnO nanoparticles.

Microstructure of as-prepared ZnO nanoparticles was assessed by X-ray diffraction (Rigaku MiniFlex-I XRD with CuK$\alpha$ radiations, wavelength $\lambda = 1.54050$, The surface morphologies were obtained using field emission scanning electron microscopy (FESEM, FEI-Apreo-S).

#### 7.3.1.3 Fabrication of piezo ZnO/PDMS microchannel

A detailed schematic of the microchannel fabrication is shown in Figure 7.1. In this work, the microchannel was designed with the help of commercial software (SOLIDWORKS®, Dassault systems). Microfluidic channels were used to study the cell physiology inflow and the effect of stresses on cancer cells due to external actuation on the channel boundary. Modeled geometry

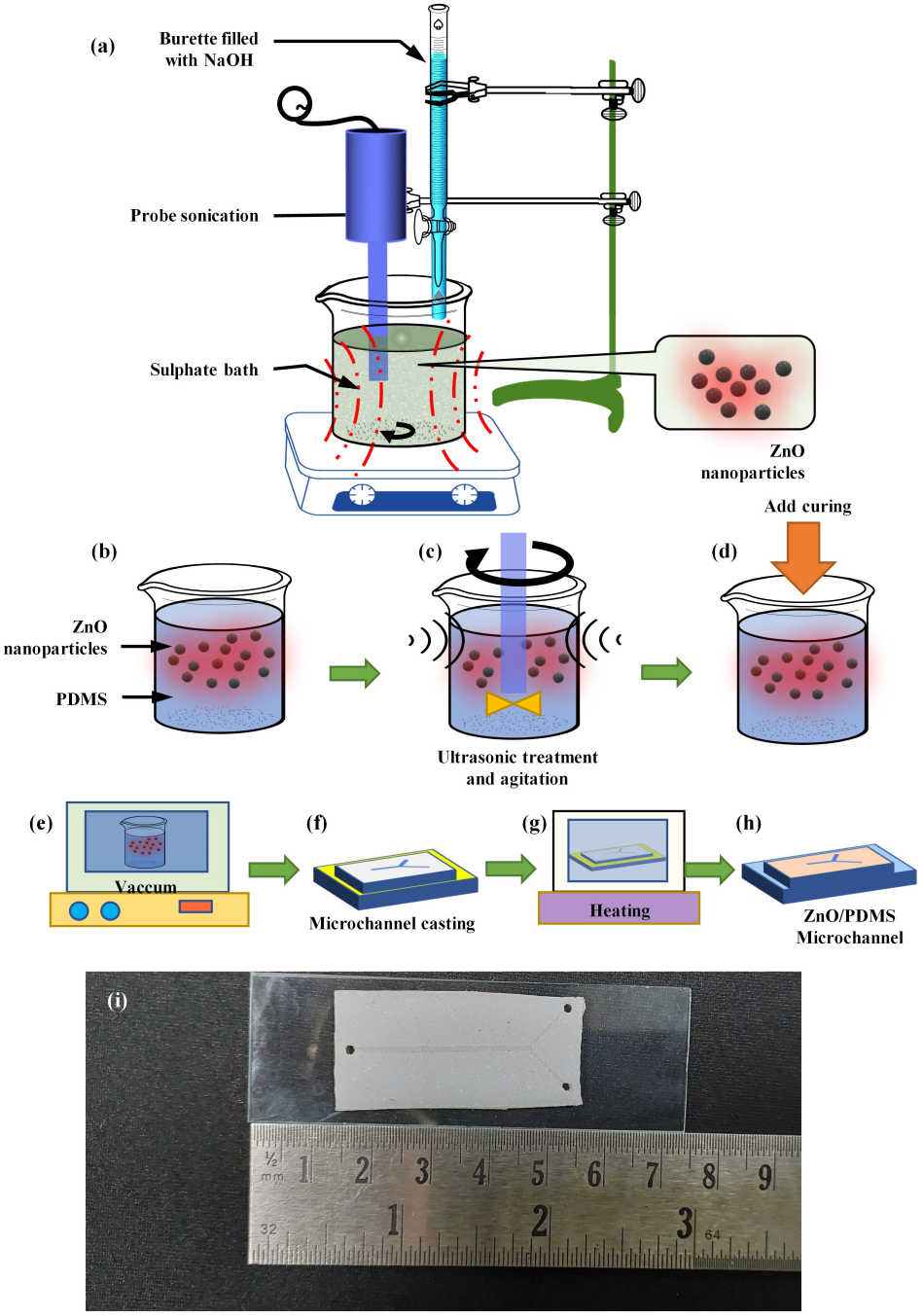


FIGURE 7.1: The schematic shows the fabrication of piezo ZnO /PDMS nanocomposite.

converted in STL format for the laser-guided engraving 3D printer (2.0 Modular 3-in-1, Snapmaker). The mold was prepared from the printer for the fabrication of the microchannel. PDMS is a well-known polymeric organic compound and due to its ability to be biomimetic, non-reactive, non-toxic, non-flammable, and transparent makes it suitable for the purpose of biological application and imaging. PDMS and hardener were mixed in a 10:1 ratio and synthesized ZnO NPs were added to the mixture and properly mixed for 10 minutes. After mixing, the mixture was poured into the mold and degassed with the help of a desiccator and vacuum pump for 2 hours. After

degassing, the mold was kept in the furnace at 70 °C for 4 hours. As the PDMS gets solidified, the prepared microchannel peels off from the mold. Thereafter, the desired open microchannel was obtained on the PDMS layer. Detailed steps are illustrated in Figure 7.1 (a-h). Bonding of obtained PDMS microchannel with the glass slide was carried out using plasma treatment. Oxygen plasma bonding is the technique in which oxygen plasma removes the organic compounds and chemically reacts with high reactive oxygen radicals and leaving the silanol (SiOH) on the surface making the surface hydrophilic and increasing surface wettability used for bonding. The plasma bonding sticks and seal the fabricated microchannels with the glass slide. Figure 7.1 (i) shows the fabricated glass bonded ZnO/PDMS microchannel.

### 7.3.2 Mechanical and electrical characterization of the microchannel.

A detailed experimental setup for electrical and mechanical characterization is depicted in Figure 7.2. The sample was kept fixed at the ends. Terminal wires were inserted at the center of the sample along the depth near the fixed ends. A function generator was used for input signals to the actuation while an oscilloscope was used to measure the output electric potential. The structure was actuated through the sinusoidal potential to an external terminal of the piezo-based microchannel under different voltages using a function generator (AFG 1102B, Tektronix). Furthermore, mechanical characterizing was done using the point load method. In the point load method, the load is applied at the center of a microchannel with the fixed-fixed end configuration. Subsequently, a different point load was applied at the center and the developed electric potential was measured through the oscilloscope.

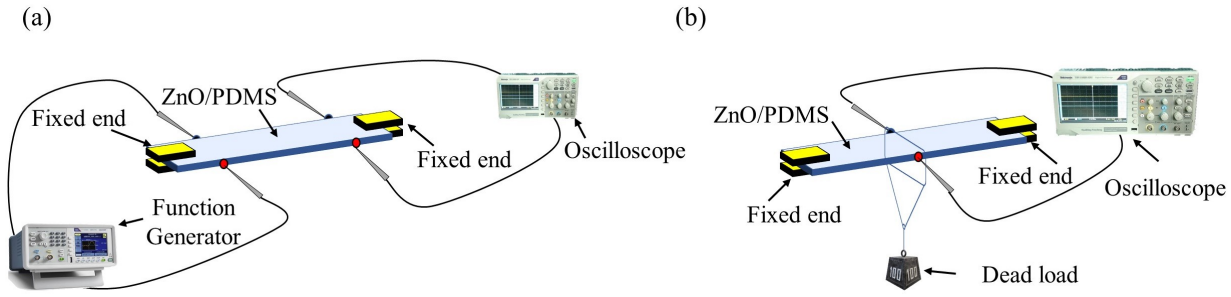


FIGURE 7.2: Detailed experimental setup for evaluating mechanical and electrical characterization of the ZnO /PDMS microchannel.

### 7.3.3 Cell culture and viability analysis

#### 7.3.3.1 Maintenance of HCC cell lines

The Hepatocellular Carcinoma cell line Huh-7 (procured from National Centre of Cell Sciences (NCCS), Pune) was cultured in DMEM (Dulbecco's Modified Eagle Medium, Hi− Media) with 10

% FBS (Fetal Bovine Serum, Hi-Media) (v/v) and 1 % Penstrep (Gibco) (v/v) and maintained at 37 °C in 5 % $CO_2$ in a carbon-dioxide incubator. The required amount of cryovials was made for all the cell lines and stored for further use in -80 °C.

#### 7.3.3.2 Cell flow through actuating microchannel

Huh-7 cancer cells were cultured in 10 cm cell culture dishes for 24 hrs. After cells reached up to 80-90 % confluency, we trypsinized the cells and centrifuged them at 2000 rpm. After centrifugation, the cells were resuspended in fresh 2ml DMEM media supplemented with 10 % FBS. Cells were subjected to flow with the flow rate of 200 µl/min through the microchannel using a peristaltic pump and analyzed at different actuation in the microchannel while the control cells flowed through the channel with no actuation. The entire experimental system was placed in a sterile condition for 1 hr at 37 °C.

#### 7.3.3.3 Cell death assay

After every condition with amplitude and frequency, we took out 50 $\mu$l of cell suspension. The cell suspension was mixed with 50 $\mu$l of 0.4% trypan blue and incubated at room temperature for 2 minutes. After 2 minutes 10 $\mu$l of the mixture was loaded in hemocytometer slides and cells were counted under a compound microscope with 20X objective. Dead cells were stained with trypan blue while the dye could not stain the live cells due to cell membrane integrity [400].

### 7.3.4 Cell morphology analysis

Figure 7.3 (a) shows the experimental setup for the measurement of the morphological changes observed in the cells during the flow under different actuation cases. An illustration of the working of the experimental setup is shown in Figure 7.3 (b). Glass bonded ZnO/PDMS microchannel was placed under the optical microscope. Cells continuously flowed in the microchannel through the inlet and outlet tubing. A function generator was used to control the actuation within the piezo microchannel. A high-speed camera was attached to the microscope to continuously monitor and record the changes in the cell morphology. Cells with distinct boundaries were traced and analyzed with ImageJ [401]. The circularity index (C) as the ratio of the major axis dimension (D) to the minor axis dimension (d) was measured to comprehend the geometrical alteration in the cells under different actuation.

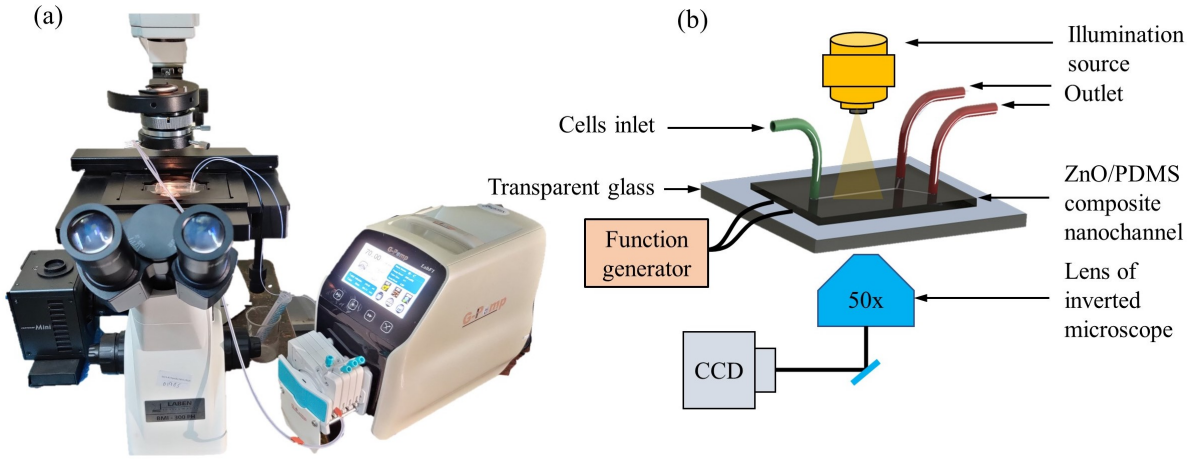


FIGURE 7.3: Detailed setup for measuring morphological changes in the cellular structure during the flow of cells in the microchannel. (a) An experimental setup showing a microchannel (without actuation) with the inlets and outlets placed under the microscope connected to the micro syringe pump (at the right) and a High-speed camera attached to the microscope at the left. (b) detailed view of the flow of the cells through the actuating microchannel.

### 7.3.5 Experimental frequency response

Figure 7.4 shows the detailed working of the experimental setup for the frequency response of flowing cells through the prepared ZnO/PDMS microchannel. In this work, cells flow through the microchannel at the flow rate of 100 $\mu$l/min. A laser source (RLM650TA-020R, Laser century) was used with a maximum of 23 mW and 650 nm wavelength powered by an external AC Voltage source of 240 V and 50 Hz. The flowing cells through the microchannel were pre-trypsinized to avoid surface adherence during experiments.

The position of the cancer cell in the microchannel was traced using an inverted microscope with 50X objective. A position-sensitive device (PSD) was used as an optical position sensor (OPS), which can detect the incident laser in two-dimensional space and trace the cell movement during the flow. The laser is focused and impinged on the flowing cell surface and gets refracted to the PSD-based sensor. The output voltage from the PSD-based sensor circuit corresponds to cell displacement in the X and Y directions and was measured by the oscilloscope (MSO46 model, Tektronix). Inlet and outlet connections through the reservoir using polypropylene tubing are shown in Figure 7.4. We measured the background frequency response from the microchannel (without flowing the cells) and recorded it as a support response. Subsequently, the frequency responses of a microchannel with flowing cells were measured. Note that each displacement of the cells and support and their corresponding frequency response was continuously recorded for a different actuation condition to obtain the experimental mean values. The different cases of actuation conditions for continuous frequency response measurements are shown in Table 7.1. The range of frequency and amplitude for the actuation was selected from the previous literature [383]. Fundamental frequencies of flowing cells were obtained from the experimental mean value

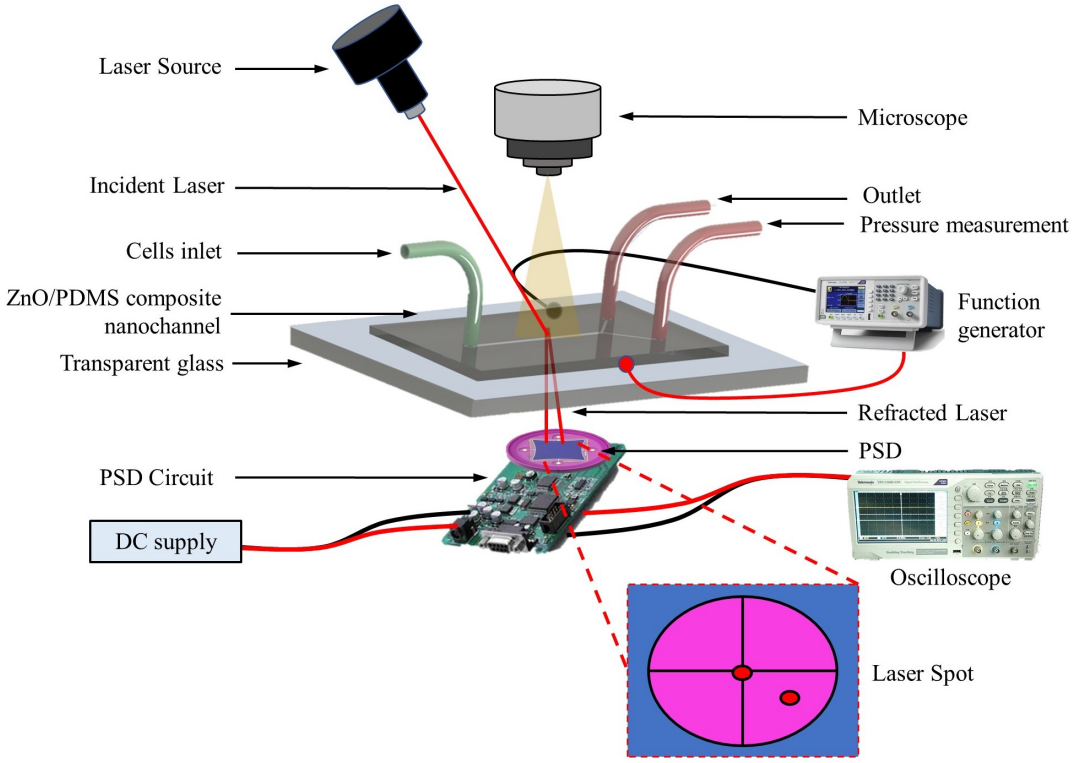


FIGURE 7.4: Detailed experimental setup for the measurement of the frequency response of the flowing cells through the microchannel.

TABLE 7.1: Different cases of the vibration conditions to the microchannel

| Cases | Actuation Type | Amplitude (µm) | Frequency (MHz) |
|---|---|---|---|
| 1 | Control | - | - |
| 2 | Low-Low | 1 | 1 |
| 3 | Low-High | 1 | 100 |
| 4 | High-Low | 100 | 1 |
| 5 | High-High | 100 | 100 |

of frequency responses for different cases of actuation [216].

## 7.4 Result

### 7.4.1 Characterization of ZnO nanoparticles

#### 7.4.1.1 Microstructure and morphology

The XRD graph of prepared ZnO nanoparticles is shown in Figure 7.5a. The diffraction peaks of XRD at different can be indexed to the hexagonal wurtzite structure of ZnO. Wherein the characteristic peaks of ZnO were obtained at 31.9°, 34.5°, 36.3°, 47.6°,56.6°, 62.9°, 66.5°, 68.0°,

and 69.3° correspond to the (100), (002), (101), (102), (110), (103), (200), (112), and (201) planes (JCPDS No. 36-1451), respectively[402]. Due to the strong diffractions of ZnO, the characteristic peaks of GO at around $26.50^0$ corresponding to the (002) plane was masked [374].

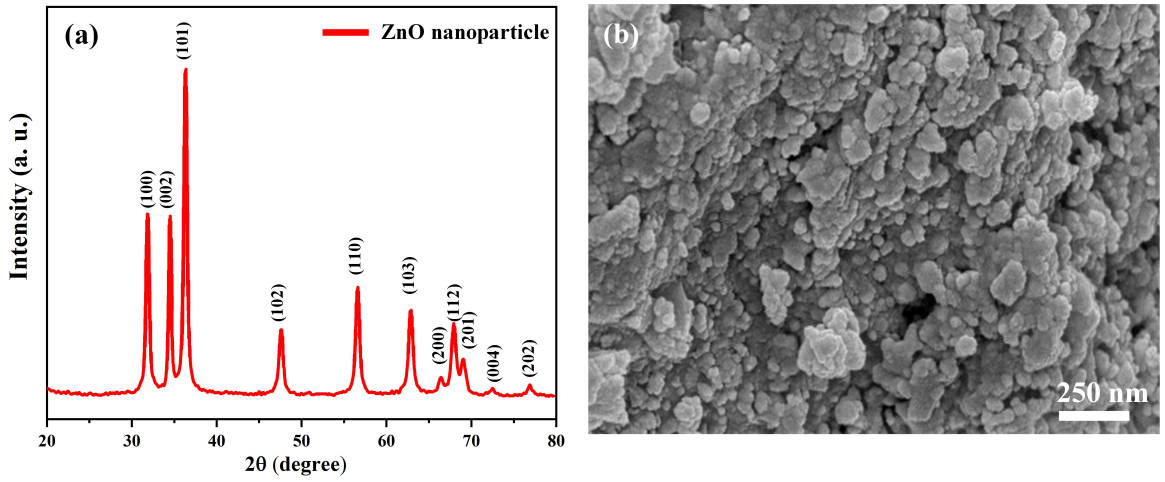


FIGURE 7.5: Material characterization of the ZnO nanoparticles.

The crystallite size of composites from the full-width half maximum (FWHM) of the (101) plane was calculated using the Scherrer equation as shown in Equation 7.1[403].

$$D = \frac{\kappa\lambda}{\beta \cos\theta} \tag{7.1}$$

here $\beta$ is FWHM in radians, $\kappa$ is Scherrer constant, $\lambda$ is the wavelength of Cu−K$\alpha$ radiation, D is the crystallite size in nm and $\theta$ is the angle of diffraction. The crystallite sizes of 33 nm were calculated for prepared ZnO nanoparticles. The SEM image of ZnO nanoparticles is displayed in Figure 7.5b. The SEM result confirms the successful fabrication of the granular shape of ZnO nanoparticles.

### 7.4.2 Mechanical and Electrical characterization of the piezo material based microchannel

Figure 7.6a shows the developed electrical potential under different applied sinusoidal voltage. It can be observed that the piezoelectric potential is developed and increases with the increase in the applied electrical voltage. 200 mV of electrical potential developed with the 8V peak-peak applied potential. Mechanical characterization based on the point load subjected to the microchannel lead to the generation of the electric potential due to the piezoelectric effect. After polarization, all the ZnO (piezoelectric particles) grain particles get polarized and align themselves. Proper alignment of the grain particles improves the voltage characteristic of the piezoelectric material

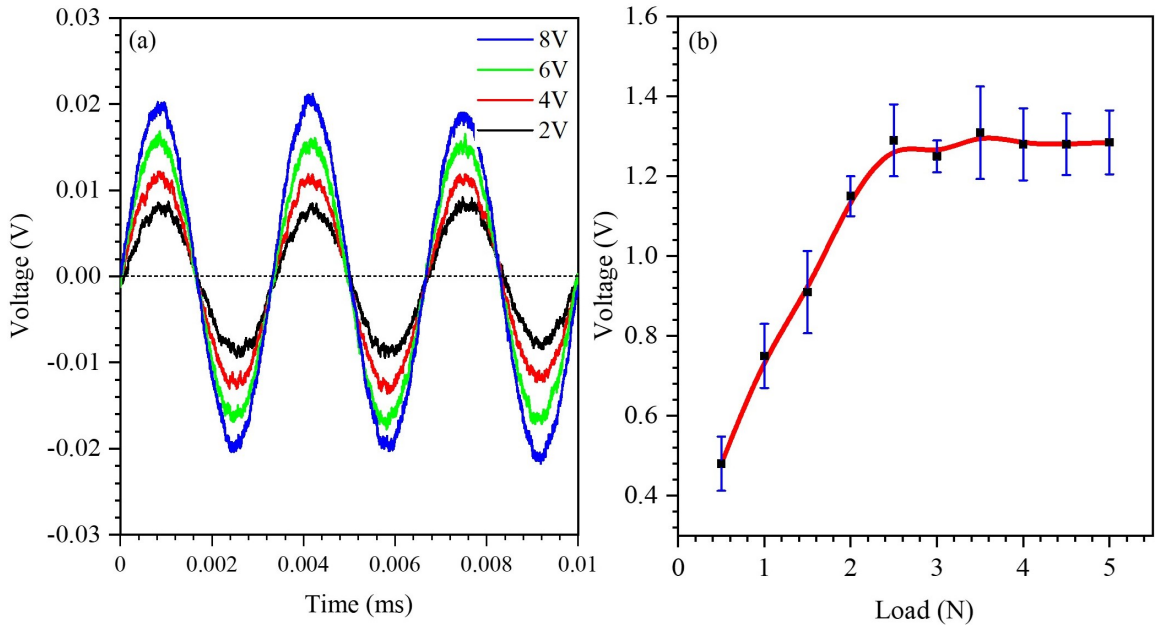


FIGURE 7.6: (a) Electrical characterisation of the ZnO/PDMS based microchannel. (b) Mechanical characterization of the ZnO /PDMS based microchannel.

in the microchannel. Thus increasing the piezoelectric effect of the microchannel. Microchannel subjected to different loading develops substantial electric voltage. It has been observed from the Figure 7.6b that there is a linear increase in the potential generation with an increase in the point load of 2.5 N. Further, with an increase in the point load remains the constant output voltage of 1.32 V. Thus, output potential within the range shows the significant piezoelectric effect generated by piezo material-based microchannel.

### 7.4.3 Morphological changes

High contrast images obtained from the high-speed imaging camera during the flow of Huh-7 cells in the microfluidic channel under different actuation cases, as shown in Figure 7.7. It has been noted that cells experience changes in shape as they flow through the actuating microchannel, as seen through changes in the circularity index (ratio of major diameter to minor diameter) as previously mentioned. Figure 7.7 (a-e) shows the morphological changes observed in the cellular structure. Control cells without actuation in the channel attained circular shapes during the flow. Circular shapes tend to possess more polygonal shapes and are observed to be changed in an elliptical while flowing through the microchannel. The cellular structure was elongated in the direction of flow, resulting in an increase in the circularity index, as depicted in Figure 7.7 (f-j). It has been observed from the histogram plots that the circularity index increases with the increase in the amplitude and frequency of the actuation. High-High case shows the maximum value of the circularity index as $1.26 \pm 0.15$. In this case, more elongation in the cellular structure was observed as compared to the other cases.

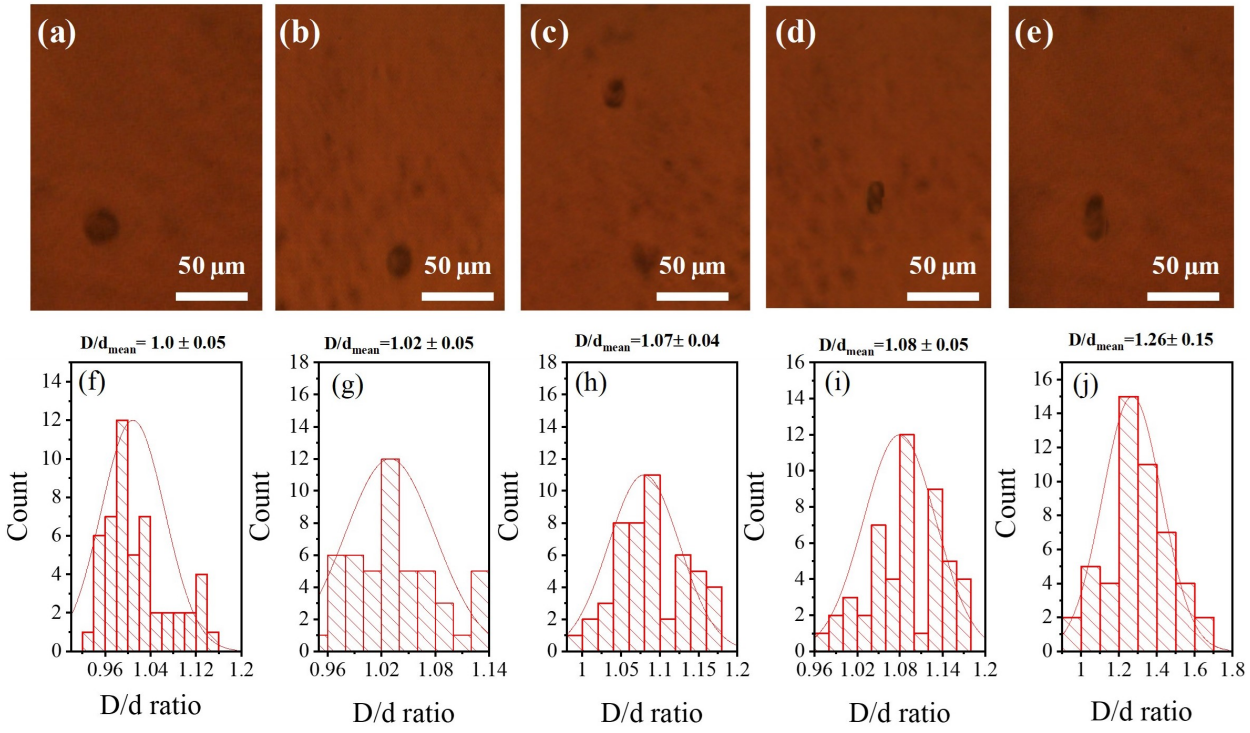


FIGURE 7.7: (a-e) High-speed camera images demonstrate the cells' sequential geometrical changes while flowing through the microchannels at different external actuation cases. (f-j) Changes in major to minor ratio for the different cases.

### 7.4.4 Experimental Frequency Response

Measurements were taken near the bifurcation part of the channel to capture the cells' maximum possible dynamic stress behavior. The transient response of the cells is acquired during the flow of the cells in the channel. Acquired time domain data were converted in the frequency domain using Fast Fourier Transform (FFT). The peak in the frequency spectrum represents the natural frequency of the cells. Figure 7.8 (b-c) shows the frequency response for the flowing cells and the channel base. The obtained transfer function of the cell with respect to the base to remove all base-related modes is shown in Figure 7.8d. The figure shows the transfer function of cell response with prominent peaks. These peaks represent the significant natural frequency by eliminating the influence of support and other influencing noise operating on the supports. The transfer function shows the natural frequency at 332 kHz for cells at the initial flow time. The obtained transfer functions of the flowing Huh-7 cells for different cases of actuations are represented in Figure 7.9. A significant shift in the natural frequency of the flowing cells was observed from the experimental data. It was noted that the natural frequency of flowing cells decreased by increasing the vibration actuation across the flow.

Furthermore, it has been observed that control cells possess a natural frequency of 331.42 kHz. A significant decrease in the natural frequency was observed for the different cases of external actuation. A maximum increase in the amplitude and frequency of the actuation (High-High)

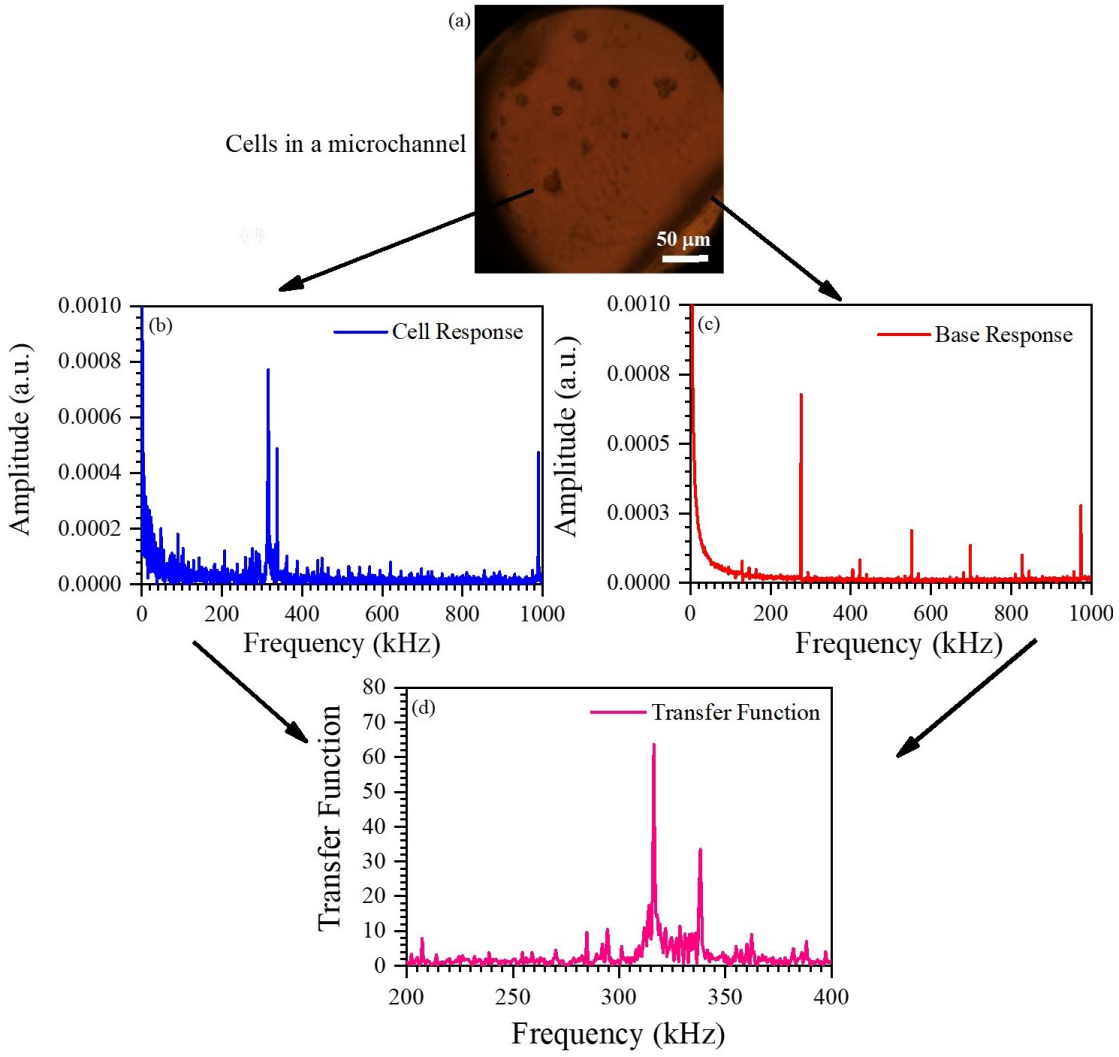


FIGURE 7.8: (a) High-speed camera image shows the flowing cells in the microchannel. (b) Frequency response of the cellular structure. (c) Frequency response of the base. (b) corresponding transfer function

reduces the natural frequency by 22.72 % compared to the control. External actuation leads to morphological changes in the cell. Thus, all cases observed a decrease in the cell's natural frequency.

### 7.4.5 Cell death analysis

Huh-7 cell suspension flowing through the microchannel was subjected to different cases of actuation whereas control was the case of without vibration. The result showed cancer cells became fragile to High–High and progressed to cell death. Trypan blue staining to dead cells confirms the increased cell death for the case of high actuation and with cell additive effect. Compared to control, there was increased cell death for cases with vibrations; here, Low–Low showed 19% cell death while High–High showed 61% cell death (Figure 7.10).

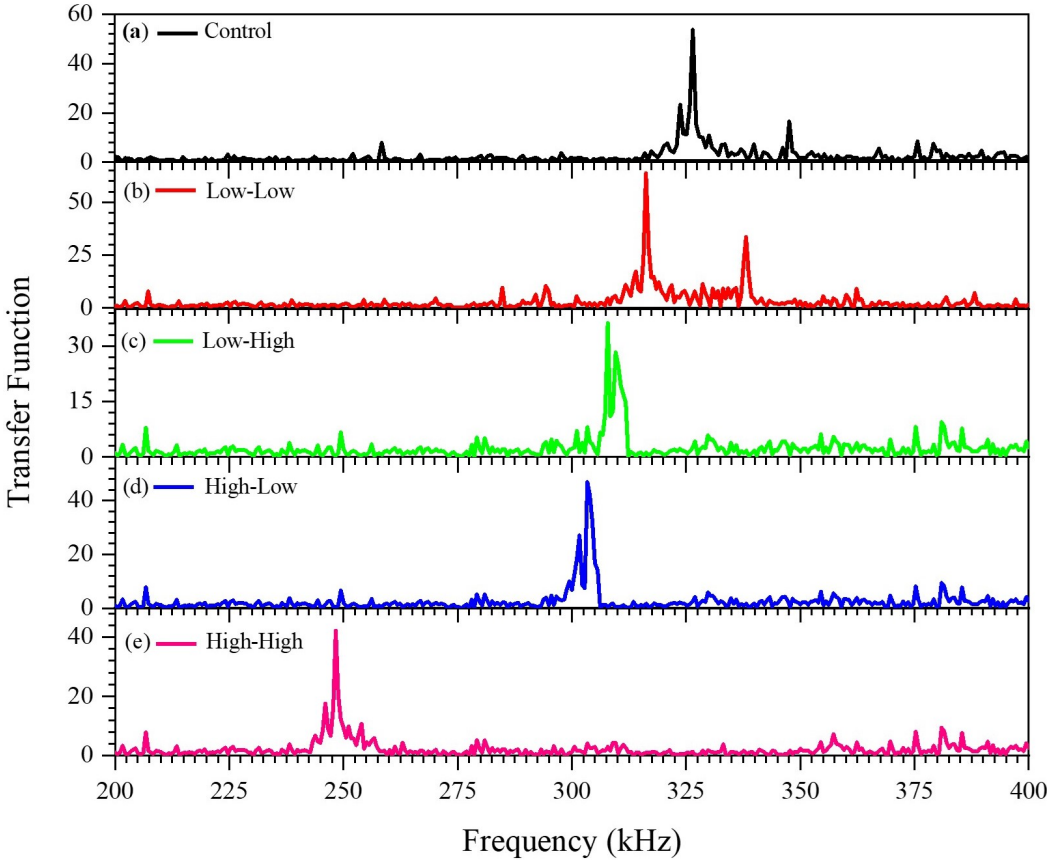


FIGURE 7.9: Frequency response graphs demonstrate the alterations in the fundamental frequency of the cells while flowing through the microchannels under different cases of actuation. peaks in the transfer show the frequency for (a) Control (b) Low- Low (c) Low-High (d) High-Low (e) High-High.

## 7.5 Discussion

The microstructure of the ZnO NPs that was prepared was determined using XRD and SEM analysis. The diffraction peaks of XRD can be indexed to the hexagonal wurtzite structure of ZnO. Due to the strong diffractions of ZnO, the characteristic peaks of GO at around $26.50^0$ corresponding to the (002) plane was masked [374]. The broadening of peaks was mainly due to the decreasing crystallite size of decorated ZnO NPs of a composite at higher temperatures. The SEM result confirms the successful fabrication of the granular shape of ZnO NPs. The particles are agglomerated in different groups. However, the agglomerated particle can be disintegrated by ultrasonication and mixing with PDMS solution.

In mechanical characterization, the point load was subjected to the microchannel cross-section led to the output signal generation as an electric potential due to the piezoelectric effect [404]. Microchannel subjected to different loading conditions ranging from 0.5 N to 5 N, which developed substantial electric voltage, as shown in Figure 7.6b. It has been observed that there is a linear increase in the potential generation with an increase in load up to 2.5 N. Further, with an

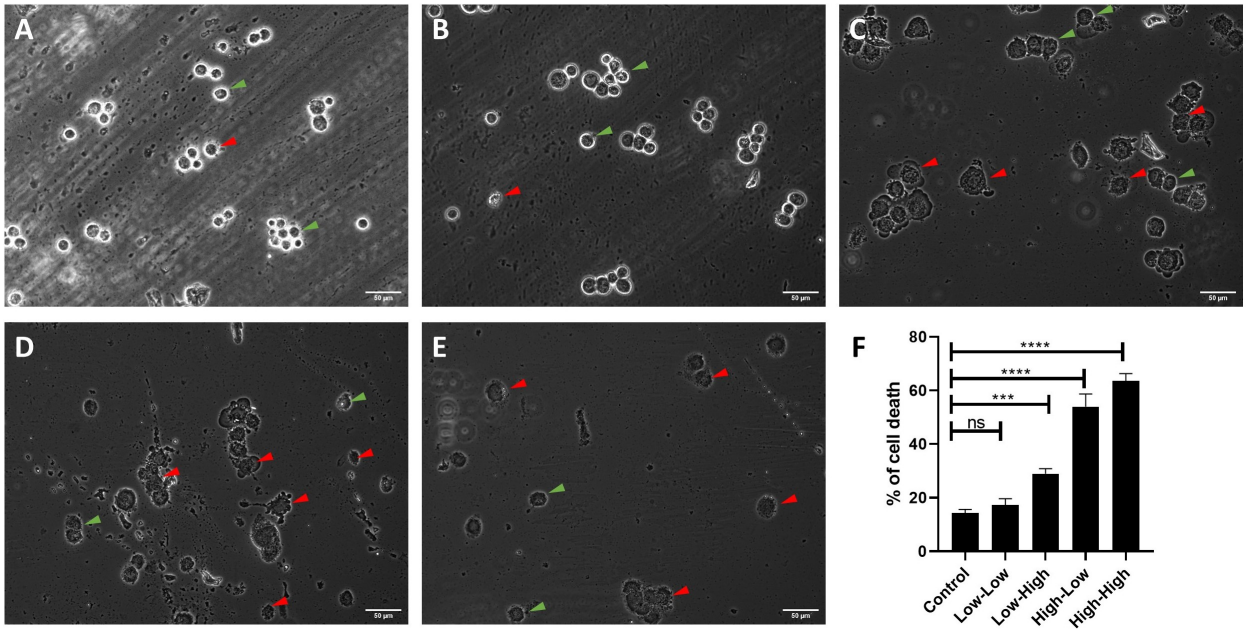


FIGURE 7.10: Trypan blue staining. Optical microscopic images of the Huh-7 cells treated with various actuation conditions on the ZNO/PDMS microchannel with a time interval of 2 hrs. The cells were stained using trypan blue dye after the vibration treatments to examine cell death. The cells indicated by red arrows are some examples of dead cells that turned blue after staining for different actuation conditions (a) control (b) Low–Low (c) Low–High (d) High-Low (e) High-High (f) % variation in the cell death after the actuation. Results are presented as means ± SD. $***$ p <0.01.

increase in load, a constant output voltage of 1.32 V was recorded. Thus, output electrical signals showed the significant piezoelectric effect generated by the prepared ZnO/PDMS composite used to develop an active microchannel. Next, the morphological changes in the cells were observed while flowing the piezo microchannel. It has been observed that the cells undergo deformation while flowing through the actuating microchannel. Cellular deformation results in morphological changes in the cells. These changes were quantified in terms of the circularity index parameter as discussed in the previous section. Figure 7.7(a-e) compares the morphological changes observed in the cellular structure. Control cells without actuation in the microchannel maintained their circular shapes during the flow. These circular morphologies tend to be polygonic and changed towards elliptical with increases in vibration actuation (amplitude and frequency). This elongated structural morphology of cells was measured through image processing software. The observation shows that an increase in the circularity index was recorded for high actuation cases, as represented in Figure 7.7(f-j). High-High actuation condition shows the maximum circularity index of 1.26 ± 0.15, which was 19.04 % higher than that of 1.02 ± 0.15 for the case of Low−Low actuation condition. These results reveal that the higher actuation causes vibrational stresses and changes the cellular stiffness [261] and thus, evident morphological changes were observed. The structural deformation with high stresses leads to cell damage at resonance and may lead to cancer cell death [265]. Further, experimental frequency response was obtained through the non-contact PSD measurements.

The transfer function of cell response with the prominent peaks in the natural frequencies of cells [405]. The natural frequency of control cells was observed at 332 kHz. Similarly, the natural frequencies of the flowing cells were obtained for all actuation cases. The obtained transfer functions of the flowing Huh-7 cells for different cases of actuations are represented in Figure 7.9. A significant shift in the natural frequency of the flowing cells was observed from the experimental data. It was noted that the natural frequency of flowing cells decreased by increasing the vibration actuation across the flow. The cell natural frequencies of 248.24± 42.13 kHz are observed for High–High actuation, which is 31.37 % lower than that of 316.13 ± 53.58 for Low–Low actuation. Meanwhile, moderate cell natural frequencies of 308.15 ± 24.28 and 314.64 ± 34.68 kHz are observed in Low–High and High–Low actuation conditions, respectively. The cell's natural frequencies are a direct function of cellular stiffness. As observed from the circularity index analysis (Figure 7.7), high actuation causes cell deformities and morphological change that may possibly reason for changes in cellular stiffness, thereby, changes in cell natural frequencies. Therefore, the highest cell natural frequencies of 326.46 ± 28.84 kHz were obtained for stiffer morphology of control cells in the case without vibrations. Notably, the resonance condition in the cellular system may lead to cell damage and even death.

Moreover, for validation of the resonance effect on the Huh-7 cells, further biological cell viability assay has been performed. The results showed that the cancer cells became fragile under High-High actuations and progressed to cell death. However, it's possible that the high actuation may have caused mechanical stress on the cells, leading to damage to their structural integrity and eventually death. Additionally, the High-High actuations might have induced an increase in the production of reactive oxygen species (ROS) which can damage the cells and induce cell death as reported in the previous studies [77], [406]. Confirmation of increased cell death was made through Trypan blue staining of dead cells. Compared to the control, there was a significant increase in cell death for cases with vibrations. Specifically, Low-Low actuations resulted in a 19% increase in cell death, while High-High actuations resulted in a 61% increase in cell death. It's worth noting that more information about the actuation process and the cellular response would be needed to understand the exact mechanism by which the cancer cells died.

## 7.6 Conclusion

In this work, ZnO/PDMS-based piezo microchannel was fabricated. Huh7 cells were analyzed while flowing through the channel. The morphological changes were observed in the cell during their flow through the microchannel under different actuation conditions. High-High actuation condition leads to a maximum circularity index within the cells. A higher circularity index tends to maximum geometrical changes that were observed for maximum amplitude and frequency actuation cases. Further, a non-invasive technique was used to determine the frequency response

of the flowing cells in the microchannel. Fundamental frequency was observed around 326.46 ± 28.84 kHz for the case of the cells flowing through the microchannel (without actuation) similarly for the High-High case it decreases to 248.24± 42.13 kHz. It was observed that there has been 21.51% decrease in the fundamental frequency of the cells with an increase in the actuation frequency from Low−Low to High−High case. Similarly, findings revealed that the cell possesses higher shear stresses and deformation which results in higher geometrical changes with the increase in the mechanical vibration. In conclusion, it is possible that mechanical properties and vibration characteristics are influenced by fluctuations in fundamental frequencies and vice versa, which are a result of ambient conditions and external stimuli. Consequently, these results are useful for the development of a device based on resonance in diagnosing the state of malignant disease.

# Chapter 8

# Atomistic analysis of effect of cholesterol on cancerous membrane protein system: Unfolding and associated resistance stresses under strain

## 8.1 Background

Cancer is a complex and devastating disease that affects millions of people worldwide. One of the critical factors that contribute to the development and progression of cancer is the abnormal behavior of cells within the body. Various factors, including genetic mutations, environmental factors, and interactions between different molecules and pathways within the cell, can cause this abnormal behavior.

One area of interest in cancer research is the role of membrane proteins and cholesterol in the development and progression of the disease. Membrane proteins are responsible for a variety of functions within the cell, including communication, transport, and signaling. These proteins are integral to the function and stability of the cell membrane, which is a critical barrier that surrounds and protects the cell. Cholesterol is another important molecule that plays a vital role in the structure and function of the cell membrane. It is a type of lipid (fat) that helps to maintain the fluidity and stability of the membrane, and it also plays a role in the transport of other molecules into and out of the cell. The experimental techniques have limitations of control, temporal resolution, cost, and time associated with it. However, Molecular simulations, on the other hand, can provide much higher spatial resolution, allowing researchers to study processes

at the atomic level at any desired time scale. It can precisely control the studied conditions, making it easier to isolate and study specific processes.

Hence in this chapter, molecular dynamics simulations are used to study the impact of cancerous membrane proteins and cholesterol on the membrane system under a strained environment. The transmembrane protein system behavior during lipid-bilayer separation at different cholesterol concentrations was investigated with their structural parameters. Stretching and unfolding of embedded protein and the associated resistance stresses on decreasing cholesterol during bilayer separation were studied. It's important to investigate the impact of the level of cholesterol in the membrane and look at the diffusion and protein resistance during straining at high concentrations. Studying the biophysical behavior of the membrane protein system leads to understanding the mechanosensitivity of transmembrane proteins under mechanical perturbation. The findings can help researchers to identify potential targets for new cancer therapies, which could lead to more effective treatments for this devastating disease.

## 8.2 Introduction

Complex protein dynamics is regulated by the local environment of permeable and impermeable cell membranes that compartmentalize intracellular space [407]. The transmembrane insulin receptor (IR) proteins provide the terminal ends for signaling and regulatory functions from cells to external stimuli [408]. The exposed domain of the protein receptors frequently contains ligand binding sites to connect with intracellular and extracellular proteins to perform regulatory functions [409]. Whereas the cell membranes are comprised of a viscoelastic structure that is directly engaged in critical mechanical phenomena such as; exocytosis and endocytosis, tethering, adhesion kinetics of molecules, fluidity, and migration processes [410], [411]. Due to the complexity associated with the biological cell membranes, it is a common method to replace them with model membranes, especially, lipid bilayers with transmembrane IR proteins [412]. These models can mimic the essential biophysical properties of the plasma membrane-associated with the cytoskeleton. Any changes in the lipid bilayer membrane including the composition of inner and outer leaflets, such as cholesterol concentration, water content and ions can critically affect the functioning of the transmembrane proteins [413]–[415].

The cholesterol found in cell membranes has a critical role in maintaining a healthy body, such as regulating neurotransmission, cell signaling, and protein sorting. Imbalanced cholesterol levels have been linked to several diseases, including Alzheimer's disease [416], cancer[417], and more. However, there is still a lack of understanding of how cholesterol contributes to essential processes in membrane protein systems.

Computational studies, specifically molecular dynamics simulations, have improved knowledge for further experimentation. Several studies provide a glimpse into the use of molecular dynamics simulations to investigate the behavior of membrane-embedded proteins [418], ions channel, aquaporins, peptides, etc in the lipid bilayer membrane system [419]–[421].

The computational modeling of a molecular system requires an initial structure of the 3D structure of cholesterol and membrane proteins that have characterized structures to understand the cholesterol-membrane protein interactions. If the membrane protein's structure is unknown, homology modeling is used to find a substitute. It is crucial to understand and know the relative position of the protein's structure, lipid membrane constituents, and cholesterols for analyzing the impact of cholesterol in any membrane protein system. However, few structures of a membrane protein co-crystallized with cholesterol exist, and identifying binding sites, if any, is necessary for studying cholesterol's effect on the protein. This can be validated through experimental methods such as NMR [422] and chemical cross-linking [423].

MD simulations provide a detailed look at the time-dependent behavior of biological macromolecules. It requires a description of the potential energy, which is usually obtained through empirical molecular force fields (FFs). The simulations can be adapted for alterations in the molecular system, such as constituents levels, type of constituents, Size of the molecular system, point mutations, etc., by controlling system variables. However, there are three main challenges in MD simulations: time-scale issues, uncertainties in empirical FFs, and approximations in the chemical system. Despite these challenges, recent advancements have allowed for atomic-level simulations at biologically relevant timescales, and biased MD methods are constantly being developed to improve sampling and the exploration of energy. For the investigation of membrane proteins, an advanced MD simulation can be used to capture both lipid bilayer self-assembly and protein-lipid interactions. To perform these simulations, FFs that have been parameterized to describe the potential energy of proteins, lipids, and their interactions must be used. Examples of these FFs include CHARMM, AMBER, and MARTINI, which are well compatible with cholesterol and other lipid molecules [424], [425]. Molecular dynamics (MD) has been widely utilized in studies on protein-lipid interactions, however, the field is moving towards more realistic membrane models as parameters for multiple lipid components become available.

A few studies based on MD simulations for membrane proteins described and shows the impact of how cholesterol affects the membrane protein system. Prakash et. al. identifies the impact of cholesterol on the transmembrane part of the ErbB2 receptor using computer-molecular simulations on both the monomers and dimer units in DPPC bilayers with varying levels of cholesterol [426]. The findings predicted that the increasing cholesterol levels in the membrane led to a reduction in the tilt angle of the helix relative to the membrane normal. This is due to an increased level of cholesterol that led to a thickening of the membrane. The transmembrane helix in ErbB2 has two GxxxG sequences which play a crucial role in its dimerization as their lack

of side chains allows the helices to fit more closely together. The study found that cholesterol generally fits more snugly around the helix compared to DPPC, with cholesterol positions along the membrane normal overlapping with the two GxxxG sequences. However, cholesterol was not found to pack around Phe671 in the helix's C-terminal, resulting in an uneven distribution of cholesterol around the helix.

Previous molecular simulation studies have aimed to correlate structure, thermodynamics, and activity in TM proteins. Fleishman et al. used molecular simulations to model the activation switch of ErbB2 activity by fixing the helix angle at -35 deg i.e.right-handed, like in GpA [427]. Results showed an interface at the C-terminus GxxxG motif (inactive state) and N-terminus (active state due to mutations). This conformational switch supports experimental data of inactive ErbB dimers in cell membranes. Beevers and Kukol et al. confirmed the presence of a right-handed ErbB2 dimer through experiments and molecular dynamics simulations in a lipid bilayer [428].

Furthermore, it has been found that the mechanical perturbation or strain to lipid bilayer can change their characteristics such as membrane thickness [429], [430], structural integrity [431], [432], and rate of diffusion [433]. These mechanically induced changes may be more crucial in the cancer environment when the cholesterol concentration continuously decreases [407], [434] and may affect the insulin receptor signaling and structure of ecto-, kinase-, and transmembrane domains of IR proteins [435]–[438]. Recently, the changes in structures of several types of IR proteins due to co-crystallized cholesterol with its concentration level have been reported [439]. Researchers have demonstrated the existence of highly organized cholesterol-rich lipids with embedded IR proteins in an unstrained lipid environment [440], which is critical for numerous biological processes [441], such as neurotransmission [442] and amyloid disorders [443]. Murphy et al. [444] have reported the studies of uniaxial and biaxial strain on the lipid bilayer membrane with variation in the cholesterol level and its impact on the individual membrane constituent and transmembrane protein function, which was in the context of nanoscale damage to the membrane and cell death. Hence it is necessary to understand the membrane–protein interaction behavior under strain. It is also important to note that, the transmembrane proteins can execute biologically important signaling and regulatory functions of cells, only when they are interconnecting across the lipid bilayer in mechanical perturbation of strain environment, [445]–[448]. Therefore, a comprehensive understanding of the properties of transmembrane protein receptors of cancer cell plasma membranes is essential for biological science and can contribute to the technological advancement in related fields such as biomedicine anti-cancer therapies and design of drug delivery nanodevices [449], [450]. However, it is quite difficult to conduct experiments on a such a nanoscale domain with limited information about the dynamics of cholesterol-protein interactions in a cell plasma membrane [438], [451]. In this work, we used the typical compositions of shahane et al. [407] to simulate cancer bilayer membrane models, which reflect the properties of transformed cancer cells at different cholesterol concentrations.

However, these models included representative lipids from a small number of common species without reflecting the complete range of lipids found in actual cells. Molecular dynamics (MD) simulations have been considered ideal for examining cholesterol's regulatory effects on IR proteins [438], [452]. Thereby, this work aimed to give insight into the effect of cholesterol bonding and interactions with membrane protein systems such as area per lipid, tilt angle, order parameter, and diffusion. Furthermore, we simulated cancerous lipid bilayer separations under a strained environment to study the cholesterol-protein interaction followed by the study of the unfolding of protein and associated resistive stresses.

## 8.3 Methods

Chemistry at Harvard Macromolecular Mechanics-GUI (CHARMM-GUI) Membrane Builder [453], [454] was used to model the cancerous lipid bilayer systems and Large-scale Atomic/Molecular Massively Parallel Simulator (LAMMPS) software [455], [456] was used for separation simulations in the strained environment.

LAMMPS and CHARMM-GUI are both software packages used for molecular simulation and modeling. Both have their own strengths and weaknesses, and the choice between the two depends on the specific needs of the user. While LAMMPS has its own modeling tools, CHARMM GUI is often preferred for its user-friendly interface and efficient energy minimization and equilibration algorithms, making it easier to model the biological system.

We started the simulation in CHARMM-GUI for its efficient energy minimization and equilibration algorithms capability, then switch to LAMMPS for its high parallel performance and ability to handle large-scale simulations, especially for the biological models with huge numbers of atoms.

Deviation of 3% was allowed between the asymmetric counterpart regions to avoid any exaggerated effects to avoid mismatch in the leaflet lipid content [407]. The homogeneous lipid subsystems were comprised of POPC, POPE, PSM, and POPS with Phosphatidylcholine (PC), Phosphatidylethanolamine (PE), Sphingomyelin (SM), and Phosphatidylserine (PS) contained 1-phosphatidyl-2-oleoyl (PO) tails. Table 8.1 provides detailed compositions of the lipid bilayer systems. Here $N_{water}$, $N_{ions}$ and $N_{atoms}$ are no· of water molecules, no· of ions and no· of atoms respectively. These molecular structures of lipid bilayer were representing cancer membranes and accordance to the derived compositions, reported by Klahn et al. [434]. Table 8.2 shows the lipid distribution in outer and inner leaflets of cancer membranes. The lipid bilayer system was modeled with decreasing cholesterol (32,16,8, and 4) molecules along with 2MFR transmembrane protein at the center. We considered the 57 residues for IR

TABLE 8.1: Composition of the lipid bilayer systems simulated

| System | Lipid Type | $N_{water}$ | $N_{ions}$ | $N_{atoms}$ |
|---|---|---|---|---|
| CHL32-Pro | PC (79), PE (101), PS (86), Chol (32), PSM (66) | 20801 | 55 | 36453 |
| CHL16-Pro | PC (79), PE (101), PS (86), Chol (16), PSM (66) | 17108 | 49 | 30386 |
| CHL8-Pro | PC (79), PE (101), PS (86), Chol (8), PSM (66) | 16100 | 47 | 28784 |
| CHL4-Pro | PC (79), PE (101), PS (86), Chol (4), PSM (66) | 15019 | 45 | 27107 |

(MTYFYVTDYLDVPSNIAKIIIGPLIFVFLFSVVIGSIYLFLRKRQPDGPLEHHHHHH that included the predicted TMD sequence (underlined) for the receptor (the sequence is based upon protein data bank www.rcsb.org/ PDB code: 2MFR).

TABLE 8.2: Lipid distribution in outer and inner leaflets of cancer membranes

| Lipids | Leaflet (outer) | Leaflet (inner) |
|---|---|---|
| POPC | 54 | 25 |
| POPE | 17 | 84 |
| POPS | 36 | 50 |
| PSM | 59 | 7 |

Each system was explicitly solvated along with water molecules and hence counterions are added for maintaining the overall charge neutrality of the system. For this study, the counter-ions used to neutralize the system are typical $K^+$ and $Cl^-$. The size of the simulation box varies with the number of cholesterol and associated composition of the membrane protein system and is the same as the size of the standard lipid-membrane-protein model obtained from the CHARMM-GUI. The molecular interactions of water molecules with the system were modeled using the CHARMM36 force field and the associated TIP3P implementation [457]. The modeled lipid-membrane systems were subjected to energy minimization followed by pre-equilibration of 1.625 ns with NPT ensemble at 310 K temperature for 2 ns before LAMMPS simulation. The systems were connected to the velocity-rescaling thermostat with a coupling time constant of 0.1 ps. All of the systems were simulated at 310 K in consistence with previous simulations of the CHARMM36 model for different phospholipids [407], [457], reproduces the correct liquid phase experimental behavior while preventing the formation of a gel phase. The lipid bilayers were aligned along the xy-plane, with the z-axis perpendicular to the membrane. Figure 8.1 shows the modeling of the membrane protein system with the inclusion of cholesterol for CHL8-PRO case. It illustrates the atomistic appearance of cholesterol and lipid membrane with transmembrane protein as a cartoon which enhance the understanding. The strain was applied along the z-direction of the system with the higher rate of $1\times10^9$ per sec [444].

We have performed consecutive simulations on a pre-equilibrated membrane protein system obtained from CHARMM-GUI. Equilibrations were performed in quadruplicate to illustrate the convergence of the outcomes. The simulation run started with the equilibration of 3 ns (including 1 ns for structural parameters and MSD calculation under stabilized energy conditions).

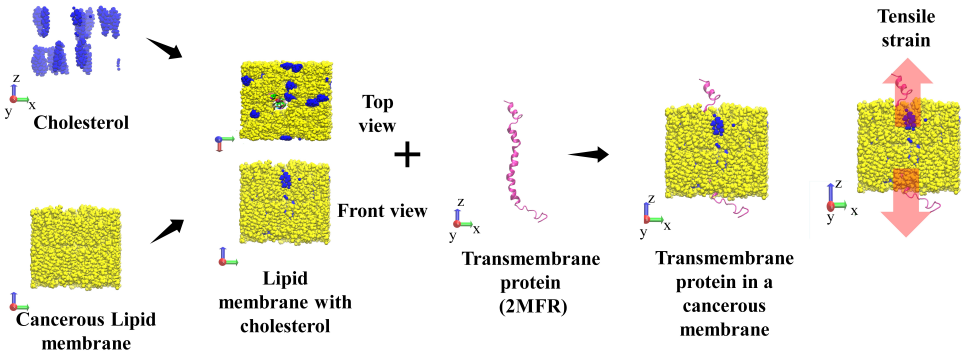


FIGURE 8.1: Modelling of membrane protein system with the inclusion of cholesterol for CHL8-PRO case. Lipid molecules are shown in yellow color, 2MFR transmembrane protein is shown in magenta color, and Cholesterols are shown in blue color. The tensile strain to the system is applied along the z-direction.

Figure 8.2 shows the equilibration performed in the initial stage of MD simulation. The system is equilibrated in a constant volume, pressure, and temperature ensemble (NPT) by applying the velocity-Verlet algorithm with time integration for all trajectories atoms at time steps of 0.001 ps. Pressure coupling was performed by utilizing the Berendsen barostat for equilibration and the Parrinello–Rahman barostat for short-range van der Waals and electrostatic cutoff, the default optimum distance of 1.2 nm was considered [458], [459]. The particle mesh Ewald (PME) method was used to compute long-range electrostatic interactions [460].

Figure 8.2 shows temperature and energy equilibration plots, that help to assess the stability and reliability of the simulation. The temperature and energy plots indicate, the system has reached equilibrium after $\approx$ 1.8 ns, which is essential for obtaining accurate results during structural parameter calculation. These plots provide valuable information about the performance and quality of the simulation, and they are essential for evaluating and interpreting the simulation results. For initial timesteps, all systems showed an abrupt change in temperature (Figure 8.2a) and potential energy (Figure 8.2b), which stabilized during the period of 3 ns. Convergence for CHL32 with protein case is shown in the supplementary Figure S3.

Started with the equilibration of 2 ns. Further, the system simulated for 1 ns to calculate the structural parameters such as area per lipid, order parameters, $S_{cd}$, and MSD. Thereafter the obtained system runs for a strained condition for 5 ns. A trial simulation of 5 ns was also performed without strain for all cases after equilibration.

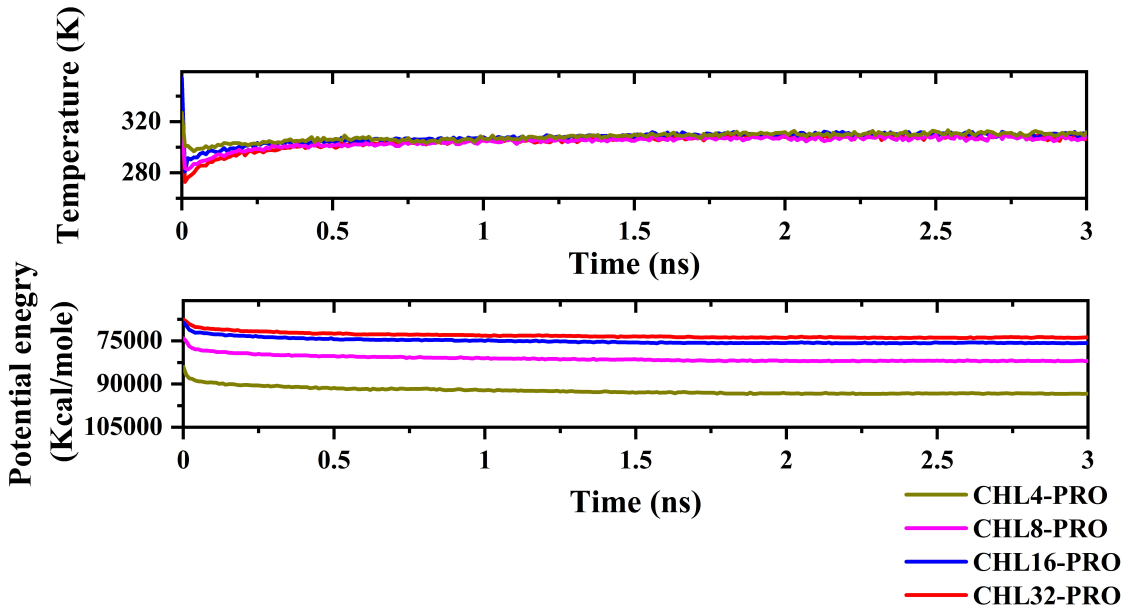


FIGURE 8.2: Equilibration of the membrane protein systems at temperature 310 K and time step 0.001 ps: (a) Temperature equilibration and (b) Potential energy equilibration.

## 8.4 Results

### 8.4.1 Structural parameters

#### 8.4.1.1 Area per lipid

The area per lipid $A_{\text{lipid}}$ is defined as the cross-sectional area at xy-plane system $A_{xy}$ divided by half the total number of lipids $N_{\text{lipid}}$ present in the bilayer, i.e., $A_{\text{lipid}} = A_{xy}/(N_{\text{lipid}}/2)$. The area per lipid for different membranes with protein was estimated using the open-source accessible software visual molecular dynamics (VMD) [461]. We considered all lipids (including cholesterol) for evaluating the total area per lipid, While for calculating the area per lipid for cholesterol and POPC, only cholesterol and POPC lipid are considered for analysis as individuals. The total area per lipid provides an overall estimate of the average area occupied by each lipid molecule in the bilayer. On the other hand, the area per POPC lipid refers specifically to the surface area occupied by a single POPC lipid molecule in the bilayer. This value is calculated by dividing the total surface area of the bilayer by the number of POPC lipids present. This measurement is useful for comparing the area occupied by different types of lipids or for characterizing the behavior of specific lipid species in a mixed bilayer system.

Figure 8.3 shows that the area per lipid of the lipid bilayers at zero membrane strain increased on decreasing the cholesterol in the lipid membrane, suggesting an additional binding of the lipid bilayer molecules. The total area per lipid increases from 69.814 ± 1.540 Å$^2$/lipid for CHL32-PRO to 74.59 ± 1.701 Å$^2$/lipid for CHL4-PRO while for POPC area per lipid increases

from 77.96 ± 1.220 Å$^2$/lipid for CHL32-PRO to 80.614 ± 1.611 Å$^2$/lipid for CHL4-PRO; these values of area per lipid in which POPC lipids are dominating corresponds closely to the reported experimental value of 78 Å$^2$/lipid to 82.2 Å$^2$/lipid for the POPC bilayer [462]. Furthermore, the computed cholesterol area per lipid for low cholesterol case (68.82 ± 1.182 Å$^2$/lipid) have an excellent agreement with the experimentally determined values by M Pasenkiewicz-Gierula et al. (66.41 Å$^2$/lipid) [463] as well as the value reported by earlier simulations conducted under similar circumstances by Kucerka et al. (69.02 Å$^2$/lipid) [464].

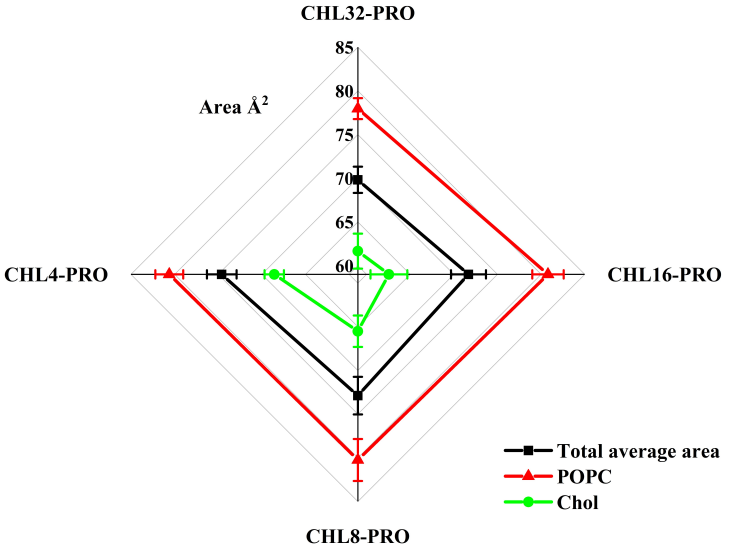


FIGURE 8.3: Area per lipid for POPC and Cholesterol at different cholesterol concentrations.

#### 8.4.1.2 Order parameter of deuterium Nuclear Magnetic Resonance (NMR)

On the other hand, the order parameter of deuterium Nuclear Magnetic Resonance (NMR) types is the most widely studied parameter to assess the order in lipid bilayers. The order parameter $S_{cd}$ may be defined as follows for each $CH_2$ group in the chains,

$$S_{CD} = \frac{1}{2}(3\langle\cos^2(\theta_{CD})\rangle - 1)) \tag{8.1}$$

Where $S_{CD}$ denotes the angle formed by a CH-bond with respect to the membrane normal and the geometry of the CH-bond with three successive $CH_2$-groups was tetrahedral. The brackets $\langle\rangle$ denote an average value of the bond angles effects in each $CH_2$-group in the lipids. The obtained graphical plot for order parameter vs. carbon position individually for the carbon chains at different cholesterol concentrations is shown in Figure 8.4. For all cases of cholesterol level, $S_{CD}$ increased by 60 – 61% (with the highest value of 0.254 ± 0.004 for CHL32-PRO) up to 6$^{\text{th}}$ carbon atom in the chain, which was near to the head region and then decreased to the lowest values

at the tail-end regions. Therefore, an increase in area per lipid was observed (Figure 8.3) with decreasing cholesterol, which allowed the spreading of hydrocarbon chains [465].

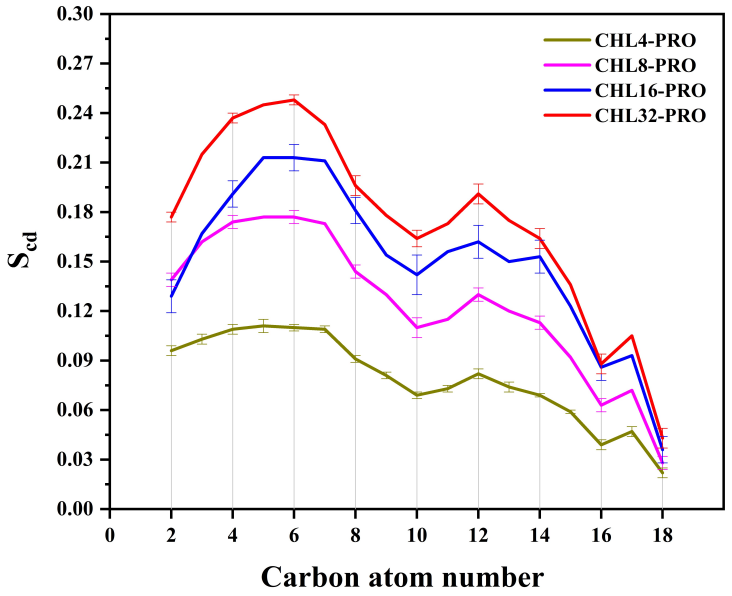


FIGURE 8.4: Order parameter of lipid membrane at different cholesterol concentrations.

#### 8.4.1.3 Tilt angle

The lipid composition varies with cholesterol content that probes into the studies of the single-chain molecules of lipids. It is evident that cholesterol can affect the orientation and organization of the hydrocarbon chains of surrounding phospholipid molecules through its rigid ring structure [466]. As a result, it is simple to determine the angle of the flat cholesterol ring system relative to the normal membrane. Here, the tilt angle is a measure between the head group of phospholipids and its typical orientation relative to the rest of the membrane [467]. The tilt angle describes the cholesterol and lipid bilayer's interaction and cholesterol orientation in the membrane. For decreasing cholesterol content in the system, the obtained tilt of the lipids molecule increased significantly by 62.6% from 20.53 $\pm$ 1.57 $^\circ$ for CHL32-PRO to 54.93 $\pm$ 1.68 $^\circ$ for CHL4-PRO, as shown in Figure 8.5.

### 8.4.2 MSD and Diffusion coefficient

The trajectories of molecules in the lipid-protein system are hard to monitor in real-time due to the unexpected paths of individual molecules, irregularity, boundary conditions, and molecular collisions within the membrane at each timestep [468], [469]. However, the simulated molecular trajectories can be used to calculate the mean square displacement ($MSD$, in Å$^2$) measurement [374], that is given as:

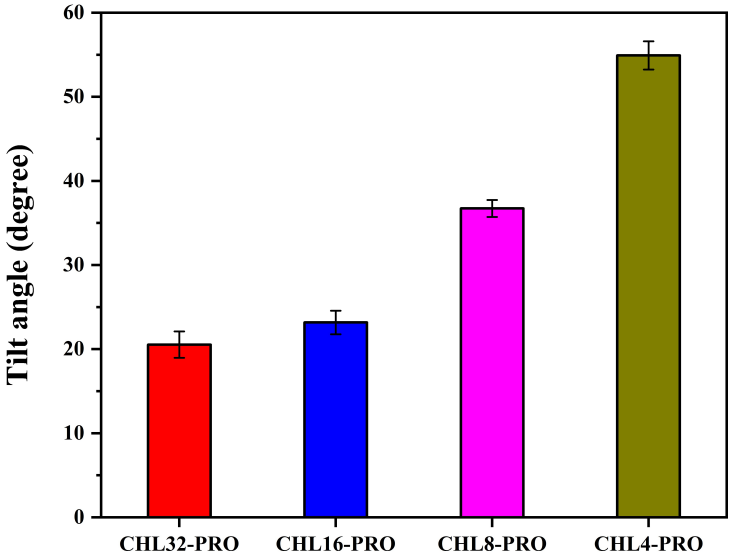


FIGURE 8.5: Average tilt angle for phospholipids molecules in the membrane-protein systems.

$$MSD(t) = \Delta(r_i(t)^2) = (r_i(t) - r_i(0))^2. \tag{8.2}$$

where, $MSD(t)$ is the value of the system at the time 't', $r_i(0)$ and $r_i(t)$ are the vector displacement of a molecule $i$ over time $t = 0$ and $t = t$, respectively. More precisely the average MSD for the lipid molecules with protein trajectories in the membrane system can be formulated as,

$$\overline{MSD}(t) = \sum_{j=1}^{N} \frac{(r_i(t) - r_i(0))^2}{N}. \tag{8.3}$$

Where N is the number of atomic sites. The obtained ($\overline{MSD}$) values are plotted with respect to time for the considered cases shown in Figure 8.6a. The ($\overline{MSD}$) values increased with respect to time due to the continuous atomic interactions inside the systems. The result shows the MSD plots are increasing at a higher rate for decreasing cholesterol levels in the membrane-protein system. The derivative of the ($\overline{MSD}$) values show the diffusivity and Brownian motion of the molecules in the membranes to estimate the dynamic properties of a membrane-protein system at different cholesterol concentrations [470]. The diffusion coefficient (D, in $Å^2$/ps) values were calculated using the Equation 8.4 [471],

$$D = \frac{\text{Slope of average RMSD}}{4}. \tag{8.4}$$

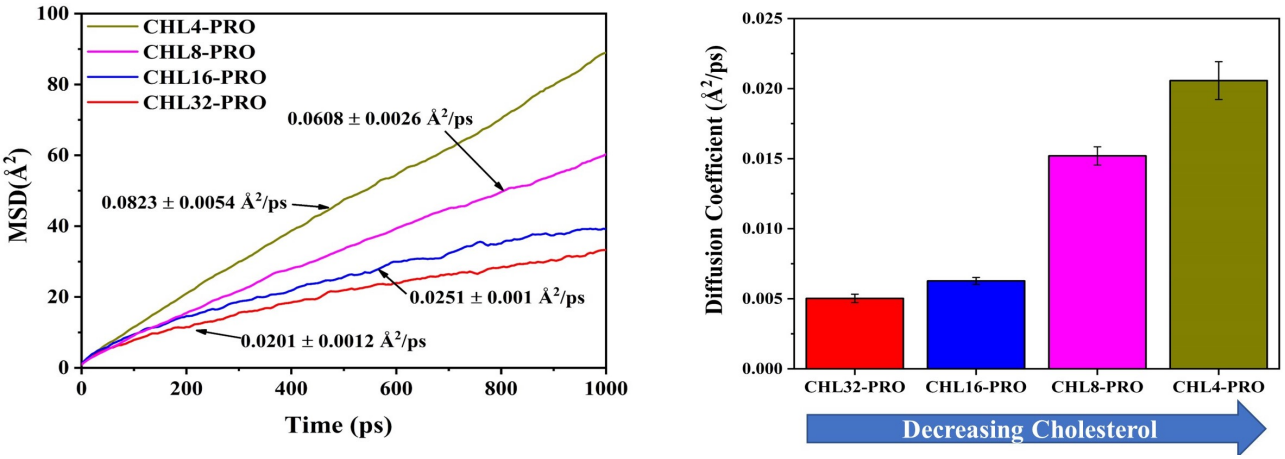


FIGURE 8.6: (a) $\overline{RMSD}$ plots and (b) average diffusion coefficients of membrane-protein systems at different cholesterol concentrations.

Figure 8.6b illustrates the calculated diffusion coefficients for different cases of cholesterol content. The diffusion coefficient value calculated from (MSD) slopes was increased from 0.005 ±0.0003 Å$^2$/ps for CHL-32 PRO to 0.020 ± 0.0013 Å$^2$/ps for CHL4-PRO. The increase in the diffusion coefficient with a decrease in cholesterol concentration showed effects of the ordering of lipid molecules and the decreased area per lipid due to decreased hydrogen bonding and van der Waal interaction, respectively. This observation was consistent with the reported experimental results showing linearly dependency of the lipid diffusion coefficient on cholesterol concentrations [415].

### 8.4.3 Behavior of transmembrane protein under membrane-protein sepration

The separation of lipids bilayer with transmembrane protein was performed under a strained environment for different cases of cholesterol concentration. The strain was applied in the z-direction of the simulation box at a constant strain rate of $10^9$ $s^{-1}$ [444], [472]. Figure 8.7 shows the simulation result for atomic arrangement and positions of upper and lower leaflets and transmembrane protein for all cases. It can be observed that the protein molecules have undergone through unfolding during the initial separation. However, the terminals of the protein were observed to be well attached across the membrane up to 1 to 1.5 ns, which indicates the proper connection and functioning of transmembrane protein for signaling between the intercellular and extracellular environments. After the unfolding of a few nanoseconds time, the protein terminals started detachment from the membrane. The detachment of protein starts after 3 ns for the CHL32-PRO case and nearly after 2 ns for CHL4-PRO case. During the detachment, the protein terminal was stretched out from the upper leaflet along with cholesterol. This was clear evidence of bonding between the protein and cholesterol.

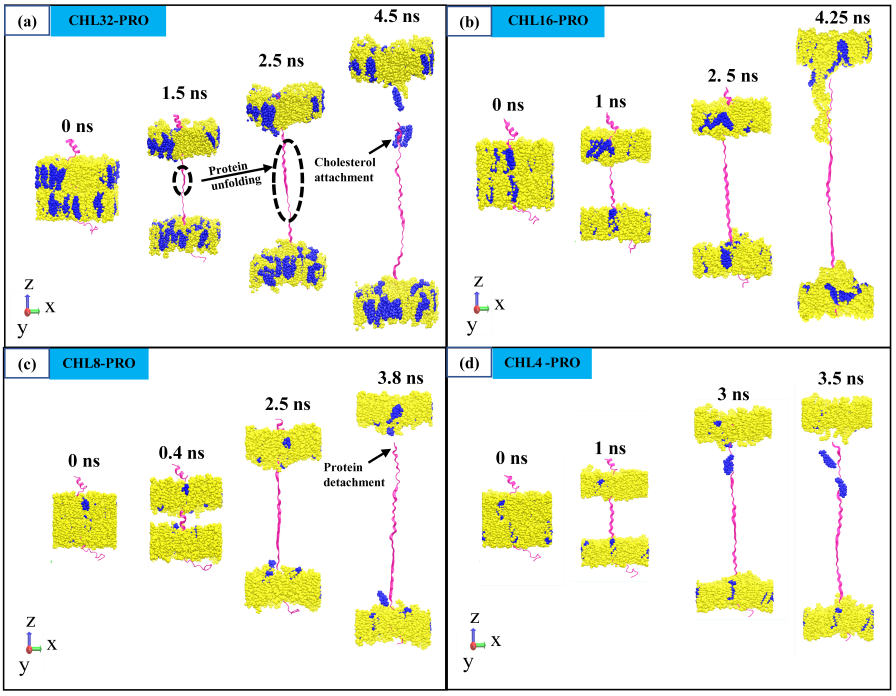


FIGURE 8.7: Simulation snapshots of membrane protein systems at different timesteps. The observed unfolding of protein during simulation is encircled in black color for CHL32-PRO case.

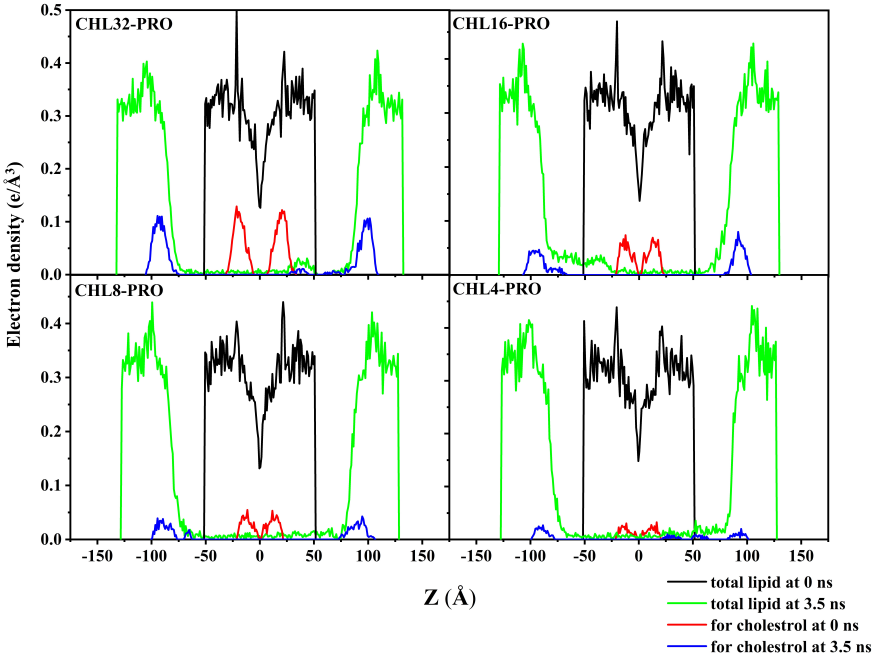


FIGURE 8.8: Electron density profile of membrane protein systems and respective cholesterols along z-direction at before and after separation.

### 8.4.4 Electron density profile

The electron density profile for all systems of different cholesterol concentrations was computed from the molecular trajectories of atoms. Figure 8.8 shows electron density profiles for the initial and final stage of separation along the z-direction for all atoms and cholesterol atoms. The higher electron densities occurred at positions of the phosphate group of lipids, which were nearly the same for all cases. However, the peak electron density of cholesterol decreased by 80.1% due to decreased cholesterol concentration from 0.121 ± 0.010 (for CHL32-PRO case) to 0.024 ± 0.003 (for CHL4-PRO case).

### 8.4.5 Average resistance stress

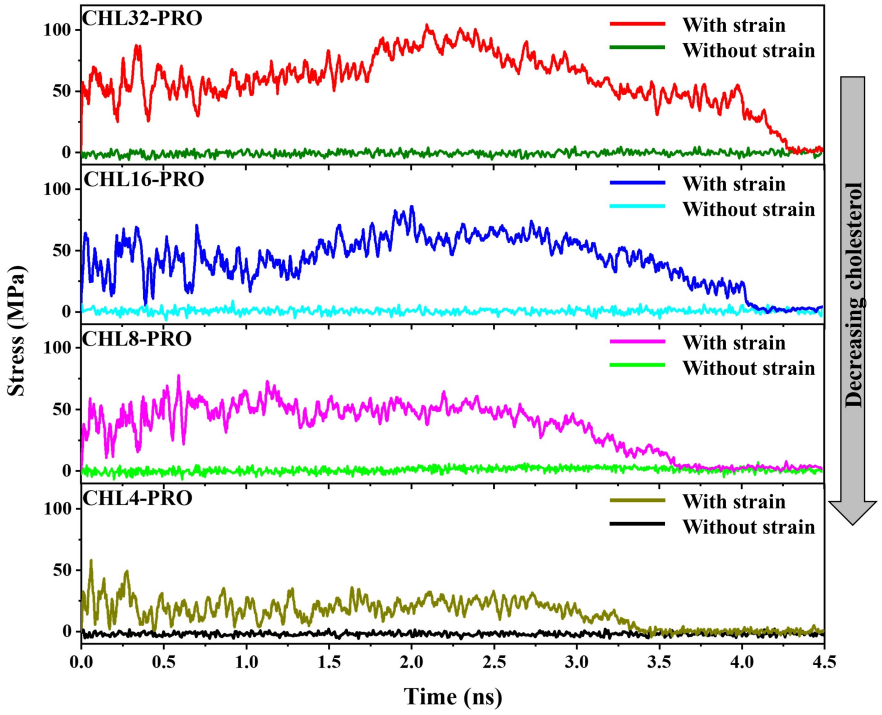


FIGURE 8.9: Average resistance stress vs. time plot for the lipid bilayer separation in the membrane protein system at different cholesterol concentrations.

Figure 8.9 shows that the average resistance stress on the lipid-protein system was different for different cases of cholesterol concentration. The comparison has been made for the different cases with and without strain on the membrane protein system. It was observed that the under no strain conditions the stresses fluctuate near the 0 value. There is no resistance offered by an individual constituent of the membrane-protein system, and are allowed to displace freely in the membrane-protein system. The low cholesterol concentration in the lipid membrane results in reduced initial resistance stress in the system and leads to early detachment failure of the transmembrane. During unfolding, the lowest average resistance stress of 19.40 ± 1.57 MPa was observed for the CHL4-PRO case, which was 68.01% lower than that of the 60.66 ± 4.12

MPa for the CHL32-PRO case. Meanwhile, moderate average resistance stress of 45.86 ± 2.04 MPa and 42.24 ± 3.18 MPa were observed for unfolding in CHL16-PRO and CHL8-PRO cases, respectively.

## 8.5 Discussion

The area per lipid of a lipid bilayer refers to the surface area that a single lipid molecule occupies within the bilayer. This value can vary depending on the type of lipid and the conditions under which the bilayer is formed. In general, the area per lipid is greatest for saturated lipids and decreases as the number of double bonds in the lipid tail increases. The area per lipid can also be affected by the degree of hydration of the bilayer, with higher hydration levels leading to a greater area per lipid. In this study, the total area per lipid increased by 6.40% on decreasing the cholesterol level, i.e. CHL32-PRO to CHL4-PRO. In contrast, POPC area per lipid increases from 77.96 ± 1.220 $Å^2$/lipid for CHL32-PRO to 80.614 ± 1.611 $Å^2$/lipid for CHL4-PRO; these values of area per lipid in which POPC lipids are dominating corresponds closely to the previously reported experimental value for the POPC bilayer [462]. In addition, the calculated area of cholesterol per lipid in instances of low cholesterol levels is consistent with the values established through previous experiments [463] and also aligns with the results from previous simulations [464]. The decrease in the number of cholesterol molecules of smaller sizes than the lipid molecules can be easily compacted across lipid molecules and thus decreased the area per lipid values.

Further, another structural parameter, i.e., $S_{CD}$ order parameter, was estimated using Equation 8.1. The order parameter is widely used to assess the degree of order in lipid bilayers. The order parameter measures the degree of alignment of the deuterium atoms within a lipid molecule, which can be used to infer the degree of mobility or rigidity of the molecule. A value of 1 for the order parameter indicates that the deuterium atoms are fully aligned and the lipid molecule is in a rigid state. In contrast, a value of 0 indicates that the deuterium atoms are randomly oriented, and the lipid molecule is in a highly mobile state. Findings predicted that for all cases of cholesterol level, $S_{CD}$ increased up to $6^{th}$ carbon atom in the chain, which was near the head region and then decreased to the lowest values at the tail-end regions. This was mainly due to the ability of cholesterol to induce biophysical changes related to its molecular structure. The cholesterol molecule may form hydrogen bonds with polar lipid groups, including the phosphate group and the carbonyls. The van der Waals interactions between hydrocarbon chains and the rigid ring structure of cholesterol could be responsible for the higher chain order for CHL32-PRO [473]. Cholesterol acts as a space filler that maintains the stability and integrity of the membrane by preventing the hydrocarbon tails of the phospholipid molecules from getting too close to one another. When cholesterol levels decrease, it allows the hydrocarbon tails to spread out more, resulting in increasing the area per lipid. Additionally, cholesterol is known to interact with the

lipids in the membrane and modulate their packing and organization, which ultimately affects the area per lipid. Hence, an increase in area per lipid was observed (Figure 8.3) with decreasing cholesterol, which allowed the spreading of hydrocarbon chains [465].

The tilt angle is a measure of the angle of the flat cholesterol ring system relative to the normal of the lipid bilayer. The tilt angle is determined by measuring the orientation of the cholesterol molecule within the bilayer. A tilt angle of 0 degrees indicates that the flat ring system of the cholesterol molecule is parallel to the normal of the bilayer. In comparison, a tilt angle greater than 0 degrees indicates that the ring system is tilted away from the normal of the bilayer. The tilt angle can also be negative, indicating that the ring system is tilted towards the normal of the bilayer.

This is an important parameter in understanding the cholesterol's role in the fluidity and stability of the bilayer. It has been observed that cholesterol molecules with a high tilt angle tend to have a more rigidifying effect on the bilayer. In contrast, cholesterol molecules with a low tilt angle tend to have a more fluidizing effect. Results predicted that in the membrane protein system with decreasing cholesterol content, the tilt of the lipids molecule increased significantly by 62.6% for CHL32-PRO compared to CHL4-PRO, as shown in Figure 8.5. At higher cholesterol concentrations, the cholesterol density distributions shrink and compact, which reduces the tilt. Whereas, at low cholesterol concentrations, tilt angle increases due to its entropic tendency to allow all accessible states [474]. It is important to note that the tilt angle is a dynamic parameter, meaning that it can change depending on the conditions of the bilayer, such as temperature, pressure, and the presence of other lipids or proteins.

Mean Square Deviation measures the structural comparison between successive molecular coordinates positions. Obtained ($\overline{MSD}$) values increased with respect to time due to the continuous atomic interactions inside the systems. The result shows the MSD plots are increasing at a higher rate for decreasing cholesterol levels in the membrane-protein system. Figure 8.6b illustrates the calculated diffusion coefficients for different cases of cholesterol content. It was observed that as the cholesterol level decreased (from CHL-32 PRO to CHL4-PRO), the diffusion coefficient value (as calculated from RMSD slopes) significantly increased. The increase in the diffusion coefficient with a decrease in cholesterol concentration showed effects of the ordering of lipid molecules and the decreased area per lipid due to decreased hydrogen bonding and van der Waal interaction, respectively. This observation was consistent with the reported experimental results showing linearly dependency of the lipid diffusion coefficient on cholesterol concentrations [415]. Hence, the decrease in cholesterol concentration has effectively intensified the diffusion across transmembrane protein and generated microscopic fluidity in the system.

The simulation results in Figure 8.7 demonstrate the atomic arrangement, position of upper and lower leaflets, and transmembrane protein under strain. It was observed that the protein molecules initially underwent significant unfolding. Still, the terminals of the protein remained

attached to the membrane for 1 to 1.5 ns, indicating proper connection and function for signaling between the intercellular and extracellular environments. However, after a few nanoseconds, the protein terminals began to detach from the membrane, with detachment starting at 3 ns for the CHL32-PRO case and nearly 2 ns for the CHL4-PRO case. During detachment, the protein terminals were stretched out from the upper leaflet along with cholesterol, indicating a bond between the protein and cholesterol. The decreasing cholesterol concentration may have impeded the resistance to the detachment of protein during the separation of bilayers due to high fluidity and less bonding with lipid headgroups. Hence early detachment of protein was observed in CHL4-PRO case.

Figure 8.8 illustrates the electron density profiles for the initial and final separation along the z-direction for all atoms and cholesterol atoms. It can be observed that the highest electron densities occurred at the positions of the phosphate group of lipids, which were similar for all cases. However, the peak electron density of cholesterol decreased by 80.1% due to a decrease in cholesterol concentration from 0.121 (in the CHL32-PRO case) to 0.024 (in the CHL4-PRO case). During the separation, these cholesterol electron densities were dispersed along with the elongated and unfolded transmembrane protein in the z-direction. This observation further supports the evidence of a bond between cholesterol and the transmembrane protein.

The average resistance stress on the lipid-protein system was different for different cases of cholesterol concentration as shown in Figure 8.9. The low cholesterol concentration in the lipid membrane leads to a decrease in initial resistance stress in the system and results in early detachment failure of the transmembrane protein. During unfolding, the resistance stresses decreased by 68.01% on decreasing the cholesterol molecule (CHL32-PRO to CHL4-PRO). Further, the resistance stresses for different cholesterol levels revealed that the results were dependent and consistent with the obtained order of lipids, area per lipid, and diffusion in the membrane (as in Figure 8.3 and Figure 8.6). Here, in a low cholesterol case, the decreased bonding across lipid membrane and increased fluidity were the predominant reasons for the decreases in resistance stress. The outcome of this atomistic study revealed that the decreasing cholesterol concentration in lipid membranes in cancerous conditions might lead to easy detachment failure of transmembrane protein that spans the entirety of the cell membrane. Hence, low cholesterol impacts the function of the protein to deliver the signaling across the cell membrane and provide gateways to permit the transport of essential metabolic elements across the membrane to keep cells alive.

## 8.6 Conclusion

Herein, the cancerous membrane protein systems were studied for lipid bilayer separation at different cholesterol concentrations under an external strain environment. The physical parameters

of the membrane protein system helped to understand the interaction between cholesterol and other constituents of the systems. It was observed that decreasing the cholesterol concentration from non-cancerous to cancerous level resulted in an increase in area per lipid and average tilt angle with the overall decrease in the order parameter. This indicates less bonding and interaction across membrane protein systems at low cholesterol concentration and, thus increase in diffusion coefficient observed on decreasing cholesterol concentration. The detachment of protein with cholesterol from lipids was observed during the simulation of lipid bilayer separation under tensile straining. This observation confirmed that transmembrane protein was bonded with cholesterol molecules in the membrane, which revealed the reason for the 68.01% decrease in resistance stress on decreasing the cholesterol concentration. The findings of this work revealed the changes in the bonding and interaction of cholesterol with other constituents of the membrane protein system, which may help in understanding the biophysical behavior of transmembrane protein at different cholesterol concentrations. This investigation may have implications in the study of the membrane protein system subjected to a strained environment developed during the treatment of cancer through acoustic therapies and the transportation of drugs through nanodevices.

# Chapter 9

# Conclusions and future scope

This thesis aimed at the experimental studies of the dynamic response of microscale biological structures to understand the changes in their internal structure and interaction with the environment that can be inferred from their mechanical characteristics. The natural frequencies of a structure carry information about its material properties, geometry, and boundary conditions. The method of measuring vibration characteristics of micro-scale structures is different from that of macroscale counterparts because using sensors and actuators on larger structures is not feasible at microscale structures. The non-contact position sensing device technique has emerged as a potent tool for measuring the vibration characteristics of micro-scale structures. We have used this tool carefully to not only read and record vibration data from several biological structures but also to push the boundaries of experimental vibration studies for obtaining higher modes of vibration and verifying our experimental results with appropriate theoretical/simulation results. Experimental data from various micro-scale structures revealed several modal frequencies of vibration, including high-quality factors (Q.F) from frequency response measurements. Each mode is independently excited, the corresponding modal frequencies are recorded and verified with analytical and FEM simulations. The study of biological structures captured several modes of vibration and revealed the shift in the corresponding frequencies due to changes in their intracellular mechanical characteristics and adhesion proteins. Additionally, the conclusions of each chapter in this thesis are presented as follows:

In chapter 2, we reported our study on bone behavior. The proposed non-invasive method of testing bones helps to determine mechanical properties such as modulus of elasticity. Analysis of the bone's response reveals its damping characteristics, and numerical analysis is used to evaluate the frequency response of femur bones. Since bones are anisotropic, homogenization using CMAS is used to optimize material properties for a numerical mechanical response. Modal and Random vibration analysis reveals the natural frequencies, which can aid in the prosthetic bone design and study real-life bone activity. The proposed method's findings of modulus of elasticity are

similar to those from finite element modeling and compared to previous research findings. This technique can be used to evaluate the mechanical properties of other biological samples, such as skin and cells.

Furthermore, chapter 3 demonstrates the time-dependent study of a normal and nanocarrier gel and cream-loaded rat skin using a non-destructive optical technique and FE modeling to evaluate the natural frequencies and Young's Modulus of the skin. The results show that the normal skin's experimental frequencies are 263.53 Hz, while skin samples with cream and cubosome loaded gel have frequencies of 184.53 Hz and 147.5 Hz, respectively. The FE results show a normal deformation mode shape at a frequency of 243.53 Hz and a wrinkling mode shape at a higher frequency. Additionally, the study found that as the stratum corneum thickness increases, there is an exponential decrease in the stresses and deformation in the skin. experimental results were compared with the numerical methods with an acceptable margin of error. Further study is needed to develop FE models that incorporate nonlinearity, Hyper elasticity, and anisotropy, as well as to minimize the experimental error by restricting rigid body movements and environmental variables. However, literature research indicates that natural frequencies of the skin can vary due to differences in elasticity at different parts of the body and with age.

This experimental technique has the potential for use in the diagnosis of diseased skin by analyzing vibrations and observing changes in the dynamic behavior of healthy and diseased skin over time. It can also be used for evaluating the in-vivo mechanical response of the skin. A lab-on-a-chip device could be developed for real-time monitoring of skin behavior during clinical treatment.

In chapter 4, previously discussed non-invasive techniques were used to measure the frequency of cancer cells. The natural frequency of cells was estimated using different viscosity modulators such as PEG, methylcellulose, and glucose. Further same has been successfully implemented on invasive and non-invasive cell lines like MCF-7 and MDA-MB-231. Rayleingh-lamb equation was used to estimate the frequency-dependent intracellular viscosity of the different cancerous cells. Findings of the biological assay such as western blot, RTPCR, PI Staining, and fluorescence imaging help in understanding the viscosity behavior of the cells. The results obtained from the biological assay and noninvasive technique were found to be consistent with each other. Further, a new approach was evolved to do the numerical modeling of the cells using COMSOL. Real 3D images were extracted from the high-contrast confocal microscopes and were used as the exact geometry model of the different cells. The viscoelastic material model was used to define the material parameters of the cells. Modal and harmonic analysis was performed to understand the dynamics of the cells under adhesion. The outcome of the experimental and numerical methods yielded similar results with minimal error. These errors are based on the assumption and the hypothesis made during the numerical analysis that contributed to the material assignment and the boundary conditions. Our findings indicate that the EMT process in cancer cells, induced by TGF-$\beta$, corresponds to a lower frequency. A lower frequency leads to lower intracellular viscosity,

leading to greater spread and mortality of cancer. Early detection of changes in frequency response suggests the prompt selection of therapeutic treatment. The proposed technique is a key component of this work, enabling distinguishing healthy and diseased cells based on frequency and early selection of frequency-based cancer treatment.

In chapter 5, we extend the previous work by introducing more realistic material modeling and adherent boundary conditions in the numerical modeling of the Huh-7 cells. A finite element model was modeled in the COMSOL Multiphysics and considered as a continuum model. Numerical analysis shows a new approach to numerical modeling that is based on the real geometry acquired from microscopic images, as discussed in the previous chapter. In this study, a primary hyperelastic material for the cytoplasmic response was considered for the analysis. The neo-Hookean model was used, in which stresses and strains are computed from a strain energy density function. To incorporate the viscoelastic behavior, generalized Maxwell branches are included in the cytoplasm portion. The nucleus is modeled without viscoelastic branches assuming that it is primarily elastic.

This study describes a relaxation test as the computational model used to validate the material properties. A rigid indenter was used for compression into the soft, viscoelastic cell, and the subsequent relaxation of the indentation force was evaluated and compared with previous experimental data. This comparison helps in validating the assumed material properties for the modeling. The numerical model was further used to evaluate the modal behavior and frequency response of the Huh-7 cells at different stiffness of the focal adhesion complexes.

A non-invasive and non-contact experimental technique was used for the frequency response of the cells and later compared with the numerical simulations. Further, Viscoelastic filament properties may also be accommodated depending on material and time scale for more accurate behavior. Estimated frequencies predict resonance, which improves the selection of the therapeutic frequency for targeting diseased cells. This study shows potential in the fields of medical devices and biomechanical modeling.

chapter 6 shows the study in relevance to the field of mechanomedicine. Nowadays, mechanical vibration is a possible biocompatible treatment approach for cancer. The study investigated the impact of mechanical vibration in the low-frequency range of 20 Hz to 60 Hz on the viability of Huh-7 cells. Results showed the morphological changes in cellular structure, becoming more polygonal and degraded. Additionally, the mathematical framework was used as the analytical model to evaluate the frequency response of the homogenized cells. Biological assays such as MTT and Annexin V/PI Staining flow cytometry were used to understand the impact of low-frequency vibrations on cell biology. It was observed that there has been a 10 % increase in the fundamental frequency of the cells with an increase in the excitation frequency from 20 Hz to 60 Hz. Similarly, findings revealed that the cell viability decreased with the increase in mechanical vibration. Observations revealed that apoptosis and necrosis increased significantly in

cells exposed to vibration compared to those in static culture. Although the specific mechanisms by which low-frequency mechanical vibration leads to cell death through apoptosis and necrosis are not fully understood. The findings suggest a potential use of mechanical vibration in cancer treatment as a form of mechanomedicine.

The dynamic behavior of cancer cells refers to the way in which cancer cells move, grow, and interact with their environment. Understanding and studying the dynamic behavior of cancer cells in an actuating micro-environment would reflect the importance of the next study in the field of Bio-NEMS application.

chapter 7 showcases the study of piezo-based microchannels that are used to enable active control of interfaces between microchannel boundaries, particles, and fluids. In this study, ZnO/PDMS-based piezo microchannel was fabricated and used for analyzing the morphological changes of Huh7 cells during the flow through the channel under different (amplitude-frequency) actuation conditions. The results depicted the highest circularity index under the High-High actuation condition, and the cells experienced higher geometrical changes at the High-High amplitude and frequency actuation condition. A non-invasive technique was used to measure the frequency response of the flowing cells. Fundamental frequency was observed around 331.2 kHz for the case of the cells flowing through the microchannel (without actuation); similarly, for the High-High case, it decreased to 249.56 kHz. It was found that the fundamental frequency decreased by 10 % as the actuation frequency increased from Low-Low to High-High. These observations reveal that cells exposed to higher shear stresses and deformation exhibited higher geometrical changes. Mechanical properties and vibration characteristics are affected by variations in fundamental frequencies, and these fluctuations may be related to ambient conditions and external stimuli. These findings have potential applications in developing a device for diagnosing the state of malignant diseases based on resonance.

The research presented in this thesis suggests that vibration measurements from a small number of cells can be used to develop diagnostic tools. The idea is that changes in the cell caused by chemical or biological factors will result in changes to the cell's structure that can be detected through changes in vibration signatures. However, more research is needed to establish normal cell frequencies and variations before these tools can be fully trusted. Overall, the studies show the potential for using vibration measurements at the micro-scale to detect changes in various structures, including non-solid structures such as biological cells.

Furthermore, chapter 8 shows the molecular dynamics study of the complex constituent of cells, viz., cell transmembrane protein system, to understand the biological phenomenon of the transmembrane protein in the system under strain environment at different cholesterol concentrations. The study found that a decrease in cholesterol concentration in membrane protein systems leads to an increase of 6.4 % in the area per lipid and 62.6 % in the average tilt angle, accompanied by a reduction in the order parameter. This indicates that lower cholesterol levels in

cancerous environments weaken the bonding and compactness of the membrane protein system. Protein stretching and unfolding were also observed during bilayer separation, and resistance stresses decreased by 68.01 % with decreasing cholesterol. Cholesterol molecules were found to be bonded with proteins, and it was discovered that cholesterol plays an important role in impeding diffusion and preventing protein detachment at high concentrations. Thus, transmembrane proteins can maintain their positions across the membrane and resist functional failure. This study demonstrates that decreased cholesterol concentration leads to significant changes in the biophysical behavior of membrane protein systems, which can affect the mechanosensitivity of transmembrane proteins under mechanical stress.

In overall conclusion, the studies presented in this thesis highlight the potential of experimental vibration studies for investigating micro-scale biological structures. This includes utilizing the fundamental natural frequency and shifts in this frequency to detect small changes in the structure, as well as utilizing higher vibration modes and corresponding frequencies for even more precise detection. Studies that examine various material modeling and boundary conditions, as well as their validation, demonstrate the capability of the technique for use in Lab-on-chip and medical diagnostic devices. These techniques are not limited to adhered micro-scale biological structures but can also be applied to cell separation and segregation in microchannels. A study based on atomistic analysis of the cell membrane with a transmembrane protein system shows the various biological phenomenon in the external strained environment. The investigation that was conducted could have significant implications for the study of membrane proteins when exposed to challenging environments, such as those created by cancer treatment using acoustic therapies and drug transportation through nanodevices. Additionally, this research has the potential to provide a new understanding of the mechanisms involved in the development and progression of cancer, as well as identify novel drug target treatments.

The thesis has a fascinating subject with enormous potential for future research. The following point highlights some future scopes of the present study:

- Development of Lab-on-chip device as the new medical diagnostic tool: The mechanical study of biological structures can lead to the development of new medical technologies for diagnosing and treating diseases. It may be possible to develop new resonance-based therapeutic techniques that are more accurate and highly sensitive by understanding the mechanical resonance behavior of tissues and cells.

- Improved prosthetics and implants: The study of the mechanical properties of biological tissues can improve the design and function of prosthetics and implants. Researchers can develop prosthetics and implants that mimic the natural movements and functions of the human body by comprehending the responses of tissues and cells to diverse mechanical stimuli.

- Understanding the damaged tissue engineering: The study investigates the biological structures and enhances the understanding of the mechanical properties of different tissues and cells which can be used to develop a new approach for growing and repairing damaged tissues.

- Better understanding of the state of disease: The mechanical study of biological structures can also help researchers to better understand the underlying causes of certain diseases. A better correlation between the state of diseases and their mechanical behavior can lead to the development of new treatments for diseases that target the mechanical aspects of the disease.

- Integration with other imaging techniques: The thesis could explore how to integrate non-invasive experimental techniques with other imaging techniques, such as confocal microscopy, electron microscopy, or X-ray microscopy, to gain a more comprehensive understanding of the dynamic behavior of biological structures.

- Multi-scale modeling: Cancer is a complex disease that involves multiple levels of the organization, from the molecular to the tissue level. Multi-scale modeling techniques can provide a more comprehensive understanding of the behavior of cancerous membrane protein systems under strain environments, and future research can focus on developing more advanced multi-scale models.

Overall, the future scope of the thesis is very vast and exciting. The research in this field has the potential to revolutionize medical technologies, prosthetics, tissue engineering, and our understanding of the disease.

# Appendix A

# Cells as a standard Voigt model

Consider a single cell's as an oscillating mass inside a viscoelastic medium and excited by an external force (Figure A.1). A spherical object with a radius of R represents the cell structure and behaves as a homogeneous and isotropic viscoelastic material. Spring and dashpot are the elements used to represent the elastic and viscoelastic components of the cell. The system can be represented using Equation A.1.

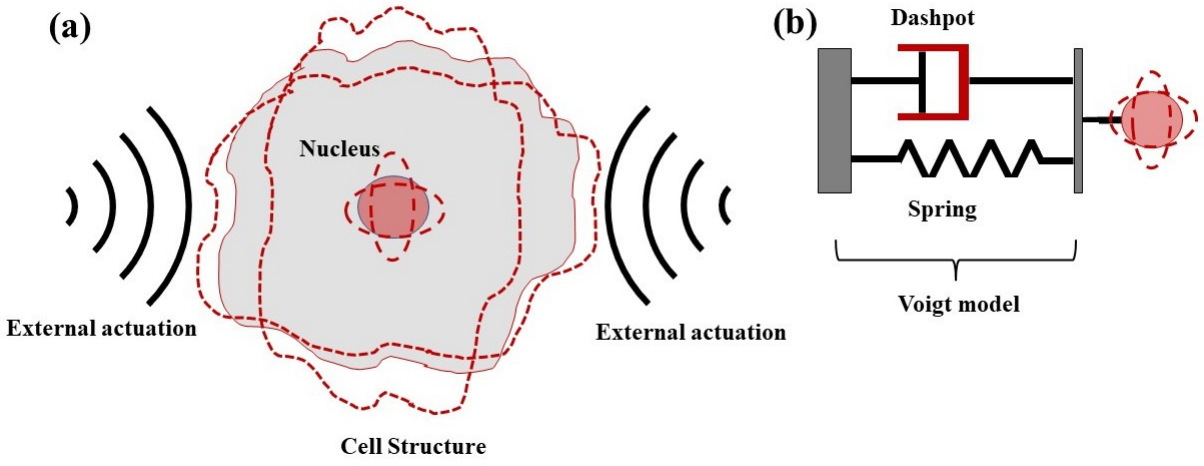


FIGURE A.1: Cell as a standard Voigt model.(a) Cell under mechanical actuation. The actuation causes morphological alterations in the cell structure. (b) Standard Voigt model for the mathematical representation of the cell. Dashpot and spring component represent the viscoelastic components of the cell.

The equation of motion for the cell system can be written as

$$f_m = m_c a_c = \frac{4}{3}\pi\rho_c R^3 \frac{d^2 u_c}{dt^2} = f_d - f_r \tag{A.1}$$

where t is the time, $f_m$ represents the inertial force, $m_c$ is the cell mass whose density is $\rho_c$, and $u_c$ is the associated displacement. Furthermore, $f_d$ is the basic driving force in the system,

that are induced by the external source. While response force $f_r$ is the combination of the two components together i.e. the elastic contribution and the viscous force response. In this case, the object is very small hence the force can be assumed to have the simple form as shown in the Equation A.2.

$$f_d = \frac{4}{3}\pi\rho_m R^3 \frac{dv_m}{dt} \tag{A.2}$$

where $v_m$ is the velocity of the cell in the medium. Initially the object is at rest, hence the boundary condition can be represented by,

$$U_c\|_{t=0} = 0, \quad \frac{Du_c}{dt}\bigg\|_{t=0} = 0 \tag{A.3}$$

Then, taking the Laplace transform of Equation A.1, we obtain

$$F_m = \frac{4}{3}\pi\rho_c R^3 s^2 U_c = F_d - F_r \tag{A.4}$$

where all the transformed components are indicated with capital letters and s is the Laplace variable. As a consequence, in Equation A.4 $F_d$ is the Laplace transform of the drive force $f_d$. Hence Equation A.2, can be written as

$$F_d = \frac{4}{3}\pi\rho_m R^3 s^2 U_m \tag{A.5}$$

In the Voigt model, the system connects with elastic and viscous components in a parallel configuration ( Figure A.1b). The response force $F_r$ is then calculated by adding the contributions of the two components together as follows:

$$F_r = F_\mu + F_G \tag{A.6}$$

where $F_G$ denotes the elastic contribution and $F_\mu$ denotes the viscous force response. For the vibration of a object in viscous fluids, the viscous force can be written as the equation shown by Basset [475], Landau and Lifshitz [476], and Or and Kimmel [312]. The expression is

$$F_\mu = 6\pi\mu R\left(1 + \sqrt{\frac{\omega R^2}{2\nu}}\right)(v_c - v_m) + \frac{2}{3p}\pi R^3\rho_m\left(1 + \frac{9p}{2}\sqrt{\frac{2\nu}{\omega R^2}}\right)(\dot{v}_c - \dot{v}_m). \tag{A.7}$$

Where $\mu$ and $\nu$ the dynamic and the kinematic viscosities of the medium, respectively, $\omega$ is natural frequency of the system and the velocities $v = \dot{u}$. It's important to note that the viscous response force structure assumed in this case is different from the classical Stokes force. This is because the equation includes frequency-dependent terms and, in addition, there seems to be an erroneous inertial contribution known as added mass, as proposed by Brennen et al. [477] that is,

$3\pi pR^3\rho_m\sqrt{\frac{2\nu}{\omega R^2}}$, $p$ (p=2 this case) is the number of elements in parallel, here used to solve the ambiguous situation raised by Or & Kimmel. While the elastic force, $F_G$, as proposed by Ilinskii et al. [478], can be written as:

$$F_G = 6\pi GR(u_c - u_m) + 6\pi R^2\sqrt{G\rho_m}(\dot{u}_c - \dot{u}_m) + \frac{2}{3p}\pi R^3\rho_m(\ddot{u}_c - \ddot{u}_m) \tag{A.8}$$

Here, the elastic response differs from the classical Hooke law. It comprises a pure elastic contribution and the effects of rapid fluctuations caused by the system's dynamic interaction with the environment. which drive the response towards the actual physical behavior. $G$ denotes the medium's elastic shear modulus, which is considered to be about one-third that of the equivalent Young's modulus according to the incompressibility hypothesis, and $u_m$ denotes the vibrational displacement in the medium. After that, the following parameters are introduced:

$$c_{0G} = 6\pi GR, c_{1G} = 6\pi R^2\sqrt{G\rho_m}, c_{2G} = 6\pi R^2\sqrt{G\rho_m} \tag{A.9}$$

and

$$c_{1\mu} = 6\pi R\mu\left(1 + \sqrt{\frac{\omega R^2}{2\nu}}\right), c_{2\mu} = \frac{2}{3p}\pi R^3\rho_m\left(1 + \frac{9p}{2}\sqrt{\frac{2\nu}{\omega R^2}}\right) \tag{A.10}$$

Additionally, the following dimensionless constant is defined:

$$\zeta = \frac{\rho_c}{\rho_m} = \frac{1}{1+\gamma} \tag{A.11}$$

Here, $\gamma = \rho_m\rho_c^{-1} - 1$ Finally, the quasi-standard Voigt viscoelastic constitutive law is written as

$$f_r = c_{0G}(u_c - u_m) + (c_{1\mu} + c_{1G})(\dot{u}_c - \dot{u}_m) + (c_{2\mu} + c_{2G})(\ddot{u}_c - \ddot{u}_m) \tag{A.12}$$

Taking Laplace transform of the response force Equation A.12, results

$$F_r = (U_c - U_m)(c_{0G} + (c_{1\mu} + c_{1G})s + (c_{2\mu} + c_{2G})s^2) \tag{A.13}$$

and, substituting Equation A.13 and (A.5) in (A.4) and after deduction we obtaine

$$\left[c_{0G} + (c_{1\mu} + c_{1G})s + \left(c_{2\mu} + c_{2G} + \frac{4}{3}\pi\rho_c R^3\right)s^2\right]\Delta U = \frac{4}{3}\pi\gamma\rho_c R^3 s V_m \tag{A.14}$$

where $\Delta U = U_c - U_m$ by solving Equation A.14, the analytical solution in terms of amplitude for the relative displacement $\Delta U$ between the cell and its surroundings has the following form.

$$\|\Delta U\|_{s=\iota\omega} = \left\|\frac{\frac{4}{3}\pi\gamma\zeta\rho_c R^3 s V_m}{c_{0G} + (c_{1\mu} + c_{1G})s + (c_{2\mu} + c_{2G} + \frac{4}{3}\pi\rho_c R^3)s^2}\right\|_{s=\iota\omega} \tag{A.15}$$

# Biography

## Brief Biography of the Supervisor

**Dr. Venkatesh KP Rao** received a Ph.D. degree in Nanobiotechnology from the Indian Institute of Science Bangalore, He has discerning experience of over 15 years in the field of micro and nanosystems. He is currently working as Assistant Professor in Mechanical Engineering Department, BITS Pilani, Pilani campus, Rajasthan, India. His research interests include MEMS, NEMS, FEM, Bioengineering, Mechanobiology, Neuroscience, and Energy Harvesting. His team is extensively working on the Lab-on-chip design for skin diagnostics for psoriasis, the mechanical behavior of cancer cells, and the design and development of the MEMS gyroscope. He has published no. of publications in reputed international peer-reviewed journals and book chapters with international publishers such as RSC, Elsevier, Springer, and Taylors & Francis. He is actively involved in sponsored research projects from government funding agencies and industries. He has a strong enthusiasm for incorporating new teaching methodologies into his classroom instruction and encouraging students to confront the demands of the modern era.

## Brief Biography of the Candidate

**Diplesh Gautam** is a full-time research scholar in the Department of Mechanical Engineering at Birla Institute of Technology and Science, Pilani, Pilani campus, Rajasthan, India. He graduated from Gyan Ganga Institute of Technology and Sciences, Jabalpur, Madhya Pradesh, India with a bachelor's degree in Mechanical Engineering in 2007. He acquired his Master's degree in 2013 from Birla Institute of Technology and Sciences, Pilani, Pilani campus, Rajasthan, India in Design Engineering. After his Master's, he worked as a Design Engineer with the research and development team of IFB global in Goa, India. He joined BITS Pilani, Pilani campus to pursue his Doctoral study in Bionanotechnology under the guidance of Dr. Venkatesh KP Rao. Before joining BITS Pilani in 2019, he has more than 9 years of experience including teaching and industry. Currently, he is working in the field of bioengineering, microfluidics, and sensor design. His area of research is in cell mechanics, biomechanics, NEMS, MEMS, and oncology.

# Bibliography


[1] S. Suresh, "Biomechanics and biophysics of cancer cells," *Acta biomaterialia*, vol. 3, no. 4, pp. 413–438, 2007.

[2] G. Bao and S. Suresh, "Cell and molecular mechanics of biological materials," *Nature materials*, vol. 2, no. 11, pp. 715–725, 2003.

[3] C. S. Chen, J. Tan, and J. Tien, "Mechanotransduction at cell-matrix and cell-cell contacts," *Annu. Rev. Biomed. Eng.*, vol. 6, pp. 275–302, 2004.

[4] M. Unal, Y. Alapan, H. Jia, *et al.*, "Micro and nano-scale technologies for cell mechanics," *Nanobiomedicine*, vol. 1, p. 5, 2014.

[5] M Radmacher, R. Tillmann, M Fritz, and H. Gaub, "From molecules to cells: Imaging soft samples with the atomic force microscope," *Science*, vol. 257, no. 5078, pp. 1900–1905, 1992.

[6] A. Reece, B. Xia, Z. Jiang, B. Noren, R. McBride, and J. Oakey, "Microfluidic techniques for high throughput single cell analysis," *Current opinion in biotechnology*, vol. 40, pp. 90–96, 2016.

[7] J. Mitchison and M. Swann, "The mechanical properties of the cell surface: Ii. the unfertilized sea-urchin egg," *Journal of experimental biology*, vol. 31, no. 3, pp. 461–472, 1954.

[8] R. L. Urbano and A. M. Clyne, "An inverted dielectrophoretic device for analysis of attached single cell mechanics," *Lab on a Chip*, vol. 16, no. 3, pp. 561–573, 2016.

[9] M. M. Haque, M. G. Moisescu, S. Valkai, A. Dér, and T. Savopol, "Stretching of red blood cells using an electro-optics trap," *Biomedical optics express*, vol. 6, no. 1, pp. 118–123, 2015.

[10] Y. Qiang, J. Liu, and E Du, "Dielectrophoresis testing of nonlinear viscoelastic behaviors of human red blood cells," *Micromachines*, vol. 9, no. 1, p. 21, 2018.

[11] P.-H. Wu, S. S. Gambhir, C. M. Hale, W.-C. Chen, D. Wirtz, and B. R. Smith, "Particle tracking microrheology of cancer cells in living subjects," *Materials Today*, vol. 39, pp. 98–109, 2020.

[12] Y. F. Dufrêne, T. Ando, R. Garcia, *et al.*, "Imaging modes of atomic force microscopy for application in molecular and cell biology," *Nature nanotechnology*, vol. 12, no. 4, pp. 295–307, 2017.

[13] A. R. Harris and G. Charras, "Experimental validation of atomic force microscopy-based cell elasticity measurements," *Nanotechnology*, vol. 22, no. 34, p. 345 102, 2011.

[14] A. Aryaei and A. C. Jayasuriya, "Mechanical properties of human amniotic fluid stem cells using nanoindentation," *Journal of Biomechanics*, vol. 46, no. 9, pp. 1524–1530, 2013.

[15] X. Meng, H. Zhang, J. Song, X. Fan, L. Sun, and H. Xie, "Broad modulus range nanomechanical mapping by magnetic-drive soft probes," *Nature communications*, vol. 8, no. 1, p. 1944, 2017.

[16] Y. Hosokawa, M. Hagiyama, T. Iino, Y. Murakami, and A. Ito, "Noncontact estimation of intercellular breaking force using a femtosecond laser impulse quantified by atomic force microscopy," *Proceedings of the National Academy of Sciences*, vol. 108, no. 5, pp. 1777–1782, 2011.

[17] R. Yasukuni, R. Fukushima, T. Iino, and Y. Hosokawa, "Pulsed-laser-activated impulse response encoder: Sensitive detection of surface elastic waves on biomimetic microsized gel spheres," *Applied Physics Express*, vol. 10, no. 11, p. 117 001, 2017.

[18] T. Iino, M. Hagiyama, T. Furuno, A. Ito, and Y. Hosokawa, "Time-course statistical evaluation of intercellular adhesion maturation by femtosecond laser impulse," *Biophysical Journal*, vol. 111, no. 10, pp. 2255–2262, 2016.

[19] K. Oikawa, S. Matsunaga, S. Mano, *et al.*, "Physical interaction between peroxisomes and chloroplasts elucidated by in situ laser analysis," *Nature Plants*, vol. 1, no. 4, pp. 1–12, 2015.

[20] S. Yamada, T. Iino, Y. Bessho, Y. Hosokawa, and T. Matsui, "Quantitative analysis of mechanical force required for cell extrusion in zebrafish embryonic epithelia," *Biology Open*, vol. 6, no. 10, pp. 1575–1580, 2017.

[21] J. Liu, J. Wen, Z. Zhang, H. Liu, and Y. Sun, "Voyage inside the cell: Microsystems and nanoengineering for intracellular measurement and manipulation," *Microsystems & Nanoengineering*, vol. 1, no. 1, pp. 1–15, 2015.

[22] H. Liu, J. Wen, Y. Xiao, *et al.*, "In situ mechanical characterization of the cell nucleus by atomic force microscopy," *ACS nano*, vol. 8, no. 4, pp. 3821–3828, 2014.

[23] E. K. Yim, E. M. Darling, K. Kulangara, F. Guilak, and K. W. Leong, "Nanotopography-induced changes in focal adhesions, cytoskeletal organization, and mechanical properties of human mesenchymal stem cells," *Biomaterials*, vol. 31, no. 6, pp. 1299–1306, 2010.

[24] M. J. Jaasma, W. M. Jackson, and T. M. Keaveny, "Measurement and characterization of whole-cell mechanical behavior," *Annals of biomedical engineering*, vol. 34, pp. 748–758, 2006.

[25] K. Pogoda, J. Jaczewska, J. Wiltowska-Zuber, *et al.*, "Depth-sensing analysis of cytoskeleton organization based on afm data," *European Biophysics Journal*, vol. 41, pp. 79–87, 2012.

[26] H. Esmaeilsabzali, "Development of a microfluidic platform for size-based enrichment and immunomagnetic isolation of circulating tumour cells," 2017.

[27] M. Urbanska, H. E. Muñoz, J. Shaw Bagnall, *et al.*, "A comparison of microfluidic methods for high-throughput cell deformability measurements," *Nature methods*, vol. 17, no. 6, pp. 587–593, 2020.

[28] J. R. Lange, C. Metzner, S. Richter, *et al.*, "Unbiased high-precision cell mechanical measurements with microconstrictions," *Biophysical Journal*, vol. 112, no. 7, pp. 1472–1480, 2017.

[29] D. R. Gossett, H. T. Tse, S. A. Lee, *et al.*, "Hydrodynamic stretching of single cells for large population mechanical phenotyping," *Proceedings of the National Academy of Sciences*, vol. 109, no. 20, pp. 7630–7635, 2012.

[30] J. P. Beech, S. H. Holm, K. Adolfsson, and J. O. Tegenfeldt, "Sorting cells by size, shape and deformability," *Lab on a Chip*, vol. 12, no. 6, pp. 1048–1051, 2012.

[31] E Evans and A Yeung, "Apparent viscosity and cortical tension of blood granulocytes determined by micropipet aspiration," *Biophysical journal*, vol. 56, no. 1, pp. 151–160, 1989.

[32] S. Suresh, "Nanomedicine: Elastic clues in cancer detection," *Nature Nanotechnology*, vol. 2, no. 12, p. 748, 2007.

[33] A. Rowat, J Lammerding, and J. H. Ipsen, "Mechanical properties of the cell nucleus and the effect of emerin deficiency," *Biophysical journal*, vol. 91, no. 12, pp. 4649–4664, 2006.

[34] J. Swift, I. L. Ivanovska, A. Buxboim, *et al.*, "Nuclear lamin-a scales with tissue stiffness and enhances matrix-directed differentiation," *Science*, vol. 341, no. 6149, p. 1 240 104, 2013.

[35] Y. Ding, G.-F. Wang, X.-Q. Feng, and S.-W. Yu, "Micropipette aspiration method for characterizing biological materials with surface energy," *Journal of Biomechanics*, vol. 80, pp. 32–36, 2018.

[36] B. Hogan, A. Babataheri, Y. Hwang, A. I. Barakat, and J. Husson, "Characterizing cell adhesion by using micropipette aspiration," *Biophysical journal*, vol. 109, no. 2, pp. 209–219, 2015.

[37] J. Brugués, B. Maugis, J. Casademunt, P. Nassoy, F. Amblard, and P. Sens, "Dynamical organization of the cytoskeletal cortex probed by micropipette aspiration," *Proceedings of the National Academy of Sciences*, vol. 107, no. 35, pp. 15 415–15 420, 2010.

[38] R. M. Hochmuth, "Micropipette aspiration of living cells," *Journal of biomechanics*, vol. 33, no. 1, pp. 15–22, 2000.

[39] N. Bufi, P. Durand-Smet, and A. Asnacios, "Single-cell mechanics: The parallel plates technique," in *Methods in cell biology*, vol. 125, Elsevier, 2015, pp. 187–209.

[40] W. Ronan, V. S. Deshpande, R. M. McMeeking, and J. P. McGarry, "Numerical investigation of the active role of the actin cytoskeleton in the compression resistance of cells," *Journal of the Mechanical Behavior of Biomedical Materials*, vol. 14, pp. 143–157, 2012.

[41] J. McGarry, "Characterization of cell mechanical properties by computational modeling of parallel plate compression," *Annals of biomedical engineering*, vol. 37, pp. 2317–2325, 2009.

[42] P.-H. Wu, D. R.-B. Aroush, A. Asnacios, *et al.*, "A comparison of methods to assess cell mechanical properties," *Nature methods*, vol. 15, no. 7, pp. 491–498, 2018.

[43] J. Étienne, J. Fouchard, D. Mitrossilis, N. Bufi, P. Durand-Smet, and A. Asnacios, "Cells as liquid motors: Mechanosensitivity emerges from collective dynamics of actomyosin cortex," *Proceedings of the National Academy of Sciences*, vol. 112, no. 9, pp. 2740–2745, 2015.

[44] B. D. Hoffman, G. Massiera, K. M. Van Citters, and J. C. Crocker, "The consensus mechanics of cultured mammalian cells," *Proceedings of the National Academy of Sciences*, vol. 103, no. 27, pp. 10 259–10 264, 2006.

[45] V. M. Laurent, E. Planus, R. Fodil, and D. Isabey, "Mechanical assessment by magnetocytometry of the cytosolic and cortical cytoskeletal compartments in adherent epithelial cells," *Biorheology*, vol. 40, no. 1, 2, 3, pp. 235–240, 2003.

[46] M. Marinkovic, K. T. Turner, L. Deng, S. Suresh, and J. J. Fredberg, *Viscoelasticity of the human red blood cell*, 2006.

[47] V. M. Laurent, R. Fodil, P. Cañadas, *et al.*, "Partitioning of cortical and deep cytoskeleton responses from transient magnetic bead twisting," *Annals of biomedical engineering*, vol. 31, no. 10, p. 1263, 2003.

[48] F. J. Alenghat, B. Fabry, K. Y. Tsai, W. H. Goldmann, and D. E. Ingber, "Analysis of cell mechanics in single vinculin-deficient cells using a magnetic tweezer," *Biochemical and biophysical research communications*, vol. 277, no. 1, pp. 93–99, 2000.

[49] C. T. Mierke, "Cancer cells regulate biomechanical properties of human microvascular endothelial cells," *Journal of Biological Chemistry*, vol. 286, no. 46, pp. 40 025–40 037, 2011.

[50] J. Chen, B. Fabry, E. L. Schiffrin, and N. Wang, "Twisting integrin receptors increases endothelin-1 gene expression in endothelial cells," *American Journal of Physiology-Cell Physiology*, vol. 280, no. 6, pp. C1475–C1484, 2001.

[51] N. Bonakdar, R. Gerum, M. Kuhn, *et al.*, "Mechanical plasticity of cells," *Nature materials*, vol. 15, no. 10, pp. 1090–1094, 2016.

[52] P. Kollmannsberger and B. Fabry, "Bahigh-force magnetic tweezers with force feedback for biological applications," *Review of Scientific Instruments*, vol. 78, no. 11, p. 114 301, 2007.

[53] K. J. Chalut, A. E. Ekpenyong, W. L. Clegg, I. C. Melhuish, and J. Guck, "Quantifying cellular differentiation by physical phenotype using digital holographic microscopy," *Integrative biology*, vol. 4, no. 3, pp. 280–284, 2012.

[54] X. Zhang, H. Kim, L. W. Rogowski, S. Sheckman, and M. JunKim, "Development and implementation of high power hexapole magnetic tweezer system for micromanipulations," in *2018 IEEE International Conference on Robotics and Automation (ICRA)*, IEEE, 2018, pp. 2670–2675.

[55] X. Wang, C. Ho, Y Tsatskis, *et al.*, "Intracellular manipulation and measurement with multipole magnetic tweezers," *Science robotics*, vol. 4, no. 28, eaav6180, 2019.

[56] C. Garzon-Coral, H. A. Fantana, and J. Howard, "A force-generating machinery maintains the spindle at the cell center during mitosis," *Science*, vol. 352, no. 6289, pp. 1124–1127, 2016.

[57] J. Guck, R. Ananthakrishnan, H. Mahmood, T. J. Moon, C. C. Cunningham, and J. Käs, "The optical stretcher: A novel laser tool to micromanipulate cells," *Biophysical journal*, vol. 81, no. 2, pp. 767–784, 2001.

[58] N. Bellini, F. Bragheri, I. Cristiani, J. Guck, R. Osellame, and G. Whyte, "Validation and perspectives of a femtosecond laser fabricated monolithic optical stretcher," *Biomedical optics express*, vol. 3, no. 10, pp. 2658–2668, 2012.

[59] T. Yang, G. Nava, P. Minzioni, *et al.*, "Investigation of temperature effect on cell mechanics by optofluidic microchips," *Biomedical Optics Express*, vol. 6, no. 8, pp. 2991–2996, 2015.

[60] J. Kas, T. Kiessling, A. Fritsch, and R. Stange, "Thermorheology of living cells–impact of temperature variations on cell mechanics," in *APS March Meeting Abstracts*, vol. 2015, 2015, G47–006.

[61] C. Chan, G Whyte, L Boyde, G Salbreux, and J. Guck, "Impact of heating on passive and active biomechanics of suspended cells," *Interface focus*, vol. 4, no. 2, p. 20 130 069, 2014.

[62] C. J. Chan, W. Li, G. Cojoc, and J. Guck, "Volume transitions of isolated cell nuclei induced by rapid temperature increase," *Biophysical journal*, vol. 112, no. 6, pp. 1063–1076, 2017.

[63] V. M. Laurent, S. Hénon, E. Planus, *et al.*, "Assessment of mechanical properties of adherent living cells by bead micromanipulation: Comparison of magnetic twisting cytometry vs optical tweezers," *J. Biomech. Eng.*, vol. 124, no. 4, pp. 408–421, 2002.

[64] M.-T. Wei, A. Zaorski, H. C. Yalcin, *et al.*, "A comparative study of living cell micromechanical properties by oscillatory optical tweezers," *Optics express*, vol. 16, no. 12, pp. 8594–8603, 2008.

[65] X. Ding, Z. Peng, S.-C. S. Lin, *et al.*, "Cell separation using tilted-angle standing surface acoustic waves," *Proceedings of the National Academy of Sciences*, vol. 111, no. 36, pp. 12 992–12 997, 2014.

[66] M. Wu, A. Ozcelik, J. Rufo, Z. Wang, R. Fang, and T. Jun Huang, "Acoustofluidic separation of cells and particles," *Microsystems & nanoengineering*, vol. 5, no. 1, p. 32, 2019.

[67] D. Hartono, Y. Liu, P. L. Tan, X. Y. S. Then, L.-Y. L. Yung, and K.-M. Lim, "On-chip measurements of cell compressibility via acoustic radiation," *Lab on a Chip*, vol. 11, no. 23, pp. 4072–4080, 2011.

[68] P. Augustsson, J. T. Karlsen, H.-W. Su, H. Bruus, and J. Voldman, "Iso-acoustic focusing of cells for size-insensitive acousto-mechanical phenotyping," *Nature communications*, vol. 7, no. 1, p. 11 556, 2016.

[69] J. H. Kang, T. P. Miettinen, L. Chen, *et al.*, "Noninvasive monitoring of single-cell mechanics by acoustic scattering," *Nature methods*, vol. 16, no. 3, pp. 263–269, 2019.

[70] E. M. Strohm, M. J. Moore, and M. C. Kolios, "Single cell photoacoustic microscopy: A review," *IEEE Journal of Selected Topics in Quantum Electronics*, vol. 22, no. 3, pp. 137–151, 2015.

[71] L. Wang, K. Maslov, and L. V. Wang, "Single-cell label-free photoacoustic flowoxigraphy in vivo," *Proceedings of the National Academy of Sciences*, vol. 110, no. 15, pp. 5759–5764, 2013.

[72] Y. Wang, K. Maslov, Y. Zhang, *et al.*, "Fiber-laser-based photoacoustic microscopy and melanoma cell detection," *Journal of biomedical optics*, vol. 16, no. 1, pp. 011 014–011 014, 2011.

[73] V. P. Zharov, E. I. Galanzha, Y. Menyaev, and V. V. Tuchin, "In vivo high-speed imaging of individual cells in fast blood flow," *Journal of biomedical optics*, vol. 11, no. 5, pp. 054 034–054 034, 2006.

[74] E. M. Strohm, E. S. Berndl, and M. C. Kolios, "Probing red blood cell morphology using high-frequency photoacoustics," *Biophysical journal*, vol. 105, no. 1, pp. 59–67, 2013.

[75] M. H. Richardson and D. L. Formenti, "Parameter estimation from frequency response measurements using rational fraction polynomials," in *Proceedings of the 1st international modal analysis conference*, Citeseer, vol. 1, 1982, pp. 167–186.

[76] X. Guo, M. Sun, Y. Yang, *et al.*, "Controllable cell deformation using acoustic streaming for membrane permeability modulation," *Advanced Science*, vol. 8, no. 3, p. 2 002 489, 2021.

[77] W. Orapiriyakul, M. P. Tsimbouri, P. Childs, *et al.*, "Nanovibrational stimulation of mesenchymal stem cells induces therapeutic reactive oxygen species and inflammation for three-dimensional bone tissue engineering," *ACS nano*, vol. 14, no. 8, pp. 10 027–10 044, 2020.

[78] R.S.Gordan, "The Structure and Function of End of the Femur," *Bone*, pp. 576–589, 2003.

[79] D. Gautam and V. K. Rao, "Classification of diaphysis based on the mechanical response of femur bone," *Vibroengineering Procedia*, vol. 29, pp. 182–188, 2019.

[80] M. Niva, M. J. Kiuru, R. Haataja, and H. Pihlajamäki, "Fatigue injuries of the femur," *The Journal of bone and joint surgery. British volume*, vol. 87, no. 10, pp. 1385–1390, 2005.

[81] S. Sivananthan, E. Sherry, P. Warnke, and M. Miller, *Mercer's Textbook of Orthopaedics and Trauma Tenth edition*. CRC Press, 2012.

[82] A. R. Manktelow, F. S. Haddad, and N. J. Goddard, "Late lateral femoral condyle fracture after anterior cruciate ligament reconstruction. a case report," *The American Journal of Sports Medicine*, vol. 26, no. 4, pp. 587–590, 1998.

[83] J. Cordey and E. Gautier, "Strain gauges used in the mechanical testing of bones. Part I: Theoretical and technical aspects," *Injury*, vol. 30, no. SUPPL. 1, 1999, ISSN: 00201383.

[84] G. I. Baroncelli, "Quantitative ultrasound methods to assess bone mineral status in children: Technical characteristics, performance, and clinical application," *Pediatr. Res.*, vol. 63, no. 3, pp. 220–228, 2008, ISSN: 00313998. DOI: 10.1203/PDR.0b013e318163a286.

[85] F. Katsamanis and D. D. Raftopoulos, "Determination of mechanical properties of human femoral cortical bone by the Hopkinson bar stress technique," *J. Biomech.*, vol. 23, no. 11, pp. 1173–1184, 1990, ISSN: 00219290. DOI: 10.1016/0021-9290(90)90010-Z.

[86] S. B. Lang, "Elastic coefficients of animal bone," *Science*, vol. 165, no. 3890, pp. 287–288, 1969.

[87] A. A. E. Orías, J. M. Deuerling, M. D. Landrigan, J. E. Renaud, and R. K. Roeder, "Anatomic variation in the elastic anisotropy of cortical bone tissue in the human femur," *Journal of the mechanical behavior of biomedical materials*, vol. 2, no. 3, pp. 255–263, 2009.

[88] M. Granke, Q. Grimal, A. Saïed, P. Nauleau, F. Peyrin, and P. Laugier, "Change in porosity is the major determinant of the variation of cortical bone elasticity at the millimeter scale in aged women," *Bone*, vol. 49, no. 5, pp. 1020–1026, 2011.

[89] R. Ashman, S. Cowin, W. Van Buskirk, and J. Rice, "A continuous wave technique for the measurement of the elastic properties of cortical bone," *Journal of biomechanics*, vol. 17, no. 5, pp. 349–361, 1984.

[90] Q. Grimal, S. Haupert, D. Mitton, L. Vastel, and P. Laugier, "Assessment of cortical bone elasticity and strength: Mechanical testing and ultrasound provide complementary data," *Medical engineering & physics*, vol. 31, no. 9, pp. 1140–1147, 2009.

[91] J. D. Maynard, "The use of piezoelectric film and ultrasound resonance to determine the complete elastic tensor in one measurement," *The Journal of the Acoustical Society of America*, vol. 91, no. 3, pp. 1754–1762, 1992.

[92] A. Migliori, J. Sarrao, W. M. Visscher, *et al.*, "Resonant ultrasound spectroscopic techniques for measurement of the elastic moduli of solids," *Physica B: Condensed Matter*, vol. 183, no. 1-2, pp. 1–24, 1993.

[93] J. Kinney, J. Gladden, G. e. a. Marshall, S. Marshall, J. So, and J. Maynard, "Resonant ultrasound spectroscopy measurements of the elastic constants of human dentin," *Journal of biomechanics*, vol. 37, no. 4, pp. 437–441, 2004.

[94] T Lee, R. Lakes, and A Lal, "Investigation of bovine bone by resonant ultrasound spectroscopy and transmission ultrasound," *Biomechanics and Modeling in Mechanobiology*, vol. 1, no. 2, pp. 165–175, 2002.

[95] A. Migliori and J. Maynard, "Implementation of a modern resonant ultrasound spectroscopy system for the measurement of the elastic moduli of small solid specimens," *Review of scientific instruments*, vol. 76, no. 12, p. 121 301, 2005.

[96] T. J. Ulrich, K. McCall, and R. Guyer, "Determination of elastic moduli of rock samples using resonant ultrasound spectroscopy," *The Journal of the Acoustical Society of America*, vol. 111, no. 4, pp. 1667–1674, 2002.

[97] A. Lebedev, L. Ostrovskii, A. Sutin, I. Soustova, and P. Johnson, "Resonant acoustic spectroscopy at low q factors," *Acoustical Physics*, vol. 49, no. 1, pp. 81–87, 2003.

[98] S. Bernard, Q. Grimal, and P. Laugier, "Accurate measurement of cortical bone elasticity tensor with resonant ultrasound spectroscopy," *Journal of the mechanical behavior of biomedical materials*, vol. 18, pp. 12–19, 2013.

[99] H Daoui, X. Cai, F Boubenider, P Laugier, and Q Grimal, "Assessment of trabecular bone tissue elasticity with resonant ultrasound spectroscopy," *Journal of the mechanical behavior of biomedical materials*, vol. 74, pp. 106–110, 2017.

[100] S. Bernard, Q. Grimal, and P. Laugier, "Resonant ultrasound spectroscopy for viscoelastic characterization of anisotropic attenuative solid materials," *The Journal of the Acoustical Society of America*, vol. 135, no. 5, pp. 2601–2613, 2014.

[101] F. F. Balakirev, S. M. Ennaceur, R. J. Migliori, B. Maiorov, and A. Migliori, "Resonant ultrasound spectroscopy: The essential toolbox," *Review of Scientific Instruments*, vol. 90, no. 12, p. 121 401, 2019.

[102] M Muller, D Mitton, M Talmant, P Johnson, and P Laugier, "Nonlinear ultrasound can detect accumulated damage in human bone," *Journal of Biomechanics*, vol. 41, no. 5, pp. 1062–1068, 2008.

[103] M. Muller, A. Sutin, R. Guyer, M. Talmant, P. Laugier, and P. A. Johnson, "Nonlinear resonant ultrasound spectroscopy (nrus) applied to damage assessment in bone," *The Journal of the Acoustical Society of America*, vol. 118, no. 6, pp. 3946–3952, 2005.

[104] B. Ferry, M. Duclos, L. Burt, *et al.*, "Bone geometry and strength adaptations to physical constraints inherent in different sports: Comparison between elite female soccer players and swimmers," *J. Bone Miner. Metab.*, vol. 29, no. 3, pp. 342–351, 2011, ISSN: 09148779. DOI: 10.1007/s00774-010-0226-8.

[105] . John R.Giudicessi, BA.Michael J.Ackerman., "NIH Public Access," *Bone*, vol. 23, no. 1, pp. 1–7, 2008, ISSN: 15378276. DOI: 10.1038/jid.2014.371. arXiv: NIHMS150003. [Online]. Available: https://www.ncbi.nlm.nih.gov/pmc/articles/PMC3624763/pdf/nihms412728.pdf.

[106] P. S. Toljamo, P. Pulkkinen, E. Lammentausta, O. Tervonen, T. Jamsa, and M. T. Nieminen, "Bone mineral density and geometry parameters determined in vitro from dual-energy digital radiography images in the assessment of bone maximal load of reindeer femora," *Acta radiol.*, vol. 54, no. 8, pp. 961–965, 2013, ISSN: 02841851. DOI: 10.1177/0284185113486372.

[107] S. M. Ott, "Cortical or trabecular bone: What's the difference?" *American journal of nephrology*, vol. 47, no. 6, pp. 373–376, 2018.

[108] K. Terada and N. Kikuchi, "Nonlinear homogenization method for practical applications," *Am. Soc. Mech. Eng. Appl. Mech. Div. AMD*, vol. 212, no. January 1995, pp. 1–16, 1995, ISSN: 01608835.

[109] K. C. Kumar, T. Tandon, P. Silori, and A. Shaikh, "Biomechanical Stress Analysis of a Human Femur Bone Using ANSYS," *Mater. Today Proc.*, vol. 2, no. 4-5, pp. 2115–2120, 2015, ISSN: 22147853. DOI: 10.1016/j.matpr.2015.07.211. [Online]. Available: http://dx.doi.org/10.1016/j.matpr.2015.07.211.

[110] D. C. Viano, "Vibrational Characteristics of the Femur," vol. 75, pp. 417–436, 1981.

[111] A. Sabale, "Experimental Analysis of Femur Bone By Strain Guage," no. 2581, pp. 343–346, 2018.

[112] S. Mathukumar, V. A. Nagarajan, and A. Radhakrishnan, "Analysis and validation of femur bone data using finite element method under static load condition," *Proc. Inst. Mech. Eng. Part C J. Mech. Eng. Sci.*, vol. 233, no. 16, pp. 5547–5555, 2019, ISSN: 20412983. DOI: 10.1177/0954406219856028.

[113] A. A. Nassar and M. A. Almudhaffar, "Vibration of bones: A case study on human femur," *J. Eng. Sci.*, vol. 14, no. 2, pp. 229 –239, 2014. DOI: 10.17605/OSF.IO/E546S.

[114] U. N. Mughal, H. A. Khawaja, and M. Moatamedi, "Finite element analysis of human femur bone," *Int. J. Multiphys.*, vol. 9, no. 2, pp. 101–108, 2015, ISSN: 17509548. DOI: 10.1260/1750-9548.9.2.101.

[115] W. R. Taylor, E. Roland, H. Ploeg, *et al.*, "Determination of orthotropic bone elastic constants using FEA and modal analysis," *J. Biomech.*, vol. 35, no. 6, pp. 767–773, 2002, ISSN: 00219290. DOI: 10.1016/S0021-9290(02)00022-2.

[116] J. H. Keyak and S. A. Rossi, "Prediction of fracture location in the proximal femur using finite element models," vol. 23, pp. 657–664, 2001.

[117] I. T. Haider, A. D. Speirs, and H. Frei, "Effect of boundary conditions, impact loading and hydraulic stiffening on femoral fracture strength," *J. Biomech.*, vol. 46, no. 13, pp. 2115–2121, 2013, ISSN: 00219290. DOI: 10.1016/j.jbiomech.2013.07.004. [Online]. Available: http://dx.doi.org/10.1016/j.jbiomech.2013.07.004.

[118] S. Miwa and T. Otsuka, "Practical use of imaging technique for management of bone and soft tissue tumors," *Journal of Orthopaedic Science*, vol. 22, no. 3, pp. 391–400, 2017.

[119] C. S. Rajapakse, A. R. Farid, D. C. Kargilis, *et al.*, "Mri-based assessment of proximal femur strength compared to mechanical testing," *Bone*, p. 115 227, 2020.

[120] Y. Shireesha, S. Ramana, and P. G. Rao, "Modelling and static analysis of femur bone by using different implant materials," *IOSR Journal of Mechanical and Civil Engineering*, vol. 7, no. 4, pp. 82–91, 2013.

[121] N. J. Cairns, C. J. Adam, M. J. Pearcy, and J. Smeathers, "Evaluation of modal analysis techniques using physical models to detect osseointegration of implants in transfemoral amputees," in *2011 Annual International Conference of the IEEE Engineering in Medicine and Biology Society*, IEEE, 2011, pp. 1600–1603.

[122] B. Lv and S. Li, "Diagnosis study on sports injuries combined with medical imaging technology," 2017.

[123] A. E. Yousif and M. Y. Aziz, "Biomechanical analysis of the human femur bone during going upstairs and sitting down," *2012 1st Natl. Conf. Eng. Sci. FNCES 2012*, pp. 1–7, 2012. DOI: 10.1109/NCES.2012.6740472.

[124] Centre, "Response of human femur to mechanical vibration," vol. 13, 1991.

[125] W. Bian, Q. Lian, D. Li, *et al.*, "Morphological characteristics of cartilage-bone transitional structures in the human knee joint and CAD design of an osteochondral scaffold," *Biomed. Eng. Online*, vol. 15, no. 1, pp. 1–14, 2016, ISSN: 1475925X. DOI: 10.1186/s12938-016-0200-3.

[126] F. S. Chau, "Effect of Pressure on Fluid Damping in MEMS Torsional Resonators with Flow Ranging from Continuum to Molecular Regime," pp. 91–106, 2008. DOI: 10.1007/s11340-007-9076-2.

[127] M. C. Hobatho, R. Darmana, J. J. Barrau, S. Laroze, and J. P. Morucci, "Natural frequency analysis of a human tibia," *IEEE/Engineering Med. Biol. Soc. Annu. Conf.*, vol. 10, no. pt2, pp. 690–691, 1988. DOI: 10.1109/iembs.1988.94933.

[128] G. Lowet, R. Van Audekercke, G. Van der Perre, P. Geusens, J. Dequeker, and J. Lammens, "The relation between resonant frequencies and torsional stiffness of long bones in vitro. Validation of a simple beam model," *J. Biomech.*, vol. 26, no. 6, pp. 689–696, 1993, ISSN: 00219290. DOI: 10.1016/0021-9290(93)90032-A.

[129] J.-Y. Rho, "An ultrasonic method for measuring the elastic properties of human tibial cortical and cancellous bone," *Ultrasonics*, vol. 34, no. 8, pp. 777–783, 1996.

[130] G. L. Niebur, M. J. Feldstein, J. C. Yuen, T. J. Chen, and T. M. Keaveny, "High-resolution finite element models with tissue strength asymmetry accurately predict failure of trabecular bone," *Journal of biomechanics*, vol. 33, no. 12, pp. 1575–1583, 2000.

[131] M. Hosseinzadeh, M. Ghoreishi, and K. Narooei, "Investigation of hyperelastic models for nonlinear elastic behavior of demineralized and deproteinized bovine cortical femur bone," *J. Mech. Behav. Biomed. Mater.*, vol. 59, pp. 393–403, 2016, ISSN: 18780180. DOI: 10.1016/j.jmbbm.2016.02.027. [Online]. Available: http://dx.doi.org/10.1016/j.jmbbm.2016.02.027.

[132] A. L. Boskey and R. Coleman, "Critical reviews in oral biology & medicine: Aging and bone," *J. Dent. Res.*, vol. 89, no. 12, pp. 1333–1348, 2010, ISSN: 00220345. DOI: 10.1177/0022034510377791.

[133] R. Sadeghi, F. Bakhtiari-Nejad, and T. Goudarzi, "Vibrational analysis of human femur bone," *Proc. ASME Des. Eng. Tech. Conf.*, vol. 8, pp. 1–8, 2018. DOI: 10.1115/DETC2018-85114.

[134] P. B. Kumar and D. R. Parhi, "Vibrational characterization of a human femur bone and its significance in the designing of artificial implants," *World Journal of Engineering*, 2017.

[135] R. J. Scheuplein, "Analysis of permeability data for the case of parallel diffusion pathways," *Biophysical Journal*, vol. 6, no. 1, pp. 1–17, 1966.

[136] J. A. Bouwstra, P. L. Honeywell-Nguyen, G. S. Gooris, and M. Ponec, "Structure of the skin barrier and its modulation by vesicular formulations," *Progress in lipid research*, vol. 42, no. 1, pp. 1–36, 2003.

[137] A. Berekméri, A. Tiganescu, A. A. Alase, E. Vital, M. Stacey, and M. Wittmann, "Non-invasive approaches for the diagnosis of autoimmune/autoinflammatory skin diseases—a focus on psoriasis and lupus erythematosus," *Frontiers in immunology*, vol. 10, p. 1931, 2019.

[138] N. J. Dhinagar and M. Celenk, "Early diagnosis and predictive monitoring of skin diseases," in *2016 IEEE Healthcare Innovation Point-Of-Care Technologies Conference (HI-POCT)*, IEEE, 2016, pp. 33–36.

[139] A. Delalleau, G. Josse, J. George, Y. Mofid, F. Ossant, and J.-M. Lagarde, "A human skin ultrasonic imaging to analyse its mechanical properties," *European Journal of Computational Mechanics/Revue Européenne de Mécanique Numérique*, vol. 18, no. 1, pp. 105–116, 2009.

[140] J. Fluhr *et al.*, "Eemco guidance for the in vivo assessment of biomechanical properties of the human skin and its annexes: Revisiting instrumentation and test modes.," *Skin Pharmacology and Physiology*, vol. 33, no. 1, pp. 44–60, 2019.

[141] M. L. Crichton, X. Chen, H. Huang, and M. A. Kendall, "Elastic modulus and viscoelastic properties of full thickness skin characterised at micro scales," *Biomaterials*, vol. 34, no. 8, pp. 2087–2097, 2013.

[142] B. You, C.-Y. Chen, C.-P. Yu, P.-H. Wang, and J.-Y. Lu, "Frequency-dependent skin penetration depth of terahertz radiation determined by water sorption–desorption," *Optics express*, vol. 26, no. 18, pp. 22 709–22 721, 2018.

[143] S Diridollou, M Berson, V Vabre, *et al.*, "An in vivo method for measuring the mechanical properties of the skin using ultrasound," *Ultrasound in medicine & biology*, vol. 24, no. 2, pp. 215–224, 1998.

[144] Q. Wang and V. Hayward, "In vivo biomechanics of the fingerpad skin under local tangential traction," *Journal of biomechanics*, vol. 40, no. 4, pp. 851–860, 2007.

[145] L Czirjak, I Foeldvari, and U Müller-Ladner, "Skin involvement in systemic sclerosis," *Rheumatology*, vol. 47, no. suppl_5, pp. v44–v45, 2008.

[146] C. Li, G. Guan, R. Reif, Z. Huang, and R. K. Wang, "Determining elastic properties of skin by measuring surface waves from an impulse mechanical stimulus using phase-sensitive optical coherence tomography," *Journal of The Royal Society Interface*, vol. 9, no. 70, pp. 831–841, 2012.

[147] C. Niezrecki, J. Baqersad, and A. Sabato, "Digital image correlation techniques for nde and shm," *Handbook of Advanced Nondestructive Evaluation*, pp. 1545–1590, 2019.

[148] A. Taghavikhalilbad, S. Adabi, A. Clayton, H. Soltanizadeh, D. Mehregan, and M. R. Avanaki, "Semi-automated localization of dermal epidermal junction in optical coherence tomography images of skin," *Applied optics*, vol. 56, no. 11, pp. 3116–3121, 2017.

[149] M. R. Avanaki and A. Hojjatoleslami, "Skin layer detection of optical coherence tomography images," *Optik*, vol. 124, no. 22, pp. 5665–5668, 2013.

[150] S. Adabi, M. Hosseinzadeh, S. Noei, *et al.*, "Universal in vivo textural model for human skin based on optical coherence tomograms," *Scientific reports*, vol. 7, no. 1, pp. 1–11, 2017.

[151] Z Xu, J Dela Cruz, C Fthenakis, and C Saliou, "A novel method to measure skin mechanical properties with three-dimensional digital image correlation," *Skin Research and Technology*, vol. 25, no. 1, pp. 60–67, 2019.

[152] E Guan, S. Smilow, M. Rafailovich, and J. Sokolov, "Determining the mechanical properties of rat skin with digital image speckle correlation," *Dermatology*, vol. 208, no. 2, pp. 112–119, 2004.

[153] R. Panchal, L. Horton, P. Poozesh, J. Baqersad, and M. Nasiriavanaki, "Vibration analysis of healthy skin: Toward a noninvasive skin diagnosis methodology," *Journal of biomedical optics*, vol. 24, no. 1, p. 015 001, 2019.

[154] Y Zhao, B Feng, J Lee, N Lu, and D. Pierce, "A multi-layered computational model for wrinkling of human skin predicts aging effects," *Journal of the mechanical behavior of biomedical materials*, vol. 103, p. 103 552, 2020.

[155] N. F. A. Manan, M. H. M. Ramli, M. N. A. A. Patar, *et al.*, "Determining hyperelastic parameters of human skin using 2d finite element modelling and simulation," in *2012 IEEE Symposium on Humanities, Science and Engineering Research*, IEEE, 2012, pp. 805–809.

[156] A Talarico, M Malvezzi, and D. Prattichizzo, "Modeling the human touch: A fem model of the human hand fingertips for haptic application," in *Proc. of the COMSOL Conf*, 2014.

[157] S. L. Evans and C. A. Holt, "Measuring the mechanical properties of human skin in vivo using digital image correlation and finite element modelling," *The Journal of Strain Analysis for Engineering Design*, vol. 44, no. 5, pp. 337–345, 2009.

[158] W. Wang, J. E. Mottershead, A. Ihle, T. Siebert, and H. R. Schubach, "Finite element model updating from full-field vibration measurement using digital image correlation," *Journal of sound and vibration*, vol. 330, no. 8, pp. 1599–1620, 2011.

[159] C. Edwards and R. Marks, "Evaluation of biomechanical properties of human skin," *Clinics in dermatology*, vol. 13, no. 4, pp. 375–380, 1995.

[160] R. Darlenski, J. Kazandjieva, N. Tsankov, and J. W. Fluhr, "Acute irritant threshold correlates with barrier function, skin hydration and contact hypersensitivity in atopic dermatitis and rosacea," *Experimental dermatology*, vol. 22, no. 11, pp. 752–753, 2013.

[161] T. Waghule, V. K. Rapalli, S. Gorantla, *et al.*, "Nanostructured lipid carriers as potential drug delivery systems for skin disorders," *Current Pharmaceutical Design*, vol. 26, no. 36, pp. 4569–4579, 2020.

[162] H. Dobrev, "In vivo study of skin mechanical properties in psoriasis vulgaris.," *Acta dermato-venereologica*, vol. 80, no. 4, 2000.

[163] V. R. Leite e Silva, M. A. Schulman, C. Ferelli, *et al.*, "Hydrating effects of moisturizer active compounds incorporated into hydrogels: In vivo assessment and comparison between devices," *Journal of cosmetic dermatology*, vol. 8, no. 1, pp. 32–39, 2009.

[164] C. Sinico and A. M. Fadda, "Vesicular carriers for dermal drug delivery," *Expert opinion on drug delivery*, vol. 6, no. 8, pp. 813–825, 2009.

[165] V. Patravale and S. Mandawgade, "Novel cosmetic delivery systems: An application update," *International journal of cosmetic science*, vol. 30, no. 1, pp. 19–33, 2008.

[166] N. G. Kotla, B. Chandrasekar, P. Rooney, *et al.*, "Biomimetic lipid-based nanosystems for enhanced dermal delivery of drugs and bioactive agents," *ACS Biomaterials Science & Engineering*, vol. 3, no. 7, pp. 1262–1272, 2017.

[167] R. Sharma, G. Kaur, and D. N. Kapoor, "Fluconazole loaded cubosomal vesicles for topical delivery," *International Journal of Drug Development and Research*, vol. 7, no. 3, pp. 0–0, 2015.

[168] R. Nithya, P. Jerold, and K. Siram, "Cubosomes of dapsone enhanced permeation across the skin," *Journal of Drug Delivery Science and Technology*, vol. 48, pp. 75–81, 2018.

[169] V. K. Rapalli, S. Banerjee, S. Khan, *et al.*, "Qbd-driven formulation development and evaluation of topical hydrogel containing ketoconazole loaded cubosomes," *Materials Science and Engineering: C*, vol. 119, p. 111 548, 2021.

[170] V. K. Rapalli, T. Waghule, N. Hans, *et al.*, "Insights of lyotropic liquid crystals in topical drug delivery for targeting various skin disorders," *Journal of Molecular Liquids*, p. 113 771, 2020.

[171] I. A. Rather, V. K. Bajpai, Y. S. Huh, *et al.*, "Probiotic lactobacillus sakei probio-65 extract ameliorates the severity of imiquimod induced psoriasis-like skin inflammation in a mouse model," *Frontiers in Microbiology*, vol. 9, p. 1021, 2018.

[172] G. Dabade, A. Kale, B. Athani, V. Sankri, S. Pawar, and S. Megeri, "A study on zoonotic tuberculosis in selected rural areas of bagalkot and belgaum districts of karnataka state," *Journal of Clinical Tuberculosis and Other Mycobacterial Diseases*, vol. 9, pp. 30–35, 2017.

[173] J. E. Bischoff, E. M. Arruda, and K. Grosh, "Finite element modeling of human skin using an isotropic, nonlinear elastic constitutive model," *Journal of biomechanics*, vol. 33, no. 6, pp. 645–652, 2000.

[174] A. F. Bertolini, "Review of eigensolution procedures for linear dynamic finite element analysis," 1998.

[175] A Powmya and M. Narasimhan, "Free vibration analysis of axisymmetric laminated composite circular and annular plates using chebyshev collocation," *International Journal of Advanced Structural Engineering (IJASE)*, vol. 7, no. 2, pp. 129–141, 2015.

[176] D. A. Dillard, B. Mukherjee, P. Karnal, R. C. Batra, and J. Frechette, "A review of winkler's foundation and its profound influence on adhesion and soft matter applications," *Soft matter*, vol. 14, no. 19, pp. 3669–3683, 2018.

[177] S. Bielfeldt, V. Schoder, U. Ely, A. Van Der Pol, J. De Sterke, and K.-P. Wilhelm, "Assessment of human stratum corneum thickness and its barrier properties by in-vivo confocal raman spectroscopy," *International Journal of Cosmetic Science*, vol. 31, no. 6, pp. 479–480, 2009.

[178] L. M. Russell, S. Wiedersberg, and M. B. Delgado-Charro, "The determination of stratum corneum thickness an alternative approach," *European journal of pharmaceutics and biopharmaceutics*, vol. 69, no. 3, pp. 861–870, 2008.

[179] S. Kruse, J. Smith, A. Lawrence, *et al.*, "Tissue characterization using magnetic resonance elastography: Preliminary results," *Physics in Medicine & Biology*, vol. 45, no. 6, p. 1579, 2000.

[180] Y.-c. Fung, *Biomechanics: mechanical properties of living tissues*. Springer Science & Business Media, 2013.

[181] M. Geerligs, "Skin layer mechanics," *Eindhoven: TU Eindhoven*, 2010.

[182] R. H. Wildnauer, J. W. Bothwell, and A. B. Douglass, "Stratum corneum biomechanical properties i. influence of relative humidity on normal and extracted human stratum corneum," *Journal of Investigative Dermatology*, vol. 56, no. 1, pp. 72–78, 1971.

[183] M. A. Kendall, Y.-F. Chong, and A. Cock, "The mechanical properties of the skin epidermis in relation to targeted gene and drug delivery," *Biomaterials*, vol. 28, no. 33, pp. 4968–4977, 2007.

[184] K. Van Vliet, G Bao, and S Suresh, "The biomechanics toolbox: Experimental approaches for living cells and biomolecules," *Acta materialia*, vol. 51, no. 19, pp. 5881–5905, 2003.

[185] M. L. Rodriguez, P. J. McGarry, and N. J. Sniadecki, "Review on cell mechanics: Experimental and modeling approaches," *Applied Mechanics Reviews*, vol. 65, no. 6, 2013.

[186] E. M. Darling and D. Di Carlo, "High-throughput assessment of cellular mechanical properties," *Annual review of biomedical engineering*, vol. 17, p. 35, 2015.

[187] B. M. Fund, "to reveal this structure . The nucIear inclusions have been," pp. 17–27,

[188] N. A. Kim, D. G. Lim, J. Y. Lim, *et al.*, "Evaluation of protein formulation and its viscosity with DSC, DLS, and microviscometer," *Journal of Pharmaceutical Investigation*, vol. 44, no. 4, pp. 309–316, 2014, ISSN: 20936214. DOI: 10.1007/s40005-014-0128-1.

[189] P. Chen, Y. Y. Huang, G. Bhave, K. Hoshino, and X. Zhang, "Inkjet-Print Micromagnet Array on Glass Slides for Immunomagnetic Enrichment of Circulating Tumor Cells," *Annals of Biomedical Engineering*, vol. 44, no. 5, pp. 1710–1720, 2016, ISSN: 15739686. DOI: 10.1007/s10439-015-1427-z.

[190] J. Lloyd Sutterby, "Falling sphere viscometer," *Journal of Physics E: Scientific Instruments*, vol. 6, no. 10, pp. 1001–1005, 1973, ISSN: 00223735. DOI: 10.1088/0022-3735/6/10/016.

[191] H. Yabuno, K. Higashino, M. Kuroda, and Y. Yamamoto, "Self-excited vibrational viscometer for high-viscosity sensing," *Journal of Applied Physics*, vol. 116, no. 12, 2014, ISSN: 10897550. DOI: 10.1063/1.4896487.

[192] N. Srivastava and M. A. Burns, "Analysis of non-Newtonian liquids using a microfluidic capillary viscometer," *Analytical Chemistry*, vol. 78, no. 5, pp. 1690–1696, 2006, ISSN: 00032700. DOI: 10.1021/ac0518046.

[193] A. A. John, "Natural frequency of cancer cells as a starting point in cancer treatment Author ( s ): Saravana Kumar Jaganathan , Aruna Priyadarshni Subramanian , Muthu Vignesh Vellayappan , Arunpandian Balaji , Agnes Aruna John , Ashok Kumar Jaganathan and Eko Supriya," vol. 110, no. 9, pp. 1828–1832, 2016. DOI: 10.18520/cs/v1.

[194] P. V. Zinin, J. S. Allen, and V. M. Levin, "Mechanical resonances of bacteria cells," *Physical Review E - Statistical, Nonlinear, and Soft Matter Physics*, vol. 72, no. 6, pp. 1–10, 2005, ISSN: 15393755. DOI: 10.1103/PhysRevE.72.061907.

[195] R. Caflisch, *(Cambridge Mathematical Library) Sir Horace Lamb M.A. LL.D. Sc.D. F.R.S., Russ Caflisch - Hydrodynamics-Cambridge University Press (1975).pdf*.

[196] C.-T. Chang and Bostwick, "An Extension Theory of Resonance of Drop," *Bulletin and Biophysics, Mathematical*, vol. 17, no. 1, pp. 35–40, 1955.

[197] R. M. Hochmuth, P. R. Worthy, and E. A. Evans, "Red cell extensional recovery and the determination of membrane viscosity," *Biophysical Journal*, vol. 26, no. 1, pp. 101–114, 1979, ISSN: 00063495. DOI: 10.1016/S0006-3495(79)85238-8. [Online]. Available: http://dx.doi.org/10.1016/S0006-3495(79)85238-8.

[198] E. Ackerman, "An extension of the theory of resonances of biological cells: III. Relationship of breakdown curves and mechanical Q," *The Bulletin of Mathematical Biophysics*, vol. 19, no. 1, pp. 1–7, 1957, ISSN: 00074985. DOI: 10.1007/BF02668287.

[199] P. V. Zinin and J. S. Allen, "Deformation of biological cells in the acoustic field of an oscillating bubble," *Physical Review E - Statistical, Nonlinear, and Soft Matter Physics*, vol. 79, no. 2, pp. 1–12, 2009, ISSN: 15393755. DOI: 10.1103/PhysRevE.79.021910.

[200] E. A. Joris, "Mechanical Resonances of Amphiuma Erythrocytes," pp. 860–865, 1969.

[201] A. Kinoshita, S. Senda, K. Mizushige, *et al.*, "Evaluation of acoustic properties of the live human smooth-muscle cell using scanning acoustic microscopy," *Ultrasound in Medicine and Biology*, vol. 24, no. 9, pp. 1397–1405, 1998, ISSN: 03015629. DOI: 10.1016/S0301-5629(98)00121-5.

[202] J. Bereiter-Hahn, "Acoustic Microscopy for Biomedical Applications," *Biomedical Imaging: Principles and Applications*, pp. 368–414, 2012. DOI: 10.1002/9781118271933.ch12.

[203] G. A. Briggs, J. Wang, and R. Gundle, "Quantitative acoustic microscopy of individual living human cells," *Journal of Microscopy*, vol. 172, no. 1, pp. 3–12, 1993, ISSN: 13652818. DOI: 10.1111/j.1365-2818.1993.tb03387.x.

[204] D. Mizuno, C. Tardin, C. F. Schmidt, and F. C. MacKintosh, "Nonequilibrium mechanics of active cytoskeletal networks," *Science*, vol. 315, no. 5810, pp. 370–373, 2007, ISSN: 00368075. DOI: 10.1126/science.1134404.

[205] D. A. Fletcher and R. D. Mullins, "Cell mechanics and the cytoskeleton," *Nature*, vol. 463, no. 7280, pp. 485–492, 2010, ISSN: 00280836. DOI: 10.1038/nature08908.

[206] M. F. Olson and E. Sahai, "The actin cytoskeleton in cancer cell motility," *Clinical and Experimental Metastasis*, vol. 26, no. 4, pp. 273–287, 2009, ISSN: 02620898. DOI: 10.1007/s10585-008-9174-2.

[207] J. Pokorný, C. Vedruccio, M. Cifra, and O. Kučera, "Cancer physics: Diagnostics based on damped cellular elastoelectrical vibrations in microtubules," *European Biophysics Journal*, vol. 40, no. 6, pp. 747–759, 2011, ISSN: 01757571. DOI: 10.1007/s00249-011-0688-1.

[208] B. C. Goodwin, "Oscillatory behavior in enzymatic control processes," *Advances in Enzyme Regulation*, vol. 3, no. C, 1965, ISSN: 00652571. DOI: 10.1016/0065-2571(65)90067-1.

[209] O. Chaudhuri, J. Cooper-White, P. A. Janmey, D. J. Mooney, and V. B. Shenoy, "Effects of extracellular matrix viscoelasticity on cellular behaviour," *Nature*, vol. 584, no. 7822, pp. 535–546, 2020, ISSN: 14764687. DOI: 10.1038/s41586-020-2612-2. [Online]. Available: http://dx.doi.org/10.1038/s41586-020-2612-2.

[210] J. Stricker, T. Falzone, and M. L. Gardel, "Mechanics of the F-actin cytoskeleton," *Journal of Biomechanics*, vol. 43, no. 1, pp. 9–14, 2010, ISSN: 00219290. DOI: 10.1016/j.jbiomech.2009.09.003. [Online]. Available: http://dx.doi.org/10.1016/j.jbiomech.2009.09.003.

[211] M. Tarantola, A. K. Marel, E. Sunnick, H. Adam, J. Wegener, and A. Janshoff, "Dynamics of human cancer cell lines monitored by electrical and acoustic fluctuation analysis," *Integrative Biology*, vol. 2, no. 2-3, pp. 139–150, 2010, ISSN: 17579694. DOI: 10.1039/b920815a.

[212] J. Rother, H. Nöding, I. Mey, and A. Janshoff, "Atomic force microscopy-based microrheology reveals significant differences in the viscoelastic response between malign and benign cell lines," *Open Biology*, vol. 4, no. MAY, 2014, ISSN: 20462441. DOI: 10.1098/rsob.140046.

[213] A. Srivastava, H. Sharma, S. Khanna, *et al.*, "Interleukin-6 Induced Proliferation Is Attenuated by Transforming Growth Factor-$\beta$-Induced Signaling in Human Hepatocellular Carcinoma Cells," *Frontiers in Oncology*, vol. 11, no. January, pp. 1–15, 2022, ISSN: 2234943X. DOI: 10.3389/fonc.2021.811941.

[214] H. Saini, H. Sharma, S. Mukherjee, S. Chowdhury, and R. Chowdhury, "Verteporfin disrupts multiple steps of autophagy and regulates p53 to sensitize osteosarcoma cells," *Cancer Cell International*, vol. 21, no. 1, pp. 1–16, 2021, ISSN: 14752867. DOI: 10.1186/s12935-020-01720-y. [Online]. Available: https://doi.org/10.1186/s12935-020-01720-y.

[215] S. Dash, P. M. Sarashetti, B. Rajashekar, R. Chowdhury, and S. Mukherjee, "TGF-$\beta$2-induced EMT is dampened by inhibition of autophagy and TNF-$\alpha$ treatment," *Oncotarget*, vol. 9, no. 5, pp. 6433–6449, 2018, ISSN: 19492553. DOI: 10.18632/oncotarget.23942.

[216] V. Kachwal, A. Srivastava, S. Thakar, *et al.*, "Engineering a light-driven cyanine based molecular rotor to enhance the sensitivity towards a viscous medium," *Materials Advances*, vol. 2, no. 14, pp. 4804–4813, 2021, ISSN: 2633-5409. DOI: 10.1039/D1MA00277E. [Online]. Available: http://xlink.rsc.org/?DOI=D1MA00277E.

[217] A. K. Pandey and R. Pratap, "Effect of flexural modes on squeeze film damping in MEMS cantilever resonators," *Journal of Micromechanics and Microengineering*, vol. 17, no. 12, pp. 2475–2484, 2007, ISSN: 09601317. DOI: 10.1088/0960-1317/17/12/013.

[218] M. Herant and M. Dembo, "Cytopede: A three-dimensional tool for modeling cell motility on a flat surface," *Journal of Computational Biology*, vol. 17, no. 12, pp. 1639–1677, 2010, ISSN: 10665277. DOI: 10.1089/cmb.2009.0271.

[219] L. Hancock, "Book Review: Book Review," *Criminology & Criminal Justice*, vol. 10, no. 4, pp. 419–420, 2010, ISSN: 1748-8958. DOI: 10.1177/1748895810383807.

[220] X. Zeng and S. Li, "Multiscale modeling and simulation of soft adhesion and contact of stem cells," *Journal of the mechanical behavior of biomedical materials*, vol. 4, no. 2, pp. 180–189, 2011.

[221] Z. Guo, X. Shi, Y. Chen, H. Chen, X. Peng, and P. Harrison, "Mechanical modeling of incompressible particle-reinforced neo-hookean composites based on numerical homogenization," *Mechanics of Materials*, vol. 70, pp. 1–17, 2014.

[222] I. Fried and A. R. Johnson, "A note on elastic energy density functions for largely deformed compressible rubber solids," *Computer methods in applied mechanics and engineering*, vol. 69, no. 1, pp. 53–64, 1988.

[223] A. Boccaccio, A. E. Uva, M. Papi, M. Fiorentino, M. De Spirito, and G. Monno, "Nanoindentation characterisation of human colorectal cancer cells considering cell geometry, surface roughness and hyperelastic constitutive behaviour," *Nanotechnology*, vol. 28, no. 4, p. 045 703, 2016.

[224] J. L. Bays and K. A. DeMali, "Vinculin in cell–cell and cell–matrix adhesions," *Cellular and Molecular Life Sciences*, vol. 74, no. 16, pp. 2999–3009, 2017.

[225] D. W. Zhou, T. T. Lee, S. Weng, J. Fu, and A. J. García, "Effects of substrate stiffness and actomyosin contractility on coupling between force transmission and vinculin–paxillin recruitment at single focal adhesions," *Molecular biology of the cell*, vol. 28, no. 14, pp. 1901–1911, 2017.

[226] P. Avitabile, "Experimental modal analysis," *Sound and vibration*, vol. 35, no. 1, pp. 20–31, 2001.

[227] M. E. Grady, R. J. Composto, and D. M. Eckmann, "Cell elasticity with altered cytoskeletal architectures across multiple cell types," *Journal of the mechanical behavior of biomedical materials*, vol. 61, pp. 197–207, 2016.

[228] I. Fried and A. R. Johnson, "A note on elastic energy density functions for largely deformed compressible rubber solids," *Computer Methods in Applied Mechanics and Engineering*, vol. 69, no. 1, pp. 53–64, 1988, ISSN: 00457825. DOI: 10.1016/0045-7825(88)90166-1.

[229] X. Zeng and S. Li, "Multiscale modeling and simulation of soft adhesion and contact of stem cells," *Journal of the Mechanical Behavior of Biomedical Materials*, vol. 4, no. 2, pp. 180–189, 2011, ISSN: 17516161. DOI: 10.1016/j.jmbbm.2010.06.002. [Online]. Available: http://dx.doi.org/10.1016/j.jmbbm.2010.06.002.

[230] G. Zhang, M. Long, Z.-Z. Wu, and W.-Q. Yu, "Mechanical properties of hepatocellular carcinoma cells," *World Journal of Gastroenterology*, vol. 8, no. 2, p. 243, 2002.

[231] C. Oomens, *Cellular and biomolecular mechanics and mechanobiology*, 2014.

[232] F. Guilak, J. R. Tedrow, and R. Burgkart, "Viscoelastic properties of the cell nucleus," *Biochemical and biophysical research communications*, vol. 269, no. 3, pp. 781–786, 2000.

[233] N. Caille, O. Thoumine, Y. Tardy, and J.-J. Meister, "Contribution of the nucleus to the mechanical properties of endothelial cells," *Journal of biomechanics*, vol. 35, no. 2, pp. 177–187, 2002.

[234] D. Ribatti, R. Tamma, and T. Annese, "Epithelial-mesenchymal transition in cancer: A historical overview," *Translational oncology*, vol. 13, no. 6, p. 100 773, 2020.

[235] J. Xu, S. Lamouille, and R. Derynck, "Tgf-$\beta$-induced epithelial to mesenchymal transition," *Cell research*, vol. 19, no. 2, pp. 156–172, 2009.

[236] G. Nagaraja, M Othman, B. Fox, *et al.*, "Gene expression signatures and biomarkers of noninvasive and invasive breast cancer cells: Comprehensive profiles by representational difference analysis, microarrays and proteomics," *Oncogene*, vol. 25, no. 16, pp. 2328–2338, 2006.

[237] G. Y. Lee and C. T. Lim, "Biomechanics approaches to studying human diseases," *Trends in biotechnology*, vol. 25, no. 3, pp. 111–118, 2007.

[238] M. Lekka, "Discrimination between normal and cancerous cells using afm," *Bionanoscience*, vol. 6, no. 1, pp. 65–80, 2016.

[239] H. Zhang, Y. Guo, Y. Zhou, *et al.*, "Fluidity and elasticity form a concise set of viscoelastic biomarkers for breast cancer diagnosis based on kelvin–voigt fractional derivative modeling," *Biomechanics and Modeling in Mechanobiology*, vol. 19, no. 6, pp. 2163–2177, 2020.

[240] A. N. Ketene, E. M. Schmelz, P. C. Roberts, and M. Agah, "The effects of cancer progression on the viscoelasticity of ovarian cell cytoskeleton structures," *Nanomedicine: Nanotechnology, Biology and Medicine*, vol. 8, no. 1, pp. 93–102, 2012.

[241] Y. Nematbakhsh, K. T. Pang, and C. T. Lim, "Correlating the viscoelasticity of breast cancer cells with their malignancy," *Convergent Science Physical Oncology*, vol. 3, no. 3, p. 034 003, 2017.

[242] S. E. Cross, Y.-S. Jin, J. Tondre, R. Wong, J. Rao, and J. K. Gimzewski, "Afm-based analysis of human metastatic cancer cells," *Nanotechnology*, vol. 19, no. 38, p. 384 003, 2008.

[243] M. K. Kuimova, S. W. Botchway, A. W. Parker, *et al.*, "Imaging intracellular viscosity of a single cell during photoinduced cell death," *Nature chemistry*, vol. 1, no. 1, pp. 69–73, 2009.

[244] H. J. Halpern, G. Chandramouli, E. D. Barth, *et al.*, "Diminished aqueous microviscosity of tumors in murine models measured with in vivo radiofrequency electron paramagnetic resonance," *Cancer research*, vol. 59, no. 22, pp. 5836–5841, 1999.

[245] J. Swanner, C. D. Fahrenholtz, I. Tenvooren, *et al.*, "Silver nanoparticles selectively treat triple-negative breast cancer cells without affecting non-malignant breast epithelial cells in vitro and in vivo," *FASEB BioAdvances*, vol. 1, no. 10, pp. 639–660, 2019.

[246] K. Luby-Phelps, "Cytoarchitecture and physical properties of cytoplasm: Volume, viscosity, diffusion, intracellular surface area," *International review of cytology*, vol. 192, pp. 189–221, 1999.

[247] E. M. Mfoumou, "A noninvasive biomechanical characterization approach for application to cell physiology and developing organs," Ph.D. dissertation, Concordia University, 2012.

[248] Y. Katsuno, S. Lamouille, and R. Derynck, "Tgf-$\beta$ signaling and epithelial–mesenchymal transition in cancer progression," *Current opinion in oncology*, vol. 25, no. 1, pp. 76–84, 2013.

[249] Y. Nematbakhsh, K. T. Pang, and C. T. Lim, "Correlating the viscoelasticity of breast cancer cells with their malignancy," *Convergent Science Physical Oncology*, vol. 3, no. 3, p. 034 003, 2017. DOI: 10.1088/2057-1739/aa7ffb.

[250] J Escribano, M. Sánchez, and J. García-Aznar, "A discrete approach for modeling cell–matrix adhesions," *Computational particle mechanics*, vol. 1, no. 2, pp. 117–130, 2014.

[251] M. Gupta, B. Doss, C. T. Lim, R. Voituriez, and B. Ladoux, "Single cell rigidity sensing: A complex relationship between focal adhesion dynamics and large-scale actin cytoskeleton remodeling," *Cell adhesion & migration*, vol. 10, no. 5, pp. 554–567, 2016.

[252] M. Vassaux and J.-L. Milan, "Stem cell mechanical behaviour modelling: Substrate's curvature influence during adhesion," *Biomechanics and modeling in mechanobiology*, vol. 16, no. 4, pp. 1295–1308, 2017.

[253] S. Mahitha, A. Das, A. R. Chowdhury, and P. Datta, "Deformation of tumor cell with variation of extracellular matrix density and cytoskeleton: Cellular growth, migration behavior," 2022.

[254] R. Krishnan, C. Y. Park, Y.-C. Lin, *et al.*, "Reinforcement versus fluidization in cytoskeletal mechanoresponsiveness," *PloS one*, vol. 4, no. 5, e5486, 2009.

[255] X. Cao, E. Ban, B. M. Baker, *et al.*, "Multiscale model predicts increasing focal adhesion size with decreasing stiffness in fibrous matrices," *Proceedings of the National Academy of Sciences*, vol. 114, no. 23, E4549–E4555, 2017.

[256] J. Gonzalez-Molina, X. Zhang, M. Borghesan, *et al.*, "Extracellular fluid viscosity enhances liver cancer cell mechanosensing and migration," *Biomaterials*, vol. 177, pp. 113–124, 2018.

[257] O. Thoumine, A. Ott, O. Cardoso, and J.-J. Meister, "Microplates: A new tool for manipulation and mechanical perturbation of individual cells," *Journal of biochemical and biophysical methods*, vol. 39, no. 1-2, pp. 47–62, 1999.

[258] K. D. Webster, W. P. Ng, and D. A. Fletcher, "Tensional homeostasis in single fibroblasts," *Biophysical journal*, vol. 107, no. 1, pp. 146–155, 2014.

[259] E. Moeendarbary and A. R. Harris, "Cell mechanics: Principles, practices, and prospects," *Wiley Interdisciplinary Reviews: Systems Biology and Medicine*, vol. 6, no. 5, pp. 371–388, 2014.

[260] P. A. Pullarkat, P. A. Fernández, and A. Ott, "Rheological properties of the eukaryotic cell cytoskeleton," *Physics Reports*, vol. 449, no. 1-3, pp. 29–53, 2007.

[261] M Fraldi, A Cugno, L. Deseri, K Dayal, and N. Pugno, "A frequency-based hypothesis for mechanically targeting and selectively attacking cancer cells," *Journal of the Royal Society Interface*, vol. 12, no. 111, p. 20 150 656, 2015.

[262] S. Boland, E. Boisvieux-Ulrich, O. Houcine, *et al.*, "Tgf beta 1 promotes actin cytoskeleton reorganization and migratory phenotype in epithelial tracheal cells in primary culture," *Journal of cell science*, vol. 109, no. 9, pp. 2207–2219, 1996.

[263] M. Schliwa, T. Nakamura, K. R. Porter, and U. Euteneuer, "A tumor promoter induces rapid and coordinated reorganization of actin and vinculin in cultured cells.," *The Journal of cell biology*, vol. 99, no. 3, pp. 1045–1059, 1984.

[264] M. A. Wozniak, K. Modzelewska, L. Kwong, and P. J. Keely, "Focal adhesion regulation of cell behavior," *Biochimica et Biophysica Acta (BBA)-Molecular Cell Research*, vol. 1692, no. 2-3, pp. 103–119, 2004.

[265] A. Geltmeier, B. Rinner, D. Bade, *et al.*, "Characterization of dynamic behaviour of mcf7 and mcf10a cells in ultrasonic field using modal and harmonic analyses," *PloS one*, vol. 10, no. 8, e0134999, 2015.

[266] J. D. Humphries, P. Wang, C. Streuli, B. Geiger, M. J. Humphries, and C. Ballestrem, "Vinculin controls focal adhesion formation by direct interactions with talin and actin," *The Journal of cell biology*, vol. 179, no. 5, pp. 1043–1057, 2007.

[267] X. Cao, "Continuum modeling of cell-extracellular environment interaction," Ph.D. dissertation, University of Pennsylvania, 2019.

[268] S. E. Cross, Y.-S. Jin, J. Rao, and J. K. Gimzewski, "Nanomechanical analysis of cells from cancer patients," in *Nano-Enabled Medical Applications*, Jenny Stanford Publishing, 2020, pp. 547–566.

[269] N. Wessells, B. Spooner, J. Ash, *et al.*, "Microfilaments in cellular and developmental processes: Contractile microfilament machinery of many cell types is reversibly inhibited by cytochalasin b.," *Science*, vol. 171, no. 3967, pp. 135–143, 1971.

[270] R. Marcu, Y. J. Choi, J. Xue, *et al.*, "Human organ-specific endothelial cell heterogeneity," *IScience*, vol. 4, pp. 20–35, 2018.

[271] B. Fallqvist, M. L. Fielden, T. Pettersson, N. Nordgren, M. Kroon, and A. K. Gad, "Experimental and computational assessment of f-actin influence in regulating cellular stiffness and relaxation behaviour of fibroblasts," *Journal of the Mechanical Behavior of Biomedical Materials*, vol. 59, pp. 168–184, 2016.

[272] C Guzman, S Jeney, L Kreplak, *et al.*, "Exploring the mechanical properties of single vimentin intermediate filaments by atomic force microscopy," *Journal of molecular biology*, vol. 360, no. 3, pp. 623–630, 2006.

[273] P. A. Janmey, U. Euteneuer, P. Traub, and M. Schliwa, "Viscoelastic properties of vimentin compared with other filamentous biopolymer networks.," *The Journal of cell biology*, vol. 113, no. 1, pp. 155–160, 1991.

[274] B. D. Hoffman, C. Grashoff, and M. A. Schwartz, "Dynamic molecular processes mediate cellular mechanotransduction," *Nature*, vol. 475, no. 7356, pp. 316–323, 2011.

[275] D. A. Fletcher and R. D. Mullins, "Cell mechanics and the cytoskeleton," *Nature*, vol. 463, no. 7280, pp. 485–492, 2010.

[276] Q. Wei, S. Wang, F. Han, *et al.*, "Cellular modulation by the mechanical cues from biomaterials for tissue engineering.," *Biomaterials translational*, vol. 2, no. 4, pp. 323–342, 2021.

[277] D. E. Discher, P. Janmey, and Y.-l. Wang, "Tissue cells feel and respond to the stiffness of their substrate," *Science*, vol. 310, no. 5751, pp. 1139–1143, 2005.

[278] S. Kumar and V. M. Weaver, "Mechanics, malignancy, and metastasis: The force journey of a tumor cell," *Cancer and Metastasis Reviews*, vol. 28, no. 1, pp. 113–127, 2009.

[279] B. Eckes, D. Dogic, E. Colucci-Guyon, *et al.*, "Impaired mechanical stability, migration and contractile capacity in vimentin-deficient fibroblasts," *Journal of cell science*, vol. 111, no. 13, pp. 1897–1907, 1998.

[280] G. Fenteany, P. A. Janmey, and T. P. Stossel, "Signaling pathways and cell mechanics involved in wound closure by epithelial cell sheets," *Current biology*, vol. 10, no. 14, pp. 831–838, 2000.

[281] H. Zhang and K.-K. Liu, "Optical tweezers for single cells," *Journal of the Royal Society interface*, vol. 5, no. 24, pp. 671–690, 2008.

[282] N. F. Läubli, J. T. Burri, J. Marquard, *et al.*, "3d mechanical characterization of single cells and small organisms using acoustic manipulation and force microscopy," *Nature communications*, vol. 12, no. 1, pp. 1–11, 2021.

[283] T. Tzvetkova-Chevolleau, A. Stéphanou, D. Fuard, J. Ohayon, P. Schiavone, and P. Tracqui, "The motility of normal and cancer cells in response to the combined influence of the substrate rigidity and anisotropic microstructure," *Biomaterials*, vol. 29, no. 10, pp. 1541–1551, 2008.

[284] C. Alibert, B. Goud, and J.-B. Manneville, "Are cancer cells really softer than normal cells?" *Biology of the Cell*, vol. 109, no. 5, pp. 167–189, 2017.

[285] G. Salbreux, G. Charras, and E. Paluch, "Actin cortex mechanics and cellular morphogenesis," *Trends in cell biology*, vol. 22, no. 10, pp. 536–545, 2012.

[286] C. Leduc and S. Etienne-Manneville, "Intermediate filaments in cell migration and invasion: The unusual suspects," *Current opinion in cell biology*, vol. 32, pp. 102–112, 2015.

[287] Y. Feng, Z. Tian, and M. Wan, "Bioeffects of low-intensity ultrasound in vitro: Apoptosis, protein profile alteration, and potential molecular mechanism," *Journal of ultrasound in medicine*, vol. 29, no. 6, pp. 963–974, 2010.

[288] F. Lejbkowicz and S. Salzberg, "Distinct sensitivity of normal and malignant cells to ultrasound in vitro.," *Environmental health perspectives*, vol. 105, no. suppl 6, pp. 1575–1578, 1997.

[289] S. Leulmi, X. Chauchet, M. Morcrette, *et al.*, "Triggering the apoptosis of targeted human renal cancer cells by the vibration of anisotropic magnetic particles attached to the cell membrane," *Nanoscale*, vol. 7, no. 38, pp. 15 904–15 914, 2015.

[290] C. Naud, C. Thébault, M. Carrière, *et al.*, "Cancer treatment by magneto-mechanical effect of particles, a review," *Nanoscale Advances*, vol. 2, no. 9, pp. 3632–3655, 2020.

[291] M. Olçum Uzan, "Invetigation of mechanical vibration effects on breast cancer cells," 2018.

[292] K. Haase and A. E. Pelling, "Investigating cell mechanics with atomic force microscopy," *Journal of The Royal Society Interface*, vol. 12, no. 104, p. 20 140 970, 2015.

[293] E. Moeendarbary, L. Valon, M. Fritzsche, *et al.*, "The cytoplasm of living cells behaves as a poroelastic material," *Nature materials*, vol. 12, no. 3, pp. 253–261, 2013.

[294] M. L. Gardel, K. E. Kasza, C. P. Brangwynne, J. Liu, and D. A. Weitz, "Mechanical response of cytoskeletal networks," *Methods in cell biology*, vol. 89, pp. 487–519, 2008.

[295] A. J. Maniotis, C. S. Chen, and D. E. Ingber, "Demonstration of mechanical connections between integrins, cytoskeletal filaments, and nucleoplasm that stabilize nuclear structure," *Proceedings of the National Academy of Sciences*, vol. 94, no. 3, pp. 849–854, 1997.

[296] K. Haase and A. E. Pelling, "Resiliency of the plasma membrane and actin cortex to large-scale deformation," *Cytoskeleton*, vol. 70, no. 9, pp. 494–514, 2013.

[297] Y.-W. Chiou, H.-K. Lin, M.-J. Tang, H.-H. Lin, and M.-L. Yeh, "The influence of physical and physiological cues on atomic force microscopy-based cell stiffness assessment," *PloS one*, vol. 8, no. 10, e77384, 2013.

[298] D. Docheva, D. Padula, C. Popov, W. Mutschler, H. Clausen-Schaumann, and M. Schieker, "Researching into the cellular shape, volume and elasticity of mesenchymal stem cells, osteoblasts and osteosarcoma cells by atomic force microscopy," *Journal of cellular and molecular medicine*, vol. 12, no. 2, pp. 537–552, 2008.

[299] T. Ohashi, Y Ishii, Y Ishikawa, T Matsumoto, and M Sato, "Experimental and numerical analyses of local mechanical properties measured by atomic force microscopy for sheared endothelial cells," *Biomedical materials and engineering*, vol. 12, no. 3, pp. 319–327, 2002.

[300] F. M. Hecht, J. Rheinlaender, N. Schierbaum, W. H. Goldmann, B. Fabry, and T. E. Schäffer, "Imaging viscoelastic properties of live cells by afm: Power-law rheology on the nanoscale," *Soft matter*, vol. 11, no. 23, pp. 4584–4591, 2015.

[301] M Sato, K Nagayama, N Kataoka, M Sasaki, and K Hane, "Local mechanical properties measured by atomic force microscopy for cultured bovine endothelial cells exposed to shear stress," *Journal of biomechanics*, vol. 33, no. 1, pp. 127–135, 2000.

[302] J. J. Wille, C. M. Ambrosi, and F. C. Yin, "Comparison of the effects of cyclic stretching and compression on endothelial cell morphological responses," *J. Biomech. Eng.*, vol. 126, no. 5, pp. 545–551, 2004.

[303] H. Haga, S. Sasaki, K. Kawabata, E. Ito, T. Ushiki, and T. Sambongi, "Elasticity mapping of living fibroblasts by afm and immunofluorescence observation of the cytoskeleton," *Ultramicroscopy*, vol. 82, no. 1-4, pp. 253–258, 2000.

[304] S. Vichare, S. Sen, and M. M. Inamdar, "Cellular mechanoadaptation to substrate mechanical properties: Contributions of substrate stiffness and thickness to cell stiffness measurements using afm," *Soft Matter*, vol. 10, no. 8, pp. 1174–1181, 2014.

[305] J. Hu, "Linear and nonlinear mechanics of mammalian cytoplasm," Ph.D. dissertation, Massachusetts Institute of Technology, 2019.

[306] A. F. Pegoraro, P. Janmey, and D. A. Weitz, "Mechanical properties of the cytoskeleton and cells," *Cold Spring Harbor perspectives in biology*, vol. 9, no. 11, a022038, 2017.

[307] E. Canetta, A. Duperray, A. Leyrat, and C. Verdier, "Measuring cell viscoelastic properties using a force-spectrometer: Influence of protein–cytoplasm interactions," *Biorheology*, vol. 42, no. 5, pp. 321–333, 2005.

[308] C. Imashiro, Y. Kurashina, T. Kuribara, M. Hirano, K. Totani, and K. Takemura, "Cell patterning method on a clinically ubiquitous culture dish using acoustic pressure generated from resonance vibration of a disk-shaped ultrasonic transducer," *IEEE Transactions on Biomedical Engineering*, vol. 66, no. 1, pp. 111–118, 2018.

[309] J. Ren, Y. Li, S. Hu, *et al.*, "Nondestructive quantification of single-cell nuclear and cytoplasmic mechanical properties based on large whole-cell deformation," *Lab on a Chip*, vol. 20, no. 22, pp. 4175–4185, 2020.

[310] B. Fallqvist, A. Kulachenko, and M. Kroon, "Modelling of cross-linked actin networks–influence of geometrical parameters and cross-link compliance," *Journal of Theoretical Biology*, vol. 350, pp. 57–69, 2014.

[311] M. Rodríguez-Nieto, P. Mendoza-Flores, D. García-Ortiz, *et al.*, "Viscoelastic properties of doxorubicin-treated ht-29 cancer cells by atomic force microscopy: The fractional zener model as an optimal viscoelastic model for cells," *Biomechanics and Modeling in Mechanobiology*, vol. 19, no. 3, pp. 801–813, 2020.

[312] M. Or and E. Kimmel, "Modeling linear vibration of cell nucleus in low intensity ultrasound field," *Ultrasound in medicine & biology*, vol. 35, no. 6, pp. 1015–1025, 2009.

[313] D. J. Ewins, *Modal testing: theory and practice*. Research studies press Letchworth, 1984, vol. 15.

[314] M. Lekka, P. Laidler, D. Gil, J. Lekki, Z. Stachura, and A. Hrynkiewicz, "Elasticity of normal and cancerous human bladder cells studied by scanning force microscopy," *European Biophysics Journal*, vol. 28, no. 4, pp. 312–316, 1999.

[315] Q. Li, G. Y. Lee, C. N. Ong, and C. T. Lim, "Afm indentation study of breast cancer cells," *Biochemical and biophysical research communications*, vol. 374, no. 4, pp. 609–613, 2008.

[316] E. Darling, S Zauscher, and F Guilak, "Viscoelastic properties of zonal articular chondrocytes measured by atomic force microscopy," *Osteoarthritis and cartilage*, vol. 14, no. 6, pp. 571–579, 2006.

[317] B Alberts, A Johnson, J Lewis, M Raff, K Roberts, and P Walter, "Molecular biology of the cell. garland science; new york, ny, usa: 2002," *Google Scholar*,

[318] S. Pellegrin and H. Mellor, "Actin stress fibres," *Journal of cell science*, vol. 120, no. 20, pp. 3491–3499, 2007.

[319] E. Hui, L. Moretti, T. H. Barker, and S. R. Caliari, "The combined influence of viscoelastic and adhesive cues on fibroblast spreading and focal adhesion organization," *Cellular and Molecular Bioengineering*, vol. 14, no. 5, pp. 427–440, 2021.

[320] K. Haase, Z. Al-Rekabi, and A. E. Pelling, "Mechanical cues direct focal adhesion dynamics," *Progress in molecular biology and translational science*, vol. 126, pp. 103–134, 2014.

[321] W. L. Anggayasti, C. Imashiro, T. Kuribara, K. Totani, and K. Takemura, "Low-frequency mechanical vibration induces apoptosis of a431 epidermoid carcinoma cells," *Engineering in Life Sciences*, vol. 20, no. 7, pp. 232–238, 2020.

[322] T. Luo, K. Mohan, P. A. Iglesias, and D. N. Robinson, "Molecular mechanisms of cellular mechanosensing," *Nature materials*, vol. 12, no. 11, pp. 1064–1071, 2013.

[323] Z. Zhao, Y. Li, M. Wang, S. Zhao, Z. Zhao, and J. Fang, "Mechanotransduction pathways in the regulation of cartilage chondrocyte homoeostasis," *Journal of cellular and molecular medicine*, vol. 24, no. 10, pp. 5408–5419, 2020.

[324] D. E. Ingber, "Cellular mechanotransduction: Putting all the pieces together again," *The FASEB journal*, vol. 20, no. 7, pp. 811–827, 2006.

[325] K. Naruse, "Mechanomedicine: Applications of mechanobiology to medical sciences and next-generation medical technologies," *Journal of Smooth Muscle Research*, vol. 54, pp. 83–90, 2018.

[326] S. Hughes, S. McBain, J. Dobson, and A. J. El Haj, "Selective activation of mechanosensitive ion channels using magnetic particles," *Journal of the Royal Society interface*, vol. 5, no. 25, pp. 855–863, 2008.

[327] P. K. Chaudhuri, B. C. Low, and C. T. Lim, "Mechanobiology of tumor growth," *Chemical reviews*, vol. 118, no. 14, pp. 6499–6515, 2018.

[328] X. Chen *et al.*, "The roles of cell stiffness in tumor cell tumorigenicity and nanoparticle-based mechanotargeting of soft cancer stem cell," 2021.

[329] F. Chowdhury, B. Huang, and N. Wang, "Forces in stem cells and cancer stem cells," *Cells & Development*, p. 203 776, 2022.

[330] H. T. Gilbert and J. Swift, "The consequences of ageing, progeroid syndromes and cellular senescence on mechanotransduction and the nucleus," *Experimental cell research*, vol. 378, no. 1, pp. 98–103, 2019.

[331] E. M. Weinheimer-Haus, S. Judex, W. J. Ennis, and T. J. Koh, "Low-intensity vibration improves angiogenesis and wound healing in diabetic mice," *PloS one*, vol. 9, no. 3, e91355, 2014.

[332] R. E. Roberts, O. Bilgen, R. D. Kineman, and T. J. Koh, "Parameter-dependency of low-intensity vibration for wound healing in diabetic mice," *Frontiers in bioengineering and biotechnology*, vol. 9, p. 654 920, 2021.

[333] D. A. Mitchison, "Basic mechanisms of chemotherapy," *Chest*, vol. 76, no. 6, pp. 771–780, 1979.

[334] C. Chaussy and S. Thüroff, "Results and side effects of high-intensity focused ultrasound in localized prostate cancer," *Journal of Endourology*, vol. 15, no. 4, pp. 437–440, 2001.

[335] P. Zinin, J. Allen III, and V. Levin, "Mechanical resonances of bacteria cells," *Physical Review E*, vol. 72, no. 6, p. 061 907, 2005.

[336] Y. Tang, L.-Y. Chen, A. Zhang, C.-P. Liao, M. E. Gross, and E. S. Kim, "In vivo non-thermal, selective cancer treatment with high-frequency medium-intensity focused ultrasound," *IEEE Access*, vol. 9, pp. 122 051–122 066, 2021.

[337] C. M. Bender, R. W. McDaniel, K. Murphy-Ende, *et al.*, "Chemotherapy-induced nausea and vomiting.," *Clinical Journal of Oncology Nursing*, vol. 6, no. 2, 2002.

[338] Z. Su, Z. Yang, Y. Xu, Y. Chen, and Q. Yu, "Apoptosis, autophagy, necroptosis, and cancer metastasis," *Molecular cancer*, vol. 14, no. 1, pp. 1–14, 2015.

[339] K. L. Rock and H. Kono, "The inflammatory response to cell death," *Annual review of pathology*, vol. 3, p. 99, 2008.

[340] M. Vanneman and G. Dranoff, "Combining immunotherapy and targeted therapies in cancer treatment," *Nature reviews cancer*, vol. 12, no. 4, pp. 237–251, 2012.

[341] G. P. Sims, D. C. Rowe, S. T. Rietdijk, R. Herbst, and A. J. Coyle, "Hmgb1 and rage in inflammation and cancer," *Annual review of immunology*, vol. 28, pp. 367–388, 2009.

[342] M. Chu, "Magnetic nanoparticles for cancer therapy through magnetic field-mediated mechanical force stimulation," in *The World Scientific Encyclopedia of Nanomedicine and Bioengineering II: Bioimplants, Regenerative Medicine, and Nano-Cancer Diagnosis and Phototherapy Volume 2: Advanced Nanomaterials for Bioimaging and Cancer Therapy*, World Scientific, 2017, pp. 163–174.

[343] S. Dutz and R. Hergt, "Magnetic particle hyperthermia—a promising tumour therapy?" *Nanotechnology*, vol. 25, no. 45, p. 452 001, 2014.

[344] S. Pongkitwitoon, G. Uzer, J. Rubin, and S. Judex, "Cytoskeletal configuration modulates mechanically induced changes in mesenchymal stem cell osteogenesis, morphology, and stiffness," *Scientific reports*, vol. 6, no. 1, pp. 1–12, 2016.

[345] W. R. Thompson, C. Guilluy, Z. Xie, *et al.*, "Mechanically activated fyn utilizes mtorc2 to regulate rhoa and adipogenesis in mesenchymal stem cells," *Stem cells*, vol. 31, no. 11, pp. 2528–2537, 2013.

[346] G. Uzer, W. R. Thompson, B. Sen, *et al.*, "Cell mechanosensitivity to extremely low-magnitude signals is enabled by a linced nucleus," *Stem cells*, vol. 33, no. 6, pp. 2063–2076, 2015.

[347] X. Yi, L. E. Wright, G. M. Pagnotti, *et al.*, "Mechanical suppression of breast cancer cell invasion and paracrine signaling to osteoclasts requires nucleo-cytoskeletal connectivity," *Bone research*, vol. 8, no. 1, pp. 1–13, 2020.

[348] V. Asati, A. Srivastava, S. Mukherjee, and P. K. Sharma, "Comparative analysis of antioxidant and antiproliferative activities of crude and purified flavonoid enriched fractions of pods/seeds of two desert legumes prosopis cineraria and cyamopsis tetragonoloba," *Heliyon*, vol. 7, no. 6, e07304, 2021.

[349] K. H. Kim and J. M. Sederstrom, "Assaying cell cycle status using flow cytometry," *Current protocols in molecular biology*, vol. 111, no. 1, pp. 28–6, 2015.

[350] L. C. Crowley, B. J. Marfell, A. P. Scott, and N. J. Waterhouse, "Quantitation of apoptosis and necrosis by annexin v binding, propidium iodide uptake, and flow cytometry," *Cold Spring Harbor Protocols*, vol. 2016, no. 11, pdb.prot087288, 2016. DOI: 10.1101/pdb.prot087288. eprint: http://cshprotocols.cshlp.org/content/2016/11/pdb.prot087288.full.pdf+html. [Online]. Available: http://cshprotocols.cshlp.org/content/2016/11/pdb.prot087288.abstract.

[351] T. Sun, Z. Yan, J. Cai, *et al.*, "Effects of mechanical vibration on cell morphology, proliferation, apoptosis, and cytokine expression/secretion in osteocyte-like mlo-y4 cells exposed to high glucose," *Cell Biology International*, vol. 44, no. 1, pp. 216–228, 2020.

[352] G. Mabilleau, R. Perrot, P. R. Flatt, N. Irwin, and D. Chappard, "High fat-fed diabetic mice present with profound alterations of the osteocyte network," *Bone*, vol. 90, pp. 99–106, 2016.

[353] H. Lai and N. P. Singh, "Acute exposure to a 60 hz magnetic field increases dna strand breaks in rat brain cells," *Bioelectromagnetics: Journal of the Bioelectromagnetics Society, The Society for Physical Regulation in Biology and Medicine, The European Bioelectromagnetics Association*, vol. 18, no. 2, pp. 156–165, 1997.

[354] H. C. Lai and N. P. Singh, "Medical applications of electromagnetic fields," in *IOP Conference Series: Earth and Environmental Science*, IOP Publishing, vol. 10, 2010, p. 012 006.

[355] Y. Kurashina, M. Hirano, C. Imashiro, K. Totani, J. Komotori, and K. Takemura, "Enzyme-free cell detachment mediated by resonance vibration with temperature modulation," *Biotechnology and bioengineering*, vol. 114, no. 10, pp. 2279–2288, 2017.

[356] C. Dal Lin, C. M. Radu, G. Vitiello, *et al.*, "Sounds stimulation on in vitro hl1 cells: A pilot study and a theoretical physical model," *International Journal of Molecular Sciences*, vol. 22, no. 1, p. 156, 2020.

[357] B. Wang, C. Bienvenu, J. Mendez-Garza, *et al.*, "Necrosis of hepg2 cancer cells induced by the vibration of magnetic particles," *Journal of magnetism and magnetic materials*, vol. 344, pp. 193–201, 2013.

[358] Y. Woo, H.-J. Lee, Y. M. Jung, and Y.-J. Jung, "Regulated necrotic cell death in alternative tumor therapeutic strategies," *Cells*, vol. 9, no. 12, p. 2709, 2020.

[359] R. S. Wong, "Apoptosis in cancer: From pathogenesis to treatment," *Journal of experimental & clinical cancer research*, vol. 30, no. 1, pp. 1–14, 2011.

[360] D. S. Ucker and J. S. Levine, "Exploitation of apoptotic regulation in cancer," *Frontiers in immunology*, vol. 9, p. 241, 2018.

[361] M. A. Md Ali, K. K. Ostrikov, F. A. Khalid, B. Y. Majlis, and A. A. Kayani, "Active bioparticle manipulation in microfluidic systems," *RSC Advances*, vol. 6, no. 114, pp. 113 066–113 094, 2016, ISSN: 2046-2069. DOI: 10.1039/C6RA20080J. [Online]. Available: http://xlink.rsc.org/?DOI=C6RA20080J.

[362] M. Samandari, K. Abrinia, and A. Sanati-Nezhad, "Acoustic Manipulation of Bio-Particles at High Frequencies: An Analytical and Simulation Approach," *Micromachines*, vol. 8, no. 10, p. 290, 2017, ISSN: 2072-666X. DOI: 10.3390/mi8100290. [Online]. Available: http://www.mdpi.com/2072-666X/8/10/290.

[363] F. Petersson, A. Nilsson, C. Holm, H. Jönsson, and T. Laurell, "Separation of lipids from blood utilizing ultrasonic standing waves in microfluidic channels," *The Analyst*, vol. 129, no. 10, pp. 938–943, 2004, ISSN: 0003-2654. DOI: 10.1039/B409139F. [Online]. Available: http://xlink.rsc.org/?DOI=B409139F.

[364] P. Augustsson, C. Magnusson, M. Nordin, H. Lilja, and T. Laurell, "Microfluidic, Label-Free Enrichment of Prostate Cancer Cells in Blood Based on Acoustophoresis," *Analytical Chemistry*, vol. 84, no. 18, pp. 7954–7962, 2012, ISSN: 0003-2700. DOI: 10.1021/ac301723s. [Online]. Available: https://pubs.acs.org/doi/10.1021/ac301723s.

[365] A. Lenshof, C. Magnusson, and T. Laurell, "Acoustofluidics 8: Applications of acoustophoresis in continuous flow microsystems," *Lab on a Chip*, vol. 12, no. 7, p. 1210, 2012, ISSN: 1473-0197. DOI: 10.1039/c2lc21256k. [Online]. Available: http://xlink.rsc.org/?DOI=c2lc21256k.

[366] P. Reichert, D. Deshmukh, L. Lebovitz, and J. Dual, "Thin film piezoelectrics for bulk acoustic wave (BAW) acoustophoresis," *Lab on a Chip*, vol. 18, no. 23, pp. 3655–3667, 2018, ISSN: 1473-0197. DOI: 10.1039/C8LC00833G. [Online]. Available: http://xlink.rsc.org/?DOI=C8LC00833G.

[367] X. Ding, S.-C. S. Lin, M. I. Lapsley, *et al.*, "Standing surface acoustic wave (SSAW) based multichannel cell sorting," *Lab on a Chip*, vol. 12, no. 21, p. 4228, 2012, ISSN: 1473-0197. DOI: 10.1039/c2lc40751e. [Online]. Available: http://xlink.rsc.org/?DOI=c2lc40751e.

[368] X. Wang, S. Chen, M. Kong, *et al.*, "Enhanced cell sorting and manipulation with combined optical tweezer and microfluidic chip technologies," *Lab on a Chip*, vol. 11, no. 21, p. 3656, 2011, ISSN: 1473-0197. DOI: 10.1039/c1lc20653b. [Online]. Available: http://xlink.rsc.org/?DOI=c1lc20653b.

[369] C. Baek, J. H. Yun, J. E. Wang, *et al.*, "A flexible energy harvester based on a lead-free and piezoelectric BCTZ nanoparticle–polymer composite," *Nanoscale*, vol. 8, no. 40, pp. 17 632–17 638, 2016, ISSN: 2040-3364. DOI: 10.1039/C6NR05784E. [Online]. Available: http://xlink.rsc.org/?DOI=C6NR05784E.

[370] K.-I. Park, S. Xu, Y. Liu, *et al.*, "Piezoelectric BaTiO 3 Thin Film Nanogenerator on Plastic Substrates," *Nano Letters*, vol. 10, no. 12, pp. 4939–4943, 2010, ISSN: 1530-6984. DOI: 10.1021/nl102959k. [Online]. Available: https://pubs.acs.org/doi/10.1021/nl102959k.

[371] Janusas, Pilkauskas, Janusas, and Palevicius, "Active PZT Composite Microfluidic Channel for Bioparticle Manipulation," *Sensors*, vol. 19, no. 9, p. 2020, 2019, ISSN: 1424-8220. DOI: 10.3390/s19092020. [Online]. Available: https://www.mdpi.com/1424-8220/19/9/2020.

[372] J. S. Rossier, A. Schwarz, F. Reymond, R. Ferrigno, F. Bianchi, and H. H. Girault, "Microchannel networks for electrophoretic separations," *Electrophoresis*, vol. 20, no. 4-5, pp. 727–731, 1999, ISSN: 0173-0835. DOI: 10.1002/(SICI)1522-2683(19990101)20:4/5<727::AID-ELPS727>3.0.CO;2-A. [Online]. Available: https://onlinelibrary.wiley.com/doi/10.1002/(SICI)1522-2683(19990101)20:4/5%3C727::AID-ELPS727%3E3.0.CO;2-A.

[373] A. Lenshof and T. Laurell, "Acoustophoresis," in *Encyclopedia of Nanotechnology*, Dordrecht: Springer Netherlands, 2015, pp. 1–6. DOI: 10.1007/978-94-007-6178-0_423-2. [Online]. Available: http://link.springer.com/10.1007/978-94-007-6178-0_423-2.

[374] A. Owhal, D. Gautam, S. U. Belgamwar, and V. K. P. Rao, "Atomistic approach to analyse transportation of water nanodroplet through a vibrating nanochannel: scope in bio-NEMS applications," *Molecular Simulation*, pp. 1–8, 2022, ISSN: 0892-7022. DOI: 10.1080/08927022.2022.2052065. [Online]. Available: https://www.tandfonline.com/doi/full/10.1080/08927022.2022.2052065.

[375] A. Munaz, M. J. A. Shiddiky, and N.-T. Nguyen, "Recent advances and current challenges in magnetophoresis based micro magnetofluidics," *Biomicrofluidics*, vol. 12, no. 3, p. 031 501, 2018, ISSN: 1932-1058. DOI: 10.1063/1.5035388. [Online]. Available: http://aip.scitation.org/doi/10.1063/1.5035388.

[376] A. Owhal, D. Boruah, and S. U. Belgamwar, "Establishment of an optical trapping curve for prediction of trapping parameters," *Optik*, vol. 208, p. 164 434, 2020, ISSN: 00304026. DOI: 10.1016/j.ijleo.2020.164434. [Online]. Available: https://linkinghub.elsevier.com/retrieve/pii/S0030402620302680.

[377] X. Xue, M. K. Patel, M. Kersaudy-Kerhoas, M. P. Desmulliez, C. Bailey, and D. Topham, "Analysis of fluid separation in microfluidic T-channels," *Applied Mathematical Modelling*, vol. 36, no. 2, pp. 743–755, 2012, ISSN: 0307904X. DOI: 10.1016/j.apm.2011.07.009. [Online]. Available: https://linkinghub.elsevier.com/retrieve/pii/S0307904X11003891.

[378] A. Hochstetter, R. Vernekar, R. H. Austin, *et al.*, "Deterministic Lateral Displacement: Challenges and Perspectives," *ACS Nano*, vol. 14, no. 9, pp. 10 784–10 795, 2020, ISSN: 1936-0851. DOI: 10.1021/acsnano.0c05186. [Online]. Available: https://pubs.acs.org/doi/10.1021/acsnano.0c05186.

[379] N. Raventhiran, R. S. Molla, K. Nandishwara, E. Johnson, and Y. Li, "Design and fabrication of a novel on-chip pressure sensor for microchannels," *Lab on a Chip*, vol. 22, no. 22, pp. 4306–4316, 2022, ISSN: 1473-0197. DOI: 10.1039/D2LC00648K. [Online]. Available: http://xlink.rsc.org/?DOI=D2LC00648K.

[380] J. Alvankarian and B. Majlis, "Tunable Microfluidic Devices for Hydrodynamic Fractionation of Cells and Beads: A Review," *Sensors*, vol. 15, no. 11, pp. 29 685–29 701, 2015, ISSN: 1424-8220. DOI: 10.3390/s151129685. [Online]. Available: http://www.mdpi.com/1424-8220/15/11/29685.

[381] S. Sohrabi, N. Kassir, and M. Keshavarz Moraveji, "Droplet microfluidics: fundamentals and its advanced applications," *RSC Advances*, vol. 10, no. 46, pp. 27 560–27 574, 2020, ISSN: 2046-2069. DOI: 10.1039/D0RA04566G. [Online]. Available: http://xlink.rsc.org/?DOI=D0RA04566G.

[382] L. Xu, A. Wang, X. Li, and K. W. Oh, "Passive micropumping in microfluidics for point-of-care testing," *Biomicrofluidics*, vol. 14, no. 3, p. 031 503, 2020, ISSN: 1932-1058. DOI: 10.1063/5.0002169. [Online]. Available: http://aip.scitation.org/doi/10.1063/5.0002169.

[383] J. Xu and D. Attinger, "Piezoelectric Actuation in Multiphase Microfluidics," in *Encyclopedia of Microfluidics and Nanofluidics*, Boston, MA: Springer US, 2013, pp. 1–10. DOI: 10.1007/978-3-642-27758-0_1766-3. [Online]. Available: http://link.springer.com/10.1007/978-3-642-27758-0_1766-3.

[384] S. Hettiarachchi, G. Melroy, A. Mudugamuwa, *et al.*, "Design and development of a microfluidic droplet generator with vision sensing for lab-on-a-chip devices," *Sensors and Actuators A: Physical*, vol. 332, p. 113 047, 2021, ISSN: 09244247. DOI: 10.1016/j.sna.2021.113047. [Online]. Available: https://linkinghub.elsevier.com/retrieve/pii/S0924424721005124.

[385] A. Veloso, X. Cheng, and K. Kerman, "Electrochemical biosensors for medical applications," in *Biosensors for Medical Applications*, Elsevier, 2012, pp. 3–40. DOI: 10.1533/9780857097187.1.3. [Online]. Available: https://linkinghub.elsevier.com/retrieve/pii/B9781845699352500012.

[386] F. Davis and S. Higson, "Biosensors for DNA and RNA detection and characterization," in *Biosensors for Medical Applications*, Elsevier, 2012, pp. 163–190. DOI: 10.1533/9780857097187.2.163. [Online]. Available: https://linkinghub.elsevier.com/retrieve/pii/B9781845699352500061.

[387] G. Destgeer, B. H. Ha, J. Park, J. H. Jung, A. Alazzam, and H. J. Sung, "Travelling Surface Acoustic Waves Microfluidics," *Physics Procedia*, vol. 70, pp. 34–37, 2015, ISSN: 18753892. DOI: 10.1016/j.phpro.2015.08.028. [Online]. Available: https://linkinghub.elsevier.com/retrieve/pii/S1875389215007695.

[388] M. Mazalan, A. Noor, Y. Wahab, S. Yahud, and W. Zaman, "Current Development in Interdigital Transducer (IDT) Surface Acoustic Wave Devices for Live Cell In Vitro Studies: A Review," *Micromachines*, vol. 13, no. 1, p. 30, 2021, ISSN: 2072-666X. DOI: 10.3390/mi13010030. [Online]. Available: https://www.mdpi.com/2072-666X/13/1/30.

[389] I. Voiculescu, F. Li, G. Kowach, K.-L. Lee, N. Mistou, and R. Kastberg, "Stretchable Piezoelectric Power Generators Based on ZnO Thin Films on Elastic Substrates," *Micromachines*, vol. 10, no. 10, p. 661, 2019, ISSN: 2072-666X. DOI: 10.3390/mi10100661. [Online]. Available: https://www.mdpi.com/2072-666X/10/10/661.

[390] S. S. Jugade and S. M. Kulkarni, "PDMS–ZnO flexible piezoelectric composites for measurement of muscle activity," *Bulletin of Materials Science*, vol. 43, no. 1, p. 209, 2020, ISSN: 0250-4707. DOI: 10.1007/s12034-020-02202-7. [Online]. Available: https://link.springer.com/10.1007/s12034-020-02202-7.

[391] X. Zhang, M.-Q. Le, O. Zahhaf, J.-F. Capsal, P.-J. Cottinet, and L. Petit, "Enhancing dielectric and piezoelectric properties of micro-ZnO/PDMS composite-based dielectrophoresis," *Materials & Design*, vol. 192, p. 108 783, 2020, ISSN: 02641275. DOI: 10.1016/j.matdes.2020.108783. [Online]. Available: https://linkinghub.elsevier.com/retrieve/pii/S0009261419310322https://linkinghub.elsevier.com/retrieve/pii/S0264127520303178.

[392] K. Jeronimo, V. Koutsos, R. Cheung, and E. Mastropaolo, "PDMS-ZnO Piezoelectric Nanocomposites for Pressure Sensors," *Sensors*, vol. 21, no. 17, p. 5873, 2021, ISSN: 1424-8220. DOI: 10.3390/s21175873. [Online]. Available: https://www.mdpi.com/1424-8220/21/17/5873.

[393] R. E. Cooper, Geoffrey M. Hausman, *The Cell: A Molecular Approach*, 7th ed. Sinauer Sunderland, 2000, p. 500.

[394] H.-S. Moon, C. E. Yoo, S. Kim, J. E. Lee, and W.-Y. Park, "Application of an open-chamber multi-channel microfluidic device to test chemotherapy drugs," *Scientific Reports*, vol. 10, no. 1, p. 20 343, 2020, ISSN: 2045-2322. DOI: 10.1038/s41598-020-77324-3. [Online]. Available: https://www.nature.com/articles/s41598-020-77324-3.

[395] R. Yusuf, Z. Duan, D. Lamendola, R. Penson, and M. Seiden, "Paclitaxel Resistance: Molecular Mechanisms and Pharmacologic Manipulation," *Current Cancer Drug Targets*, vol. 3, no. 1, pp. 1–19, 2003, ISSN: 15680096. DOI: 10.2174/1568009033333754. [Online]. Available: http://www.eurekaselect.com/openurl/content.php?genre=article\&issn=1568-0096\&volume=3&issue=1\&spage=1.

[396] J. Wang, N. Seebacher, H. Shi, Q. Kan, and Z. Duan, "Novel strategies to prevent the development of multidrug resistance (MDR) in cancer," *Oncotarget*, vol. 8, no. 48, pp. 84 559–84 571, 2017, ISSN: 1949-2553. DOI: 10.18632/oncotarget.19187. [Online]. Available: https://www.oncotarget.com/lookup/doi/10.18632/oncotarget.19187.

[397] F. W. Kremkau, "Cancer therapy with ultrasound: A historical review," *Journal of Clinical Ultrasound*, vol. 7, no. 4, pp. 287–300, 1979, ISSN: 00912751. DOI: 10.1002/jcu.1870070410. [Online]. Available: https://onlinelibrary.wiley.com/doi/10.1002/jcu.1870070410.

[398] B. J. Schwarz and M. H. Richardson, *Experimental Modal Analysis*. Orlando, FL: CSI Reliability Week, 1999, p. 12. [Online]. Available: https://www.maintenance.org/fileSendAction/fcType/0/fcOid/399590942963653618/filePointer/399590942964787702/fodoid/399590942964787700/28-_Experimental_Modal_Analysis.pdf.

[399] S. Aghlara-Fotovat, A. Nash, B. Kim, R. Krencik, and O. Veiseh, "Targeting the extracellular matrix for immunomodulation: applications in drug delivery and cell therapies," *Drug Delivery and Translational Research*, vol. 11, no. 6, pp. 2394–2413, 2021,

ISSN: 2190-393X. DOI: 10.1007/s13346-021-01018-0. [Online]. Available: https://link.springer.com/10.1007/s13346-021-01018-0.

[400] W. Strober, "Trypan Blue Exclusion Test of Cell Viability," in *Current Protocols in Immunology*, Hoboken, NJ, USA: John Wiley & Sons, Inc., 2001. DOI: 10.1002/0471142735.ima03bs21. [Online]. Available: https://onlinelibrary.wiley.com/doi/10.1002/0471142735.ima03bs21.

[401] H. W. Hou, M. E. Warkiani, B. L. Khoo, *et al.*, "Isolation and retrieval of circulating tumor cells using centrifugal forces," *Scientific Reports*, vol. 3, no. 1, p. 1259, 2013, ISSN: 2045-2322. DOI: 10.1038/srep01259. [Online]. Available: https://www.nature.com/articles/srep01259.

[402] A. Owhal, A. D. Pingale, S. U. Belgamwar, and J. S. Rathore, "Preparation of novel Zn/Gr MMC using a modified electro-co-deposition method: Microstructural and tribo-mechanical properties," *Materials Today: Proceedings*, vol. 44, no. xxxx, pp. 222–228, 2021, ISSN: 22147853. DOI: 10.1016/j.matpr.2020.09.459. [Online]. Available: https://doi.org/10.1016/j.matpr.2020.09.459https://linkinghub.elsevier.com/retrieve/pii/S2214785320371753.

[403] A. Owhal, A. D. Pingale, S. Khan, S. U. Belgamwar, P. N. Jha, and J. S. Rathore, "Electro-codeposited $\gamma$-Zn-Ni/Gr composite coatings: Effect of graphene concentrations in the electrolyte bath on tribo-mechanical, anti-corrosion and anti-bacterial properties," *Transactions of the IMF*, pp. 1–8, 2021, ISSN: 0020-2967. DOI: 10.1080/00202967.2021.1979815. [Online]. Available: https://www.tandfonline.com/doi/full/10.1080/00202967.2021.1979815.

[404] J. Zhang, C. Wang, and W. Chen, "Surface and piezoelectric effects on the buckling of piezoelectric nanofilms due to mechanical loads," *Meccanica*, vol. 49, no. 1, pp. 181–189, 2014, ISSN: 0025-6455. DOI: 10.1007/s11012-013-9784-x. [Online]. Available: http://link.springer.com/10.1007/s11012-013-9784-x.

[405] V. Kachwal, A. Srivastava, S. Thakar, *et al.*, "Engineering a light-driven cyanine based molecular rotor to enhance the sensitivity towards a viscous medium," *Materials Advances*, vol. 2, no. 14, pp. 4804–4813, 2021, ISSN: 2633-5409. DOI: 10.1039/D1MA00277E. [Online]. Available: http://xlink.rsc.org/?DOI=D1MA00277E.

[406] K. Krajnak, "Frequency-dependent changes in mitochondrial number and generation of reactive oxygen species in a rat model of vibration-induced injury," *Journal of Toxicology and Environmental Health, Part A*, vol. 83, no. 1, pp. 20–35, 2020.

[407] G. Shahane, W. Ding, M. Palaiokostas, and M. Orsi, "Physical properties of model biological lipid bilayers: insights from all-atom molecular dynamics simulations," *Journal of Molecular Modeling*, vol. 25, no. 3, p. 76, 2019, ISSN: 1610-2940. DOI: 10.1007/s00894-019-3964-0. [Online]. Available: http://link.springer.com/10.1007/s00894-019-3964-0.

[408] K. Mardilovich, S. L. Pankratz, and L. M. Shaw, "Expression and function of the insulin receptor substrate proteins in cancer," *Cell Communication and Signaling*, vol. 7, no. 1, p. 14, 2009, ISSN: 1478-811X. DOI: 10.1186/1478-811X-7-14. [Online]. Available: https://biosignaling.biomedcentral.com/articles/10.1186/1478-811X-7-14.

[409] P. Yeagle, *The Membranes of Cells*. Netherlands: Elsevier Science, 2016, p. 452.

[410] E. Evans and R. Hochmuth, "Membrane viscoelasticity," *Biophysical Journal*, vol. 16, no. 1, pp. 1–11, 1976, ISSN: 00063495. DOI: 10.1016/S0006-3495(76)85658-5. [Online]. Available: https://linkinghub.elsevier.com/retrieve/pii/S0006349576856585.

[411] D. Drabik, G. Chodaczek, S. Kraszewski, and M. Langner, "Mechanical Properties Determination of DMPC, DPPC, DSPC, and HSPC Solid-Ordered Bilayers," *Langmuir*, vol. 36, no. 14, pp. 3826–3835, 2020, ISSN: 0743-7463. DOI: 10.1021/acs.langmuir.0c00475. [Online]. Available: https://pubs.acs.org/doi/10.1021/acs.langmuir.0c00475.

[412] S. F. Fenz and K. Sengupta, "Giant vesicles as cell models," *Integrative Biology*, vol. 4, no. 9, p. 982, 2012, ISSN: 1757-9694. DOI: 10.1039/c2ib00188h. [Online]. Available: https://academic.oup.com/ib/article/4/9/982-995/5204469.

[413] G. van Meer, D. R. Voelker, and G. W. Feigenson, "Membrane lipids: where they are and how they behave," *Nature Reviews Molecular Cell Biology*, vol. 9, no. 2, pp. 112–124, 2008, ISSN: 1471-0072. DOI: 10.1038/nrm2330. [Online]. Available: http://www.nature.com/articles/nrm2330.

[414] E. Oldfield, M. Meadows, D. Rice, and R. Jacobs, "Spectroscopic studies of specifically deuterium labeled membrane systems. Nuclear magnetic resonance investigation of the effects of cholesterol in model systems," *Biochemistry*, vol. 17, no. 14, pp. 2727–2740, 1978, ISSN: 0006-2960. DOI: 10.1021/bi00607a006. [Online]. Available: https://pubs.acs.org/doi/abs/10.1021/bi00607a006.

[415] A. Filippov, G. Orädd, and G. Lindblom, "The Effect of Cholesterol on the Lateral Diffusion of Phospholipids in Oriented Bilayers," *Biophysical Journal*, vol. 84, no. 5, pp. 3079–3086, 2003, ISSN: 00063495. DOI: 10.1016/S0006-3495(03)70033-2. [Online]. Available: https://linkinghub.elsevier.com/retrieve/pii/S0006349503700332.

[416] L. A. Shobab, G.-Y. R. Hsiung, and H. H. Feldman, "Cholesterol in alzheimer's disease," *The Lancet Neurology*, vol. 4, no. 12, pp. 841–852, 2005.

[417] J. Montero, A. Morales, L. Llacuna, *et al.*, "Mitochondrial cholesterol contributes to chemotherapy resistance in hepatocellular carcinoma," *Cancer research*, vol. 68, no. 13, pp. 5246–5256, 2008.

[418] J. Gumbart, Y. Wang, A. Aksimentiev, E. Tajkhorshid, and K. Schulten, "Molecular dynamics simulations of proteins in lipid bilayers," *Current opinion in structural biology*, vol. 15, no. 4, pp. 423–431, 2005.

[419] D. Sengupta and A. Chattopadhyay, "Molecular dynamics simulations of gpcr–cholesterol interaction: An emerging paradigm," *Biochimica et Biophysica Acta (BBA)-Biomembranes*, vol. 1848, no. 9, pp. 1775–1782, 2015.

[420] S. A. Kharche and D. Sengupta, "Dynamic protein interfaces and conformational landscapes of membrane protein complexes," *Current Opinion in Structural Biology*, vol. 61, pp. 191–197, 2020.

[421] M. Javanainen, "Universal method for embedding proteins into complex lipid bilayers for molecular dynamics simulations," *Journal of chemical theory and computation*, vol. 10, no. 6, pp. 2577–2582, 2014.

[422] S. Hiller, R. G. Garces, T. J. Malia, V. Y. Orekhov, M. Colombini, and G. Wagner, "Solution structure of the integral human membrane protein vdac-1 in detergent micelles," *Science*, vol. 321, no. 5893, pp. 1206–1210, 2008.

[423] J. J. Hulce, A. B. Cognetta, M. J. Niphakis, S. E. Tully, and B. F. Cravatt, "Proteome-wide mapping of cholesterol-interacting proteins in mammalian cells," *Nature methods*, vol. 10, no. 3, pp. 259–264, 2013.

[424] A. N. Leonard, E. Wang, V. Monje-Galvan, and J. B. Klauda, "Developing and testing of lipid force fields with applications to modeling cellular membranes," *Chemical reviews*, vol. 119, no. 9, pp. 6227–6269, 2019.

[425] K. Pluhackova and R. A. Böckmann, "Biomembranes in atomistic and coarse-grained simulations," *Journal of physics: condensed matter*, vol. 27, no. 32, p. 323 103, 2015.

[426] A. Prakash, L. Janosi, and M. Doxastakis, "Gxxxg motifs, phenylalanine, and cholesterol guide the self-association of transmembrane domains of erbb2 receptors," *Biophysical Journal*, vol. 101, no. 8, pp. 1949–1958, 2011.

[427] S. J. Fleishman, J. Schlessinger, and N. Ben-Tal, "A putative molecular-activation switch in the transmembrane domain of erbb2," *Proceedings of the National Academy of Sciences*, vol. 99, no. 25, pp. 15 937–15 940, 2002.

[428] A. J. Beevers and A. Kukol, "The transmembrane domain of the oncogenic mutant erbb-2 receptor: A structure obtained from site-specific infrared dichroism and molecular dynamics," *Journal of molecular biology*, vol. 361, no. 5, pp. 945–953, 2006.

[429] O. P. Hamill and B. Martinac, "Molecular Basis of Mechanotransduction in Living Cells," *Physiological Reviews*, vol. 81, no. 2, pp. 685–740, 2001, ISSN: 0031-9333. DOI: 10.1152/physrev.2001.81.2.685. [Online]. Available: https://www.physiology.org/doi/10.1152/physrev.2001.81.2.685.

[430] B. Martinac and O. P. Hamill, "Gramicidin A channels switch between stretch activation and stretch inactivation depending on bilayer thickness," *Proceedings of the National Academy of Sciences*, vol. 99, no. 7, pp. 4308–4312, 2002, ISSN: 0027-8424. DOI: 10.1073/pnas.072632899. [Online]. Available: https://pnas.org/doi/full/10.1073/pnas.072632899.

[431] P. D. Blood, G. S. Ayton, and G. A. Voth, "Probing the Molecular-Scale Lipid Bilayer Response to Shear Flow Using Nonequilibrium Molecular Dynamics," *The Journal of Physical Chemistry B*, vol. 109, no. 39, pp. 18 673–18 679, 2005, ISSN: 1520-6106. DOI: 10.1021/jp0530449. [Online]. Available: https://pubs.acs.org/doi/10.1021/jp0530449.

[432] R. S. Cantor, "Lateral Pressures in Cell Membranes: A Mechanism for Modulation of Protein Function," *The Journal of Physical Chemistry B*, vol. 101, no. 10, pp. 1723–1725, 1997, ISSN: 1520-6106. DOI: 10.1021/jp963911x. [Online]. Available: https://pubs.acs.org/doi/10.1021/jp963911x.

[433] M. A. Haidekker, T. Ling, M. Anglo, H. Y. Stevens, J. A. Frangos, and E. A. Theodorakis, "New fluorescent probes for the measurement of cell membrane viscosity," *Chemistry and Biology*, vol. 8, no. 2, pp. 123–131, 2001, ISSN: 10745521. DOI: 10.1016/S1074-5521(00)90061-9. [Online]. Available: https://linkinghub.elsevier.com/retrieve/pii/S1074552100900619.

[434] M. Klähn and M. Zacharias, "Transformations in plasma membranes of cancerous cells and resulting consequences for cation insertion studied with molecular dynamics," *Physical Chemistry Chemical Physics*, vol. 15, no. 34, p. 14 427, 2013, ISSN: 1463-9076. DOI: 10.1039/c3cp52085d. [Online]. Available: http://xlink.rsc.org/?DOI=c3cp52085d.

[435] S. S. Deol, P. J. Bond, C. Domene, and M. S. Sansom, "Lipid-Protein Interactions of Integral Membrane Proteins: A Comparative Simulation Study," *Biophysical Journal*, vol. 87, no. 6, pp. 3737–3749, 2004, ISSN: 00063495. DOI: 10.1529/biophysj.104.048397. [Online]. Available: https://linkinghub.elsevier.com/retrieve/pii/S0006349504738424.

[436] J. P. Incardona and S. Eaton, "Cholesterol in signal transduction," *Current Opinion in Cell Biology*, vol. 12, no. 2, pp. 193–203, 2000, ISSN: 09550674. DOI: 10.1016/S0955-0674(99)00076-9. [Online]. Available: https://linkinghub.elsevier.com/retrieve/pii/S0955067499000769.

[437] G. Hedger and M. S. Sansom, "Lipid interaction sites on channels, transporters and receptors: Recent insights from molecular dynamics simulations," *Biochimica et Biophysica Acta (BBA) - Biomembranes*, vol. 1858, no. 10, pp. 2390–2400, 2016, ISSN: 00052736. DOI: 10.1016/j.bbamem.2016.02.037. [Online]. Available: https://linkinghub.elsevier.com/retrieve/pii/S0005273616300773.

[438] J. Grouleff, S. J. Irudayam, K. K. Skeby, and B. Schiøtt, "The influence of cholesterol on membrane protein structure, function, and dynamics studied by molecular dynamics simulations," *Biochimica et Biophysica Acta (BBA) - Biomembranes*, vol. 1848, no. 9, pp. 1783–1795, 2015, ISSN: 00052736. DOI: 10.1016/j.bbamem.2015.03.029. [Online]. Available: https://linkinghub.elsevier.com/retrieve/pii/S000527361500108X.

[439] R. Sheng, Y. Chen, H. Yung Gee, *et al.*, "Cholesterol modulates cell signaling and protein networking by specifically interacting with PDZ domain-containing scaffold proteins," *Nature Communications*, vol. 3, no. 1, p. 1249, 2012, ISSN: 2041-1723. DOI: 10.1038/ncomms2221. [Online]. Available: http://www.nature.com/articles/ncomms2221.

[440] P. L. Yeagle, "Non-covalent binding of membrane lipids to membrane proteins," *Biochimica et Biophysica Acta (BBA) - Biomembranes*, vol. 1838, no. 6, pp. 1548–1559, 2014, ISSN: 00052736. DOI: 10.1016/j.bbamem.2013.11.009. [Online]. Available: https://linkinghub.elsevier.com/retrieve/pii/S0005273613004069.

[441] K. Simons and R. Ehehalt, "Cholesterol, lipid rafts, and disease," *Journal of Clinical Investigation*, vol. 110, no. 5, pp. 597–603, 2002, ISSN: 0021-9738. DOI: 10.1172/JCI0216390. [Online]. Available: http://www.jci.org/articles/view/16390.

[442] J. A. Allen, R. A. Halverson-Tamboli, and M. M. Rasenick, "Lipid raft microdomains and neurotransmitter signalling," *Nature Reviews Neuroscience*, vol. 8, no. 2, pp. 128–140, 2007, ISSN: 1471-003X. DOI: 10.1038/nrn2059. [Online]. Available: http://www.nature.com/articles/nrn2059.

[443] M. Bucciantini, S. Rigacci, and M. Stefani, "Amyloid Aggregation: Role of Biological Membranes and the Aggregate–Membrane System," *The Journal of Physical Chemistry Letters*, vol. 5, no. 3, pp. 517–527, 2014, ISSN: 1948-7185. DOI: 10.1021/jz4024354. [Online]. Available: https://pubs.acs.org/doi/10.1021/jz4024354.

[444] M. A. Murphy, M. F. Horstemeyer, S. R. Gwaltney, *et al.*, "Nanomechanics of phospholipid bilayer failure under strip biaxial stretching using molecular dynamics," *Modelling and Simulation in Materials Science and Engineering*, vol. 24, no. 5, p. 055 008, 2016, ISSN: 0965-0393. DOI: 10.1088/0965-0393/24/5/055008. [Online]. Available: https://iopscience.iop.org/article/10.1088/0965-0393/24/5/055008.

[445] R. G. Morris and M. S. Turner, "Mobility Measurements Probe Conformational Changes in Membrane Proteins due to Tension," *Physical Review Letters*, vol. 115, no. 19, p. 198 101, 2015, ISSN: 0031-9007. DOI: 10.1103/PhysRevLett.115.198101. [Online]. Available: https://link.aps.org/doi/10.1103/PhysRevLett.115.198101.

[446] D. P. Tieleman, H. Leontiadou, A. E. Mark, and S.-J. Marrink, "Simulation of Pore Formation in Lipid Bilayers by Mechanical Stress and Electric Fields," *Journal of the American Chemical Society*, vol. 125, no. 21, pp. 6382–6383, 2003, ISSN: 0002-7863. DOI: 10.1021/ja029504i. [Online]. Available: https://pubs.acs.org/doi/10.1021/ja029504i.

[447] J. Neder, B. West, P. Nielaba, and F. Schmid, "Coarse-grained simulations of membranes under tension," *The Journal of Chemical Physics*, vol. 132, no. 11, p. 115 101, 2010, ISSN: 0021-9606. DOI: 10.1063/1.3352583. [Online]. Available: http://aip.scitation.org/doi/10.1063/1.3352583.

[448] E. S. Haswell, R. Phillips, and D. C. Rees, "Mechanosensitive Channels: What Can They Do and How Do They Do It?" *Structure*, vol. 19, no. 10, pp. 1356–1369, 2011, ISSN: 09692126. DOI: 10.1016/j.str.2011.09.005. [Online]. Available: https://linkinghub.elsevier.com/retrieve/pii/S0969212611003169.

[449] M. R. Prausnitz and R. Langer, "Transdermal drug delivery," *Nature Biotechnology*, vol. 26, no. 11, pp. 1261–1268, 2008, ISSN: 1087-0156. DOI: 10.1038/nbt.1504. [Online]. Available: http://www.nature.com/articles/nbt.1504.

[450] C.-Y. Lin, C.-H. Lee, Y.-H. Chuang, *et al.*, "Membrane protein-regulated networks across human cancers," *Nature Communications*, vol. 10, no. 1, p. 3131, 2019, ISSN: 2041-1723. DOI: 10.1038/s41467-019-10920-8. [Online]. Available: http://www.nature.com/articles/s41467-019-10920-8.

[451] J. Fantini and F. J. Barrantes, "How cholesterol interacts with membrane proteins: an exploration of cholesterol-binding sites including CRAC, CARC, and tilted domains," *Frontiers in Physiology*, vol. 4, pp. 1356–1369, 2013, ISSN: 1664-042X. DOI: 10.3389/fphys.2013.00031. [Online]. Available: http://journal.frontiersin.org/article/10.3389/fphys.2013.00031/abstract.

[452] F. Zakany, T. Kovacs, G. Panyi, and Z. Varga, "Direct and indirect cholesterol effects on membrane proteins with special focus on potassium channels," *Biochimica et Biophysica Acta (BBA) - Molecular and Cell Biology of Lipids*, vol. 1865, no. 8, p. 158 706, 2020, ISSN: 13881981. DOI: 10.1016/j.bbalip.2020.158706. [Online]. Available: https://linkinghub.elsevier.com/retrieve/pii/S1388198120300986.

[453] S. Jo, J. B. Lim, J. B. Klauda, and W. Im, "CHARMM-GUI Membrane Builder for Mixed Bilayers and Its Application to Yeast Membranes," *Biophysical Journal*, vol. 97, no. 1, pp. 50–58, 2009, ISSN: 00063495. DOI: 10.1016/j.bpj.2009.04.013. [Online]. Available: https://linkinghub.elsevier.com/retrieve/pii/S0006349509007917.

[454] Y. Andoh, S. Okazaki, and R. Ueoka, "Molecular dynamics study of lipid bilayers modeling the plasma membranes of normal murine thymocytes and leukemic GRSL cells," *Biochimica et Biophysica Acta (BBA) - Biomembranes*, vol. 1828, no. 4, pp. 1259–1270, 2013, ISSN: 00052736. DOI: 10.1016/j.bbamem.2013.01.005. [Online]. Available: https://linkinghub.elsevier.com/retrieve/pii/S0005273613000096.

[455] A. T. N. Vo, M. A. Murphy, T. W. Stone, P. K. Phan, M. I. Baskes, and R. K. Prabhu, "Molecular dynamics simulations of phospholipid bilayer mechanoporation under different strain states—a comparison between GROMACS and LAMMPS," *Modelling and Simulation in Materials Science and Engineering*, vol. 29, no. 5, p. 055 015, 2021, ISSN: 0965-0393. DOI: 10.1088/1361-651X/abfeaf. [Online]. Available: https://iopscience.iop.org/article/10.1088/1361-651X/abfeaf.

[456] S.-P. Fu, Z. Peng, H. Yuan, R. Kfoury, and Y.-N. Young, "Lennard-Jones type pair-potential method for coarse-grained lipid bilayer membrane simulations in LAMMPS," *Computer Physics Communications*, vol. 210, pp. 193–203, 2017, ISSN: 00104655. DOI: 10.1016/j.cpc.2016.09.018. [Online]. Available: https://linkinghub.elsevier.com/retrieve/pii/S0010465516302892.

[457] J. B. Klauda, R. M. Venable, J. A. Freites, *et al.*, "Update of the CHARMM All-Atom Additive Force Field for Lipids: Validation on Six Lipid Types," *The Journal of Physical Chemistry B*, vol. 114, no. 23, pp. 7830–7843, 2010, ISSN: 1520-6106. DOI: 10.1021/jp101759q. [Online]. Available: https://pubs.acs.org/doi/10.1021/jp101759q.

[458] M. Parrinello and A. Rahman, "Polymorphic transitions in single crystals: A new molecular dynamics method," *Journal of Applied Physics*, vol. 52, no. 12, pp. 7182–7190, 1981, ISSN: 0021-8979. DOI: 10.1063/1.328693. [Online]. Available: http://aip.scitation.org/doi/10.1063/1.328693.

[459] H. J. C. Berendsen, J. P. M. Postma, W. F. van Gunsteren, A. DiNola, and J. R. Haak, "Molecular dynamics with coupling to an external bath," *The Journal of Chemical Physics*, vol. 81, no. 8, pp. 3684–3690, 1984, ISSN: 0021-9606. DOI: 10.1063/1.448118. [Online]. Available: http://aip.scitation.org/doi/10.1063/1.448118.

[460] T. Darden, D. York, and L. Pedersen, "Particle mesh Ewald: An N  log( N ) method for Ewald sums in large systems," *The Journal of Chemical Physics*, vol. 98, no. 12, pp. 10 089–10 092, 1993, ISSN: 0021-9606. DOI: 10.1063/1.464397. [Online]. Available: http://aip.scitation.org/doi/10.1063/1.464397.

[461] W. Humphrey, A. Dalke, and K. Schulten, "VMD: Visual molecular dynamics," *Journal of Molecular Graphics*, vol. 14, no. 1, pp. 33–38, 1996, ISSN: 02637855. DOI: 10.1016/0263-7855(96)00018-5. [Online]. Available: https://linkinghub.elsevier.com/retrieve/pii/0263785596000185.

[462] J. Pan, S. Tristram-Nagle, and J. F. Nagle, "Effect of cholesterol on structural and mechanical properties of membranes depends on lipid chain saturation," *Physical Review E*, vol. 80, no. 2, p. 021 931, 2009, ISSN: 1539-3755. DOI: 10.1103/PhysRevE.80.021931. [Online]. Available: https://link.aps.org/doi/10.1103/PhysRevE.80.021931.

[463] M Pasenkiewicz-Gierula, K Murzyn, T Róg, and C Czaplewski, "Molecular dynamics simulation studies of lipid bilayer systems.," *Acta biochimica Polonica*, vol. 47, no. 3, pp. 601–11, 2000, ISSN: 0001-527X. [Online]. Available: http://www.ncbi.nlm.nih.gov/pubmed/11310963.

[464] N. Kučerka, J. Pencer, M. P. Nieh, and J. Katsaras, "Influence of cholesterol on the bilayer properties of monounsaturated phosphatidylcholine unilamellar vesicles," *The European Physical Journal E*, vol. 23, no. 3, pp. 247–254, 2007, ISSN: 1292-8941. DOI: 10.1140/epje/i2007-10202-8. [Online]. Available: http://link.springer.com/10.1140/epje/i2007-10202-8.

[465] J. P. Nicolas, "A molecular dynamics study of an archaeal tetraether lipid membrane: Comparison with a dipalmitoylphosphatidylcholine lipid bilayer," *Lipids*, vol. 40, no. 10, pp. 1023–1030, 2005, ISSN: 0024-4201. DOI: 10.1007/s11745-005-1465-2. [Online]. Available: http://doi.wiley.com/10.1007/s11745-005-1465-2.

[466] C. Hofsäß, E. Lindahl, and O. Edholm, "Molecular Dynamics Simulations of Phospholipid Bilayers with Cholesterol," *Biophysical Journal*, vol. 84, no. 4, pp. 2192–2206, 2003, ISSN: 00063495. DOI: 10.1016/S0006-3495(03)75025-5. [Online]. Available: https://linkinghub.elsevier.com/retrieve/pii/S0006349503750255.

[467] M. K. Baker and C. F. Abrams, "Dynamics of Lipids, Cholesterol, and Transmembrane $\alpha$-Helices from Microsecond Molecular Dynamics Simulations," *The Journal of Physical Chemistry B*, vol. 118, no. 47, pp. 13 590–13 600, 2014, ISSN: 1520-6106. DOI: 10.1021/jp507027t. [Online]. Available: https://pubs.acs.org/doi/10.1021/jp507027t.

[468] A. S. Reddy, D. T. Warshaviak, and M. Chachisvilis, "Effect of membrane tension on the physical properties of DOPC lipid bilayer membrane," *Biochimica et Biophysica Acta (BBA) - Biomembranes*, vol. 1818, no. 9, pp. 2271–2281, 2012, ISSN: 00052736. DOI: 10.1016/j.bbamem.2012.05.006. [Online]. Available: https://linkinghub.elsevier.com/retrieve/pii/S000527361200154X.

[469] J.-H. Jeon, H. M.-S. Monne, M. Javanainen, and R. Metzler, "Anomalous Diffusion of Phospholipids and Cholesterols in a Lipid Bilayer and its Origins," *Physical Review Letters*, vol. 109, no. 18, p. 188 103, 2012, ISSN: 0031-9007. DOI: 10.1103/PhysRevLett.109.188103. [Online]. Available: https://link.aps.org/doi/10.1103/PhysRevLett.109.188103.

[470] R. M. Venable, F. L. Brown, and R. W. Pastor, "Mechanical properties of lipid bilayers from molecular dynamics simulation," *Chemistry and Physics of Lipids*, vol. 192, pp. 60–74, 2015, ISSN: 00093084. DOI: 10.1016/j.chemphyslip.2015.07.014. [Online]. Available: https://linkinghub.elsevier.com/retrieve/pii/S0009308415300190.

[471] T. K. Fujiwara, K. Iwasawa, Z. Kalay, *et al.*, "Confined diffusion of transmembrane proteins and lipids induced by the same actin meshwork lining the plasma membrane," *Molecular Biology of the Cell*, vol. 27, no. 7, P. Bassereau, Ed., pp. 1101–1119, 2016, ISSN: 1059-1524. DOI: 10.1091/mbc.E15-04-0186. [Online]. Available: https://www.molbiolcell.org/doi/10.1091/mbc.E15-04-0186.

[472] A. Zgorski, R. W. Pastor, and E. Lyman, "Surface Shear Viscosity and Interleaflet Friction from Nonequilibrium Simulations of Lipid Bilayers," *Journal of Chemical Theory and Computation*, vol. 15, no. 11, pp. 6471–6481, 2019, ISSN: 1549-9618. DOI: 10.1021/acs.jctc.9b00683. [Online]. Available: https://pubs.acs.org/doi/10.1021/acs.jctc.9b00683.

[473] H. A. Scheidt, D. Huster, and K. Gawrisch, "Diffusion of Cholesterol and Its Precursors in Lipid Membranes Studied by 1H Pulsed Field Gradient Magic Angle Spinning NMR," *Biophysical Journal*, vol. 89, no. 4, pp. 2504–2512, 2005, ISSN: 00063495. DOI: 10.1529/biophysj.105.062018. [Online]. Available: https://linkinghub.elsevier.com/retrieve/pii/S0006349505728915.

[474] G. Khelashvili, G. Pabst, and D. Harries, "Cholesterol Orientation and Tilt Modulus in DMPC Bilayers," *The Journal of Physical Chemistry B*, vol. 114, no. 22, pp. 7524–7534, 2010, ISSN: 1520-6106. DOI: 10.1021/jp101889k. [Online]. Available: https://pubs.acs.org/doi/10.1021/jp101889k.

[475] A. B. Basset, *A treatise on hydrodynamics: with numerous examples*. Deighton, Bell and Company, 1888, vol. 2.

[476] L. Landau and E. Lifshitz, "Fluid mechanics. translated from the russian by jb sykes and wh reid," *Course of Theoretical Physics*, vol. 6, 1987.

[477] C. Brennen, "A review of added mass and fluid inertial forces.," 1982.

[478] Y. A. Ilinskii, G. D. Meegan, E. A. Zabolotskaya, and S. Y. Emelianov, "Gas bubble and solid sphere motion in elastic media in response to acoustic radiation force," *The Journal of the Acoustical Society of America*, vol. 117, no. 4, pp. 2338–2346, 2005.